A parametric study on the compactibility of Ti-6Al-4V during direct powder rolling

Prepared by:

Hiranya Naicker

This dissertation is submitted for the degree of Master of Science in Materials Engineering

In the Department of Mechanical Engineering
University of Cape Town

February 2019

Key Words: Powder Metallurgy, Roll compaction theory, Ti-6Al-4V, Sintering, Blended elemental

Declaration

I know the meaning of plagiarism and declare that all the work in the document, save for that which is properly acknowledged, is my own. This dissertation has been submitted to the Turnitin module (or equivalent similarity and originality checking software) and I confirm that my supervisor has seen my report and any concerns revealed by such have been resolved with my supervisor.

I have not allowed, and will not allow anyone to copy my work with the intention of passing it off as his or her own work.

Name: **Hiranya Naicker**

Signature: Signed by candidate

Date: 8 February 2019

Acknowledgements

The financial assistance of the National Research Foundation (NRF), the Council for Scientific and Industrial Research (CSIR) and the Department of Science and Technology (DST) towards this research is hereby acknowledged. Opinions expressed and conclusions arrived at, are those of the author and not necessarily to be attributed to the aforementioned.

The author would like to acknowledge the following for their help and support throughout her studies:

- To my parents and siblings for their love and support throughout the undertaking of this project.
- To my supervisor, Professor RD Knutsen, for his support and guidance with the project.
- To Dr. Chikosha from the CSIR for her support with the project.
- To the students and staff at the Centre for Materials Engineering (CME) for their help, pleasant company and bananagrams.
- To the UCT mechanical engineering workshop for their assistance with many aspects of this project.
- To the Electron Microscope Unit (EMU) for all their assistance with the SEM.
- To the Department of Mechanical Engineering at the University of Cape Town for affording me the opportunity to undertake the current research.
- To Dr. Richard Curry for all his assistance on various pieces of equipment around the lab, specifically for his help with the vacuum furnace.
- To Mr. Velile Vilane for all the late nights and support with all things titanium.
- And finally, to Mr. Richard Whittemore, I will be eternally grateful to you for all the help and support you have provided over the years. Thank you.

Abstract

The widespread use of titanium and its alloys in structural applications has been limited to few high-end applications. The dominant reason for this being cost implications. These high costs arise from extracting titanium from its mineral form as well as that of the manufacturing processes to develop a final product. Since producing titanium products includes expensive starting stock, high machinability costs and high wastage, a need for a process that may minimize one or more of these factors is necessary. One such technology that exists is a branch of powder metallurgy (PM), direct powder rolling (DPR) which allows for a continuous approach to produce strip or sheet metal. Products developed by this process are however known to possess inferior properties to its wrought counterpart.

The present study comprises of a parametric study observing how two different blends of powder differ in the development of Ti-6Al-4V strip by employing the blended elemental (BE) approach to direct powder rolling. The objectives of this work include predicting the compaction behavior of the two respective blends during powder rolling to inform the production of high density green strip and to compare the outcomes of the prediction method to experimentally determined results using a gravity-fed laboratory-scale rolling mill with roll diameter of 265 mm and roll width of 150 mm. Johanson's rolling theory was applied to predict rolling outcomes and a fixed set of rolling parameters were implemented for the simulation and experimental segment of this dissertation.

The two blends being investigated include blending titanium powder with an elemental blend consisting of aluminium and vanadium powders (B1) and a master alloy blend of a 60Al-40V master alloy (B2). These two blends were used to validate the Johanson simulated rolling data. Fixed parameters applied to the rolling mill included using a roll speed of 14 rpm, roll face width of 65 mm and gravity-fed hopper outlet diameter of 25 mm. Variable roll gaps of 0.5, 1 and 1.5 mm were studied. Average relative green densities of B1 and B2 strips achieved at a roll gap of 1 mm were 77% and 73% respectively. Rolling performance of the B1 powder blend were higher than that of B2, reaching higher green densities and showing superior formability, as rolling at smaller roll gaps was achievable for B1 and not B2. Green strength of B1 and B2 strips at a roll gap of 1 mm reflected similar outcomes where B1 strips required a greater breaking load to fracture samples when compared to B2 indicating a stronger self-supporting compact. Furthermore, the Johanson rolling model proved to overestimate reasonable roll pressure values, although, the general trend of compactibility between B1 and B2 powder blends was reasonably predicted showing B1 to be more compressible than B2 during powder rolling.

Subsequent sintering at 1200 °C for 3 hours in a vacuum environment was applied to green strips to further densify and homogenize strips. Average relative sintered densities achieved for B1 and B2 strips rolled at a roll gap of 1 mm were 78% and 87% respectively. While green densities of B1 strips were higher than that of B2 strips, it was evident that the addition of the 60Al-40V master alloy to blend B2 resulted in superior sinterability as final sintered densities surpassed that of B1, even when starting at a lower green density after rolling. SEM/EDX was used to evaluate what effect sintering had on homogenization. A standard wrought Ti-6Al-4V specimen was used as the benchmark to compare homogenization results. B2 strips homogenized more than B1 strips when comparing to the baseline wrought sample.

It was concluded that both B1 and B2 powders used to create Ti-6Al-4V strip by direct powder rolling (DPR) exhibited high levels of porosity and a subsequent step is necessary to fully densify the material. While B1 strips exhibit superior rollability with higher green densities and green strength; after applying a sintering practice to both B1 and B2 strips, B2 sintered densities surpassed those of B1 and prove to homogenize to a greater degree than B1 strips. The superior roll compaction ability and inferior sinterability for B1 powders was attributed to the elemental powder, aluminium. While the addition of ductile aluminium to B1 aids roll compaction, its low melting point results in large pores evolving at sintering temperatures almost twice its melting point.

Table of Contents

List of Figures

List of Tables

Abbreviations and nomenclature

BCC	Body Centred Cubic
BE	Blended Elemental
CME	Centre for Materials Engineering
CP	Commercially Pure
DPR	Direct Powder Rolling
EDX	Energy Dispersive X-Ray Spectroscopy
ETD	Everhart-Thornley Detector
GA	Gas Atomised
HCP	Hexagonal Close Packed
HDH	Hydride-Dehydride
LM	Light Microscopy
MA	Master Alloy
PA	Pre-Alloyed
PM	Powder Metallurgy
SD	Standard Deviation
SEM	Scanning Electron Microscopy
XRD	X-ray Diffraction
β_{trans}	Beta-transus

μ	Wall friction coefficient
D	Roll diameter
d	Pocket size
P_0	Feed pressure
RW	Roll width
S	Roll gap
V_α	Volume at $\theta = \alpha$

V_θ	Volume between arc length segments ΔL at position θ
α	Nip angle
γ	Density
δ	Effective angle of internal friction
ΔL	Arc length
θ	Angular position in roll compaction
θ_{mp}	Angular position where the roll pressure is at its maximum
κ	Compressibility constant
σ	Normal stress
σ_1	Major principal stress
σ_2	Minor principal stress
σ_α	Mean normal stress at position $\theta = \alpha$
σ_θ	Mean normal stress at position θ
τ	Shear stress
ϕ	Wall friction angle
γ_α	Bulk density at $\theta = \alpha$
γ_θ	Bulk density at θ

1. Introduction

1.1 Subject of this study

The subject of this study is to investigate how two different blends of metal powders perform during direct powder rolling and whether these powders can successfully produce near fully dense homogeneous Ti-6Al-4V strip. The study includes a modelling component whereby a powder rolling theory developed by Johanson (1965)[1] was used to validate experimental results against the outputs of the simulation during the powder rolling stage of this study.

1.2 Background to the study

Properties such as excellent corrosion resistance and a high strength to weight ratio make titanium and its alloys an attractive structural metal aimed to be used in a wide range of applications. Ti-6Al-4V is known to be the flagship alloy from the titanium alloy family and is the most widely used, accounting for over 50% of titanium products made globally. However it is the high costs associated with the production of titanium products which leads to its limited widespread use[2].

One of the reasons for this high production cost is attributed to the costly and energy intensive process of extracting titanium from its mineral state. Another cause of this high cost are processes further upstream from mineral refinement such as machining, where titanium is said to be ten times as costly to machine when compared to aluminium products[3].

This has led to a number of innovative methods being investigated to reduce the cost of titanium products, one of which includes powder metallurgy (PM) technology. PM is particularly promising for producing near-net-shape components, reducing waste and limiting the need for costly machining. There are two distinct ways PM technology may be applied from the perspective of powder material selection that is, pre-alloyed (PA) and blended elemental (BE) approaches. Powder metallurgy (PM) using pre-alloyed (PA) powders makes use of powders generated from an ingot of the desired alloy produced by conventional means, while blended elemental (BE) PM incorporates blending either elemental powders, master alloy powders and/or a mixture of both in the appropriate respective ratios to create the desired alloy. The PA approach has proven to produce components with mechanical properties comparable to wrought products produced by conventional ingot metallurgy. The high cost of PA powders is however a pitfall of using this powder type and its primary use is mostly to simplify the manufacturing of near-net-shape products. BE powders on the other hand are a cheaper alternative to producing PM titanium alloy products. The titanium powder used in BE PM can be a direct reduction powder as opposed to PA powders. A drawback of using these elemental titanium powders is the impurity level present, namely oxygen and chlorine contamination. These two elements in particular have catastrophic effects further downstream as they prevent high densities from being achieved and limit the weldability of the metal[4,5].

Developing a more economically viable method to produce titanium and titanium alloy products would allow for their widespread use across a broader spectrum of industries, where high strength, low density materials will become an important material design criterion with rising fuel prices.

This research therefore aimed to investigate the feasibility of developing a cost effective process for producing Ti-6Al-4V strip by direct powder rolling (DPR) using low cost blended elemental (BE) powders. The research intended to create strip by rolling from two different BE powder blends, improve their densities and homogenise the material to improve the mechanical properties.

1.3 Objectives of this study

This study investigated two different blended elemental (BE) powder blends: B1 comprises of titanium, aluminium and vanadium elemental powders and B2 comprises of titanium elemental powder and a 60Al-40V master alloy powder.

This study aimed to achieve the following:

- Determine powder characteristics of BE powder blends B1 and B2 by conducting particle size analysis tests, uniaxial pressing tests, shear tests and wall friction tests.

- Create Ti-6Al-4V strip by employing BE direct powder rolling (DPR) using two different blends of BE powders.

- Implement Johanson's powder rolling theory and simulate powder rolling performance by obtaining rolling pressure data. This data will be acquired based on measured powder characteristic parameters and roll press dimensions from the Centre for Materials Engineering (CME) laboratory-scale rolling mill.

- Compare B1 and B2 powder behaviours and properties at a varying roll gap during the powder rolling stage.

- Characterise B1 and B2 green strips with respect to strip dimensions, density and green strength.

- Validate the predicted outcomes from the Johanson model against experimental data with respect to relative green density of rolled strips.

- Compare the contribution of sintering processes on B1 and B2 powders with respect to density, microstructure and homogenisation.

1.4 Scope and Limitations

The primary objectives of this study were: to investigate whether Ti-6Al-4V strip may be created using BE powders; how two different powder blends perform when applied to the direct powder rolling (DPR) methodology and; to determine how effective the Johanson model is at describing compaction during DPR.

Certain powder rolling parameters were controlled. The reason for this is based on a study by Zhang (2015)[6], where the author identified optimal conditions for rolling speed, roll face width and hopper outlet diameter when investigating DPR on stainless steel and CP-titanium (commercially pure) powders on the CME laboratory-scale rolling mill. The feed pressures used for the Johanson model were estimated based on a relationship defined by Simon and Guigon (2000)[7].

The relative densities calculated and presented in this study were calculated as a percentage of the theoretical full density of Ti-6Al-4V (4.43g/ml). Chlorine content of metal powders was not evaluated.

Given the measuring of green and sintered densities involved a destructive method, the samples used to compare the effects of sintering from green to sintered state were not the same, although process conditions were exactly the same.

Due to limitations of strip dimensions, three-point bend test standard specimen dimensions could not be achieved.

1.5 Plan of development

This dissertation begins with a brief background of an introduction to titanium and its alloys in Chapter 2.1 giving details on basic metallurgical concepts for this particular material and thermal treatments. Chapter 2.2 proceeds with a detailed analysis of powder metallurgy (PM) technology covering its importance in its application for low cost titanium products and fundamentals in techniques and procedures followed when investigating PM technology. Chapter 2.3 outlines roll compaction theory and Johanson's approach to understanding this technique. Chapter 2.4 concludes the literature survey of this dissertation exploring sintering theory and sintering applications to titanium and its alloys. Chapter 3 introduces the experimental methodology followed as well as materials used. Chapters 4 and 6 present and discuss powder and green strip properties acquired during the study. Chapter 5 describes the direct powder rolling (DPR) model implementation and results. Validation of the Johanson model against experimental findings are discussed in Chapter 7. In Chapter 8, as-sintered B1 and B2 strips are analysed and discussed describing densities, porosities and homogenisation attributes. Finally, Chapter 9 highlights the major conclusions reached based on the findings and Chapter 10 makes recommendations based on the conclusions drawn.

2. Literature Review

2.1 Introduction to titanium

Titanium and its alloys are predominantly used in high-end applications relating to aerospace, electronics and biomedical fields. This is attributed to their low density (4.51g/cm^3)[2] to strength ratio (approximately 60% the density of steels and nickel-based superalloys[2]), strong biocompatibility and excellent corrosion resistance. Titanium's high affinity for oxygen results in an immediate and spontaneous stable, thin, tightly bound oxide film upon exposure to air or water[8]. This accounts for its excellent corrosion resistance. Titanium can be strengthened significantly through alloying with other metals and deformation processing. There is however limited use of this metal and its alloys due to high production costs. For this reason, advantages associated with widespread use of titanium should be balanced against an additional cost factor.

2.1.1 Crystal structures and alloy types

Titanium is an allotropic material. As such, it is stable in various crystallographic forms at different temperatures. For titanium, two allotropes exist, namely an alpha (α) and beta (β) phase. At ambient temperature and pressure, the crystal structure is hexagonal closed packed (HCP) α-phase which transforms to a body centred cubic (BCC) structure (β-phase) at elevated temperatures (Figure 2.1). At room temperature, the α phase is stable. At elevated temperatures, the α-phase transforms into the β-phase, at the β-transus (β_{trans}) temperature of 882°C[8]. The β_{trans} is defined as the lowest equilibrium point at which the material is fully β [2,8].

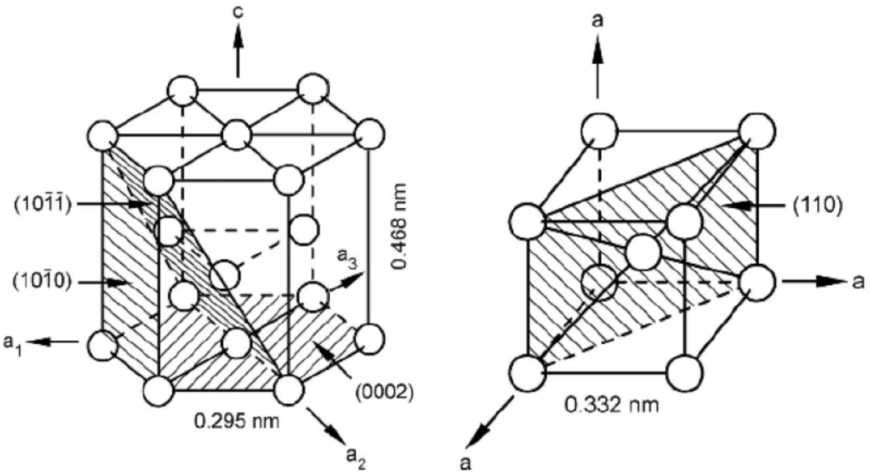

Figure 2.1: Crystal structures of HCP α (left) and BCC β (right) titanium[2]

The temperature ranges in which the α and the β-phases exist can be expanded by additions of α (Al, O, N, C, etc.) and β (V, Mo, Fe, Cr, etc.) stabilizing elements. These alloying elements are used to stabilise α or β-phases. They are used in retaining the β-phase at room temperature while coexisting with the α-phase.

Titanium alloys can be separated into four classes[1]:

- α - non-heat treatable alloys containing neutral alloying elements (e.g. tin) and/or α-stabilisers
- Near- α
- α -β -heat treatable alloys containing a combination of α and β-stabilisers
- β- alloys in a metastable state composed of fully retained β-phase (obtained on quenching) containing β-stabilisers (e.g. vanadium, molybdenum). Can be solution treated and aged
- Near-β.

The different classes mentioned above describe a chemistry and microstructure type which is seen after processing. An α alloy is one which does not usually form the β-phase. A near- α alloy will form a limited amount of β-phase on heating, and so microstructurally appears very similar to an α alloy at lower temperatures. An α-β alloy is one which will undergo a complete transformation to the β phase on heating but will transform back to the α-phase along with some β-phase still retained and/or transformed on cooling. A β-alloy is one which will be inclined to retain the β-phase, which formed initially at elevated temperatures, on cooling to lower temperatures permanently. This β-phase formed initially on cooling is however a metastable phase. This may result in possible precipitates forming during subsequent heat treatments.

2.1.2 Effects of alloying elements

Various alloying elements will have an effect on the microstructure and properties of titanium. α-stabilisers such as aluminium and oxygen will increase the temperature where α is stable, while β-stabilisers such as vanadium and molybdenum allow for the β-phase to stabilise at lower temperatures. α and β stabilisers are distinguished by how soluble the element is in each respective phase. An α-stabiliser is more soluble in the α-phase, while a β-stabiliser will have increased solubility in the β-phase. In addition, these stabilisers can have an effect on altering the β-transus (β_{trans}), where α-stabilisers raise the β_{trans} due to its α-stabilising properties and vice versa for β-stabilisers. The β_{trans} is a critical parameter to control as it is often used as a reference to some incremental temperature above or below the β_{trans} for deformation processing and heat treatments.

The flagship and most widely used titanium alloy is the α + β alloy Ti-6Al-4V. It consists of 6 wt. % aluminium and 4 wt. % vanadium (remaining balance is titanium). A schematic of a ternary phase diagram of Ti-6Al is presented in Figure 2.2a. MS represents the martensite start temperature, and the chemical composition for Ti-6Al-4V is indicated by a vertical dashed line on the 4 wt. % vanadium content on the x-axis. Ti-6Al-4V is an α + β alloy at temperatures below the β_{trans} and the chemical compositions of the α and β phases change with decreasing temperatures[8]. Since vanadium has higher solubility in the BCC structure, it enriches the β-phase and so stabilises this phase at low temperatures. Aluminium however favours the HCP structure and has higher solubility in the α-phase resulting in raising the $\beta_{trans.}$. The microstructure presented Figure 2.2b shows Ti-6Al-4V slowly cooled from above the β_{trans}. Here the β-phase is seen as a thin dark seam around the lighter α-lamellae phase. Given the nature of alloying elements, elemental partitioning is apparent in equilibrium α and β phases, where the α-phase will be enriched with aluminium while the β-phase will be aluminium deficient. The inverse is true for the vanadium content[9].

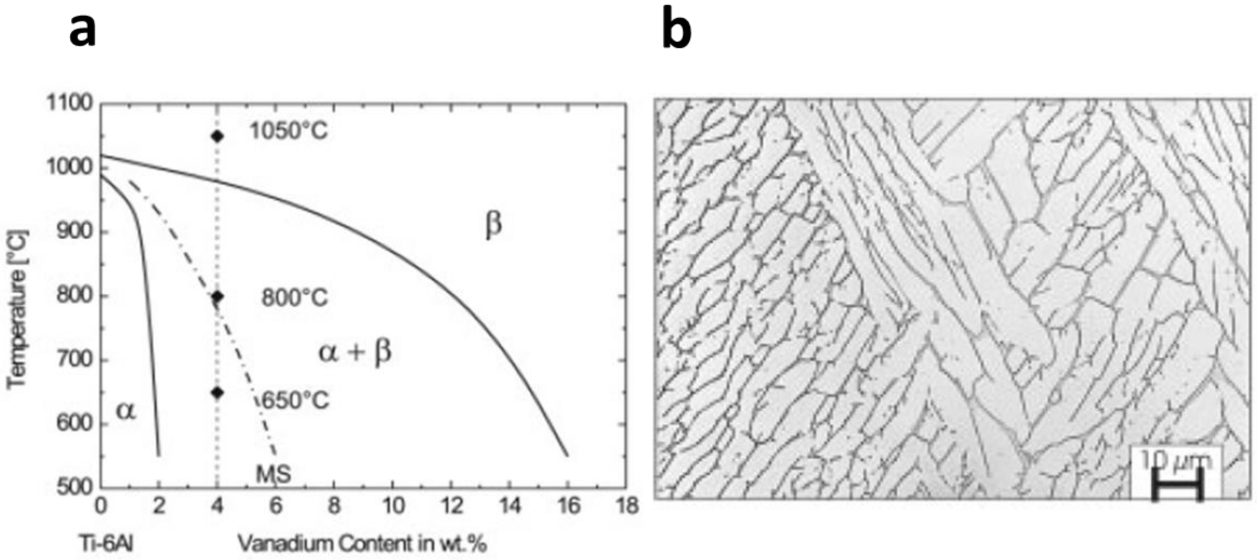

Figure 2.2: a) A schematic ternary phase diagram of Ti-6Al and b)microstructure of furnace cooled Ti-6Al from 1050°C [8]

2.1.3 *Thermal treatments and phase transformations of Ti-6Al- 4V*

Ti-6Al-4V is an alloy which can undergo various heat treatments such as annealing, quenching, tempering etc. to acquire the desired properties. The microstructure is dependent on the chemical composition of the alloy, processing history and heat treatments. Thermomechanical processing in combination with specific heat treatments are used to develop a specific microstructure or property.

The β_{trans} is seen to increase from 882°C to 995°C [8] with the addition of alloying elements for Ti-6Al-4V. The α- and β-stabilisers have different effects on the phase transformations observed. Aluminium being the α-stabiliser serves to increase the β_{trans} temperature allowing the α-phase to be stable at higher temperatures. Consequently vanadium, a β-stabiliser lowers the temperature at which the β-phase is stable[2]. An additional important group are impurity elements[10]. These elements with smaller atomic radii occupy interstitial sites within the crystal lattice and include elements such as oxygen, hydrogen, carbon and nitrogen. Hydrogen acts as a β-stabiliser while oxygen acts as an α-stabiliser. Above the β_{trans}, a commercial alloy is completely in the β-phase (Figure 2.2a). It is also important to note that titanium has an extremely high affinity for oxygen[2], especially at elevated temperatures.

Microstructure

On heating, the transformation from α to β is as a result of a diffusional transformation. Two noteworthy phase arrangements include lamellar (Figure 2.2b) and equiaxed microstructures. Due to the nature of the recrystallization process, both microstructural types may have fine or coarse arrangements depending on the heat treatment cycle. Slow cooling from the β-field will result in a finer lamellar structure and become coarser as the cooling rate is reduced. Martensitic structures are formed on rapid quenching from the β-field leading to a needle-like structure. For the equiaxed structure to develop, recrystallization must occur. Without sufficient deformation in the α + β field introducing cold work into the material, recrystallization will not follow. Microstructure informs mechanical behaviour in titanium alloys. Ductility and strength are improved in finer microstructures while coarser microstructures are more resistant to creep and fatigue. Equiaxed structures will have improved ductility and fatigue strength while lamellar structures have higher fracture toughnesses and creep resistance[8].

2.2 Powder metallurgy

With the widespread use of titanium being limited due to economic challenges, a number of innovative techniques have been explored to create an affordable demand for the metal and its alloys. One such technique is powder metallurgy (PM) technology. Powder metallurgy (PM) is a technique that relies on converting fine metal powders into solid components. One of the high costs associated with titanium production is machining costs for wrought components into final products. This suggests there is a market for near-net-shape fabrication techniques. For this reason, powder metallurgy (PM) is an attractive approach as there is an efficient use of material; complex shapes may be achieved; and reduced processing steps are conceivable.

2.2.1 Introduction

Powder metallurgy (PM) has been described as a processing route for the manufacturing of components from metal powders. The process can be broken down into four stages[11]:

1. Manufacturing of powders
2. Mixing or blending of powders
3. Compacting

4. Sintering

After powder production, blending may take place in the case of an alloy where elemental powders must be distributed homogeneously throughout the powder mixture. The powder is then pressed into a "green compact".. A "green compact" will maintain its shape through mechanical bonding as a result of compaction, however no chemical bonding would have occurred between powder particles. This compact is then heated to a certain temperature below the material melting point in a controlled atmosphere for a predefined period of time. This improves the properties of the compact by inducing solid state diffusion by promoting binding between particles. This process is referred to as sintering[11]. This is PM in its most basic form and is known as the "press and sinter" approach. There are however many more branches of PM that involve more complex practices. Figure 2.3 shows the general methodology followed in PM processing.

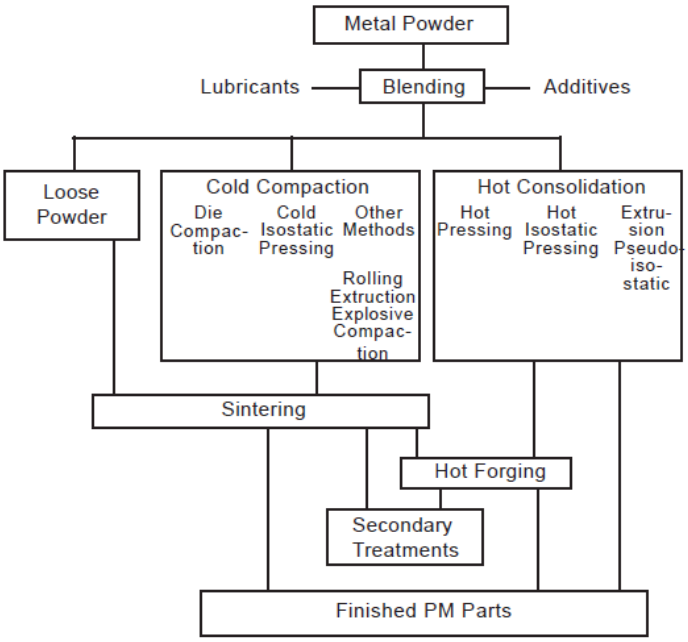

Figure 2.3: Basic steps of the Powder metallurgy process[11]

2.2.2 *The Importance of Researching Powder Metallurgy*

Pressing metal powders into specific shapes is not a new technology. Modern PM techniques began in the 1920s where tungsten carbide components were made and mass production of porous bronze bushings for bearings were prepared. From this it can be seen that the PM approach was initially (and still is) concerned with the manufacturing of materials or components which were difficult or impossible to be done by alternate means[12]. PM has expanded more rapidly in recent years primarily due to three potential reasons: economical processing, unique properties and captive processes. Using the PM production method to make precision components is an economical, rapid and high volume process route[12]. As the PM industry progressed, it challenged conventional production methods as it became apparent that near net-shape engineering components could be made by following the PM approach. Requirements for early structural components were modest and thus the 10% porosity retained was satisfactory for use. The attractiveness of this process was accounted for in its ability to produce parts to specific dimensions at a relatively low cost[13].

There has been much advancement in the industry since then, with improvements in the level of mechanical properties achievable due to improved densification techniques. This has allowed for components produced by the PM approach to compare to those manufactured by conventional methods[13]. However to ensure adequate mechanical properties may be achieved, a minimum of 98% sintered density is necessary[14].

2.2.3 The Importance of Density in Powder Metallurgy

Porosity in products produced via the PM route is inherent and can reach high levels. These levels of porosity can be attributed to cold compaction, as each particle remains discreet[13]; and the subsequent mechanism of sintering. This method of consolidation through sintering results in more pore formation in comparison to a melting operation as it coheres by means of diffusion. Mechanical properties of the material are significantly impaired with the presence of these pores due to the stress concentration associated with them. In essence, when using the PM process for structural component fabrication, the relative density is of high importance. The relative density is given as a percentage of theoretical density of the material. By this, a relative density of 100% would result in a fully dense structure and a relative density of 90% is that containing 10% (by volume) porosity[13]. The relationship between certain mechanical properties and porosity of sintered steel is given in Figure 2.4. This study on PM steels resulted in tensile strengths varying with relative density while the impact strength and elongation at fracture show a stronger dependence on porosity.

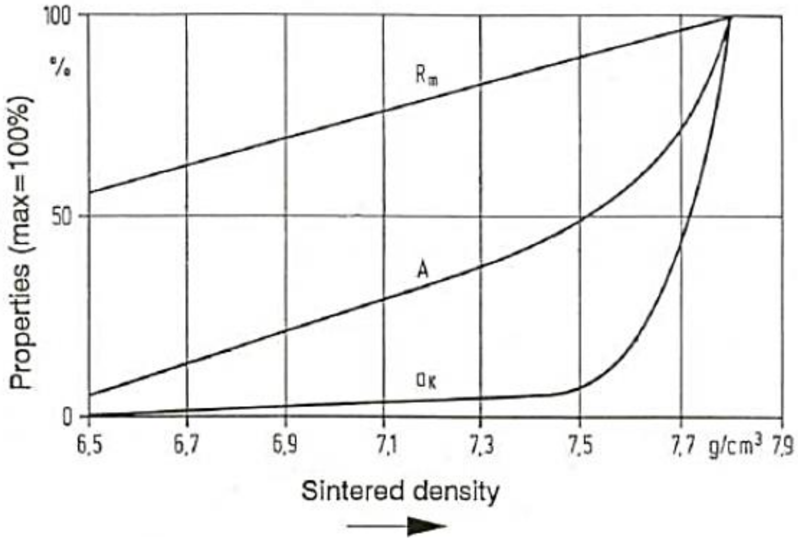

Figure 2.4: Graph illustrating resulting mechanical properties as a function of its sintered density of sintered steel where; *Rm* represents tensile strength, *A* is elongation at fracture and *ak* is the impact strength[13]

2.2.4 Powder Production

Most metals are transformable into powder, however the approach in producing the metal powder differs depending on specific material properties of the metal and the way they are refined from their natural state. Properties of a product processed by the PM route will depend on the properties of metal powder such as particle size and size distribution, particle shape and surface texture of particles. There is an extensive range of techniques that may be used to produce metal powders. Some of the most significant manufacturing methods employed may be categorised into three main groups that is through, chemical, mechanical or physical means.

Chemical methods

Metals transformed into powders through chemical methods are done so by chemical reduction or decompositional techniques. Chemical reduction makes use of mostly reducing either oxides, halides or the salt of metals from the solid, gaseous or in-solution state. The production of iron sponge fines is a classic example of reducing iron oxide by chemical means. Other common preparations of metal powders through electrolytic means include that of copper, beryllium and nickel powders[12].

Physical methods

Physical methods of producing powders include that of atomisation and electrolytic practices. Electrolytic techniques make use of having the metal deposit very lightly onto the cathode of the cell by altering various chemical and physical conditions of the process. This method produces a high purity product and is quite costly compared to others. Atomisation of metals into powders involve melting the metal and fragmenting it into small particles. This is done by various means and leads to further subdivisions of this technique: gas, water and centrifugal atomisation. This method has gained popularity because of its high purity product and customisation abilities. The general principle involves forcing a liquid through an opening while introducing a stream of gas or liquid onto the extruding melt. Gas atomised powders are generated by aiming high-pressure inert gasses such as argon or nitrogen. This stream of gas strikes the liquid metal at an angle where surface tensional forces of the liquid metal spheroidizes the droplet resulting in particles with spherical shapes and smooth surfaces. It is possible to control powder sizes by altering pressure and jet configuration from which the gas stream originates. Gas atomisation (GA) is usually used in the manufacturing of reactive metals and preparation of super-alloys. The method does however have high energy costs attached to it. Water atomisation follows a similar principle whereby the gas used to cool and fragment the liquid metal is replaced by a high-pressure water stream. This method is not used in reactive metals such as titanium, as oxidation is prevalent. Particle morphology is irregular in shape with rough oxidised surfaces. Some advantages that come with atomisation include the ability to produce pre-alloyed (PA) powders, particle compositional uniformity, controlling particle size and morphology, high purity powders and lower entrapped gas porosity [12].

Centrifugal atomisation makes use of a fast spinning container or disc that ejects molten metal. An example of centrifugal atomisation, is rotating electrode process (REP). REP takes the material in the form of a rod electrode, and rotates it rapidly while simultaneously melting the material on its opposite end by an electric arc. The molten metal rotates off the bar and forms solid particles in an inert atmosphere within the container. This process was developed mostly for the production of high purity, low oxygen titanium alloys and super-alloys. Particle shapes are spherical and surfaces smooth. A drawback of REP was tungsten contamination originating from the stationary electrode used in the process. This was resolved through the development of plasma rotating electrode process (PREP) [12].

Mechanical methods

It is not common to make use of mechanical means primarily in the manufacturing of powders. These methods make use of a combination of impact, shear, compression and attrition to generate powder particles. This way of producing powder is usually used in special cases where for example fracture of the material is easily achieved. A ball mill is a common piece of equipment used in the mechanical processing of powders. A ball mill consists of hard, wear resistant balls enclosed in a rotating drum, milling the material into smaller particles. Unfortunately contamination of powders is high for this method[12].

2.2.5 Production and properties of titanium powder

Some conventional titanium powder production methods include those discussed in section 2.2.4 that is PREP and GA, both of which produce high quality spherical powders. Hydride-dehydride (HDH) and sponge fines are however cheaper powder alternatives and are most commonly used in direct powder rolling (DPR) practices.

Almost any source of titanium feedstock may be used to produce powders through the HDH process. These include titanium sponge generated by the Kroll or Hunter process, commercially pure titanium (CP-Ti) and from the widely used alloy Ti-6Al-4V. This is because HDH makes use of a unique property of titanium; its ability to absorb and diffuse high amounts of hydrogen; and subsequently reverse this process through very basic vacuum thermal treating. HDH is a reversible two-step process that uses hydrogen as a temporary alloying element. This process follows four main steps; hydriding, milling, screening and dehydriding. Hydriding the feedstock embrittles it, which allows it to be crushed and milled into smaller particles easily. These particles are subsequently screened (see Figure 2.11) to achieve the desired size followed by a final dehydriding step to regain the chemical composition and mechanical properties of a ductile titanium powder[15]. ASTM standard B-348 is a common guideline

used to assess the quality and properties of titanium sponge and CP-Ti powders and categorises them into grades 1-4 or grade 5 for Ti-6Al-4V.
Sponge fines are by-products of the Kroll and Hunter reduction processes. The sponge is crushed and screened to isolate the appropriate size and are also source of low cost powders.

Powders produced via different processing routes will not only result in a range of powder characteristics but also have cost implications. For direct powder rolling (DPR) to compete with conventional wrought product, the price of powder should be at a minimum. Figure 2.5 illustrates cost projections of titanium powders produced by various powder processing methods. It is clear from this figure that sponge fines and HDH powders are in the low cost titanium powder range while PREP and GA powders are among the most expensive powder types. Since a main driver behind direct powder rolling (DPR) is to reduce overall costs, HDH and sponge powders are the most popular choice.

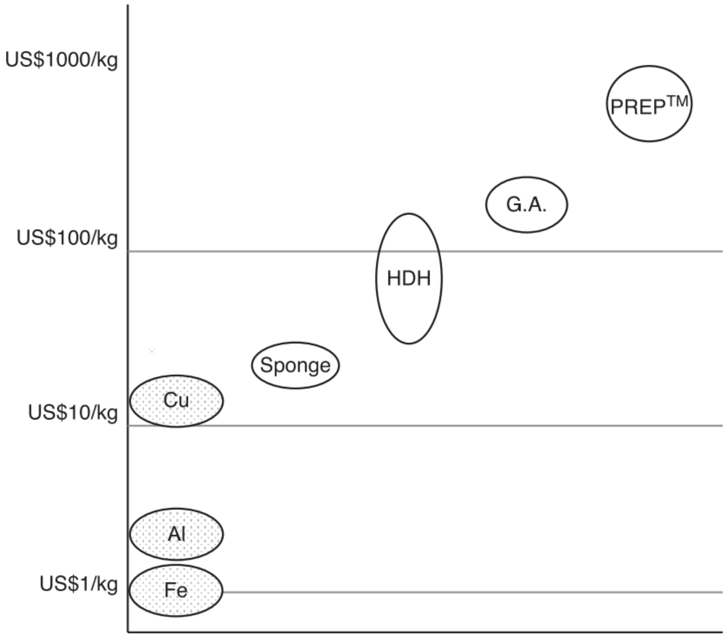

Figure 2.5: Figure showing Cost differences of titanium powders processed via various methods. Copper, aluminium and iron powder prices are included for comparison[16]

2.2.6 Effects of oxygen and chlorine contamination on titanium powder

Residual oxygen and chlorine have long been particularly problematic impurities in titanium powders. Titanium's notorious affinity for oxygen is well known. While the passive oxide layer around titanium accounts for its inert behaviour and corrosion resistance, high oxygen levels can be detrimental to its final mechanical properties. The oxides that have dissolved within the metal are what usually cause embrittlement and inferior mechanical properties. Yan, et al. (2014)[17] found that oxygen levels in Ti-6Al-4V powders above 0.33 mass % have severe effects on the tensile ductility of the alloy. Figure 2.6 from Yan, et al. (2014) shows this effect of oxygen embrittlement past a critical oxygen content.

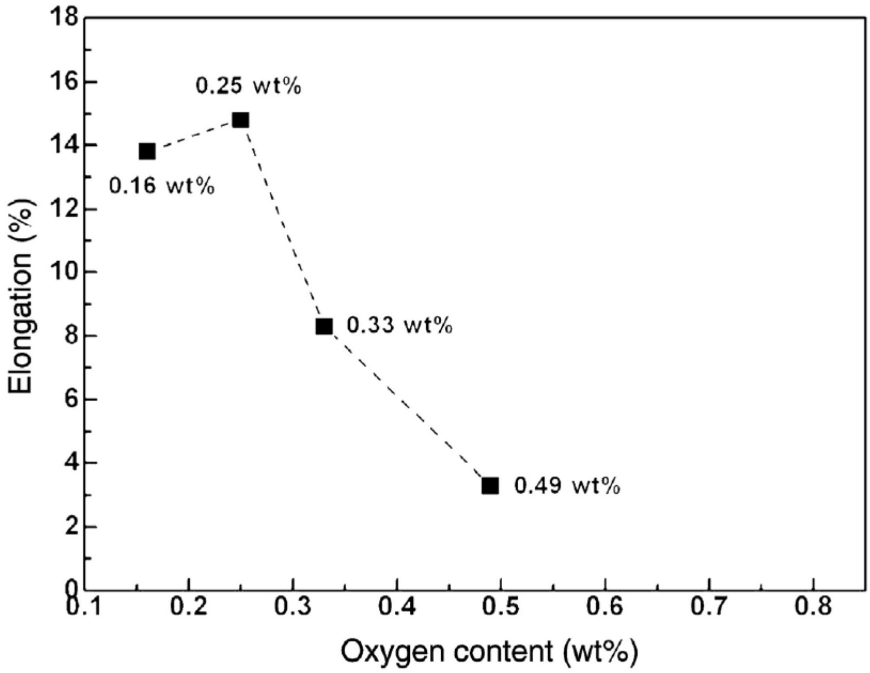

Figure 2.6: Observation of tensile ductility with increasing oxygen content in as-sintered Ti-6Al-4V[17]

Residual chlorides are common impurities found in titanium powders made from Kroll or Hunter sponge as chlorination is a step used in both processes (Figure 2.7). Chlorine contamination may have detrimental effects on titanium. These include affecting sinterability of titanium powders and degrading weldability of titanium products. Figure 2.7 summarises chlorine levels present in titanium powders depending on their processing route[18]. Sinterability of titanium powders can be heavily affected by the amount of residual chlorine present. On sintering, residual chlorine may evolve into its gaseous state resulting in large gas pockets leading to excessive porosity and degrading densification mechanisms. This results in reductions in the fracture toughness and fatigue properties of the final products[16]. Welding titanium may also be difficult beyond a certain critical chlorine level. The volatile nature of chlorine causes “splashing-like” effects during welding. Du Pont (1950s) and Imperial Clevite (1970s) had demonstrated the ability to produce titanium strip through direct powder rolling (DPR). They however never commercialised the process due to weldability constraints found in PM strip products. The volatile nature of chlorine impurities confined within PM microstructures caused salt build-up on welding electrodes resulting in an unstable arc forming on welding. They estimated that a critical chlorine level existed that should not be passed for acceptable weldability[16]. Further studying of this critical chlorine concentration found that weldability may be improved if chlorine levels were no more than 150ppm[19].

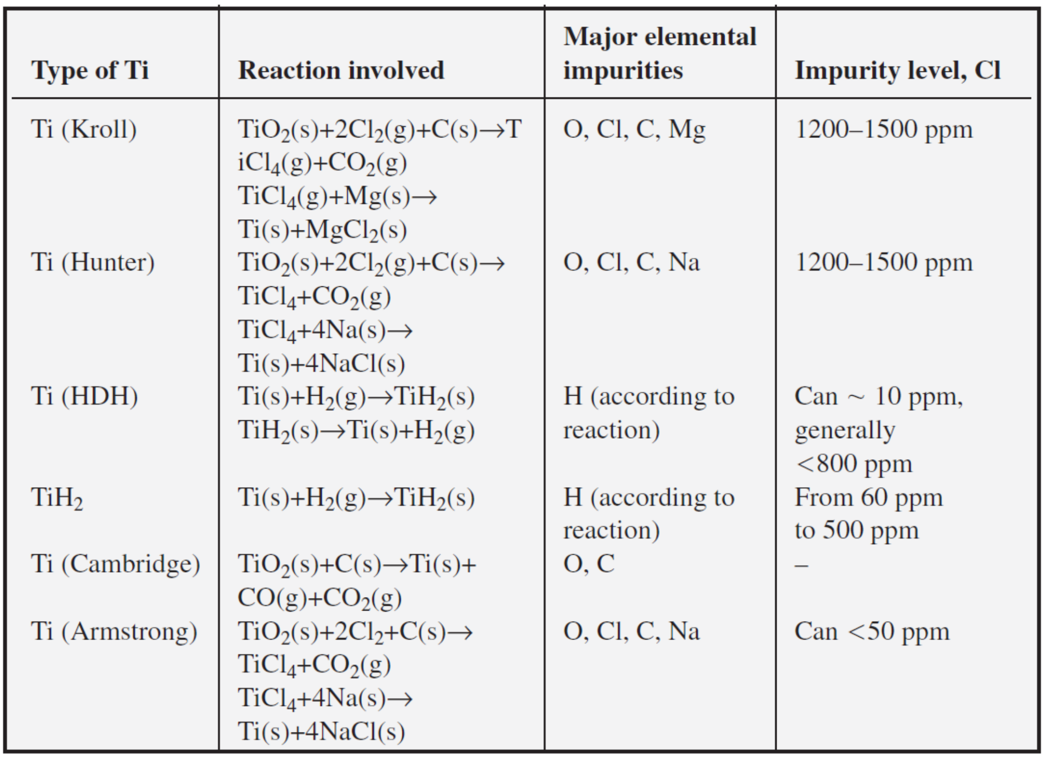

Type of Ti	Reaction involved	Major elemental impurities	Impurity level, Cl
Ti (Kroll)	$TiO_2(s)+2Cl_2(g)+C(s) \rightarrow TiCl_4(g)+CO_2(g)$ $TiCl_4(g)+Mg(s) \rightarrow Ti(s)+MgCl_2(s)$	O, Cl, C, Mg	1200–1500 ppm
Ti (Hunter)	$TiO_2(s)+2Cl_2(g)+C(s) \rightarrow TiCl_4+CO_2(g)$ $TiCl_4+4Na(s) \rightarrow Ti(s)+4NaCl(s)$	O, Cl, C, Na	1200–1500 ppm
Ti (HDH)	$Ti(s)+H_2(g) \rightarrow TiH_2(s)$ $TiH_2(s) \rightarrow Ti(s)+H_2(g)$	H (according to reaction)	Can ~ 10 ppm, generally <800 ppm
TiH_2	$Ti(s)+H_2(g) \rightarrow TiH_2(s)$	H (according to reaction)	From 60 ppm to 500 ppm
Ti (Cambridge)	$TiO_2(s)+C(s) \rightarrow Ti(s)+CO(g)+CO_2(g)$	O, C	–
Ti (Armstrong)	$TiO_2(s)+2Cl_2+C(s) \rightarrow TiCl_4+CO_2(g)$ $TiCl_4+4Na(s) \rightarrow Ti(s)+4NaCl(s)$	O, Cl, C, Na	Can <50 ppm

Figure 2.7: Concentration of chlorine as a by-product of various processing of titanium powders[18]

2.2.7 Powder Characterisation

Powder properties have great effects on production parameters and properties of final components. As such it is vital to have a clear understanding of various powder properties and how they influence the production process[13]. Important powder characteristics are described here.

Particle Shape

Various powder processing routes result in a range of particle shape morphologies. Figure 2.8 illustrates a brief overview of what morphologies may arise depending on which powder processing route was taken. With such a great variety of possible particle shapes, comparing sizes between particles of different shapes is very difficult.

Particle Size

A spherical particle shape allows for the simplest and most accurate way to quantify the size and shape of a particle as only one dimension is required, the diameter. It is common for many particle size analysis techniques to make the general assumption that every particle is a sphere and report the value of some equivalent diameter. A common technique used to measure particle size is by laser diffraction. In laser diffraction measurements, a laser beam passes through a sample with discrete particles. The particle sizes are measured by detecting the intensity of the scattered light produced.

The angle at which the scattered light is measured and this is what distinguishes between particle sizes. Small particles will scatter light at large angles relative to the beam and the inverse is true for large particles. Data is collected continuously throughout the measurement and a particle size distribution is the outcome[20]. This is due to particles being within a certain size range. On large industrial scales it is very difficult (nearly impossible) to prepare powder particles of the exact size.

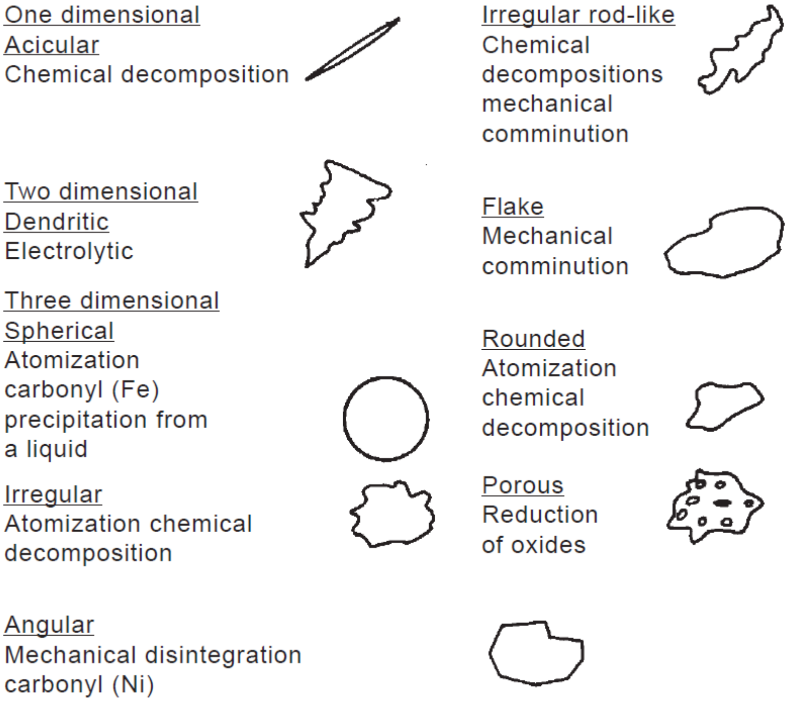

Figure 2.8: System of particle shape characterisation coupled with processing route [12]

Most laser diffraction systems will measure solid particles in suspensions as well as dry powders in air. Equivalent diameters are determined by taking the physical measured value (i.e. scattered light) and determining the size of the sphere that could produce these data. While this method may not be the most accurate, shapes of particles produced by most industrial processes are such that the assumption of a sphere does not cause major problems. It should however be noted that particles with very high aspect ratios (needles, fibres etc.) may potentially be problematic downstream [16]. As a particle becomes more irregular in shape, defining its size accurately becomes more and more difficult because of its multidimensional nature.

To interpret particle size distributions and analyse data, a basic understanding of statistics is required. The output for such particle analysers may resemble that of Figure 2.9, a symmetric distribution where the mean is equivalent to the median which is equivalent to the mode. The mean value is calculated in a similar fashion to that of an average. Median values are those where half of the data resides above this point and the other half below. The median can also be known as D50. The mode represents the particle size that is repeatedly found in the distribution.

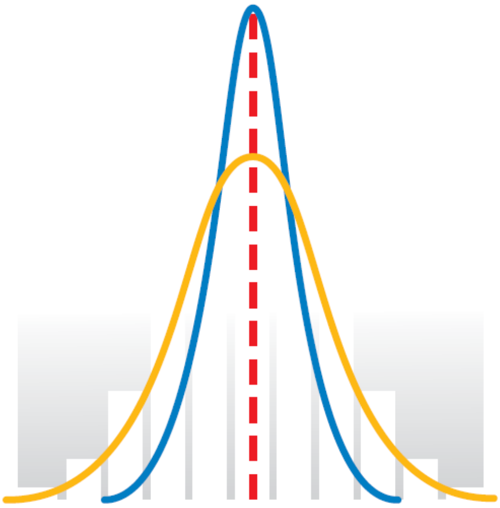

Figure 2.9: Symmetric distribution[21]

Most commonly, laser diffraction results are expressed by reporting the D10, D50 and D90. This approach defines the distribution width on the x-axis and shows what percentage of the population lies below a particular particle size. D50, the median, is defined as the value where half the population lies below this particle size. Similarly, 10 percent of the population lies below D10, and 90 percent below D90. Figure 2.10 depicts what each of these three terms represent on a particle distribution[21]. Standard deviation (SD) is also an important output when considering distribution widths. By convention, 68.27% of the total population will lie within ±1 standard deviation and 95.45% will lie within ±2 standard deviations.

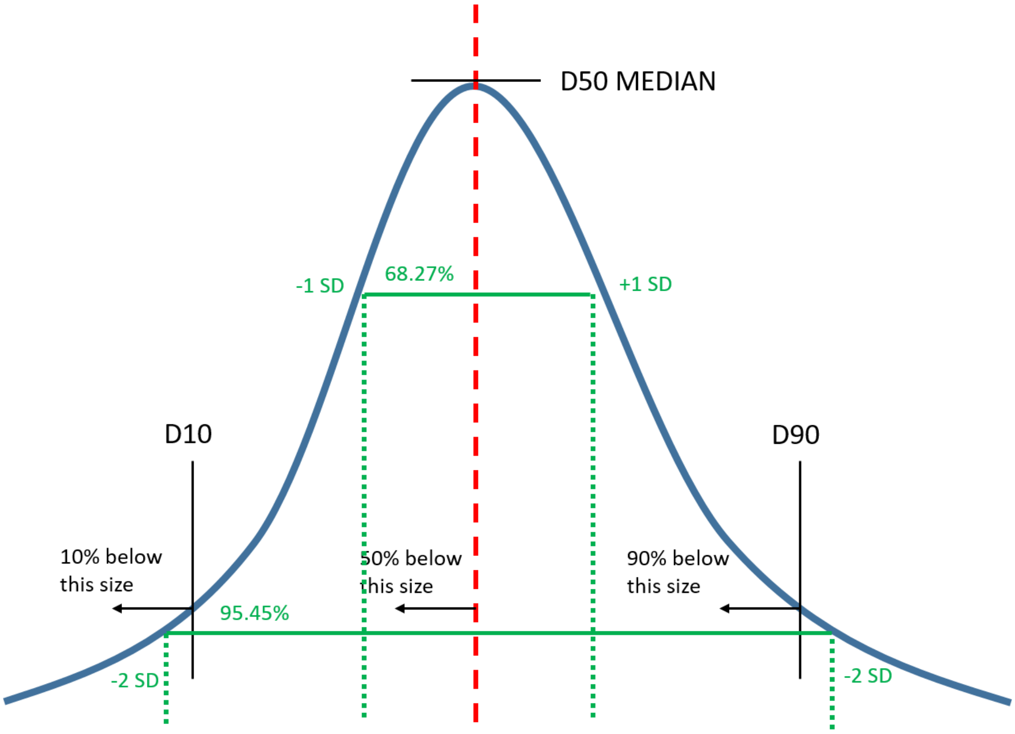

Figure 2.10: Normal distribution showing D10, D50 and D90. The mean (D50) value is flanked by 1 and 2 standard deviation (SD) points

Screening is a popular choice for separating powders by size. Screens comprise of a mesh made from square openings of a particular size. Wires are orthogonal to each other with a standard thickness of 52μm. A "mesh" number is allocated to each screen depending on how many wires in an inch are perpendicular to the wire direction. These mesh numbers correlate to a specific size which may pass through the screen. Since mesh number relates to number of wires placed within a certain area, the more wires there are, the higher the mesh number, and the smaller the opening. Additionally, mesh numbers are usually accompanied by either a + or – sign. If the sign is +, the powder will pass through that specific mesh. If however the sign is -, the powder will not pass through that mesh. For example, a powder described as -100 mesh will pass through a 100 mesh screen while that described as +100 mesh will not pass through a 100 mesh screen. A powder described as -100 +200 mesh will allow powder to pass through the 100 mesh screen but not a 200 mesh screen. Screens are layered as in Figure 2.11 with screens of increasing mesh numbers. Screens are disturbed to allow particles to move through the mesh. While screening is widely used because of its ability to distinguish sizes of large quantities with relative ease, it is not the most accurate method with 3-7% allowed variation for openings as manufacturing tolerance[22].

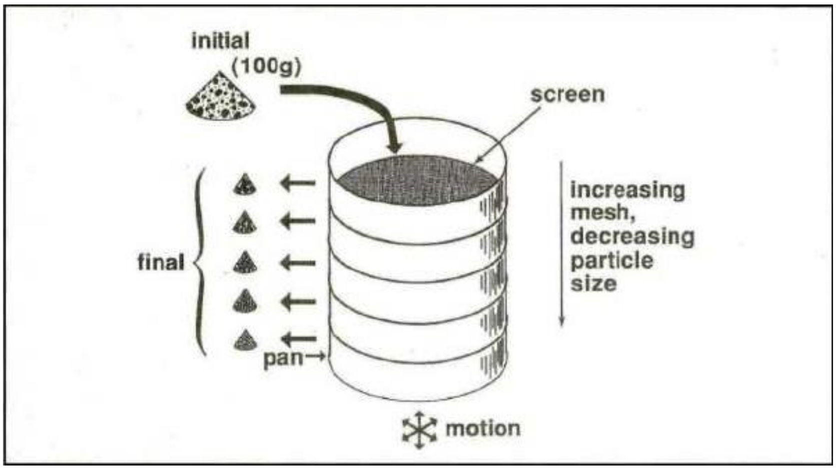

Figure 2.11: Illustration of screening powders for particle size characterisation by layering mesh screens of large openings to smaller ones (top-down)[23]

2.2.8 Powder Compaction

Compaction of metal powders may be achieved under various conditions. The primary purposes of powder compaction are to consolidate the powder into a specific shape, to attain a green body of certain level of strength and porosity and to attain a green body as close to the desired final dimensions as possible, while also taking into account any post-processing changes. There are many ways to go about powder compaction such as continuous or discontinuous processing, employing mechanical or hydraulic presses and more[12].

Die compaction is one of the more common approaches for near-net shape powder compaction and is economical and fairly simple. It makes use of dies of a specific shape where the powder is poured and a subsequent pressing action. Powders behave differently to fluids under pressure and do not assume the same density throughout the compact. Inter-particle friction and wall-particle friction do not transfer pressure uniformly resulting in this distribution in the compact. Pressing involves filling the die with powder, pressing to achieve the desired green density and ejection of the green body. There are various mechanisms of die compaction. These mechanisms are relative to the way the tool elements move in relation to each other, namely, the upper punch, lower punch and die. A typical type of compaction used involves a floating die and an upper punch pressing. Here the lower punch is stationary with the upper punch moving into a die supported by a spring. When the powder-die wall friction exceeds that of the spring, the die wall is carried down[12].

There are two main categories of compaction pressing that is, mechanical or hydraulic. Presses can operate under loads from about 3 to 1000 tons. Hydraulic presses make use of fluid pressure on pistons to generate a compressive force while mechanical presses use the energy stored in a flywheel to operate the press[12].

The term "apparent density" is referred to as the state of the powder where it has not been agitated. This density is controlled by inter-particle friction in the bulk powder. Before compaction takes place, particles rearrange themselves as they are poured into the die configuration, filling large spaces in-between. Subsequently, once particles have rearranged themselves and filled the die, a compaction step will further densify the powder into a green compact. Figure 2.12 gives a brief overview of powder behaviour during pressing and compaction with an increase in pressure. During the compaction stage, particles plastically deform at localised points of contact between each other. New contact points are formed as pressure and contact area increases. These high pressures can cause very small metal bonds, a type of cold welding, that assist in keeping the form of the compact. When the pressure is reduced and compact ejected, the powder will attempt to spring-back depending on the elastic properties of the material [12,23,24].

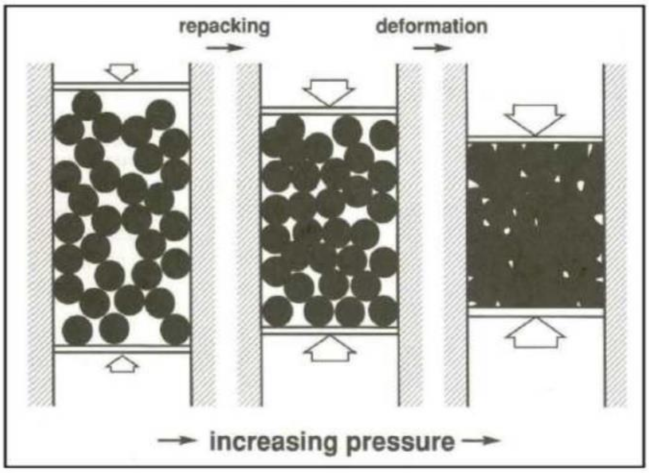

Figure 2.12: Densification mechanisms of powder compaction during uniaxial pressing[23]

A green compact is formed at the start of any PM processing route. High pressures (generally between 100-1000MPa) are applied to metal powders to initiate densification. The influence of such high pressures causes powder particles to be cold welded. At particle interfaces where contact is made, these high pressures are localised. This concentrated force causes powder particles to squash, deform and slide against one another disrupting any oxide or surface layers to form a minor metal bond[24]. A resulting green compact with green strength based on this solid-state fusion is formed.

Green compaction is not only dependent on the compaction method but also powder morphology. Atomised powders for example are generally not favoured when forming green compacts. While their flow properties may be superior due to their spherical shape[24], typical compaction pressures (300-950 MPa) are not high enough to cause them to adhere. Spherical powders pack extremely uniformly. This only allows six points of contact most of the time. More irregularly shaped particles with rough surfaces and protrusions are generally favoured in powder compaction as there is more of a chance of a greater number of bonds to be formed during pressing. Their irregular shape also allows for an interlocking action which further improves their mechanical strength and stability. Such powders include those of the sponge fine and HDH powder type.

Powder choices for preform fabrication of alloys will usually involve a choice of blended elemental (BE), master alloy (MA) or pre-alloyed (PA) powders. Furthermore, most PA powders are spherical in shape making compaction more difficult as particles will not lock as well, and PA powders are generally stronger, creating further difficulty in compaction at room temperature. For example, a compaction pressure of 965 MPa (roughly the yield strength of Ti-6Al-4V) is required to press 100 mesh PA Ti-6Al-4V to 80% theoretical density while only 413 MPa is required to press BE powder to the same density. In addition, PA powders are more costly than BE powders making BE powders more attractive from an economic perspective[25].

The outcome of compaction has direct implications on green strength and eventually, the properties of a component after sintering. If a minimum acceptable green density could be known to achieve a near fully dense component after sintering, process optimisation may be achieved in the compaction stage. Alman and Gerdemann (2004)[26] found it possible to achieve a fully dense compact after sintering titanium powder, provided the initial green density is in excess of ~90%[26]. Unfortunately, high pressures to achieve these high densities can cause particle fractures and die wear which is generally avoided due to limitations of equipment; or avoided when complex shapes are involved.

Powder packing during compaction

Mixing particles of different sizes allows decreased porosity and a higher packing ratio. Figure 2.13 illustrates how spherical particles of different sizes result in a range of pore sizes. For larger particles

Figure 2.13a larger voids are evident as a result of larger diameters and particles making contact at surfaces. Figure 2.13b shows how reducing the particle size will cause a reduction in pore volume however the number of pores will increase as each particle will occupy a smaller volume. When mixing particles of different sizes, particle packing mechanisms outlined in Figure 2.13c arise, where introducing particles of a smaller size will fill gaps and further reduce pore volume. When producing alloys using the BE approach in PM, it is common that the alloying powder particle sizes are smaller than that of the base powder to allow for this type of packing (Figure 2.13).

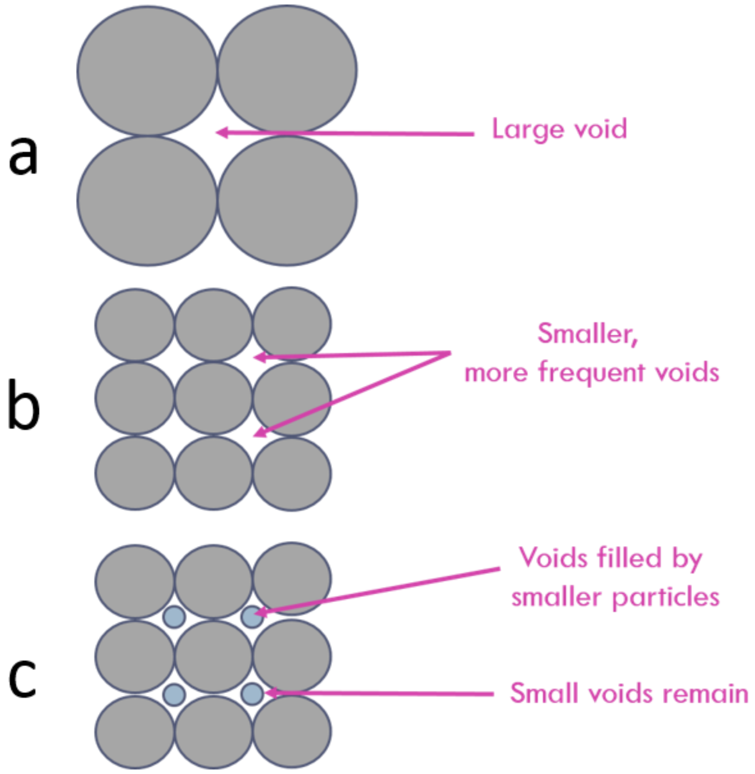

Figure 2.13: Schematic of how spherical particles of different sizes will pack where (a) illustrates larger particles creating larger voids, (b) shows smaller particles result smaller voids, and (c) exhibits mixing powders of different sizes fills voids

Effect of powder shape and size on compaction

As discussed previously, powder sizes can vary on extreme scales from near perfectly spherical to highly irregular shapes that are difficult to define. These shapes can have an impact on their compaction behaviour. For example, highly irregular particles that are brittle are usually more susceptible to fragmenting during compaction. This could in turn lead to a higher green density as the small fragments formed on crushing fill in the open spaces that had formed on crushing[27]. Spherical particles on the other hand are generally not favourable for green compaction. Pressures as high as 275-690MPa are generally not high enough to keep them from falling apart. They tend to pack very uniformly, so uniformly that this type of packing hinders consolidation. Their uniform packing causes them to make contact at usually only six points. Small metal bonds may form between contact points if the pressures are high enough. These bonds are what will hold particles together. If however these bonds are not formed, once pressure has been released, the particles will revert back to an uncompressed form and not hold form[24].

Particle size will also have an effect on compaction as discussed previously. For titanium powders, processing routes can determine the outcome and distribution of powders. Figure 2.14 depicts the distribution of a number of titanium powders against their respective processing route.

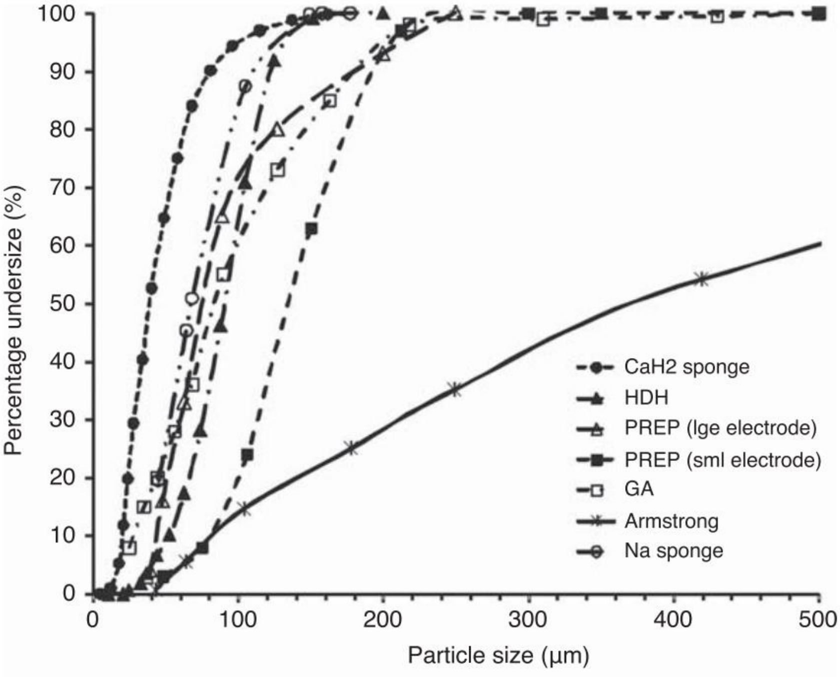

Figure 2.14: Particle size distributions for various commercial titanium powder processes[28]

2.2.9 *Powder Shear Test*

The shear properties of a powder provide insight to its flow properties. Shear testing characterises the powder in a consolidated state. It measures the powder's behaviour as it transitions from no-flow to flow. When a powder is subjected to particular storage environment it experiences consolidation stresses which have an effect on density and mechanical forces between particles. As such, for flow to occur the yield point of the powder in that consolidated state must be overcome. Some physical powder characteristics such as size, shape and roughness will greatly affect the yield point. Measuring shear properties is vital as this information is necessary to know whether powder will flow adequately in process or if some kind of hindrance may occur to prevent effective flow.

To better describe and understand the flow behaviour of powders, a simplified description of a uniaxial compression test model is described below. This will describe the stresses in bulk solids on compression. The uniaxial compression test can be presented on a plot with shear stresses as a function of normal stresses in Figure 2.15.

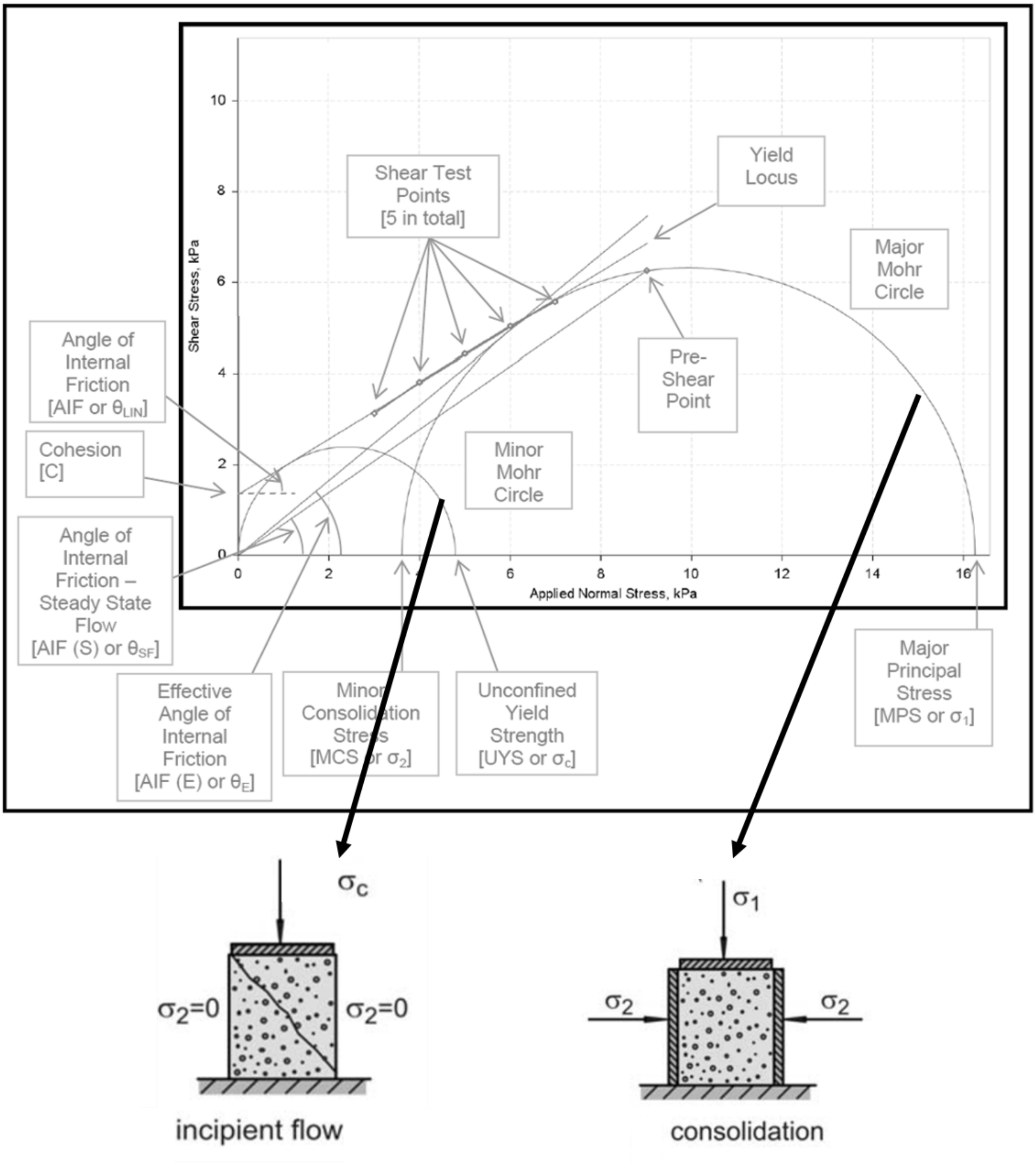

Figure 2.15: Graphical analysis of shear cell tester results from J. Schwedes and D.Schulz (1990)[22],[29]

Initially, the bulk material sample is loaded by the major principal stress σ_1 in the vertical direction. This is the consolidation stress and is described by the major Mohr circle. The minor consolidation stress, σ_2 is the stress acting horizontally on the bulk sample. The vertical stresses and horizontal stresses are principal stresses. After the consolidation stage, the sample is relieved of this consolidation stress and the hollow cylinder casing is removed. The specimen is then loaded with increasing vertical stresses. Since there is no load applied to the lateral walls and there is no casing restricting those planes, the horizontal load or minor horizontal stress (σ_2) is unaffected by the vertical load and equals zero. The normal stress intercept of the smaller Mohr circle describes the unconfined state of the bulk solid after consolidation. Failure of the sample on increasing vertical compressive loads is caused by the stress defined as the unconfined yield strength σ_c. Once failure has commenced, the yield limit has been reached and no more load may be applied to the sample [29].

Uniaxial compression testing to determine flow properties has its limitations. Parameters such as internal friction and wall friction cannot be determined from these tests and yield strength values obtained are lower than what they should be[22]. A more robust technique introduced by Jenike and Shield (1959)[30] was developed, the so-called translational shear cell tester. Here the bulk material is loaded vertically by a normal stress (σ) to consolidate the sample. It is then subjected to shear deformation resulting in a horizontal shear stress (τ). The force acting on the sample increases as the shear stress increases. A distinctive relationship can then be drawn between normal and shear stresses for each respective material being tested. Similarly, to the uniaxial compression test, to measure the yield locus, two steps are required: The sample first needs to be consolidated, which in this case is referred to as a pre-shear. Secondly, shear failure must occur to determine and measure the yield limit of the sample. This relationship between normal and shear stresses is typically illustrated graphically through a Mohr diagram with coordinates of normal and shear stress values. Once plotted, the curve obtained always yields a straight line whereby the yield locus is observed for a bulk material. Flow parameters can then be found from these yield loci, thus a yield locus in important in determining flow properties of bulk materials.

There are a number of shear cell designs that have been developed to test for a powder's shear properties. These include Translational Shear Cells, Annular Shear Cells and the FT4 Rheometer Shear Cell. Shear cell testing has been used for understanding powder behaviour in hoppers. This makes these tests useful in hopper design. Due to the nature in which the test operates, these tests are not suitable in predicting powder behaviour in low stress or dynamic applications such as mixing, filling and feeding[31].

2.3 Roll compaction

An alternate means to compacting metal powders is through roll compaction. It is an industrial process used in producing strip and sheet metal of high density and strength. Initially, it was primarily used in the compaction of coal briquettes, however further developments has led to roll compaction being implemented in a wide variety of continuous mass production industries such as pharmaceuticals, food, chemical and metallurgical[32]. The basic principles behind a roll-press are to compact compressible particulate material by subjecting it to high stresses from an applied pressure generated between two rolls rotating in opposite directions. This leads to the formation of a compact of continuous strip or discreet briquettes.

Roll-type presses are seen to be more advantageous over the classic die press because of its ability to continuously exert a high pressure on the moving granular solid as it passes through the rotating rolls. This proves more economical as high production volumes are possible[33]. In most cases, a roll press can produce tablets five times faster than a die compaction press. Further development and design of roll compaction aims to improve on flow properties of particulate material, ensure homogeneity of particulate formulations and increasing bulk density conducive to preventing segregation in pharmaceutical drugs[34]. Another promising feature are the cost savings associated with the practice, namely energy consumed, where energy is only required to drive the feeding system, rolls and any hydraulic adjustment mechanisms. Costs associated with drying are also kept to a minimum for wet roll compaction[35]. However, dry granulation processing is even more advantageous since a liquid binder is not required, thus physically or chemically moisture sensitive materials can be processed and a drying stage is not necessary. Particulate materials with either a low melting point or those that degrade when exposed to high temperatures may be used[34]. There is however a drawback, as an increase in production speed is followed by a product of substandard or reduced quality. Therefore it is best to implement roll compaction for products of low unit value that can tolerate imperfections.

To this day, relevant research is limited and very little is understood of roll-type presses for granular solids owing to the many contributing factors (roll-press design and material properties) and an inherent complex nature. There have been attempts at developing models of roll compaction to further aid in design of the roll press and improved control over the process. However, as a result of the numerous contributing factors influencing performance of the process, a comprehensive model has yet to be developed. This results in most information on this technology being empirically based. This knowledge is however limited and does not expose any significant correlation between the design of the press and material properties of the granular solid. While it may be possible to optimise parameters and performance using trial-and-error methods, time becomes an issue as do operating costs. This provides more incentive to understand more about this technology in a theoretical manner for a more rational approach to powder compaction via roll-press. It will make it easier to develop relationships and formulate methods to assist in adopting this system to a specific powder and final product guidelines. Various approaches have been taken in an attempt to model the behaviour of the system. Most of the initial work on roll-press powder compaction was acquired from sheet metal rolling. Unfortunately the methods used in these workings cannot simply be transferred to rolling mills dealing with granular solids. Three main models exist to describe roll compaction of powder using either: the Johanson model[1,36], the Slab analysis method[36] and/or Finite Element Analysis (FEA)[34,36].

Efforts are currently emphasized on collecting experimental data on powder characteristics, compacts and roll press data to correlate against theoretical results and evaluate their worth. Problems arise where characterisation of powder is difficult to measure, moreover powder compacts are altered during compaction stages.

Chapter 2 explores key fundamental concepts of roll compaction theory and a study on the Johanson model and how it may be applied to granular solids.

2.3.1 Roll compaction theory

The roll compaction process involves the use of a roll-press consisting of two counter rotating cylindrical rolls mounted in such a way which allows their axes of rotation to be parallel (Figure 2.16). The raw material is fed through the space between the rolls by gravity (for vertically fed presses), by a screw mechanism or a combination of the two. The material is drawn through the gap between the rolls by the action of friction between powder particles and roll surface. The powder is subjected to high stresses in the region between the rolls resulting in compaction and a self-supporting green body. Green body shapes may be created and controlled by introducing depressions or pockets by altering roll surfaces to generate the desired shape.

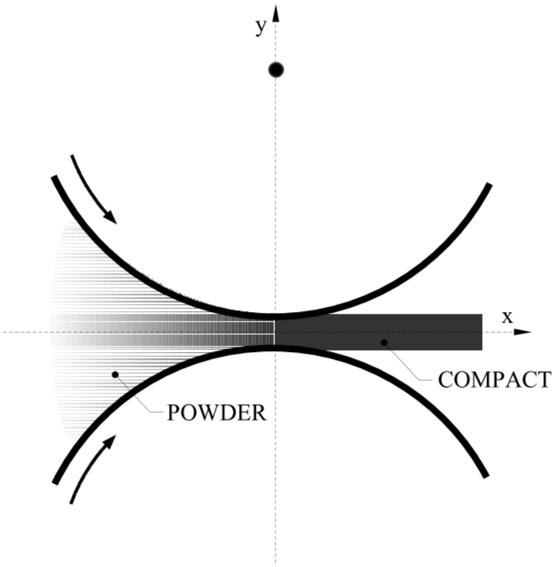

Figure 2.16: Basic roll-press illustration[37]

Roll presses consist of the same basic components and similar configurations. They may have rolls positioned horizontally, vertically or inclined at an angle. Raw material may be fed by gravity for vertically fed presses, via a screw mechanism or a combination of the two. The feeding system can heavily influence resultant compacted products and overall efficiency of the process. To achieve a homogeneous product the powder must sufficiently fill the roll gap in a continuous manner.

Fine powders display poor flow properties[32,37–39]. A reason for this is ineffective de-aeration, where air between particles cannot escape and offsets feeding of the press. As such, gravity fed systems are generally avoided and screw feeders are employed as they allow for improved control of the feed pressure. Gravity fed systems work best for powders that do not exhibit strong cohesive forces and flow well as the feed pressure is dependent on gravity. Chikosha, et al. (2014)[39] investigated the effects of various powder shapes and sizes during roll compaction. Overall final densities were found to be dependent on flowability and particle sizes. Flowability was observed to be highest for irregularly shaped large particles. Insufficient feeding due to poor powder flow in a gravity fed system will decrease the nip angle and maximum pressure applied.

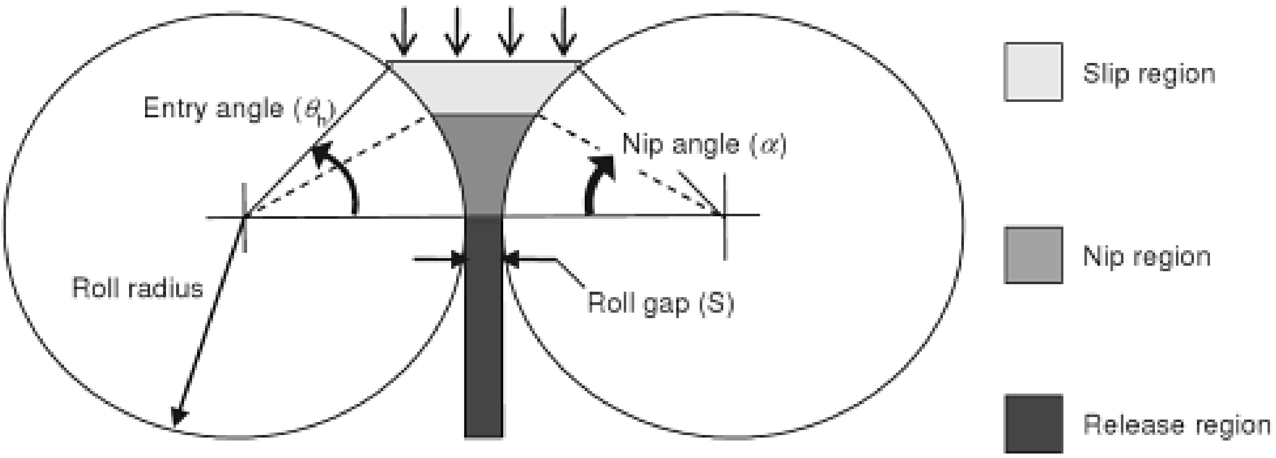

Figure 2.17: Schematic diagram of vertically fed roll compaction process[34]

Compaction may be divided into three main regions based on what the material is exposed to and how it behaves (Figure 2.17). In the slip region, powder particles rearrange themselves and begin to move at a speed slower than that of the rolls. This is also referred to as the entry zone. The second zone, the nip region, is where compaction takes place. Here, particles fracture and/or deform plastically under the high stresses supplied by the rolls[40]. The nip region has been defined to begin at a point determined by the nip angle (α), when the wall velocity of the powder is equal to that of the rolls. This is where powder sticks to the wall and no longer slips and where most of compaction occurs. It is in this region where a maximum roll pressure will be reached. The final zone, the release region, is where the self-supporting green compact exits the rolls and expands elastically due to the decrease in pressure as it exits the nip region. The compact now moves at a speed faster that the rolls as it is pushed out causing slip in the opposite direction before the compact is completely detached from the rolls. Friction effects are the primary mechanisms by which powder is pulled into the roll gap. Frictional forces become significant when the rolls move faster than the compact/material. This difference between frictional forces between the slip and nip region creates a net frictional force that drives the powder into the gap. As such, if the wall friction coefficient is low, the material would not be pulled through the rolls[34,41].

There are many parameters involved when studying powder roll compaction and isolating the most significant and critical parameters to develop a prediction method are an even greater challenge. These parameters include roll-press geometry, material properties, boundary conditions and loads that have been extracted and simplified based on one's understanding of powder roll compaction and what may be considered to be relevant when trying to achieve a desired result. Below is a more detailed description of how these parameters may be distinguished based on various categories, relevant for successful roll compaction adapted from Balicki and Michrafy (2003)[37]:

Operating parameters	• Roll force • Roll Torque • Roll Velocity • Feed pressure • Gravity • Inertia
Geometric parameters	• Roll diameter • Roll width • Gap size
Powder parameters	• Internal (effective) angle of friction • Cohesion • Admissible stress • Compressibility • Bulk density
Tribological parameters	• Friction between powder and roll surface

Understanding all relevant powder properties is vital to creating correct models for roll compaction and characterisation of these powders is of great importance for the success of the prediction.

2.3.2 The Johanson Model

Johanson (1965)[1] was the first to give a detailed account of predicting the performance of granular materials during roll compaction by developing mathematical relationships between roll press dimensions, material properties and operating parameters. At this time, information and data gathered to infer roll press design were of an empirical nature only. From this it was obvious to develop some kind of mathematical relationship between powder properties, operating parameters and press dimensions to optimise and assist in the continuous compaction of granular solids. It was the first model that allowed for the calculation of roll forces and pressures. The model allowed for the prediction of material behaviour during compaction. It depends on roll dimensions, feed powder material properties and operating conditions. This model allowed for roll forces and pressures to be calculated and overall predictions of how a material will behave on compaction.

Johanson made accommodations for indentations or pockets denoted as d present in rolls. For the purposes of this dissertation, the roll surfaces were assumed to be smooth and free of these indentations. Assumptions were necessary to implement the model as some parameters and properties are difficult to measure and control. This model assumes[1]:

1. The material is isotropic, cohesive, compressible and frictional
2. The material is subjected to continuous shear deformation on rolling
3. The material experiences plane strain in the nip region
4. The contact area between the powder and rolls is very small making the curvature of the powder-roll interface negligible
5. The rolls are fixed.

Using these assumptions, Johanson defined two distinct regions in the zone between the rolls: a) a slip region, where the material slips along the roll surface and b) the nip region, where no slip occurs and a boundary condition is set. These regions are given schematically in Figure 2.18. The model is based around the definition of these two distinct regions. In the slip region, the powder moves between the rolls at some constant pressure with the aid of a hopper. Material bulk properties are conserved in this region and no change in density is observed. The powder then continues to move further into the roll gap. There is a slight force exerted by the powder onto the roll-face, however the powder still slips as the pressure is not great enough. As the powder is pulled into the roll-gap, it begins to move at the same velocity as the roll, at which point the powder stops slipping. The point at which this occurs is called the nip angle (α), as defined by Johanson. This point was one of the most important definitions and findings of Johanson's work. The nip angle is a marker for the start of compaction and occurs where $\theta = \alpha$. At this point the powder is drawn into the rolls into the nip region (Figure 2.18). A pressure is thus exerted on the powder as more is drawn between the rolls forcing the compact to be continuously deformed by shear forces until the powder reaches the smallest region between the rolls, the roll gap, and is compacted to a thickness equivalent to this size. The compact finally passes through the release region, where its velocity exceeds that of the roll [1,42].

With this model, the maximum pressure exerted on the material during compaction can be determined. The final density of the compact may be predicted by combining information gathered from experimental pressure-density relationships and maximum pressures predicted from the model. Roll torque and force may also be calculated.

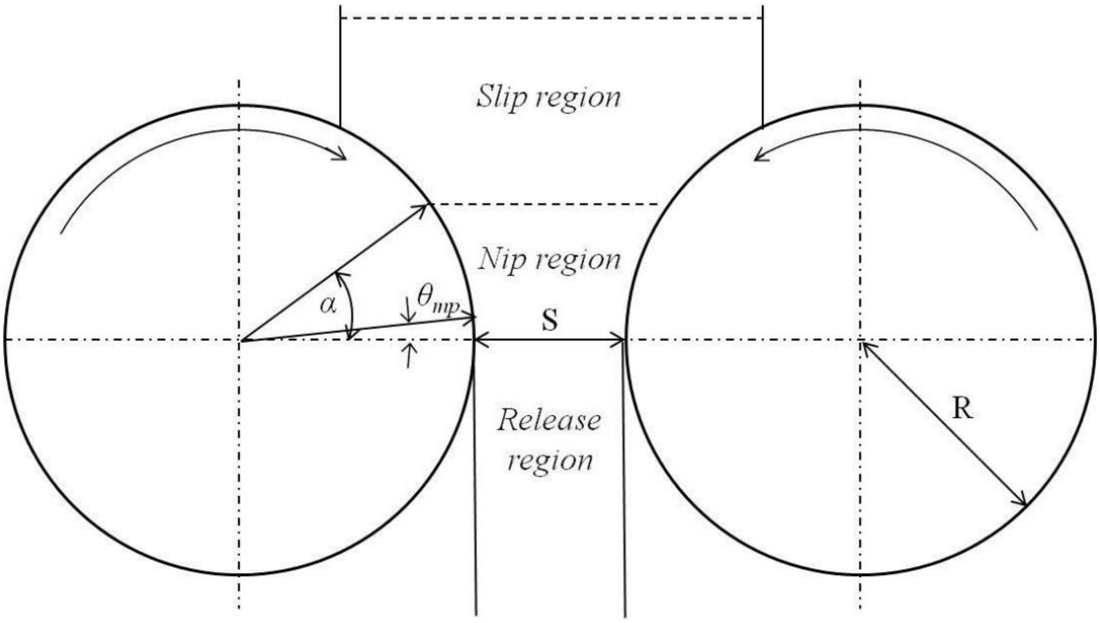

Figure 2.18: Illustration of roll compaction based on the Johanson model (1965) showing the slip, nip and release regions. R is the radius of roll, S is the minimum roll gap, α is the nip angle and θ_{mp} is the angular position where the roll pressure is at its maximum (adapted from Yu (2012)[42])

Pressure distribution in the slip region

Johanson introduced the Jenike yield criterion for steady state particle flow in his theory of roll compaction. The material used in roll compaction must adhere to the effective yield function (Equation 2-1) proposed by Jenike and Shield (1959)[30] and is assumed to be isotropic, frictional, cohesive and compressible. This function applies to the region between the rolls where the powder experiences plane strain and slips against the surface of the rolls. The effective angle of internal friction (δ) describes the yield behaviour of the powder.

$$\sin\delta = \frac{\sigma_1 - \sigma_2}{\sigma_1 + \sigma_2}$$

Equation 2-1

where σ_1 is the major principal stress and σ_2 the minor principal stress.

The start of the nip region is initiated when the powder makes contact with the rolls at a feed angle, θ_h, and the feed pressure P_0, is the predominant stress acting on the powders (Equation 2-2). It is possible to deduce that the mean normal stress ($\sigma = \frac{\sigma_1 + \sigma_2}{2}$, for any angle θ, where θ represents the angular position during roll compaction) stays constant for a distance after P_0 and θ_h are applied, and increases as the powder moves further into the roll gap until the smallest region is reached, where θ = 0.

$$\sigma = \frac{P_0}{1 - \sin\delta}$$

Equation 2-2

Results from powder characterisation, the wall friction angle, ϕ, and effective angle of internal friction, δ, may be used in calculation to determine the powder feed angle θ_h according to Equation 2-3. Both the wall friction angle ϕ, and effective angle of internal friction δ, may be determined by powder shear testing [30] (Section 2.2.9) [42].

$$\theta_h = \frac{\Phi + \arcsin\left(\frac{\sin\Phi}{\sin\delta}\right)}{2}$$

Equation 2-3

The powder material assumes to adhere to the effective yield function proposed by Jenike and Shield (1959)[30] which is graphically represented in Figure 2.19. It describes the friction condition for slip between the powder and roll surface. This friction is usually denoted as the slope, μ, but and may also be represented as a wall friction angle ϕ (tan (ϕ) = μ).

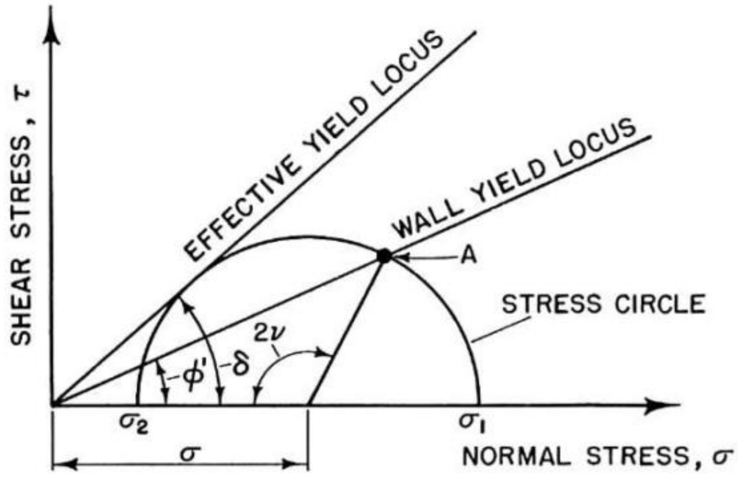

Figure 2.19: Internal and wall yield loci[1]

To appropriately determine the pressure distribution, Johanson deduced that the frictional condition for slip along the roll surface and the feed pressure P_0 were adequate boundary conditions to use the Jenike-Shield criterion in calculating this distribution before the nip region ($\theta > \alpha$) [1].

Pressure distribution in the nip region

Defining the nip region was one of the most important concepts introduced by Johanson. This region assists with understanding where the majority of powder compaction takes place. No slip exists in this region according to the model, with powder being treated as solid elements that are compacted to ultimately achieve a density equal to that of the minimum roll gap. An empirically based pressure-density relationship, that may be obtained from uniaxial compression tests proposed by Jenike and Shield (1959)[30], is used to describe the compressibility of powder (compressibility factor, κ). The pressure distribution in the nip region may be acquired using this factor (κ) provided the nip angle and pressure at the position are known.

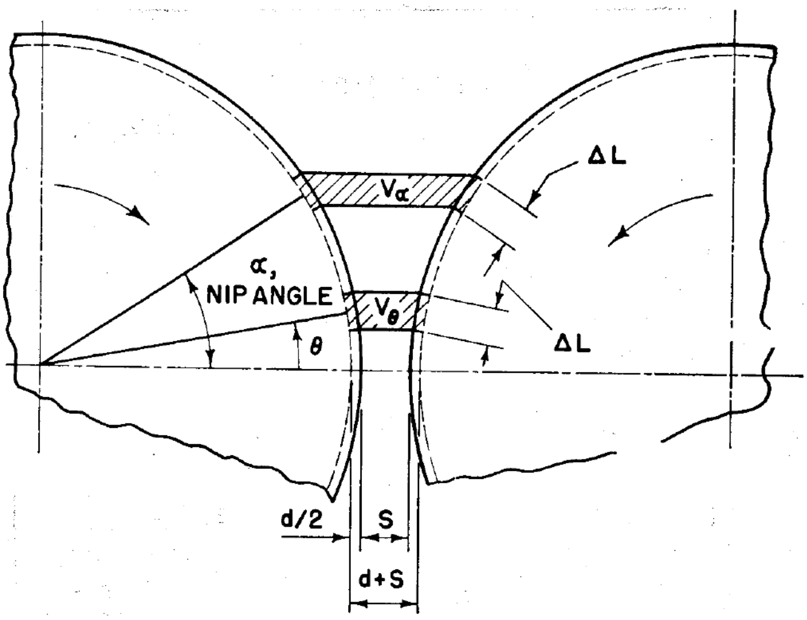

Figure 2.20: Schematic diagram illustrating deformation of particulate matter in the nip region (Johanson, 1965), d= pocket size and S= minimum roll gap[1]

The powder does not experience any slip along the roll surface and must be compressed to the minimum roll gap. Johanson (1965)[1] applied mass conservation represented by Equation 2-4, where a volume V_α must be compressed to a volume V_θ between the same arc-length (ΔL) segments (Figure 2.20). Continuity requires that densities γ_α and γ_θ are related to these volumes by Equation 2-4:

$$\frac{\gamma_\alpha}{\gamma_\theta} = \frac{V_\theta}{V_\alpha}$$

Equation 2-4

Compressibility of a powder as proposed by Jenike and Shield (1959) is the variation of relative density as applied pressure changes. A material property (compressibility factor, κ) was presented by Johanson (1965)[1] to describe what occurs as the powder is compressed. This compressibility factor is derived from a pressure-density relationship determined experimentally by a uniaxial pressing test. The pressure-density relationship is presented as density as a function of pressure on logarithmic scales, presenting an increasing linear function shown in Figure 2.21.

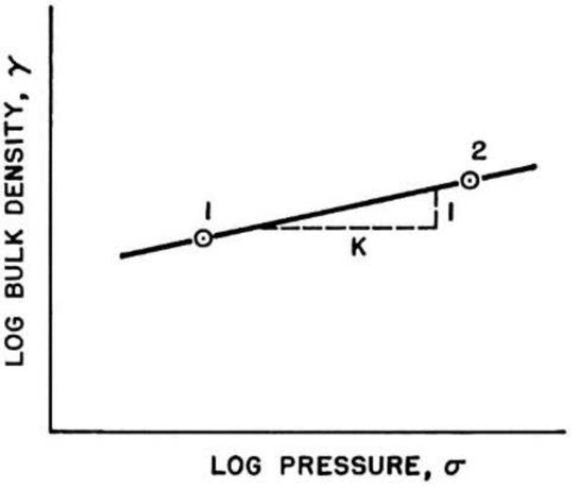

Figure 2.21: Pressure-density relationship (Johanson, 1965)[1]

The pressure-density linear function is given by Equation 2-5:

$$\frac{\sigma_\theta}{\sigma_\alpha} = \left(\frac{\gamma_\theta}{\gamma_\alpha}\right)^\kappa$$

Equation 2-5

σ_θ and γ_θ represent the normal stress and density of the powder at an angular position θ, and exponent κ is a material property constant representing the compressibility of a powder for a given moisture content, temperature and time of compaction. Johanson (1965)[1] states that at the minimum roll gap *S*, θ = 0, and θ will have positive values in the slip and nip regions. Johanson incorporated the nip pressure (σ_α) into the pressure-density relationship seen in Equation 2-5. Patel, et al. (2010)[43] proposed this parameter defines the lower bounds at which this relationship may apply and serves as a fitting parameter with corresponding density γ_α.

$$log\sigma_\theta - log\sigma_\alpha = \kappa(log\gamma_\theta - log\gamma_\alpha)$$

Equation 2-6

The compressibility factor was attained in relation to continuity of powders outlined in Equation 2-5. On the assumption that the lower bound of the equation is known, obtaining compressibility can be achieved by plotting points of pressure-density data obtained experimentally on a logarithmic scale and can be expressed as seen in Equation 2-6. The linear behaviour of this relationship allows for the compressibility constant κ to be evaluated by the inverse of the slope. This relationship can therefore be described by Equation 2-7[42].

$$log\gamma_i = \log\frac{1}{\kappa}\ log\sigma_i + C_i$$

Equation 2-7

where γ_i and σ_i represent the instantaneous density and normal stress in uniaxial compression and C_i is a constant associated with deformed powder at low stresses ($< \sigma_\alpha$). This relationship may only be applied to regions where stress and density follow a logarithmic relationship[42].

In this study, pressure and stress are interchangeable terms as a result of there being one source of pressure in each region. An example of this can be given for the case of the nip region where the primary stress is predominantly caused by the roll pressure ($\sigma = P_{\text{roll}}$).

Equation 2-8 is derived from Equation 2-4 and Equation 2-5 and expresses the relationship between the stress at any angle θ and the stress at the nip angle σ_α.

$$\sigma_\theta = \sigma_\alpha \left(\frac{\gamma_\theta}{\gamma_\alpha}\right)^{\kappa} = \sigma_\alpha \left(\frac{V_\alpha}{V_\theta}\right)^{\kappa}$$

Equation 2-8

For a smooth pocket-less roll surface (d = 0), the volume of powder V_θ between arc-length segments ΔL, roll diameter D and roll width W is given by:

$$V_\theta = \left[d + \left[S + D(1 - \cos\theta)\cos\theta\right]\right]\Delta L W$$

Equation 2-9

The pressure distribution between the rolls can be determined by combining Equation 2-8 and Equation 2-9 resulting in Equation 2-10 provided the nip angle α is known.

$$\sigma_\theta = \sigma_\alpha \left[\frac{\frac{d}{D} + \left(1 + \frac{S}{D} - \cos\alpha\right)\cos\alpha}{\frac{d}{D} + \left(1 + \frac{S}{D} - \cos\theta\right)\cos\theta}\right]^{\kappa}$$

Equation 2-10

The major principal stress acts as the dominant source of stress in the nip region compared to the minor principal stress. This allows for the pressure exerted on the powder by the rolls to be assumed equal to the major principal stress.

Defining the nip angle (α)

Johanson (1965)[1] suggested that at some point during roll compaction the powder stops slipping and begins to travel at the same velocity as the rolls. At this moment there is no relative motion between the powder and the rolls and the angular position at which this took place is denoted as the nip angle, α. Johanson was able to develop mathematical relationships to describe pressure distributions for the slip and no slip conditions in the system. Given the assumption of a there being a transition from slip to no slip, Johanson postulated that the nip angle α could be determined at the point where the slip and nip pressure gradient coincide.

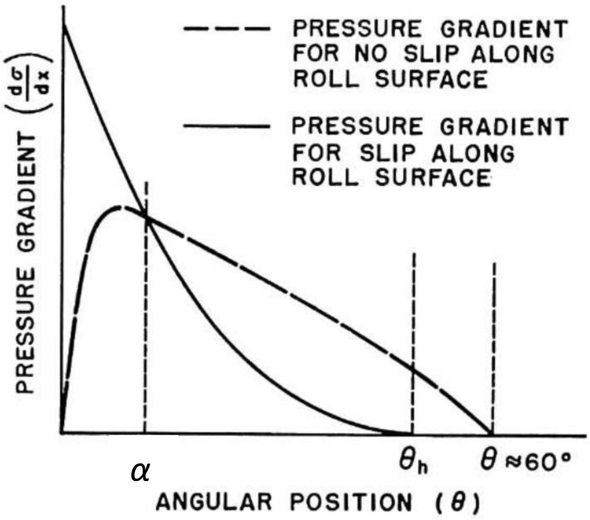

Figure 2.22: Vertical pressure gradient vs. angular position between rolls adapted from Johanson, 1965[1] with the addition of the nip angle α being incorporated into the original image

The solid curve in Figure 2.22 illustrates a typical pressure gradient profile for the slip condition along the roll surface while the dashed line show the condition where no slip occurs. The intersection of these two curves results in the angular position where the nip region begins i.e. the nip angle α. Figure 2.22 may further be characterised into its nip and slip regions where the nip region is between angular position 0 to α, and the slip region is between angular positions θ and the point where the pressure gradient of the slip state tends to 0 or θ_h. θ_h may also be related to the point of feed pressure P_0 [1].

$$\left(\frac{d\sigma}{dx}\right) = \frac{4\sigma\left(\frac{\pi}{2} - \theta - \nu\right)\tan\delta}{\frac{D}{2}\left[\left(1 + \frac{S}{D} - \cos\theta\right)\right]\left[\cot(A - \mu) - \cot(A + \mu)\right]}$$

Equation 2-11

Assuming slip occurs along the roll surface, the pressure gradient for this condition is given Equation 2-11 and is derived from the Jenike-Shield[30] effective yield locus equation (Equation 2-1) coupled with equilibrium conditions that form a solvable system of hyperbolic-type equations, of which the explanation of deriving this calculation method is beyond the scope of this dissertation.

The pressure gradient equation where no slip occurs is given by[42]:

$$\left(\frac{d\sigma}{dx} = \frac{\kappa\sigma_\theta\left(2\cos\theta - 1 - \frac{S}{D}\right)\tan\theta}{\frac{D}{2}\left(1 + \frac{S}{D} - \cos\theta\right)\cos\theta}\right)$$

Equation 2-12

Assuming that the gradients and pressures at the transition point are equal ($\sigma_{slip} = \sigma_{no\ slip}$), the angle of nip α may be calculated by equating Equation 2-11 and Equation 2-12 and solving for where $\theta = \alpha$[42].

Variables used in Equation 2-11 and Equation 2-12 come from the yield and wall loci (Figure 2.19) and are given by the following[42]:

$$A = \frac{\theta + \nu + \frac{\pi}{2}}{2}$$

Equation 2-13

$$\mu = \frac{\frac{\pi}{4} - \frac{\delta}{2}}{2}$$

Equation 2-14

$$\nu = \frac{\pi - arcsin\left(\frac{\sin\Phi}{\sin\delta}\right)}{2}$$

Equation 2-15

2.3.3 Other works employing Johanson's theory

Johanson's theory on roll compaction was the first complex model designed to assist in providing the necessary information for calculating critical parameters in roll compaction. It contributed greatly in equipment design and in understanding and optimising operations and processing of granular materials during roll compaction. This method has predominantly been investigated experimentally in pharmaceutical and food industries. Yusof, et al. (2005)[44] carried out roll compaction experiments on maize powder[45] while using Johanson's model to predict roll force and torque. In this investigation the predicted values were in fair agreement with empirical findings.

Investigations conducted by Bindhumadhavan, et al. (2005)[45] also used Johanson's work to validate experimental findings in pharmaceutical excipients. Here an attempt was made to validate the sensitivity of Johanson's model to measurements of peak pressure taken on a roll compactor. Results showed that the prediction is valid and was able to accurately predict the peak pressure for microcrystalline cellulose but was unable to account for the influence of roll speed.

2.3.4 Limitations of Johanson's theory

While works by Johanson allowed for opportunities to better understand, refine and predict roll compaction, the model has its limitations where a need for a more in depth analysis is required to achieve more reliable results.

Simplifications of powder behaviour in the nip region may lead to large discrepancies when high compaction pressures (>100MPa) are applied, highly compressible materials are used, or variations in roll speeds are investigated since the model does not account for the effects of roll speed. This could lead to insufficient feeding and inadequate bulk densities being achieved with poor strength (Dec, et al., 2003)[36].

One of the most important definitions of the model, the nip angle (α), also has its limits. The nip angle may only be determined if the frictional properties and compressibility constant κ are measured accurately using uniaxial compression and shear cell testing. Measuring the wall friction angle for instance is quite a sensitive technique. Since this parameter is for a powder in contact with a given wall surface, it depends greatly on the nature of that specific wall's material surface. When measuring this parameter, care should be taken in ensuring the same wall material with the exact surface finish as the roll be used when testing for this parameter. In practice however this is not easily done. It may also be argued that shear cell test data may not give accurate results as they generally vary with the applied normal stresses. Leturia, et al. (2013)[38] conducted investigations of flow properties of cohesive powders using various testing methods including methodologies provided by FT4 Powder Rheometer (Freeman Technology[31]). To compare testing methods, a variety of materials were used to evaluate their ability in distinguishing between different powders. Testing methods covered low to high stress levels to compare and examine the hypothetical relationship between them. It was found that characterisation techniques showed variation and have different working ranges depending on the cohesiveness of the powder. The techniques may be used for very similar materials however it was concluded that flow properties cannot be predicted by only one indicator and several different characterisation methods are needed to better characterise powder flow properties.

2.3.5 Investigations into DPR as a feasible manufacturing method to produce titanium and titanium alloy products

There have been a number innovative attempts aimed at producing low cost titanium and titanium alloy products. Direct powder rolling (DPR) is one of those attempts at developing a continuous process to create fully consolidated strip and sheet from titanium powders. There have been a number of processing routes that have been developed to consolidate metal strip from titanium powders using roll compaction[19,46–48]. Metal powders (elemental, BE or PA) are passed through a standard rolling mill, and the applied pressure exerted by the rolls force the powders to be consolidated into a self-supporting green strip. The strip is subsequently subjected to further sintering and rerolling (hot or cold) to produce a final flat product with desired porosity levels[46] or fully dense sheet[49]. A variety of approaches has been investigated and include powder rolling of free-flowing powders, sintering, followed by a cold roll and anneal step; direct hot rolling of the roll compacted sheet, and hot rolling sandwiched layers of roll compacted sheet enclosed in a steel can[50]. While all of these methods have been developed, for direct powder rolling to succeed, low-cost powders must be readily available. If the metal in powder form competes with the price of the metal in ingot form, roll compaction may suffer from economic feasibility. This process therefore requires an in-depth evaluation from a costing standpoint.

In the 1960s, a process was developed to produce strip from titanium sponge fines using direct powder rolling by DuPont. Mechanical properties were said to be comparable to wrought titanium product and the process allowed for the product to be manufactured at a commercial level with large quantities outputted. The strips unfortunately retained residual sodium chloride locked in its microstructure. This prevented the strip to be welded and the project abandoned[15].

Park, et al.(2012)[51] applied direct powder rolling to make thin sheets from – 100 mesh HDH powders using a gravity fed system with two-horizontal counter-rotating rolls. Sintering was in a vacuum environment at 1000°C and 1200°C. . The authors were able to produce sheets without any rolling defects and achieve thicknesses and widths of 1.5 mm and 300 mm; and sintered densities of 85% to 90%. The authors followed sintering with cold rolling and annealing with a thickness reduction of approximately 50% to achieve strips of around 0.5 mm. Mechanical properties and a microstructural evaluation revealed good tensile properties and a near fully dense strip. Optimum tensile properties were exhibited when using sintering temperatures between 1050°C. and 1150°C.

The CSIRO[52] in Australia have been working on developing a continuous process to produce titanium and titanium alloy strip using DPR principles (Figure 2.23). Their procedure involves dry compaction of powders through cold rolling to form a self-supporting green strip; this strip is subsequently fed into a preheating station where the strip is exposed to high temperatures for a few minutes generated rapidly in an argon atmosphere before it is then transferred to a hot rolling station; all in a continuous fashion.

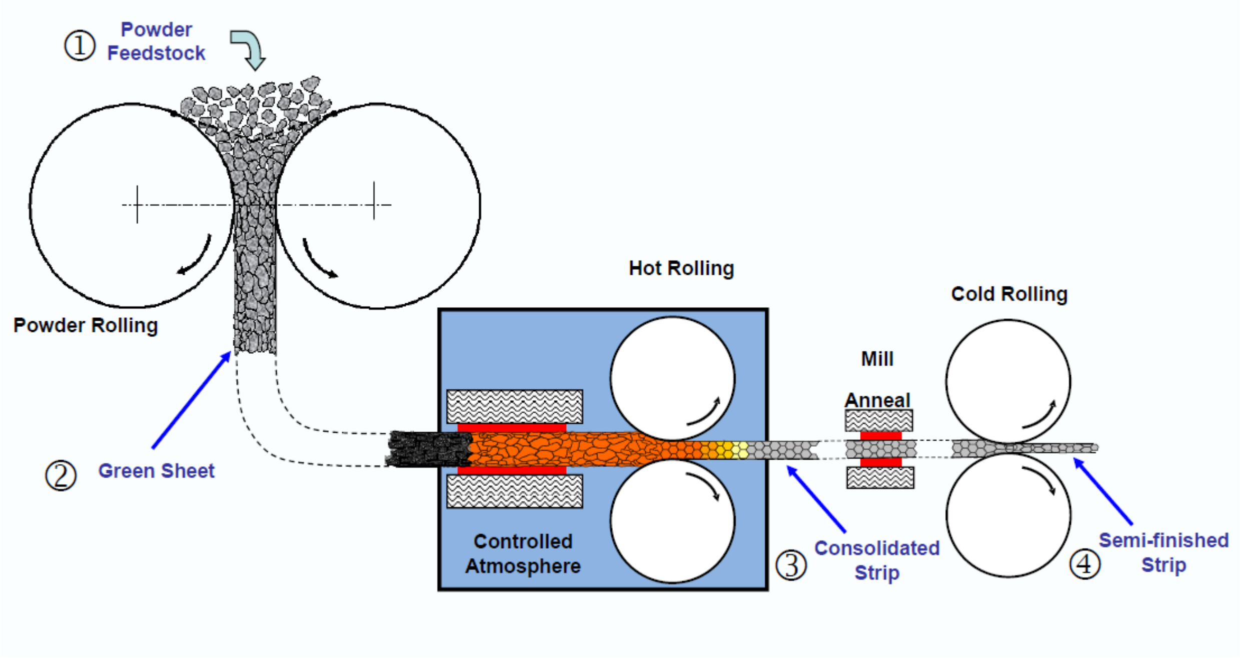

Figure 2.23: Schematic of CSIRO's direct powder rolling continuous process for producing CP-titanium strip[52]

Most of CSIRO's efforts at producing titanium and titanium alloy strip has been focussed on that of thin gauged products, typically around <1.5 mm from CP-Ti, BE and PA powders. Most of their work has been conducted on grade 2 HDH titanium powders which have been identified as exhibiting poor flowing properties with oxygen, nitrogen and hydrogen contents of 0.14 wt.%, 0.011 wt.% and 0.014 wt.%[15].

A gravity fed system is used where powder is fed vertically into a pair of horizontal rolls which compact the powder into a green sheet giving theoretical densities in the range of 75% to 90% and thicknesses in the range of about 1.5mm to 3mm. This range allows for a reduction of around 40% to 55% at the hot rolling densification stage. Uniformity in all dimensions of the strip is vital to the successful progression of the continuous process as well as final properties of strip. This is recognised in part by controlling rolling and material parameters and includes but is not limited to; roll speed, roll gap, particle size distribution and frictional interactions between powders and roll face[53].

2.4 Sintering

Sintering has been in practice for thousands of years. Examples of early sintered products were bricks heated in fire for improved strength. Many more examples exist for sintered ceramic structures in ancient eras including porcelain[54]. The development of a durable lamp filament from tungsten powder for Thomas Edison marked the dawn of industrial modern age sintering and powder metallurgy[55]. From this point on sintering practices gained much traction, particularly in the field of technical ceramics and refractories.

Sintering may be described as a group of particles confined to a particular dimension under which chemical bonding may occur under the influence of a thermal treatment. This in turn creates a coherent body with improved strength and integrity. It is a thermally activated process, where powder particles adhere by diffusional mass transport of atoms. As contact and growth between particles increase, a decrease in free surface evolves leading to shrinkage of open pore volume. The process is highly complicated and involves several mechanisms of material transport[13].

The temperature chosen during the heat treatment is usually below the melting point (T_m) of the major constituent, typically between 0.5 to 0.75 T_m[56]. For sintering to occur there must be a decrease in the free energy of the system. The mechanism and sequence of sintering is difficult to define precisely. The reason for this difficulty is due to changes happening simultaneously or consecutively. Pinpointing these changes poses a real challenge to understanding the mechanisms from one material to another. Sintering is complex and case specific. For any given material and set of sintering parameters there are likely to be different driving forces, stages and material transport mechanisms associated with each case[12].

2.4.1 Sintering and its mechanisms

Sintering is driven by the reduction in surface free energy of compacted particles (for solid-state sintering). Two processes are in constant competition to reduce this energy, that is, densification and coarsening (Figure 2.24). In densification, material is transported by atomic diffusion from grains to pores. Coarsening is the rearrangement of material around pore surfaces while making no improvements to reducing pore volume [54,57].

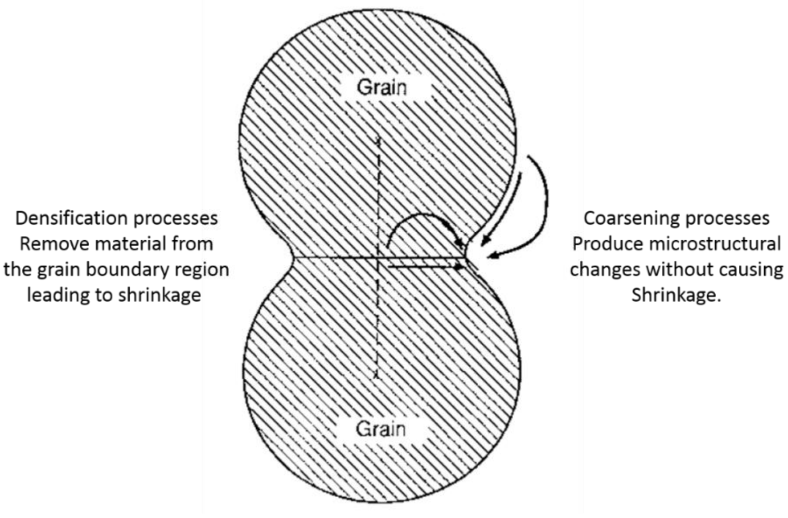

Figure 2.24: Schematic of material transport on a microstructural level distinguishing between densification and coarsening on sintering[57]

Some typical sintering techniques include solid-state, liquid-state, pressure-assisted and activated sintering. Liquid-state sintering involves the presence of a liquid phase during sintering. This may occur whereby the liquid phase arises upon sintering of a primary constituent contained within the original green compact. Alternately a liquid phase may be introduced to the original green compact before or during the early stages of sintering. Liquid-state sintering is sensitive to particle size and green density. It is understood that high green densities and larger particles counteract the advantages that come with melting[12]. Activated sintering requires lowering the activation energy for sintering to occur. A common practice for inducing such behaviour would be to supplement the powder with a chemical additive. This addition results in improved densification[12]. Solid state sintering is one of the more commonly performed sintering techniques and is discussed further.

Solid state sintering

The evolution of sintering is a continuous process from discrete particles to final sintered body. Initially atoms are excited and begin to diffuse creating sharp concave necks between particles. Densification is minimal here. The stress gradient arising from interfacial energies acting over a curved surface acts as a driving force for mass flow. In the instance of neck growth, initially for small necks, this gradient may be large. This stress gradient drives mass flow to the necking region. Most of densification occurs here. This leads to a microstructure consisting of fused solid particles surrounded by a network of interconnected pores. As the neck is enlarged, the curvature gradient subsides, retarding growth. The effects of coarsening and grain growth become apparent following the formation of this microstructure. The interconnected pores begin to separate forming isolated pores[57].

Solid-state sintering consists of atomic rearrangement in the solid-state. The powder does not melt and the mode of densification is by atomic diffusion in the solid state. It can be described by the two-sphere model (Figure 2.25). Two spheres of equal diameter (D) make contact and express weak Van der Waals interactions at their interfaces which hold them together (Figure 2.25a). As heat is added to the system the first stage of sintering commences by the growth of a “neck” at the particle interface. The beginnings of a grain boundary take form where initial contact was made between particles (Figure 2.25b). As sintering progresses so does the size of the necking region. With this increase in neck size and grain boundary development, fewer grains emerge with a larger average grain size. As such, shrinkage occurs as the distance between particles decreases, while pore morphology approaches a more spherical shape. This theory suggests if infinite time is permitted during sintering, the two particles or spheres will coalesce into one with a lower surface area than a combination of the two starting particles (Figure 2.25d). In reality, contacts are made between many particles resulting in densification along many planes [54,57,58].

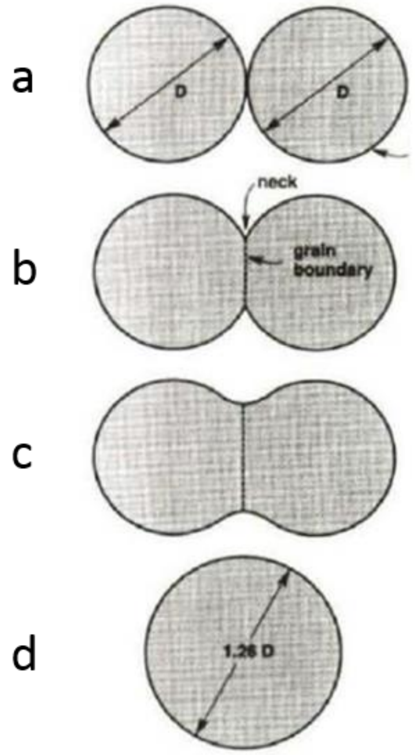

Figure 2.25: Two-sphere sintering model where (a) is the initial point of contact between the two spheres; (b) shows the beginnings of neck and grain boundary formation; (c) further progression of neck growth and (d) a fully merged larger sphere[59]

2.4.2 *Influence of the green body on sintering*

Sintering behaviour and microstructural evolution of a powder compact is heavily influenced by the properties and condition it is in prior to sintering. Some of these include initial relative green density, composition, powder packing and particle size and shape. Subsequently, these too may have a direct impact on mechanical properties such as ductility and strength.

For compacts with low green densities, full densification may never be reached due to neck stabilisation before pores have been removed. It is possible for the neck size to reach an equilibrium where further growth of this region is determined by grain growth[54].

The effects of particle size and packing have significant implications on sintering. These properties may affect sintering rates, homogeneity of microstructures and considerably alter final mechanical properties. While widespread particle size distributions will allow for higher packing density in a compact leading to reduced porosity in its green state (Section 2.2.8), controlling the microstructure on sintering becomes more of a challenge. When there is a mix of particles with varying sizes, grain growth of larger grains occurs more rapidly and outcompetes any small grains that exist. While a high density may be attained, it comes at the expense of a uniform microstructure which may limit its mechanical properties. If a homogeneous microstructure is to be achieved both homogeneous packing and a narrow size distribution of particles are necessary. Spherical particles are ideally suited for this outcome[56]. Generally, the rate of densification increases with smaller particles, high temperatures, high green densities and extended times[54,56].

2.5 Sintering titanium and its alloys

Producing near net shape titanium has its clear advantages, such as eliminating the need to machine the notoriously difficult metal as well as reduced material consumption since the metal is also difficult to recycle by conventional means. A titanium part may be made many different ways from powder. However, the simplest most economically attractive method is the press and sinter approach.

Kroll (the metallurgist who developed the widely known industrial Kroll process to produce metallic titanium) ran one of the first sintering trials in argon at 0.066 atm. Samples were composed of elemental powders and pressed at 207 MPa. A significant contribution was made in 1946 by Dean, et al., where titanium was sintered in vacuum due to its high affinity for oxygen, nitrogen, carbon and hydrogen. This methodology would later be adopted widely by most working with pressed and sintered titanium powders. Argon is still used in sintering practices as it is a simple operation and economically more viable. However, problems are associated with the use of argon such as removal of volatiles. As a precaution, when using commercially pure argon in sintering it is necessary to purify it before it enters the region of sintering[16].

Titanium powders are surrounded by a thin oxide film, which is estimated at around 10nm thick[16]. Many metal powders have this persistent oxide layer which may prohibit sintering. Titanium however differs from most metals where it allows for the diffusion of oxygen within the metal. It was found that the film completely dissolves in the β-phase after approximately 60 minutes at 1000°C[60].

Titanium sinters in both the α and β regions. A dilatometric study was done on powders pressed at 300 MPa with a size range of 3-45 μm showing sintering initiating at around 700°C while still in the α-phase after holding for 1 hour. The sintering range is between 700-1350°C and sintered density generally increases with sintering temperature[16]. Starting with a higher green density generally assists with achieving a higher sintered density[25,61]. Having a higher green strength also assists with the component keeping its shape and avoiding uncontrolled shrinkage. High compaction pressures can achieve green densities, however particle size also plays a significant role. Powders of smaller particle sizes result in more surface to grain boundary area for diffusion to take place and shorter distances to travel. They also will result in smaller pore sizes in the green state making pore healing in sintering easier.

2.5.1 Powder properties and its effect on sintering

Various powder properties will have an effect on the way the green body will behave during sintering. Powder shape, packing ability, size and composition all play vital roles in the success of sintering. In the case of elemental powders, the source of titanium powders and their production route can be vital in its ability to sinter. Sponge fines for example can have different reducing agents when producing the titanium sponge before crushing to obtain the sponge fines used in sintering. The choice of reducing agent can affect the levels of chloride present in the material and residual chlorine is known to create porosity in sintered parts. Sponge reduced by sodium produce larger amounts of fines and usually holds reduced chloride levels compared to magnesium reduced sponge[62].

The effects of particle size are also highly influential to the rate at which sintering and densification may occur. For instance, smaller particles will have faster rates of sintering and grain coarsening due to their high surface energies[13,54].

Robertson and Schaffer (2009)[61] pressed and sintered HDH titanium powders with particle sizes in the range of <150μm, <45μm, <20 μm and PA Ti-6Al-4V powders in the range of 45 to 150 μm, to determine the effect of particle size on their green and sintered densities. Titanium powders with larger particle sizes showed a slight increase in green density. This comparison was based on full particle size distributions of powders. To improve on investigating the relationship between powder size and green density, powders were sieved further to narrower size ranges (e.g. 38 to 45 μm, 45 to 63 μm etc.). This was to limit the varying particle size variables. Very little variation was noticed in this case. The initial compaction study with the full particle size range of powders showed higher green densities. This is presumably attributed to improved packing ability with a wider distribution.

To track the sintering progress from the green state, Robertson and Schaffer (2009)[61] made use of a densification parameter (Equation 2-16). The densification parameter takes into consideration the change in density from green state to sintered state as a percentage of the theoretical density of the material, in this case titanium. The effect of particle size on densification has been summarized in Figure 2.26. The three titanium powders displayed in the figure clearly illustrate how the densification parameter increases as particle size is reduced. The closer the densification parameter is to unity, the closer the sintered part is to the theoretical density of that material.

Significant findings of Robertson and Schaffer's (2009)[61] study included the following:

- Titanium powders with wide particle size distributions showed high green and sintered densities. Creating smaller particle bin sizes did not improve overall densities.
- The compaction pressure had more of an effect on the green density than the variable particle sizes used.

- An increase in compaction pressure improved both green and sintered densities with little effect on the densification parameter.
- The densification parameter increased with decrease in particle size.

Where the densification parameter (ΔD) is defined as:

$$\Delta D = \frac{\rho_{sintered} - \rho_{green}}{\rho_{theoretical} - \rho_{green}} \times 100$$

Equation 2-16 [61]

where ρ_{sintered} is the sintered density of a compact, ρ_{green} is the green density of a compact and $\rho_{\text{theoretical}}$ is the theoretical density of the material under investigation.

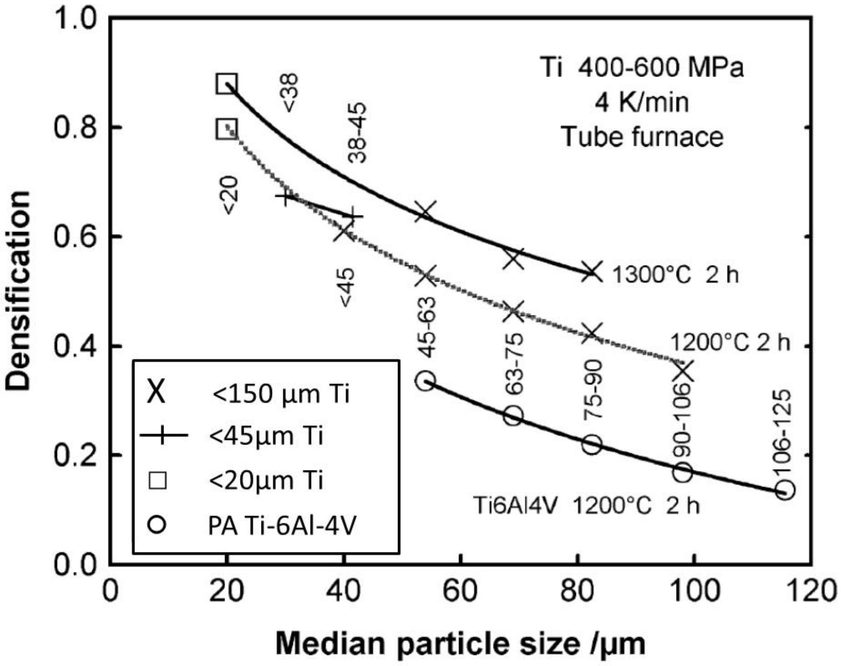

Figure 2.26: Adapted from Robertson and Schaffer (2009)[61] illustrating the effects of particle size on densification of titanium powder pressed (400-600MPa) sintered at 1200 °C and 1300 °C for 2 h

These last two points illustrate the implications of mechanical pressings and the limitations of sintering. If the compaction pressure is increased, the green density will increase, and as such, the sintered density will also increase. However the ability for a certain material to improve solely by the practice of sintering is not significantly affected (densification parameter). This "improved" density was only as a result of a higher density input (at the green state) before sintering as a result of an increase in compaction pressure. The material seems to still be limited by fundamental sintering principles despite an increase in green density.

Gülsoy, et al. (2014)[63] conducted a study to observe the effects of particle morphology on microstructural and mechanical properties of injection moulded Ti-6Al-4V powders. All samples were sintered at 1300°C for 20 hours in a vacuum environment. The effect of initial green densities of spherical powders had different outcomes after sintering. It was found that higher green densities had higher sintered densities compared to spherical samples that started with lower green densities. It was also found that spherical powders exhibited better sintering compared to irregular powders where spherical samples could reach 99.3% of theoretical density while irregular only 99.7%. The porosity present in irregular powders was higher than spherical and as a result deteriorated its tensile performance. Porosity in general improved for both powder types however the rate was greater in spherical powders. This improvement was attributed to higher packing of spherical powders compared to irregular shaped powders. Once the sintering temperature was reached, inherent porosities that occur between contact area of all particles were closed by α and β-phases. Due to the poorer packing of irregular particles, these pores did not close and were more prevalent. It is important to note that packing was a critical factor in the solidification of these injection moulded components. With higher green densities, higher sintered densities can be achieved.

2.5.2 Sintering Ti-6Al-4V

There are a few ways to sinter the titanium alloy Ti-6Al-4V. The most obvious defining choice would be the choice of powder. The two most common choices would be between pre-alloyed, PA, or blended elemental, BE, powders. There are numerous combinations of BE powder to try which could involve master alloy blends, elemental blends and combinations of the two. Each has different compaction and sintering properties as the powder compositions and properties vary. Each method has its advantages and disadvantages. PA powders are chemically more consistent and homogeneous as they are essentially alloys made by conventional means through ingot metallurgy that are then converted to powder. But their high strength makes compaction very difficult and high cost makes them economically unattractive. PA powders have also exhibited green densities lower than those made from HDH powders. Sintered densities follow suit and it was recommended that to achieve a sintered density in the range of 93-95% for the press-and-sinter approach of PA powders, pressures of >950MPa must be attained in the pressing stage and sintered at 1300°C[25]. It is generally not advised to use PA powders for the press-and-sinter method. Instead, PA powders are used in hot isostatic pressing and metal injection moulding applications[2]. For the press-and-sinter method, the use of BE powders has been adopted.

Abkowitz (1986)[64] found the green densities of cold isostatically pressed BE Ti-6Al-4V compressed at pressures up to 413 MPa reached 85% and their relative sintered densities reached 95% theoretical density at temperatures in the range of 1200 – 1315°C. These PM products may be used in non-critical applications and in the case where wrought standard tensile properties are required, sintered parts may be hot isostatically pressed to 99+% density. The cost benefits of using this approach come from reduced powder costs, low energy costs and improved machinability. The ability to consolidate BE powders at room temperatures gives advantages over PA powders.

Fujita, et al. (1996)[65] observed the outcomes of using HDH powder in a process called the TiARA process. This method was recorded to achieve densities in excess of 99% using the BE approach. In the early stages of the press-and-sinter of titanium powders, a hot isostatic pressing step was included to close porosity after sintering. The TiARA process eliminates the hot isostatic pressing step making it economically more advantageous. The TiARA process went through a series of changes from its original state. An important recommendation of the original process was that of controlling particle sizes of both the base titanium powder and alloying powders. Where the base powders are larger than the alloying powder[16,65]. Fujita, et al. (1996)[65] made use of HDH powders as they have lower chloride levels.

2.5.3 Elemental powders and master alloy additions

While base titanium powders may influence compaction and sintering of a powder, remaining additions used to create the alloy are just as important. BE powders used in titanium alloy PM refers to metal powders that are added to titanium powder as elemental or master alloy additions. BE is generally favoured in PM as it has cost and near-net-shape advantages over PA powders when creating a component out of an alloy. There are however, advantages and disadvantages with respect to the choice of BE method (elemental/master alloy). These choices can have variable cost implications and can influence processes such as compaction and sintering.

Figure 2.27[66] shows how the green density is affected at three different compaction pressures depending on the powder mixture of Ti-6Al-4V. Ivasishin, et al. (2002)[66] studied the effects of various powder mixtures based on titanium and titanium hydride powders with alloying additions of either master alloys, or elemental powders with different particle sizes, using the press and sinter method. Variable compaction pressures between 300-1000 MPa were applied. The authors hypothesized that to achieve maximum density for the final product, it is necessary to achieve high green densities at the compaction stage and further improve on this density by sintering the compact. Compaction results showed mixtures with titanium powders achieving higher densities at the same compaction pressure compared to those with titanium hydride base powders. This is because compaction mechanisms are very different between the two titanium base powders. Titanium hydride powders are brittle, fracture on compaction, and have a lower strength limit. Titanium powders however deform under compaction and are ductile. Mixture 2 (Figure 2.27) gave the best compaction result. This was attributed to the ductile base titanium and the high purity of the constituents involved. The variable particle sizes of alloying powders had no significant effect on the density any of the compacts.

Samples were sintered at 1350°C and density changes are given in Figure 2.28. This figure shows clearly how the densities of the various powder mixtures vary significantly. Ivasishin, et al. (2002)[66] discussed how individual parameters produced these results. Two primary themes were identified, the effect of titanium base powder particle size and the effect of the alloying addition method. For the mixtures where alloying additions were in the form of elemental powders, only slight increases and in the case of

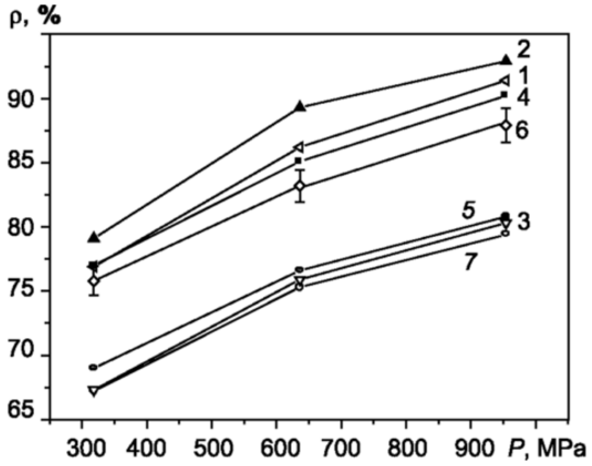

Mixture	Description	Methods of addition
1	Ti, −100 μm, 1% impurities, including 0.29%O	Elemental powders Al: 98%, −100 μm V: 99%, −100 μm
2	Ti, +100–200 μm, 0.7% impurities, including 0.29%O	Elemental powders Al: 98%, −100 μm V: 99%, −100 μm
3	TiH_2, −100 μm, 1% impurities, including 0.30%O	Elemental powders Al: 98%, −100 μm V: 99%, −100 μm
4	Ti, −100 μm, 1% impurities, including 0.29%O	Elemental powders Al: 95%, −20 μm V: 98%, −40 μm
5	TiH_2, −100 μm, 1% impurities, including 0.30%O	Elemental powders Al: 95%, −20 μm V: 98%, −40 μm
6	Ti, −100 μm, 1% impurities, including 0.29%O	Master alloy powders Ti-35Al: 98.5%, −100 μm V-25Al: 98.3%, −100 μm
7	TiH_2, −100 μm, 1% impurities, including 0.30%O	Master alloy powders Ti-35Al: 98.5%, −100 μm V-25Al: 98.3%, −100 μm

Figure 2.27: Pressing characteristics of cold compacted mixtures 1-7 and corresponding table outlining mixture compositions 1-7[66]

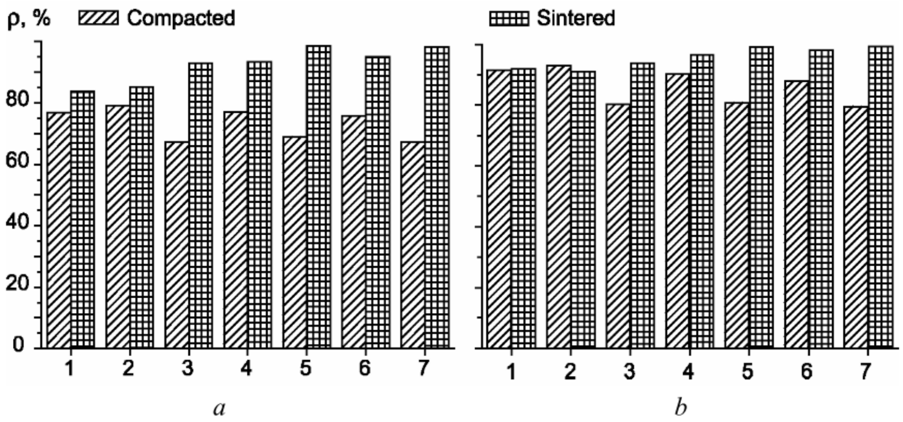

Figure 2.28: Comparing densities before and after sintering at 1350°C of compacts of compacted Ti-6Al-4V mixtures 1-7. Compacting pressure (a) 320; (b) 960 MPa[66]

mixture 2, a decrease was observed. These low final densities after sintering were attributed to swelling due to a reaction between titanium and molten aluminium. Once these large pores are formed on heating, they are unable to fully compensate for the swelling effect and the subsequent "healing" and closing of these pores cannot continue to completion upon further annealing at higher temperatures. The authors also stated that another contributing factor to this inability to fully close porosity at these sites is due to a layer of intermetallic compounds that have formed at the point of contact. Relative densities for these compacts with base titanium powder and elemental powder additions above 92% could not be achieved. Using master alloy additions showed noticeably improved results (mixture 6) compared with mixtures 1, 2 and 4. The melting point of the master alloy exceeds that of the sintering temperature preventing a liquid phase from forming.

Mixtures 4 and 5 with smaller and more dispersed elemental alloying powders exhibited an improved density upon sintering. The authors attributed this increased sintered density to the reaction of aluminium with titanium in the solid phase due to the aluminium's small particle size. This would in turn lessen the swelling effect noted previously. In addition, the pores that would form once aluminium particles have melted would be so small, and be more readily able to heal on further heating at higher temperatures[66].

When does alloying commence in BE compacts

Fujita, et al. (1996)[65] tracked BE compacts over a range of sintering temperatures evaluating their microstructural evolution. Figure 2.29 shows the various stages of sintering for these compacts. It tracks the stages of sintering covering dilatometric effects and the start and end homogenisation using X-ray diffraction. The authors found that alloying commences at 1000°C in Ti-6Al-4V master alloy compacts with alloying completing at 1200°C. The method used to confirm these claims was by observing X-Ray diffraction (XRD) patterns of Ti-6Al-4V compacts.

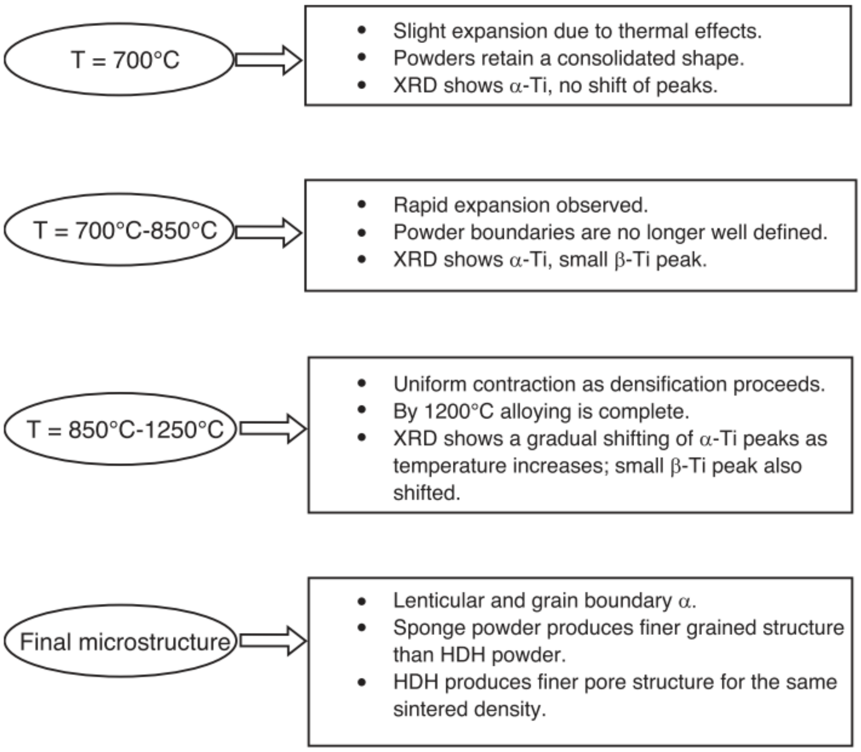

Figure 2.29: Flow diagram describing the stages of sintering for the TiARA process compiled by Qian, et al. (2010)[28] based on the works of Fujita, et al. (1996)[65]

Measuring homogeneity

Sintering alloys becomes more difficult when employing the BE approach as an additional process other than densification must occur, homogenisation. Full homogenisation is influenced heavily on the chemistry of alloying constituents and their ability to redistribute themselves within the metal matrix. Diffusion mobility, phase-composition and the manner in which each constituent influences and affects the mechanisms of sintering and homogenisation are some of the main factors to consider when designing a treatment.

X-ray diffraction (XRD) and energy dispersive X-ray spectroscopy (EDX) are common techniques used in determining chemical homogeneity of an alloy compact post sinter. Each has its own limitations due to the capabilities of the technique. XRD is a bulk compositional analytical technique that exploits the characteristic pattern of diffraction angles and intensity of diffraction beam that is unique to a crystal. By observing what crystal structures are present in the material, one can deduce the composition of the material and for whether instance if it has been homogenised. A drawback of this technique is its inability to perform localised analysis of the material. It is not easy to determine if localised diffusion has taken place and to what extent it has occurred.

EDX mapping couples electron microscope imaging with a special detector that can identify the chemical composition at a specific position chosen by the operator. Localised information may be captured with ease in homogeneous or single phase samples. Multiphase samples with variable composition depending on the location within the sample becomes more complicated. Consider Figure 2.30 where zinc atoms are randomly spread in a base of some pure composition. There are two components here with distinct boundaries and divisions separating the two. Depending on how the analysis is carried out, misleading information could be obtained. In one scenario an area could be analysed including predominantly zinc particles in the interaction volume. Thus giving the appearance that the sample has a higher concentration of zinc. In another instance however, at a different location, the interaction volume may miss most of the zinc particles present, leading to a lower concentration of zinc for the same sample.

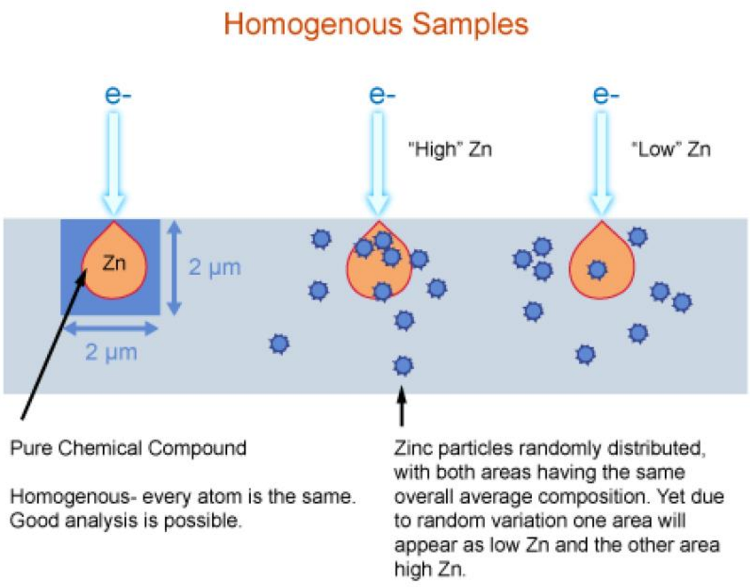

Figure 2.30: An illustration of how quantitative EDX analysis can be affected by a multiphase sample[67]

Defining an appropriate length scale to determine whether sufficient diffusion has taken place in the case of a multiphase alloy such as Ti-6Al-4V is also a challenge that must be overcome. Generating compositional information from too small an area could result in false negatives as the data gathered may be skewed to represent for example the α-phase which is rich in aluminium. This gives the impression of incomplete diffusion as higher aluminium concentrations may be detected. On the other hand if the area of analysis is too large, so large so as to capture an area where efficient mechanical blending of the powder blend reflects the composition of the alloy, the results could indicate the sample has been homogenised when in fact it had not. And the observation is that of unhomogenised areas in the appropriate ratio given the field of view. The results are showing the correct fraction of titanium, aluminium and vanadium in the (large) area of analysis. They are not showing whether diffusion took place.

2.6 Review conclusions

This chapter discussed the underlying principles for the application of direct powder rolling of titanium and its alloys. Theoretical models were described to describe the process and fundamental mechanisms of powder metallurgy, roll compaction and sintering were discussed. While there have been past attempts at understanding direct powder rolling, DPR, in practice, knowledge is still limited due to the complexities related to roll compaction and sintering of titanium alloys from diverse powder sets and operating conditions. It was concluded that DPR is heavily affected by roll compaction parameters, feed powders (particle size, flowability and frictional properties), and sintering parameters (soak time, temperature). Thus, a general model of the process with guidelines on process design and output performance has yet to be described.

CSIRO's model for direct powder rolling[52] is one of the most recent and successful technologies that have used the principles of this process to produce titanium and titanium alloy flat sheet. These guidelines are used and discussed in this dissertation.

3. Materials and Methods

Roll compaction depends greatly on feed powder properties. This study followed the blended elemental (BE) approach of Ti-6Al-4V for direct powder rolling (DPR) utilising two specific blends which are referred to as B1 (Blend 1) and B2 (Blend 2). B1 consists of commercially pure titanium (CP-Ti) blended with commercially pure aluminium and commercially pure vanadium. B2 consists of CP-Ti and a 60Al-40V master alloy (MA) powder. Preparation of powders influences these properties. To understand the influence of these properties, powders underwent a number of detailed analyses to characterise them. Techniques used to characterise powders are introduced in Section 3.1. Typical powder properties include particle size, shape, density, frictional and flow properties. Methods used to measure these properties are discussed. A roll compactor was used for compression. Rolling speeds and gaps were manipulated and tested as the parameters influence green strip density. Section 3.5 introduces the experimental layout and procedure during rolling operations. Sintering affects density and homogenisation of BE compacts. In Sections 3.7 and 3.8 sintering specifications and methods used to determine homogenisation are discussed.

3.1 Materials

Titanium, aluminium and vanadium powders were supplied by Chengdu Huarui Industrial Co., Ltd and 60Al-40V MA powders were supplied by Reading Alloys. Titanium, vanadium and 60Al-40V MA powders were produced via the HDH method. Since this work aimed to reduce manufacturing costs of titanium products, HDH powders were preferred as they are more economically viable and of a lower cost compared to other methods. HDH powders are also known to show good compactibility which makes them a reasonable choice in the field of DPR[68].

3.1.1 Particle specifications and characterisation techniques

Table 3.1 gives powder specifications for all powders used in this study. Powder production method, mesh sizes and expected powder particle size range information was supplied by the manufacturer. Oxygen and nitrogen contents were analysed by the Light Metals Division at CSIR, Pretoria using an ELTRA O/N analyser.

Table 3.1: Powder specifications

Metal powder	Powder production type	Mesh size	Size range (µm)	Oxygen (wt %)	Nitrogen (wt %)
Titanium	HDH	-100+200	74<Ti≤149	0.17±0.01	0.01±0.001
Aluminium	Nitrogen atomised	-100+325	44<Al≤149	0.98±0.04	0.01±0.001
Vanadium	HDH	-325	V≤44	0.98±0.01	0.03±0.001

60Al-40V MA	HDH	-230	MA≤63	0.21±0.01	0.003±0.001

Powder particle size distribution

Particle sizes for each powder were analysed at CSIR South Africa using a Microtrac Laser Diffraction particle analyser. This measurement is based on the difference in light diffracting off particles of various sizes. The instrument provided a measurement range from 0.02 to 2000 µm. Particle size analysis requires a sample volume of approximately 7-9 grams per test. Tests were done in triplicate for each powder type. Summarised data for titanium, aluminium, vanadium and 60Al-40V master alloy powders are listed as cumulative and mean distributions and discussed in Section 4.1.

Particle shape analysis

SEM images were taken using a FEI Nova NanoSEM 230 ETD detector. Images shown in Figure 3.1 show that powders were all irregular in shape. As expected, the titanium and MA particles were highly angular with the vanadium particles less so, whereas the aluminium particles were somewhat elongated and nodular. This observed nodular shape may be due to rapid cooling leaving insufficient time for surface tension to minimise their surface areas into spheres.

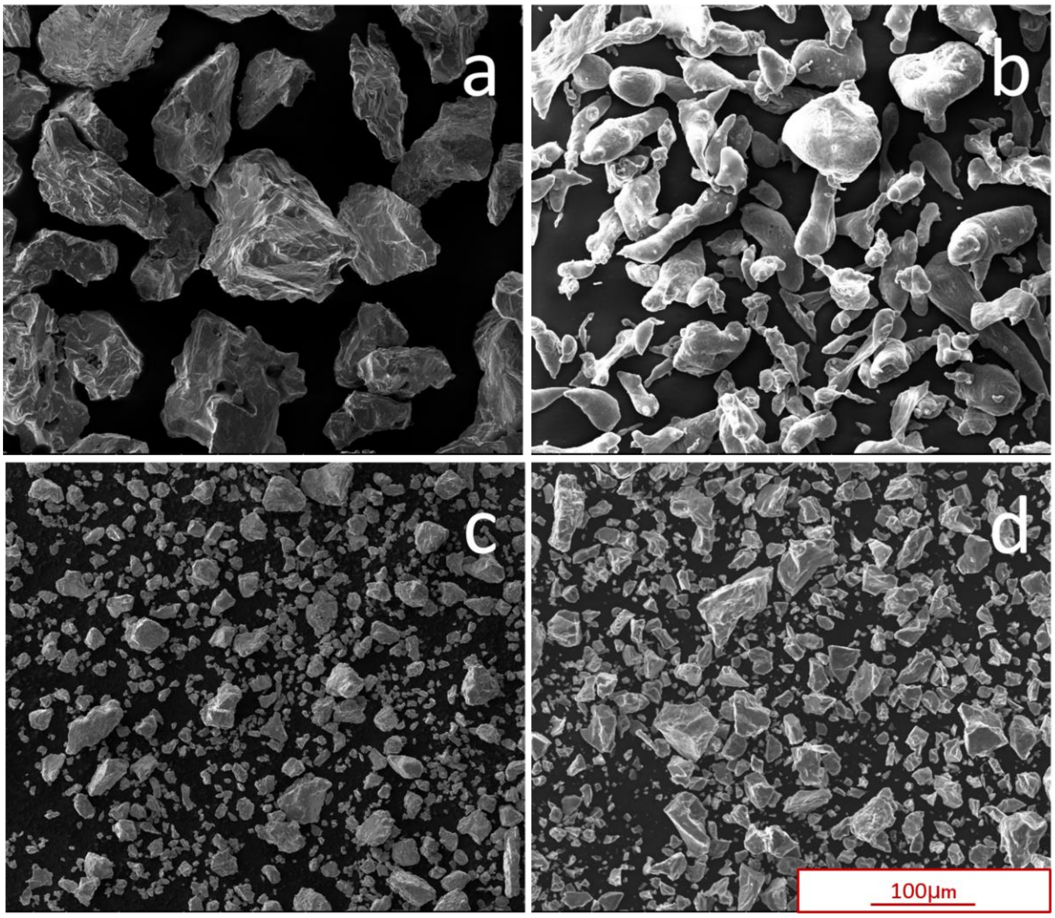

Figure 3.1: SEM/SE images of a) titanium; b) aluminium; c) vanadium and d) 60Al-40V master alloy powders

3.2 Density measurement

Density measurements for both green and as-sintered compacts were carried out following the ASTM B962 standard. Apparatus used is shown in Figure 3.2. This set-up consists of a mass balance, a “bridge”, a specimen support structure and a beaker. The specimen to be measured was held in a wire basket attached to the specimen support structure. This was suspended into the beaker containing water.

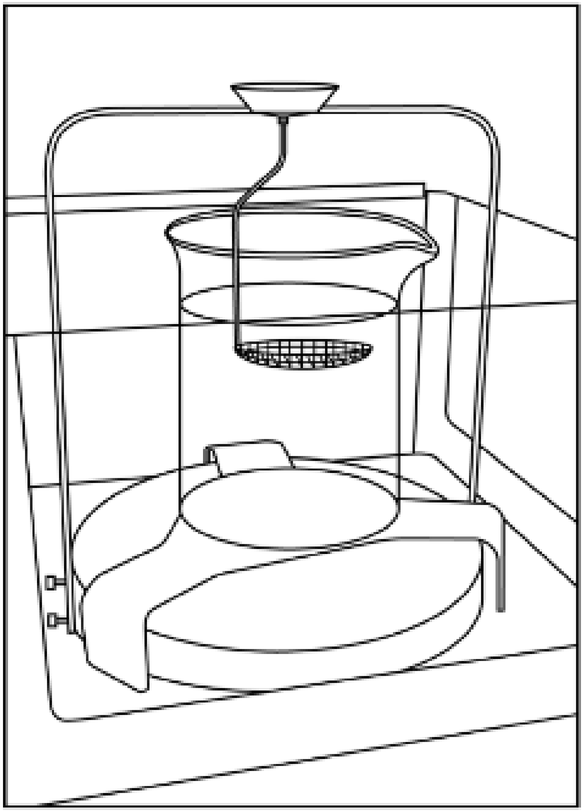

Figure 3.2: Apparatus used in density measurements of green and as-sintered compacts. Showing the support 'bridge' beneath the beaker above the mass balance with specimen support structure attached to the mass balance.

Measurement and calculating of the density involves five steps: the mass of the sample in air (A); the mass of the oil-impregnated sample in air (B); the mass of the oil-impregnated sample and sample support structure immersed in water (C); the mass of the oil-impregnated sample support immersed in water (E); the density of the water at its specific temperature (ρ_w). With these measurements it is possible to calculate the relative density (D_s) using the formula:

$$D_s = \frac{A\rho_w}{B - (C - E)}$$

Equation 3-1

The relative density of green and sintered compacts was calculated as a percentage of the theoretical full density of Ti-6Al-4V (4.43g/cm^3)[8].

3.3 Microstructural analysis

Grinding and polishing

Samples were ground and polished employing standard Ti-6Al-4V methods as indicated in Table 3.2.

Table 3.2: Grinding and polishing steps used for microscopy sample preparation

Step	Polishing pad	Speed (rpm)	Force (kN)	Lubricant	Time (min)
1	800 SiC	150	30	Water	2:00
2	1200 SiC	150	30	Water	2:00
3	MD Dac	150	30	3μm Diamond Suspension	5:00
4	MD Chem	150	30	OP-Nap colloidal silica	5:00

Light Microscopy (LM)

Bright field LM was used to study grain and porosity morphology of etched samples using Kroll's reagent after being subjected to grinding and polishing steps outlined in Table 3.2. A Reichert MeF3A inverted light microscope fitted with a Leica 320 camera and Leica DCF acquisition software was used for LM.

3.4 Critical parameters and implementation of direct powder (DPR) rolling simulation

Uniaxial compression tests were done at the CSIR Light Metals Division.

3.4.1 Compressibility constant (K)

B1 and B2 powder blends were compressed uniaxially into cylindrical green compacts using a floating die press of diameter 17.5 mm. Each compact held a mass of approximately 5g. Tests were conducted under loads which correspond to maximum pressures of approximately 50 – 1500 MPa. Section 2.3.2 details the methodology of how the compressibility constant κ was calculated.

3.4.2 *Frictional and flow properties*

The ability for a powder to flow depends on the adhesive forces between particles which plays a critical role in powder compaction. Two methods to investigate frictional and flow properties of powders include the Hall flow and shear cell test.

Hall flow test

The Hall flow test involves taking 50 g of a metal powder and recording the time it takes to flow though the orifice of a Hall flowmeter funnel (Figure 3.3). The test follows ASTM B213 standard guidelines.

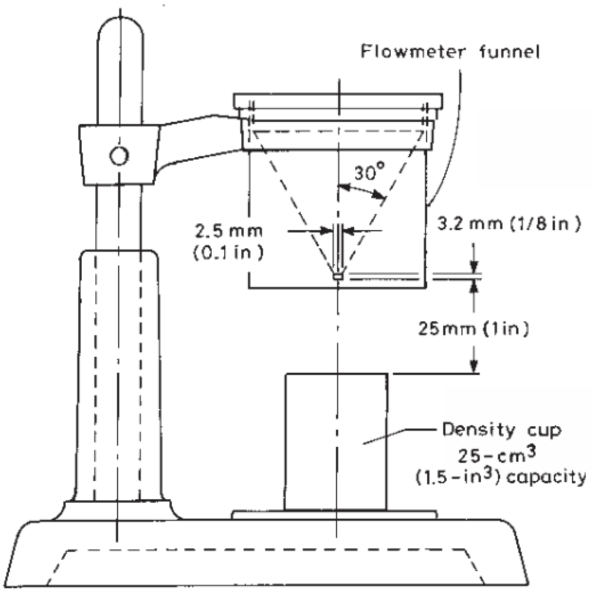

Figure 3.3: Hall flowmeter[12]

B1 and B2 powder blends were subjected to Hall flow tests. Three tests were done per sample and detailed results are given in Appendix A.

Shear cell test

A rotational shear cell module was used to determine the effective angle of internal friction (δ). The test was measured using a FT4 Powder Rheometer (Freeman Technology, United Kingdom) with a pre-consolidation stress of 9 kPa and normal stresses within a range of 3 – 7 kPa. The wall friction angle (ϕ) was also measured using the same equipment with normal stresses in the range of 3 – 7 kPa and against a wall friction disk with surface roughness $R_a \sim 2.5$ μm. Shear and wall friction tests were carried out twice. Section 2.2.9 gives an overview of powder shear testing. The actual testing procedure used in this study is given below.

Procedure

Shear cell testing mainly comprises a circular cross sectional rotating vessel holding the powder sample as in Figure 3.4. A shear head component is attached to induce rotational (shear stress) and vertical loads (normal stress). As the shear head moves downward along the normal plane to make contact with the top of the powder, it induces a normal stress. The shear head will continue to move further into the powder specimen until the required normal stress is established. For shear stress induction the shear head should rotate where a shear plane is established below the ends of the blades. The powder will resist rotation of the shear head and with increasing shear stress the powder bed will eventually fail when a maximum shear stress is reached. This maximum shear stress is known as the yield point or point of incipient failure. The normal stress remains constant for the duration of this shear test.

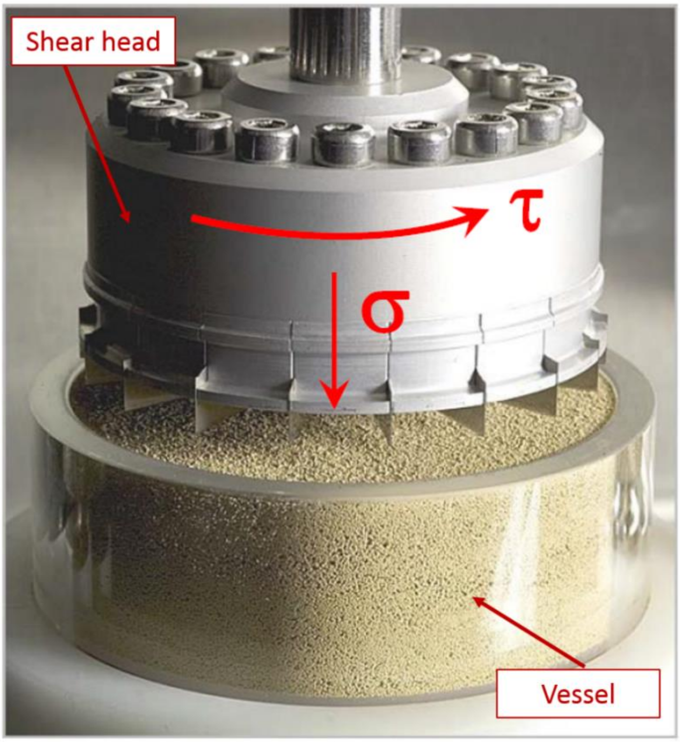

Figure 3.4: FT4 Powder Rheometer Shear cell where τ is the shear stress and σ is the normal stress. Adapted from (Freeman Technology)[31]

Table 3.3: Shear cell test fixture details

Vessel size	Pre-consolidating stress level	Starting accessory	Vessel specification
25 mm	9 kPa	23.5 mm blade	25 mm x 10 ml split vessel

Table 3.3 gives shear test cell dimensions and specifications for the test used in this study. Figure 3.5 details how the Jenike-Shield loci are constructed. A complete yield locus is measured using one sample. To measure another point of the yield limit in the same samples, after shearing to failure, the

normal stress is increased to σ_{pre} (pre-shear stress), which correlats to the normal stress applied initially at the first pre-shear. The sample is then pre-sheared again under this same normal stress until steady-state flow is reached. Once the sample has been relieved of the shear stress, the normal stress is reduced to another value of σ_{sh} (shear stress) < σ_{pre}, where the sample is sheared again resulting in another point of the yield limit that may be represented in the σ, τ-plot. After shearing, the sample is again pre-sheared, then sheared, and this continues until an adequate number of data points of the yield limit are known for the yield locus to be determined[29].

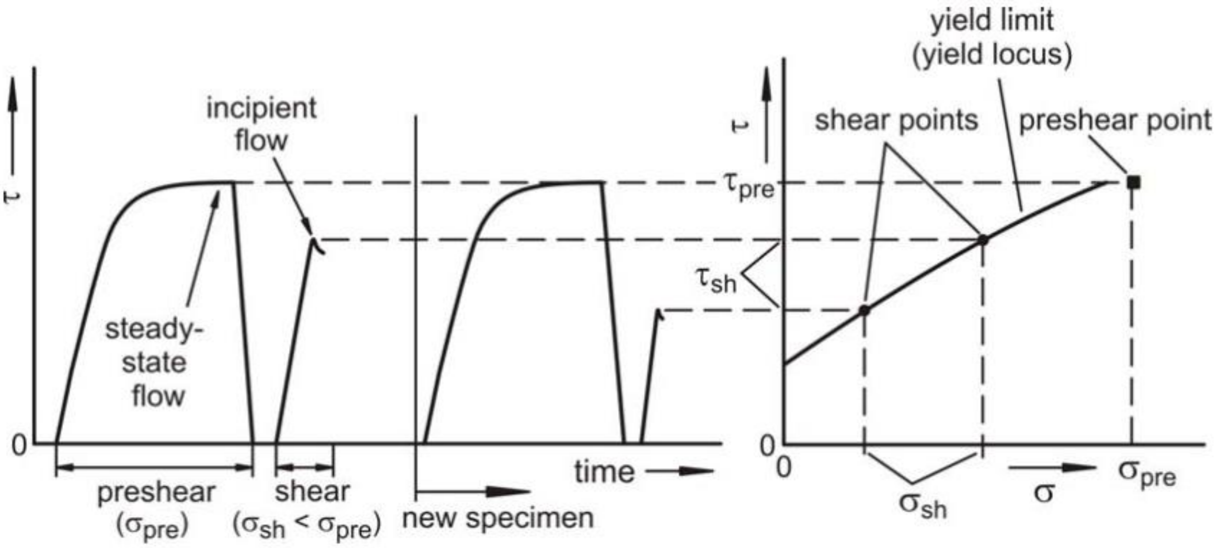

Figure 3.5: Plot of shear stress vs. time and yield locus from Schulze (2010) [29]

The yield locus may be obtained by plotting each value of incipient shear stress τ and corresponding normal stress σ on the σ, τ coordinate system illustrated in Figure 3.6 with yield loci being drawn from these points.

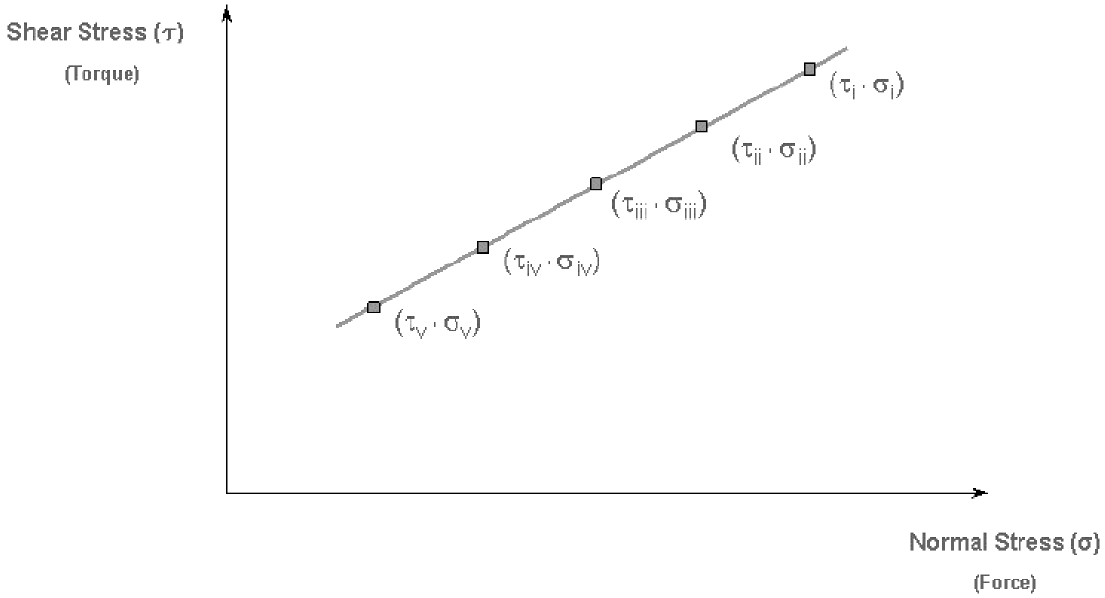

Figure 3.6: Typical yield loci plot from Freeman Technology (2010)[31]

Table 3.4 details the normal stresses, σ, applied to B1 and B2 powder blends in shear cell testing. These values correlate to the representative illustration given in Figure 3.6.

Table 3.4: Applied normal stresses for shear cell test on B1 and B2 powder blends

Normal stress (kPa)	σ_i	σ_{ii}	σ_{iii}	σ_{iv}	σ_v
B1 and B2 powder blends	7	6	5	4	3

Finding the effective angle of internal friction (δ)

To investigate the effective angle of internal friction δ, the yield locus is required. The effective yield locus defined by Jenike (1964)[69] is represented by the dashed straight line passing through the origin of the σ, τ-plot lying tangential to the major Mohr's circle. This stress circle characterises the stresses in the sample at the end of consolidation (steady-state flow). This line encompasses the σ-axis containing the effective angle of internal friction δ. Since the major Mohr's stress circle is that of steady-state flow, δ may be used as a measure, if the internal friction is at steady-state flow. This test was conducted at five normal stresses outlined in Table 3.4 in triplicate for B1 and B2 powder blends.

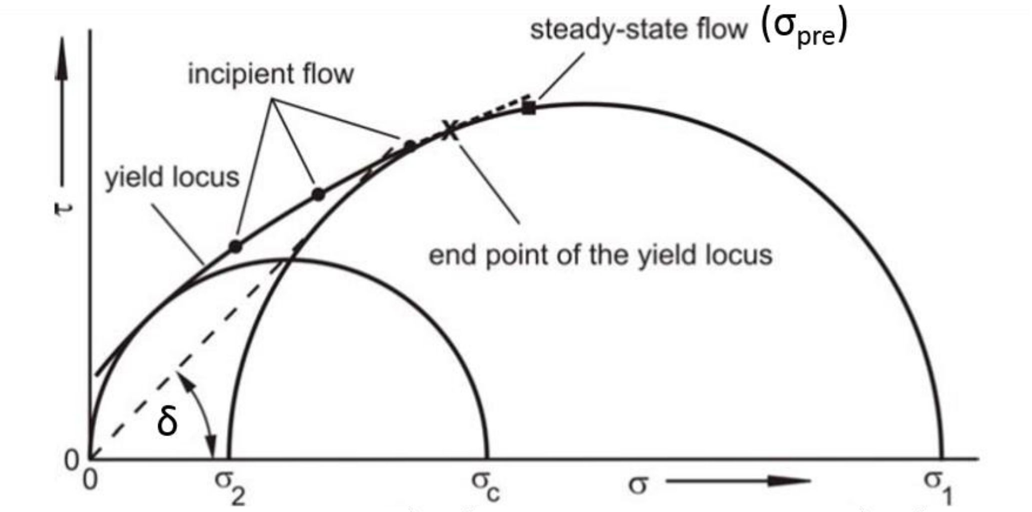

Figure 3.7: Yield locus diagram to illustrate how to determine effective angle of internal friction (δ) adapted from Schulze (2010); where σ_{pre} is the pre-shear stress, σ_1 is the major principal stress, σ_2 is the minor principal stress and σ_c is the unconfined yield stress. [29]

Finding the wall friction angle (Φ)

The friction that results from the interaction between the powder and the roll surface is known as the wall friction. The wall friction test is similar to that of the shear cell test with the exception of the wall friction disc being used in place of the shear head blade.

Table 3.5: Wall friction test fixture details

Vessel size	Pre-consolidating stress level	Surface roughness ~ R_a	Starting accessory	Vessel specification
25 mm	9 kPa	2.5 μm	23.5 mm blade	25mm x 10ml split vessel

Initially the powder is subjected to a vertical normal stress as the wall friction disc head makes contact with the surface of the powder bed until the required normal stress σ_w is reached. The powder bed is then shifted relative to the wall material surface, inducing a shear stress τ_w. This causes a shear plane to form between the disc and powder surfaces. The torque increases as the powder bed resists the rotation of the wall friction head. This resistance increases until it is overcome where the maximum torque is seen. The wall friction head continues to rotate for a pre-defined period of time. The torque required to maintain this rotation is measured and allows for a steady-state shear stress to be determined.

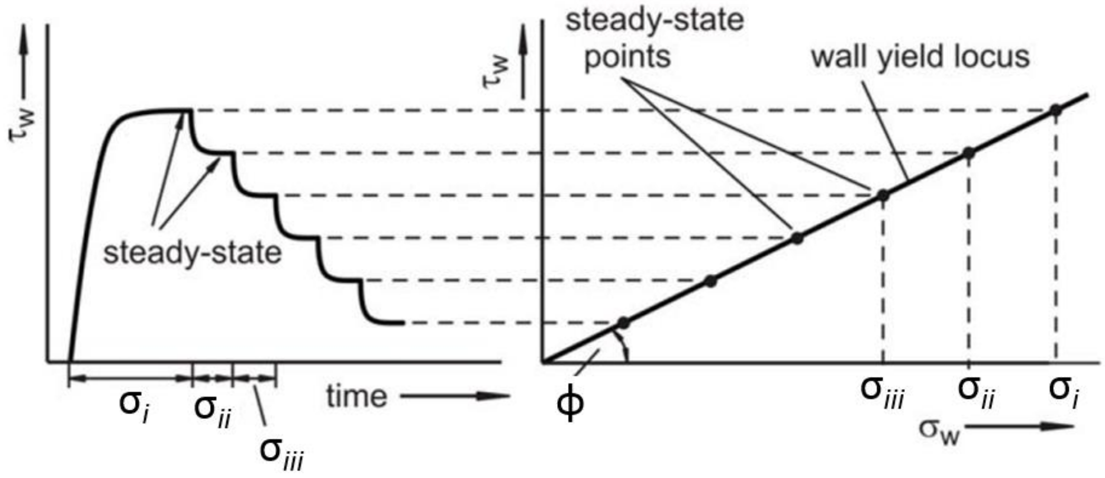

Figure 3.8: test profile of wall shear stress in a wall friction test adapted from Schulze (2010)[29]

Table 3.6: Applied normal stresses for wall friction test on B1 and B2 powder blends

Normal stress (kPa)	σ_i	σ_{ii}	σ_{iii}	σ_{iv}	σ_v
B1 and B2 powder blends	7	6	5	4	3

The wall friction is measured at incrementally decreasing wall normal stresses. A pre-consolidating normal stress of 9 kPa is applied. The shear process is initiated when normal load σ_i is applied and rotation begins. The wall shear stress, τ_w, increases. As the test continues, the increase of the wall shear stress starts to dip until a constant wall shear stress is obtained, resulting in steady-state shear stress. After steady-state is achieved, the normal load is reduced. With each decrease in normal stress, its corresponding shear stress also decreases (Figure 3.8). After some time, a steady-state shear stress is achieved again, each time reducing the normal stresses from $\sigma_{i\text{-}v}$. Through this sequence, the values of steady-state wall friction at five normal stresses (Table 3.6) are measured. Each pair of values of wall normal stress and steady-state wall shear stress are plotted on a σ_w, τ_w-diagram as illustrated on the right-hand side of Figure 3.8. The line generated by passing through the measured points is the wall yield locus.

The wall yield locus is a yield limit similar to the yield locus. It describes what wall shear stress, τ_w, is required to move the powder bed continuously along the wall surface under a specific wall normal stress, σ_w. The wall friction may be quantified by calculating the wall friction angle, ϕ. The wall friction angle may be constructed by plotting each of the steady-state shear stress values against their corresponding normal stresses. Figure 3.9 illustrates how the wall friction angle ϕ may be calculated from the wall yield locus.

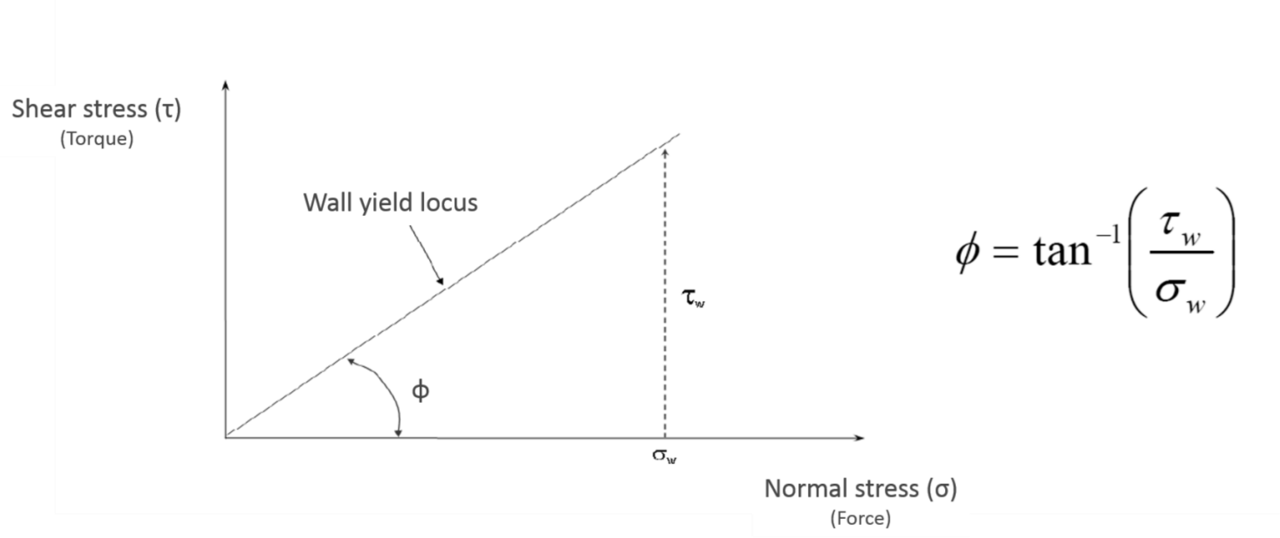

$$\phi = \tan^{-1}\left(\frac{\tau_w}{\sigma_w}\right)$$

Figure 3.9: Determining the wall friction angle (ϕ) adapted from Freeman Technology[31]

3.4.3 Rolling simulation

Using Johanson's theory on roll compaction and MATLAB mathematics software, a direct powder rolling (DPR) simulation was developed by Balicki and Michrafy[37] and Zhang, et al.[6] to better understand compaction pressure on rolling. For the purposes of this study, input parameters were divided into material properties and roll-press dimensions (fixed and variable) per powder blend. The theory and simulation were designed in such a way where relative density is inferred by predicted maximum pressure (from MATLAB simulation) coupled with densities from a uniaxial compression study (Section 3.4.1). Both B1 and B2 powder blends were investigated at varying roll gaps. A more detailed illustration of how the simulation was applied is shown in Figure 3.10. The objective was to calculate the theoretical maximum pressure for different assumed roll gaps after taking into account the material property inputs (determined from Sections 3.4.1 to 3.4.2) and the nominated roll press dimensions.

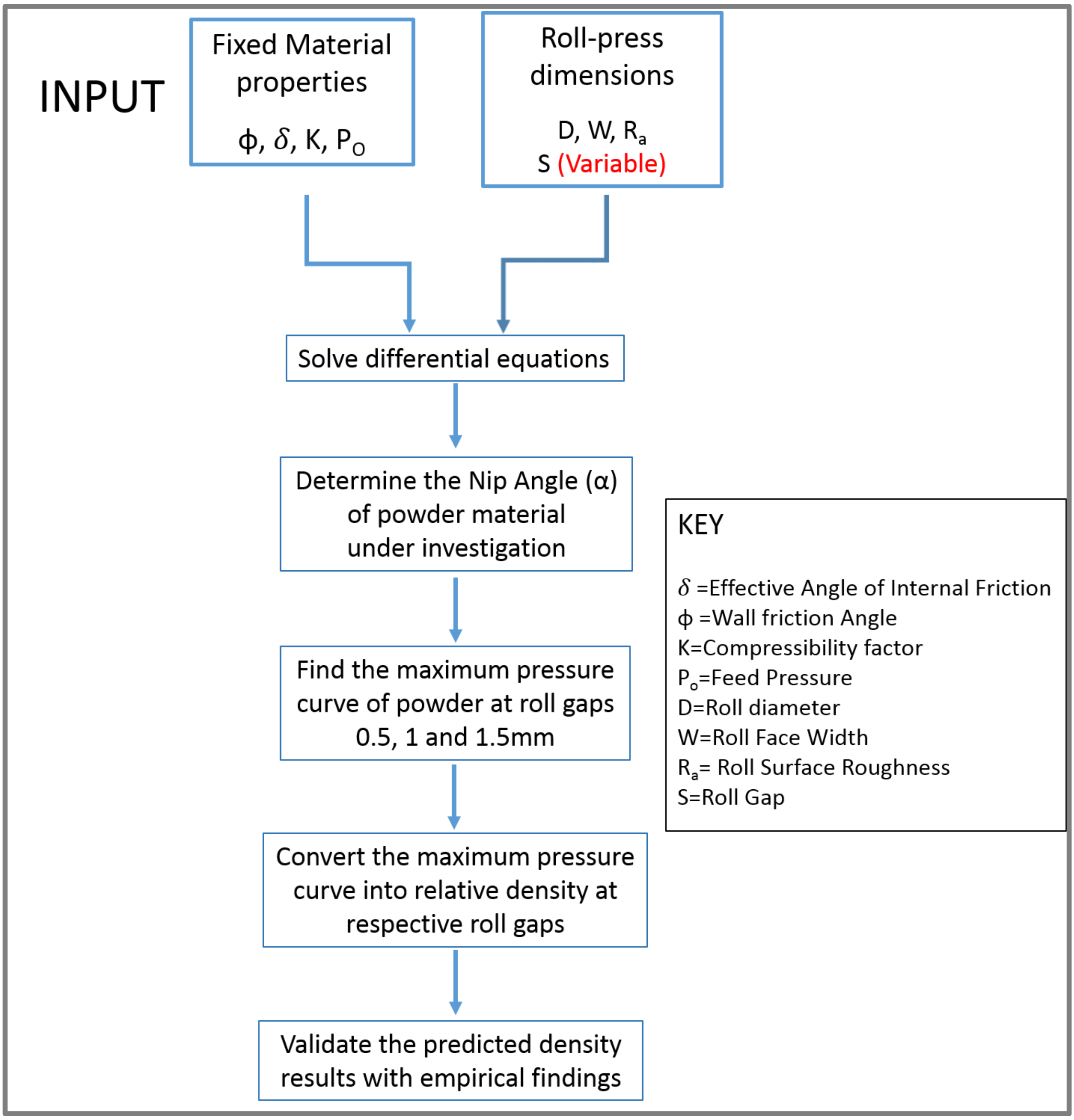

Figure 3.10: Flow diagram showing algorithm for DPR simulation based on Johanson's theory (1965)[1]. Adapted from Zhang (2015)[6]

3.5 Direct powder rolling (DPR) methodology

Direct powder rolling (DPR) experiments were carried out at the University of Cape Town within the Centre for Materials Engineering laboratory facilities on a laboratory scale gravity-fed vertical rolling mill (Figure 3.11). This rig set-up was equipped with two horizontally arranged rolls of diameter 265 mm with mean surface roughness of 2.5 µm. The roll gap (S) could vary between 0.5 to 5 mm and roll face width (RW) between 0 to 150 mm. The roll face width was controlled by two adjustable aluminium side plates mounted onto the feed zone shown in Figure 3.11b. The roll speed range permitted on this rig was 0 to 14 rpm. Powder feed rate was controlled by a gravity feed hopper of diameter 250 mm.

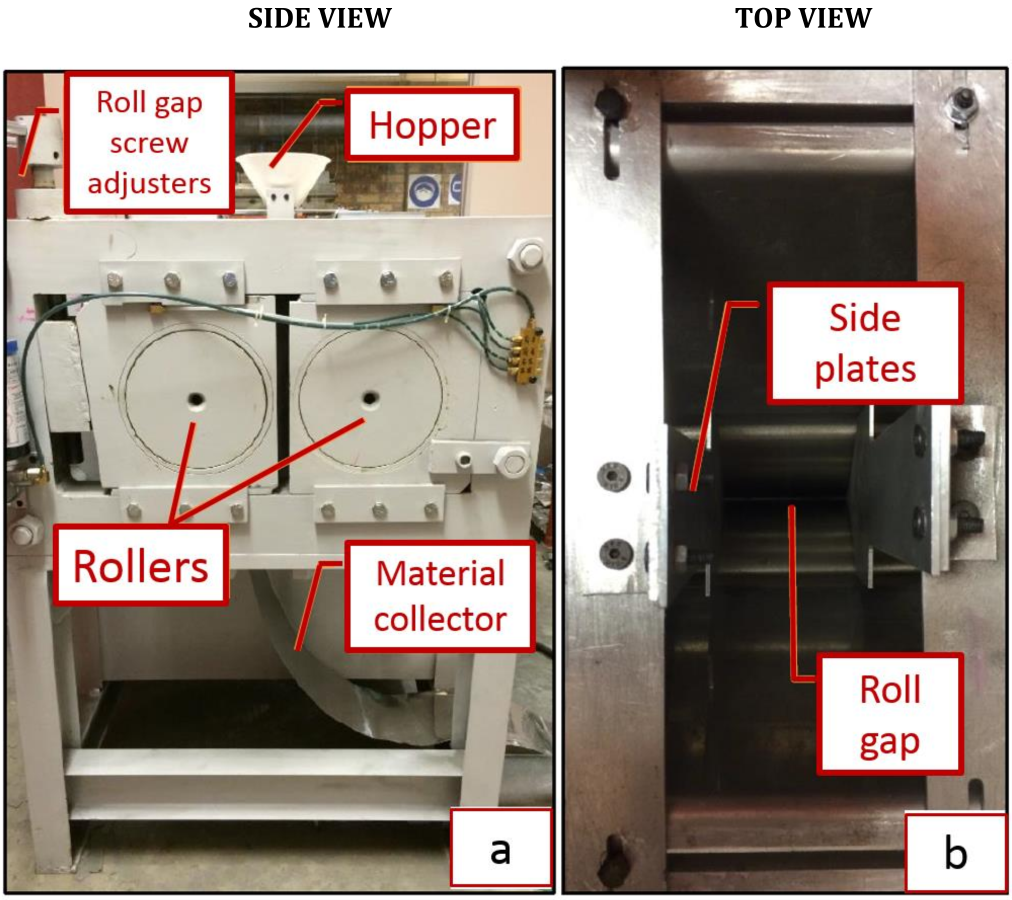

Figure 3.11: Gravity-fed laboratory scale vertical roll compactor

The roll face width was kept constant at 65 mm. A roll speed of 14 rpm was applied across all specimens for initial compaction. The volume of powder used for roll gaps 1 and 1.5 mm was 150 ml while a roll gap 0.5 mm used 100 ml of powder. The reduction in material volume for decreasing roll gaps was necessary to prevent overloading of the rig. Figure 3.12 illustrates the rolling methodology employed during this study.

Both B1 and B2 powder blends were used in this study to compare how each powder blend behaves on rolling. For rolling, a comparative study was conducted at varying roll gaps. For the B1 powder blend, roll gaps 0.5, 1 and 1.5 mm were studied. Three strips were produced at roll gaps 1.5 and 1 mm while two strips were produced at a roll gap of 0.5mm (Figure 3.12). For the B2 powder blend, two roll gaps were investigated (1 and 1.5mm). Rolling was done in triplicate at these roll gaps. A roll gap of 0.5 mm for B2 powders was not permitted as rolls seized as a result of overloading. Strip lengths vary from 300 – 400 cm.

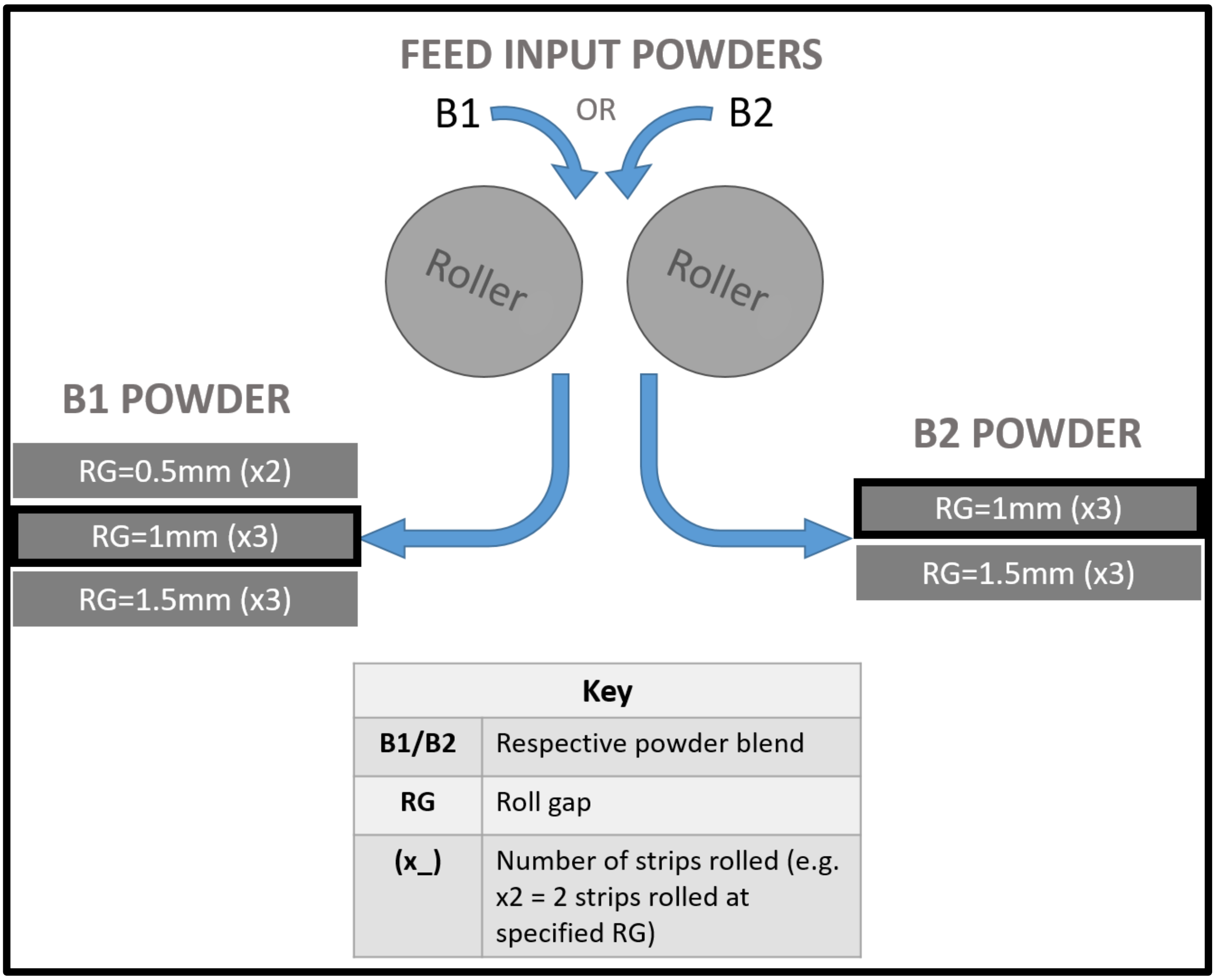

Figure 3.12: DPR experimental methodology

Table 3.7: Selected roll gaps for B1 and B2 powder blends

Powder blend	Roll gap, S (mm)		
	0.5	1	1.5
B1	✓	✓	✓
B2		✓	✓

All green strips were documented and analysed according to characteristics and properties observed. These include green density, strip width and strip thickness and are discussed in Chapter 6.

3.6 Green strength measurements

Green strength measurements were carried out on an INSTRON 3365 Dual Column Universal Tester fitted with a three-point bending jig set-up shown in Figure 3.13. The bending jig design was based on ASTM standard B312-14. A 10 kN load cell was attached and a displacement speed of 1 mm/min was employed. 2 x B1 strips (denoted as 1B1 & 2B1) and 2 x B2 (denoted as 1B2 & 2B2) rolled at 1 mm were used in testing using the same rolling setup as discussed in Section 3.5. Six samples (31 mm × 13 mm) from each strip were sectioned along the length and green strengths were recorded.

Green strength was calculated according to the stress equation:

$$GS = \frac{3FL}{2T^2W}$$

Equation 3-2

where:

GS = Green strength (MPa)

F = Breaking force required to rupture (N)

L = length of span between supporting pins of test fixture (=25 mm)

W = Sample width

T = Sample thickness.

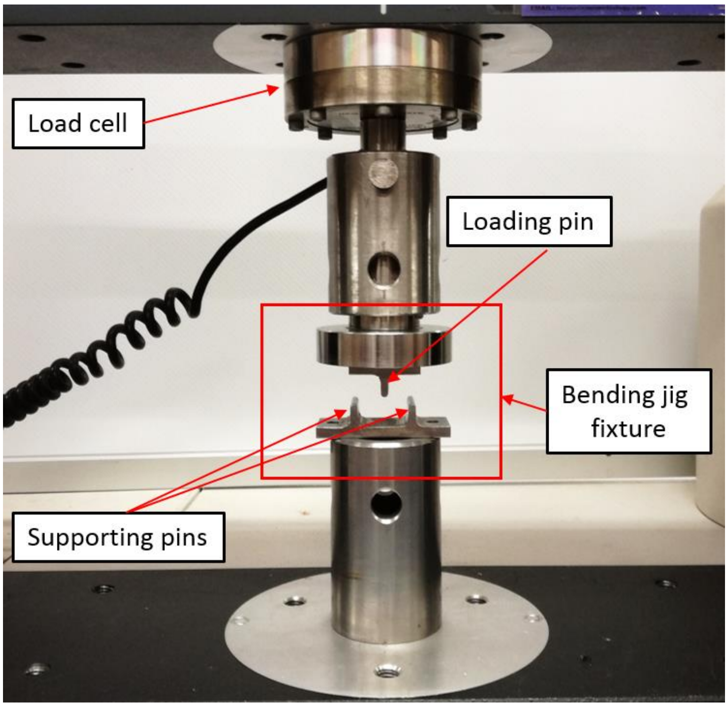

Figure 3.13: Photograph of three-point bending set-up for green strength investigation

3.7 Sintering B1 and B2 green specimens

Sintering experiments were conducted on B1 and B2 green strips. For comparative analyses between blends, strips rolled at a roll gap of 1 mm were used. The sampling of strips is explained in detail below.

To exclude the variation in density along the strip length (discussed in Section 6.1) and accumulate more discrete data points, two 20 mm× 30 mm samples were sectioned across the strip width. This method allows for a more accurate representation of sample evolution from green to sintered state, as less of a variation in density was observed across strip width. Two adjacent samples of 20 mm× 30 mm were sectioned from the same region along the strip length. The first sample was used in its green state to obtain the green density value. The second sample undergoes sintering, and density measurements were subsequently carried out. The green and sintered densities were compared against each other to observe sintering effects. This process was repeated along the length of the strips. An illustration of this can be seen in Figure 3.14. It was important to sample pairs of specimens across the width of the strip since the green density was found to vary along the length of the strip.

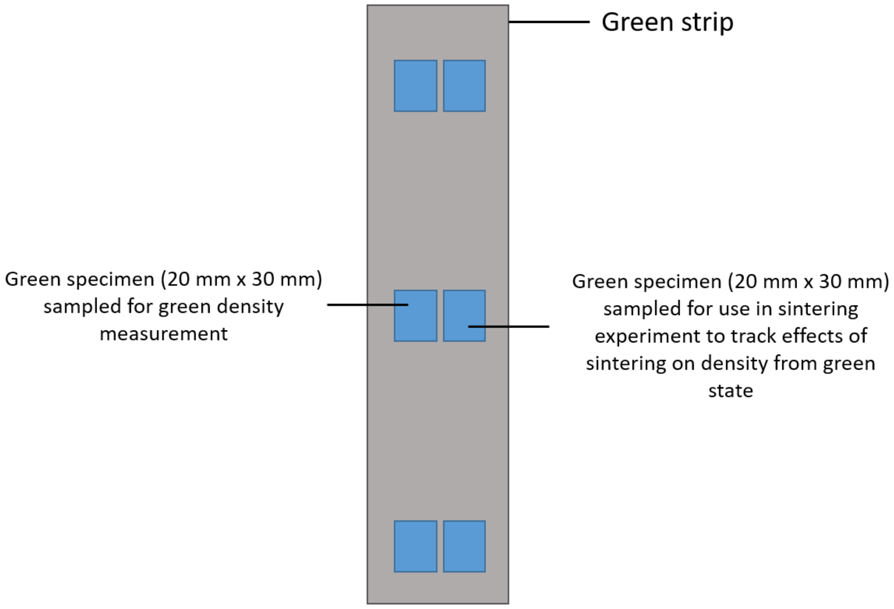

Figure 3.14: Illustration of the sampling technique used in sintering experiments for B1 and B2 strips

Green samples underwent vacuum sintering at 1200°C in a horizontal furnace (Figure 3.15) reaching pressures lower than 10^{-5} mbar. Heat treatments allowed for a heating rate of 6.6°C/min followed by a furnace cool after sintering.

Figure 3.15: Horizontal vacuum sintering furnace with mullite tube

3.8 Assessing homogeneity of sintered specimens using Energy Dispersive X-Ray Spectroscopy (EDX)

Energy-dispersive X-ray spectroscopy (EDX) provides an opportunity to very readily perform compositional analysis at varying length scales depending on the size of the scanning raster selected in the SEM. This approach provides good opportunity to assess the degree of homogenization in metal alloys. In the case of continuous solid solution alloys (single phase), the choice of length scale is quite straight-forward in that complete homogenization will ultimately be reflected when spot analysis (stationary beam) produces the same composition everywhere in the metal sample. However, the situation becomes more complicated when multi-phase alloys are investigated since the inherent element partitioning between the phases will influence the analysis. The homogenization of Ti-6Al-4V produced via the blended elemental (BE) powder metallurgy (PM) process makes a challenging case for this method of analysis. The challenge is to be able to measure the degree of diffusional mixing of the titanium, aluminium and vanadium powder particles whilst being able to account for the element partitioning that occurs between the α and β-phases that constitute the Ti-6Al-4V alloy. The appropriate length scale for EDX analysis is influenced by initial powder size and the fine lamellar α/β micro-structure that evolves on cooling to room temperature, where certain regions in the lamellar structure are enriched with a particular alloying element. In the case of Ti-6Al-4V, the α-phase, shown as the lighter phase in Figure 3.16b is enriched with aluminium, while the pencil-like outline of the darker β-phase is enriched with vanadium. SEM X-ray mapping shows this spatial distribution of elements in Figure 3.16a; where the element of interest is reflected by the number of counts detected for a given point in the scan, and a corresponding pixel in the X-ray map for that element is given as a level of brightness.

The present study investigated the relative degree of homogenization that occurred during the sintering of DPR strips produced from B1 and B2 powder blends in order to optimize the choice of powder and sintering conditions. In particular, the approach to the EDX analysis is highlighted to illustrate the difference in homogenization progress for the respective powder blends. The EDX data were acquired using an Oxford X-Max Silicon Drift Detector coupled to an FEI NanoSEM 230. The beam spot size, primary voltage (20 keV), and acquisition time were adjusted to maintain dead times ranging between 30-40% and to identify minimum total X-ray counts required to limit statistical variation. Samples were prepared as outlined in Table 3.2 to obtain a flat surface cross-section of strips.

Consider Figure 3.17, where there is a mixed arrangement of dark and light particles of 6 light to 10 dark, ratio of 3:5. This total area in the black rectangle is referred to as the initial sample. Area A halves the sample arrangement still yielding the ratio of 3:5, or the true representative of dark to light particles present in the bag. Area B cuts particles giving a ratio of 1.5:3, which still represents the true ratio of the arrangement for dark to light. Area C however starts to deviate from this true representative mix with the smallest area D showing only dark particles present in the sample. Choosing an appropriate length scale is thus fundamental to acquiring accurate and reliable information.

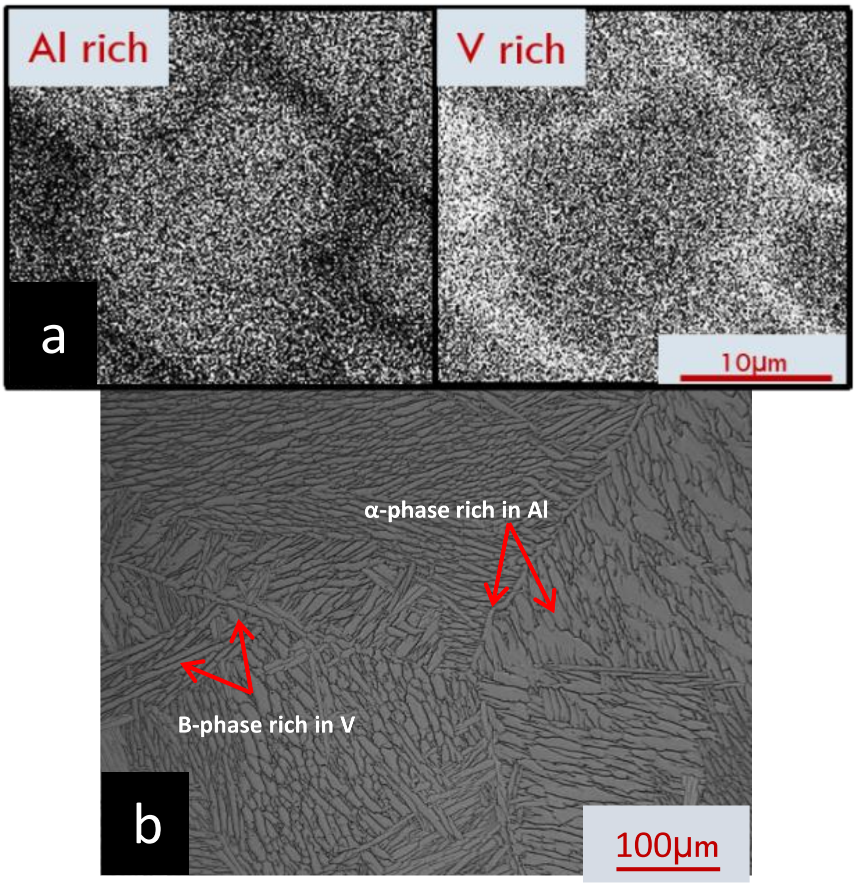

Figure 3.16: (a) SEM/EDX elemental map where bright inherently indicates high element levels; and (b) light micrograph of wrought Ti-6Al-4V showing elemental distribution in the α/β microstructure

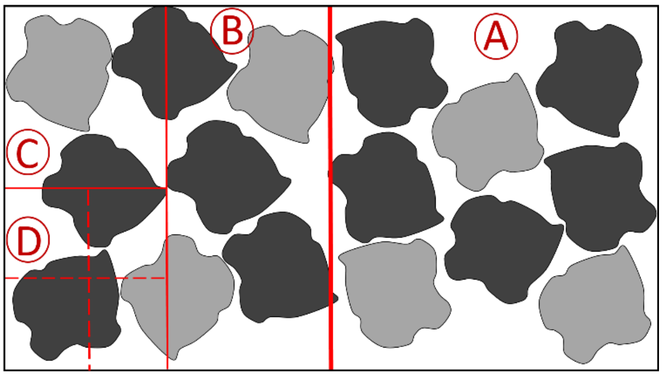

Figure 3.17: Illustration of an arrangement of dark and light particles showing how different area perspectives and sizes can influence the true ratio of dark to light particles

Since spot analysis is not suitable given the two-phase nature of Ti-6Al-4V, it was first necessary to determine the minimum scan area that would exclude the effects of α/β element partitioning. To this end a highly refined wrought Ti-6Al-4V sample was analysed under beam conditions ranging from stationary spot to dynamic area scans as large as 1.4x1.4 mm^2. This sample was used as a benchmark to assist with developing the appropriate technique for elemental analysis using SEM/EDX.

When dealing with randomly distributed powder particles of discrete composition, one needs to be mindful of the limiting scan area size above which the EDX analysis will always yield the same composition. Consequently, it is important that homogenization is compared across a range of length scales. The aluminium (Al) and vanadium (V) levels for several locations relating to each of the specific scan areas are indicated in Figure 3.18 for the wrought specimen.

Figure 3.18 shows a number of individual points representing Al and V concentrations from SEM/EDX scans of a wrought Ti-6Al-4V sample. These elemental concentrations were measured at various length scales or areas, A2-spot. These length scales are the areas from which Al and V concentrations are collected, where area A2 represents the largest scan area and spot is the smallest.

Although there was some fluctuation in aluminium and vanadium levels in zones A2-A4, the fluctuation became much more noticeable in zone A5 and even more so in A6. The interpretation is that when the scan area reduced to 10 x 10 μm^2 and below, the non-uniform diffusion of the α-phase (aluminium rich) and β-phase (vanadium rich) causes inhomogeneity in the analysis.

This procedure was extended to B1 and B2 sintered samples with the addition of a larger scan area being examined resulting in scan areas as large as 3 x 3 mm^2.

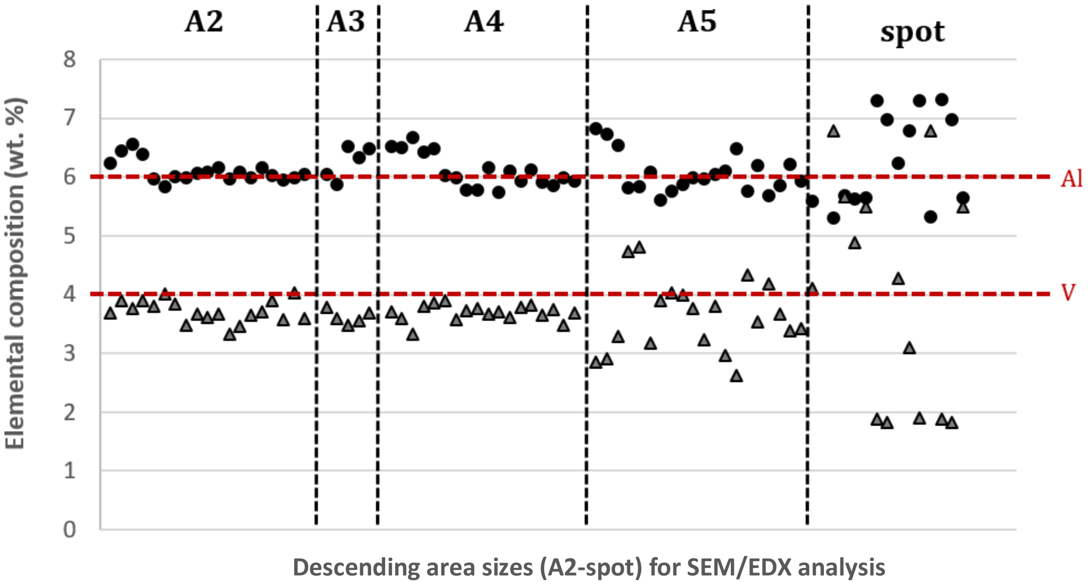

Figure 3.18: EDX analysis at various length scales for a wrought Ti-6Al-4V specimen (A2=1.4x1.4mm^2; A3=350x350µm^2; A4=100x100µm^2 and A5=10x10µm^2)

4. Results and discussion of properties and characteristics of metal powders

All powders used were analysed to identify key physical characteristics to investigate the effects of starting material on final strip product. This analysis includes particle size characterisation, compressibility testing and frictional and flow properties.

4.1 Particle size distribution of metal powders

All powders used in this investigation were sampled for particle size analysis. Summarised statistical data for titanium, aluminium, vanadium and MA powders are listed in Table 4.1. Cumulative and mean distributions of powders are shown in Figures 4.1 and 4.2.

Table 4.1: Particle size characterisation of metal powders

Metal powder	Particle size (µm)				Mesh particle size range (µm)
	D10	**D50**	**D90**	**Standard deviation**	
Titanium	81.2	125.7	181.9	38.4	74<Ti≤149
Aluminium	38.5	74.6	142.3	39.9	44<Al≤149
Vanadium	11.1	25.2	49.5	14.6	V≤44
60Al-40V	12.9	39.6	63.8	19.3	MA≤63

Reporting a singular value to describe a powder/particle size is not an accurate representation of the material being investigated. For this reason, particle size distributions are preferred. Defining a particle size distribution's width is therefore fundamental to understanding how particles in the powder are observed. A common approach to define this distribution width is to cite three values on the x-axis of a particle size distribution plot (Figure 2.10). These three values are the D10, D50 and D90. D50 is defined as the diameter (in micrometres) where half of the powder population will lie above or below this value. Similarly, D90 is the diameter where 90 percent of the population lies below, and D10 where 10 percent of the population lies below. The standard deviation is also a critical parameter in defining the width or spread of data where 68.27% of the total population will lie within ±1 standard deviation and 95.45% will lie within ±2 standard deviations.

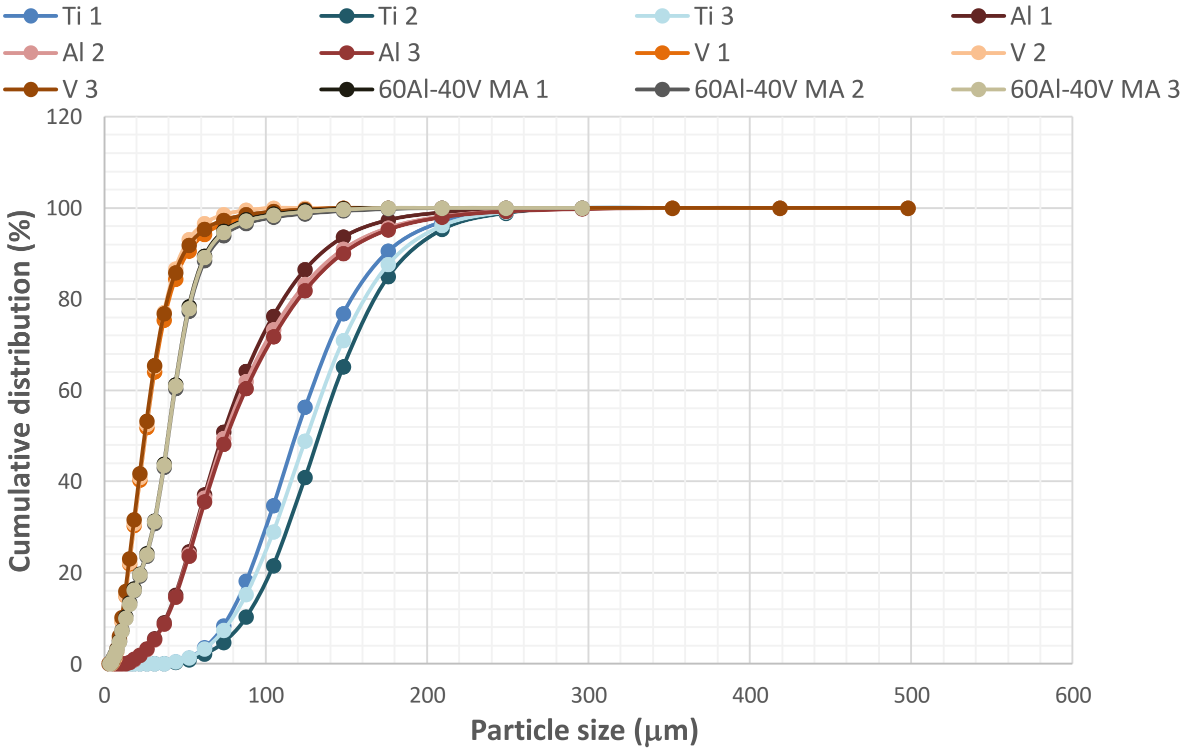

Figure 4.1: Particle size distributions of each powder type under investigation done in triplicate

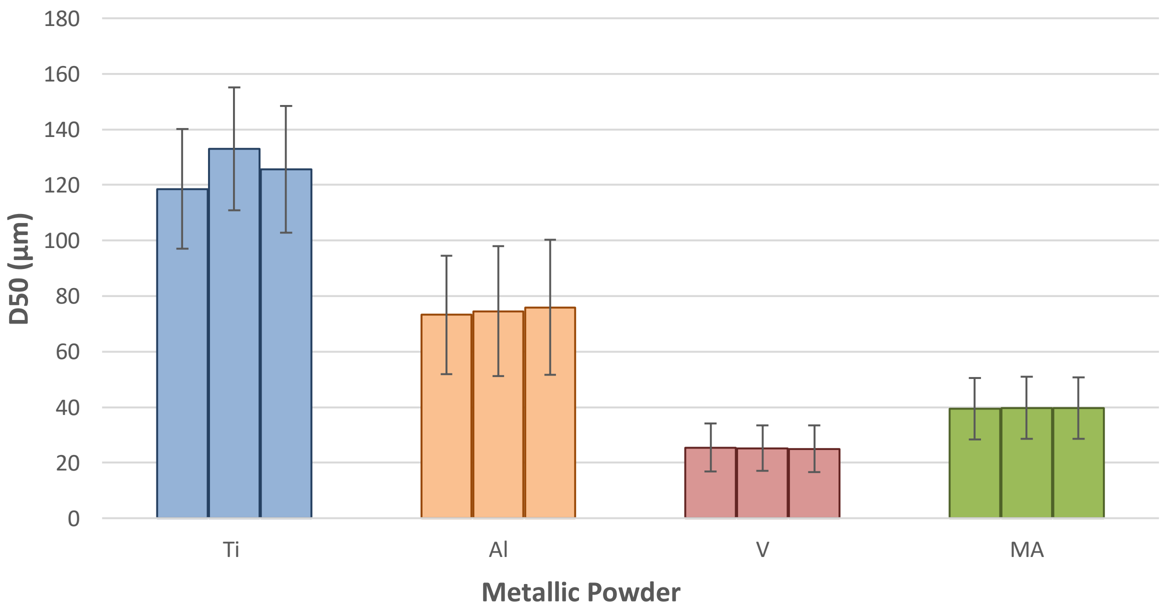

Figure 4.2: Mean particle sizes of each powder type under investigation where testing was done in triplicate, where error bars reflect standard deviations o0f sample sets

Results from the particle size analyser and corresponding mesh sizes and are given in Table 4.1. The MA powder was within the particle size range specified by the supplier. The lower assumed limit of 44 µm for aluminium was slightly above the D10 of the particle analysis. The D90 of vanadium powders (49.5 µm) is above the upper limit of the mesh (44 µm) and the upper limit of titanium's mesh size

(149 µm) is well below the D90 observed in the particle analysis at 181.9 µm. Larger particles observed for titanium powders may be caused by granules with sides longer than the screen mesh size.

Figures 4.1 and 4.2 show that the titanium base powders had the largest particle size. Smaller diameter alloying powders are generally favoured to improve the packing density of particles. When considering powder blends of various constituents, packing density will increase if the particle size distribution has been extended. When studying the packing density of multi-particle binary sand systems, Sohn and Moreland (1968)[70] observed packing densities to peak when sand mixtures contained 55 – 75% of the larger component.

Particle size and morphology have significant implications with respect to compressibility and flowability of powders as well as green strength, density and sinterability of compacts. Chikosha, et al. (2014)[39] studied the influence of titanium powders (-45µm) particle shape on compressibility and flowability during DPR. They observed improved compressibility of titanium sponge fines followed by angular powders, with spherical powders exhibiting the poorest compressibility. Titanium sponge fines are irregular in shape and sponge-like. Their irregular shape may improve interlocking abilities on compaction. Similarly, HDH powders which are angular in shape, may exhibit similar compressibility properties as their ability to interlock is also evident. The flowability results were best for angular powders followed by spherical and finally sponge. Chikosha, et al. (2014)[39] further investigated the effects of particle sizes on compressibility and flowability for powders possessing the same morphology. It was found that compressibility increased for powders with smaller particle sizes while flowability decreased[37,42].

B1 (titanium + aluminium + vanadium) and B2 (titanium + MA) powder blends have very similar particle size distributions since base titanium powders were from the same stock and vanadium and MA powders were in a similar particle size range (on the lower end of the scale) with similar angular morphologies. The aluminium powder, present only in the B1 powder blend, possesses different shape and size characteristics compared to other powders. Figure 4.1 shows aluminium's particle size distribution followed a similar curve to that of all powders under investigation, however its size is clearly the next largest after titanium with an average D50 of 74.6µm and D90 of 142.3 µm. These larger particles present in the B1 blend could have resulted in different packing mechanisms where larger spaces between particles may arise due to inefficient packing being used for alloying powders between larger titanium particles. Aluminium powder accounted for 6 wt % of the B1 composition. Aluminium thus had a larger weight of the alloying constituents for this blend, with the smaller vanadium powders only accounting for 4 wt %. Large aluminium particles could result in large gaps evolving during packing which may not have been able to close on sintering. B2 powder contains 10 wt

% of MA powder, allowing for a larger proportion of smaller particles to sit in between base titanium powders.

Morphology and nature of powders are also significant. While spherical powders may pack uniformly and improve sinterability, high compaction pressures are required to hold green bodies together[24]. This makes angular and irregularly shaped powders a better fit when attempting dry compaction of powders as these particles will mechanically interlock and thereby reinforce their green strength. Both B1 and B2 blends had angular powder constituents. Powder blend B1 however has one powder with a slightly different morphology namely, aluminium. The nodular, protruding shape of the aluminium powders shown in Figure 3.1b could potentially have aided further with compaction. While the particle size distribution was on the larger end of the scale, the aluminium powder had two properties which may have assisted with compaction: its ductility and its morphology. The combination of the two may haveallowed for the irregular nodular protrusions to fit in between particles and lock further on compaction, pressing the softer powder between harder titanium and vanadium powders, and thus holding the entire structure together. The B1 blend may therefore have allowed for a stronger self-supporting green compact compared to the B2 blend.

4.2 Pressure-density relationship from cold uniaxial pressing test

Experimental work was conducted to investigate the behaviour of the feed powder blends (B1 and B2) in compression through uniaxial compression tests. Section 3.4.1 outlines the procedure followed. The data gained from these tests were used to develop a relationship to predict the maximum pressure during rolling in an empirical fashion. It should be understood that uniaxial compaction and compaction during rolling does differ. Uniaxial compaction relies mostly on hydrostatic pressure while shear stresses dominate in roll compaction, assisting more in densifying the compact.

Compressibility and pressure-density relationships were considered in this section. The compressibility constant (κ) defined by Johanson (1965)[1] was used to describe compressibility. Results for each powder blend were compared to explore the influence of their distinct properties on κ. The compressibility of each powder blend is shown in Figure 4.3. Green densities of uniaxial compacts were determined according to the ASTM standard B962 as outlined in Section 3.2.

Uniaxial compression tests show the expected trend in density with an increase in applied pressure for B1 and B2 powder blends as seen in Figure 4.3. A high level of compressibility was observed with maximum green densities achieved being 4.28 g/cm^3 (96.6% theoretical) for both powder blends. B2 powder blends subjected to low compaction pressures (58 MPa) were not self-supporting and hence this parameter was omitted from the graph resulting in one less data point for the B2 compressibility curve. However despite the different particle size distributions in B1 and B2 powder blends, and the ductile nature of the aluminium powder, they had similar compressibility.

Extrapolating Johanson's compressibility constant (κ)

The Johanson model requires a compressibility constant, κ to describe the compressibility of powder. Jenike and Shield (1959)[30] proposed this constant may be obtained from uniaxial compression tests by developing a relationship between pressure and density. This constant is an important variable to define as it is necessary for defining the pressure distribution in the nip region.

By producing plots on a logarithmic scale (Figures 4.4 and 4.5) of compressibility curves (Figure 4.3), and taking the reciprocal of the gradient of these linear logarithmic scaled plots, a compressibility factor, κ, for each powder blend was extracted. Equation 2-7 was used to fit the results obtained from uniaxial compression tests and to evaluate the compressibility of feed powders. Highly compressible materials will reproduce small κ values, and the inverse applies for less compressible materials (Johanson, 1965)[1]. While there was little difference in κ values for each blend, B1 powders exhibited improved compressibility compared to B2 powders with a smaller κ-value of 5.47 compared to 5.79. This improved compressibility was seen in its ability to hold its form at low compaction pressures and may be attributed to the presence of the ductile aluminium powder constituent. For the purposes of roll pressure modelling, the pressure range for the pressure-density curves was selected to be in the range of the rolling mill setup used to produce green strip. The relationship describing the pressure-density curve is a vital one used to determine the pressures required to design a rolling mill setup that will produce green strip of the desired density.

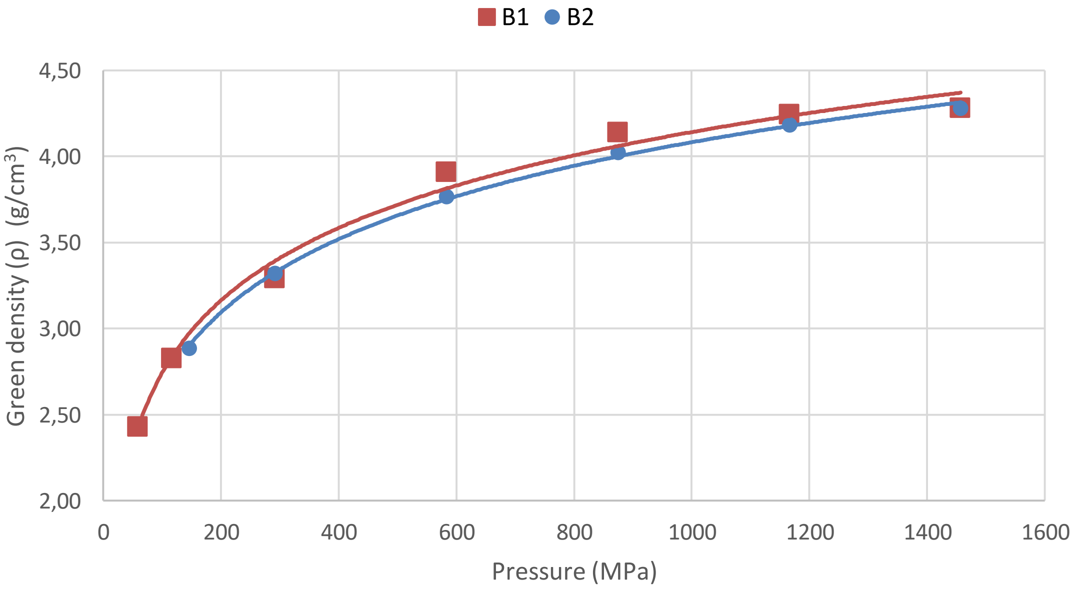

Figure 4.3: Compressibility curves for B1 and B2 pressings

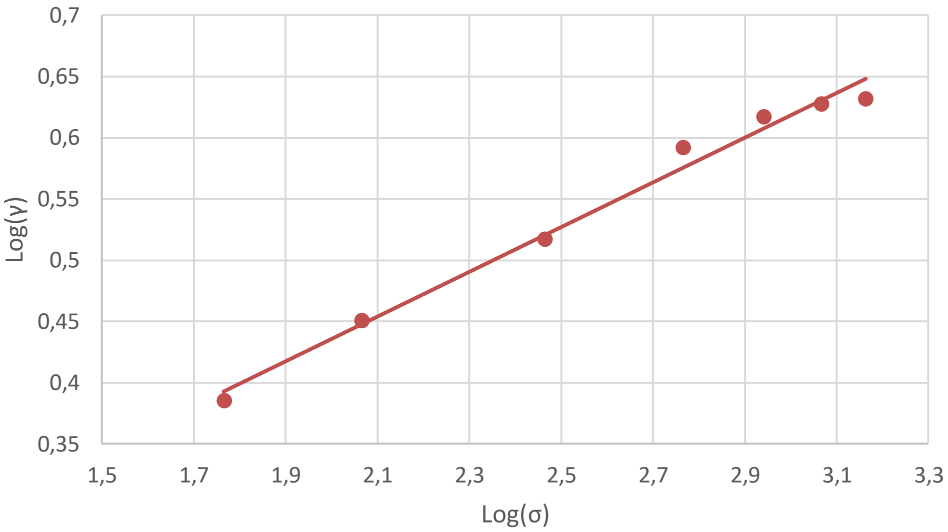

Figure 4.4: Logarithmic relationship between green density (γ) and normal stress (σ) during uniaxial compression for determining compressibility constant for B1 powders based on Johanson's approach[1]

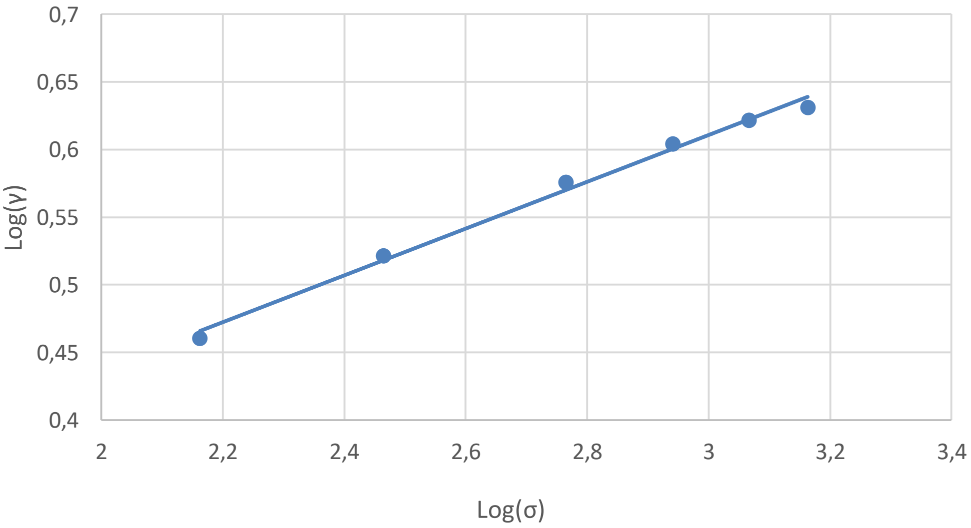

Figure 4.5: Logarithmic relationship between apparent green density (γ) and normal stress (σ) during uniaxial compression for determining compressibility constant for B2 powders based on Johanson's approach[1]

4.3 Frictional and flow properties

Powder shear cell tests

Shear cell testing was done in triplicate for feed powder blends (B1 and B2). Yield loci for B1 and B2 powder blends are given in Appendix E. Section 3.4.2 outlines the procedure followed for shear cell testing.

Internal frictional properties of respective powder blends may be described by the effective angle of internal friction (δ) and the flow function (ff_c). These parameters were obtained from the shear cell test. The flow function is a common qualitative parameter used to describe the flowability of powders and may be divided into three groups describing type of flow (Table 4.2) according to the categories outlined by Jenike (1964)[69].

Table 4.2: Flowability and bulk densities of feed powder blends

Powder blend	Flow function ff_c	Type of flow	Tapped bulk density g/cm³	Hall flow velocity (s/50g)
B1	$4 < ff_c < 10$	Easy-flowing	1.94 ± 0.0230	65
B2	$10 < ff_c$	Free-flowing	1.96 ± 0.0116	65

Bulk solids with high ff_c values exhibit good flowability but are less compressible[38]. B1 and B2 powder blends fell into the easy-flowing and free-flowing categories of the flow function index. Figure 4.3 showed the variation in compressibility according to a normal stress applied. Both powder blends exhibit similar behaviour with respect to compressibility with the exception of the B2 powder blend not being able to be compacted at low compaction pressures. The ff_c values of the B2 powder blend fell into a category showing better flow properties in comparison to the B1 powder blends. This very slight difference may be overlooked as this method of quantifying flowability is generally used in a qualitative sense. Hall flow velocity results indicated that B1 and B2 powder blends both gave a time of 65 s for 50 g of powder to flow through a Hall flowmeter indicating extremely similar flow.

Wall friction analysis

Wall friction testing was done in triplicate for B1 and B2 powder blends. Shear stresses acquired from the wall friction tests were plotted as a function of the applied normal stresses and can be found in Appendix E. Wall friction angles (ϕ) for each blend is shown in Table 4.3 and Table 4.4. The surface roughness used in this test represented that of the Centre for Materials Engineering rolling mill with a surface roughness (R_a) of 2.5 μm. From this it can be seen that the B2 powder blend displayed slightly higher wall friction angles than B1. Higher wall friction angles and effective angles of internal friction of feed powders will result in a higher roll pressure during roll compaction[1]. This small difference could lead to higher pressures during roll compaction.

Table 4.3: Wall friction test results for B1 powders

Series name	BD (g/ml)	**ϕ** (°)	**ϕ_{average}** (°)
Yield locus a	1.92	10.10	9.92 ± 0.33
Yield locus b	1.93	10.13	
Yield locus c	1.90	9.53	

Table 4.4: Wall friction test results for B2 powders

Series name	**BD (g/ml)**	**ϕ (°)**	**ϕ_{average} (°)**
Yield locus d	1.96	12.03	11.58 ± 0.43
Yield locus e	1.96	11.52	
Yield locus f	1.95	11.18	

Shear cell test data are necessary to complete the Johanson model. The parameters extracted from these tests which are necessary for the Johanson model include: the compressibility constant (κ), wall friction angle (ϕ) and effective internal friction angle (δ). The remaining parameters derived from shear cell and wall friction tests are given in Appendix E.

It is apparent that flow properties of B1 and B2 powder blends were similar given the testing method. Both blends were free-flowing with similar bulk densities. Compressibility of the B2 powder blend however seemed to display inferior properties compared to the B1 powder blend when compacting at lower pressures. This behaviour observed in uniaxial compaction may affect the B2 powder blend's performance during roll compaction.

5. Results and Discussion of Powder Rolling Simulation Using Johanson's Theory

A powder rolling model was developed to predict values of certain rolling mill parameters that should be considered to generate specifically tailored strips with desired properties. MATLAB was the platform used to create and implement simulated results coupled with Johanson's roll compaction theory[1] to guide the simulation structure. Zhang (2015)[6] developed this model in based on research originally conceptualised by Balicki and Michrafy (2003)[37]. Rolling mill dimensions and geometric data were taken from the Centre for Materials Engineering powder rolling mill. Nomenclature used in the rolling simulation is as follows:

S	Roll gap (variable mill factor)
D	Roll Diameter (fixed mill factor)
K	Compressibility factor (powder characteristic)
δ	Effective angle of internal friction (powder characteristic)
μ	Friction coefficient (powder characteristic)
P_o	Feed pressure (powder characteristic)
α	Nip angle
RW	Roll face width(fixed mill factor)

5.1 Nip angle determination and analysis

The nip angle contains important information for describing boundary conditions that are necessary to define when implementing a rolling model for compaction of granular solids. This angle assists with indicating where the majority of compaction is believed to occur given the specific rolling setup defined. Measurement of the nip angle is extremely challenging, and the literature[6,36,37,42,44,45,71] suggests that the Johanson model provides adequate capabilities to return the nip angle in gravity fed systems, with simulation results in agreements with experimental data[36].

This section comprises one set of simulation results in determining the nip angle at a roll gap, S of 1 mm and roll face width (RW) of 65 mm for each feed powder blend (B1 and B2). Plots for identifying the nip angles for B1 and B2 powder blends are shown in Figures 5.1 and 5.2.

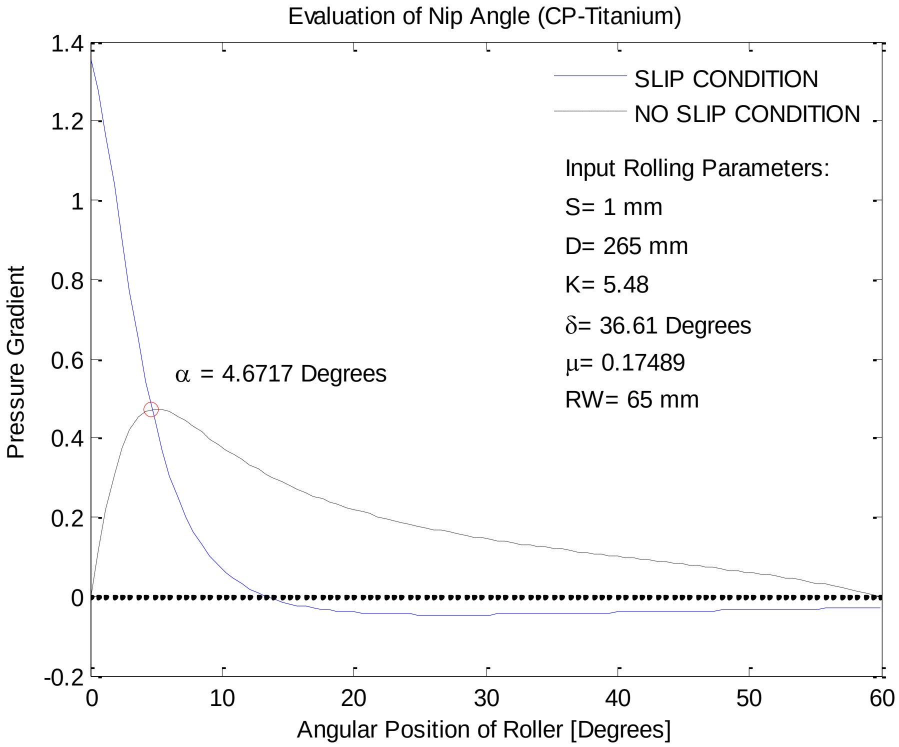

Figure 5.1: Pressure gradient as a function of position of rolls for nip angle determination of B1 powder

The nip angle is a vital parameter for the simulation as it holds information on the limits of the region where most of compaction takes place. Physical measurements of the nip angle are very difficult which is why Johanson's[1] definition of the nip angle was a significant contribution to understanding the boundary conditions of the compaction region, allowing for the estimation of the nip angle with fair representivity[1,36].

Two rolling parameters were varied in this study: roll gap (S) and powder blend (B1 and B2). Roll gaps 0.5, 1 and 1.5 mm were chosen based on a study on roll compaction of Cp-titanium and stainless steel powders by Zhang (2015)[6]. This study was conducted in the Centre for Materials Engineering laboratory at the University of Cape Town, using the same laboratory-scale rolling mill used in the current study and identical MATLAB code used for the current roll compaction simulation. Zhang[6] found this roll gap range to be suitable given the limitations of the rolling mill for the practical segment of the study. All three roll gaps for each powder blend and respective nip angles were calculated (Table 5.2). Pressure gradients at a roll gap of 1 mm are represented in this section for comparative purposes between B1 and B2 blends. Pressure gradient curves for B1 and B2 powder blends at roll gaps 0.5 and 1.5 mm are given in Appendix F.

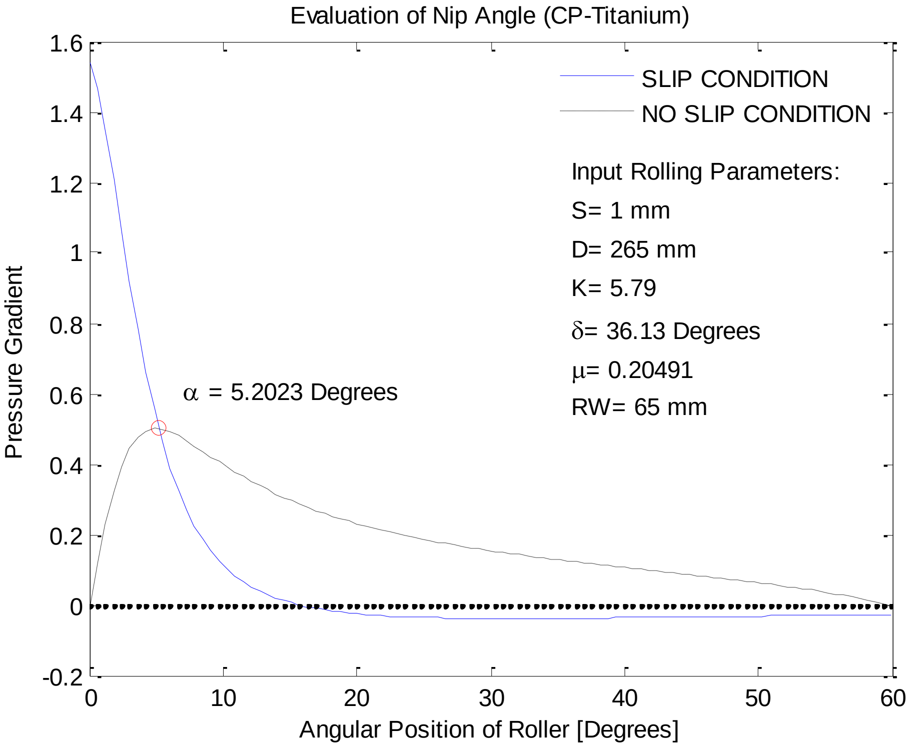

Figure 5.2: Pressure gradient as a function of position of rolls for nip angle determination of B2 powder

The nip angles at S = 1 mm for B1 and B2 powder blends are 4.67° and 5.20°, respectively. The nip angle indicates the beginning of compaction between the rolls in direct powder rolling. It allows for the estimation of the size of the compaction zone and hence the degree of compaction. Larger nip angles generally allow for a greater degree of compaction to occur and maximum pressures to be reached. The nip angle may be determined by isolating the point of intersection between the slip and no slip curves as seen in Figures 5.1 and 5.2 for each powder blend. The outcome of the nip angle is extremely sensitive to certain powder characteristics. An increase in internal friction will result in more powder being drawn between rolls and thereby returning a denser compact. The compressibility factor (κ), effective angle of internal friction (δ) and wall friction angle (ϕ) are the main parameters that influence what the nip angle will be. Large wall and internal friction angles will result in larger nip angles, while large compressibility factors yield smaller nip angles. Table 5.1 gives a summary comparing the effective internal friction angle (δ), wall friction angles (ϕ), compressibility constants (κ) and nip angles (α) at a roll gap of 1 mm. Nip angle calculations are quite sensitive to wall friction angles ϕ , and an increase in ϕ will result in a larger nip angle. The B2 powder blend's wall friction results yielded a larger ϕ value than that of the B1 powder blend. This could suggest why the B2 blend's nip angles were consistently larger at various roll gaps (Table 5.2).

Bindhumadhavan, et al. (2005) found from Johanson's definitions, that the apparent nip angle is independent of roll gap and roll speed. Roll gap had little significant effect on the outcome of the nip angle (Table 5.2), with very slight fractional differences when progressing from a 0.5 mm roll gap to a 1.5 mm roll gap. This may be attributed to the S/D ratio tending toward zero for roll gaps (S) that were very small relative to the roll diameter when calculating pressure.

Table 5.1: Summary of simulation parameters and nip angles at a roll gap S=1mm for B1 and B2 powder blends

Powder blend	Simulation parameters			
	Effective angle of internal friction, δ (°)	**Wall friction angle, ϕ (°)**	**Compressibility constant, κ**	**Nip angle, α (S=1mm) (°)**
B1	36.61	9.92	5.47	4.67
B2	36.13	11.58	5.79	5.20

Table 5.2: Nip angle at various roll gaps S

Roll gap S (mm)	Nip angle (°)	
	B1	**B2**
0.5	4.66	5.19
1	4.67	5.20
1.5	4.68	5.21

5.2 Pressure distributions and maximum roll pressures

Determining the maximum roll pressure was the final result of the simulation and was used to obtain an estimation of the green density of strips by applying the Johanson model. Roll pressure distribution was simulated once the nip angle had been defined. The roll pressure distributions for feed powder blends B1 and B2 are given in Figure 5.3 with roll gap S=1 mm.

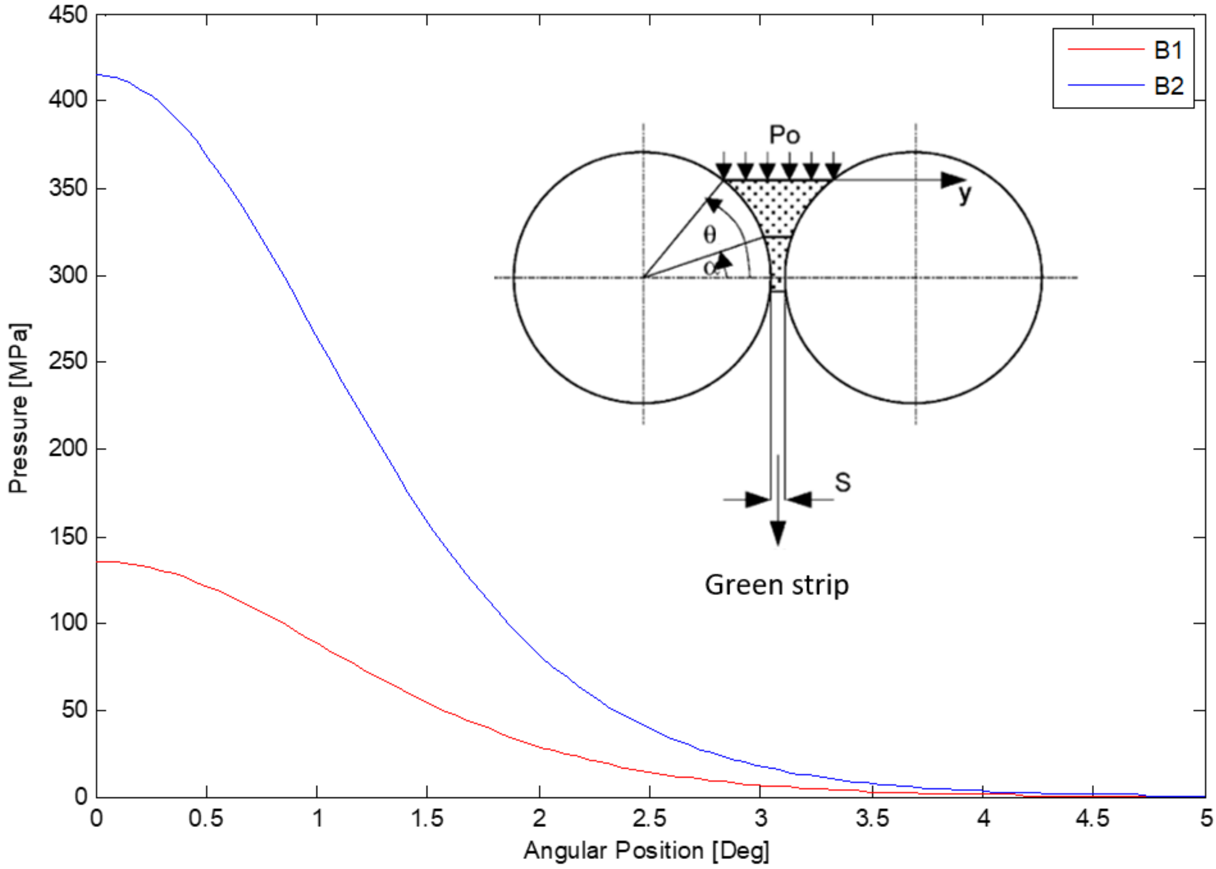

Figure 5.3: Roll pressure distribution during roll compaction for B1 feed powders at S=1mm. With corresponding illustration of the roll gap, where P_0= feed pressure; θ= angular position; α=nip angle and S= roll gap.

Feed pressures used in this simulation were based on a relationship between material bulk density and feed pressure established by Simon and Guigon (2000)[7]. It should be noted that feed pressures used were estimates based on the investigations performed by the Simon and Guigon (2000)[7] as no pressure transducers were attached to the laboratory rolling rig to measure the pressure directly. These feed pressures for B1 and B2 powder blends informed by Simon and Guigon (2000)[7] are given in Appendix C.

Typical pressure distributions in the nip region during roll compaction are shown in Figure 5.3. Where, the angle was set as zero as the pressure reaches the maximum value. With a decreasing angle approaching the neutral angle, the pressure reached a maximum. The neutral angle as described by Johanson, was assumed to correspond to the minimum roll gap. At this point the maximum pressure was assumed to occur at the minimum roll gap. Both B1 and B2 blends followed similar outcomes with the maximum pressure observed to be near the narrowest part of the roll gap (where the angular position equals zero). It can therefore be assumed that maximum pressure gave a reasonable representation of the general trend of pressure distribution in the nip region.

Maximum rolling pressures for B1 and B2 powder blends were shown to be 135 MPa and 415 MPa respectively for a roll gap of 1 mm. From this it is clear that roll compaction was potentially greater for the B2 blend compared to the B1 blend. This is expected as the nip angle for B2 is greater. A larger nip angle allowed for more powder to be pulled between the rolls in the nip region where most of the compaction took place, resulting in a higher pressure required to densify the material.

Figure 5.4 shows the effects of altering the size of the roll gap on the maximum pressure achieved in the simulation for each blend. The roll gap size range selected from 0.5 to 2 mm was chosen to best represent the capabilities of the rig used in generating green strips. A roll gap smaller than 0.5 mm was beyond the limitations of the rolling mill; roll gaps of 2 mm barely produced green strips of reasonable width and length, while roll gaps greater than 2 mm exceeded the point at which any material was compacted at all.

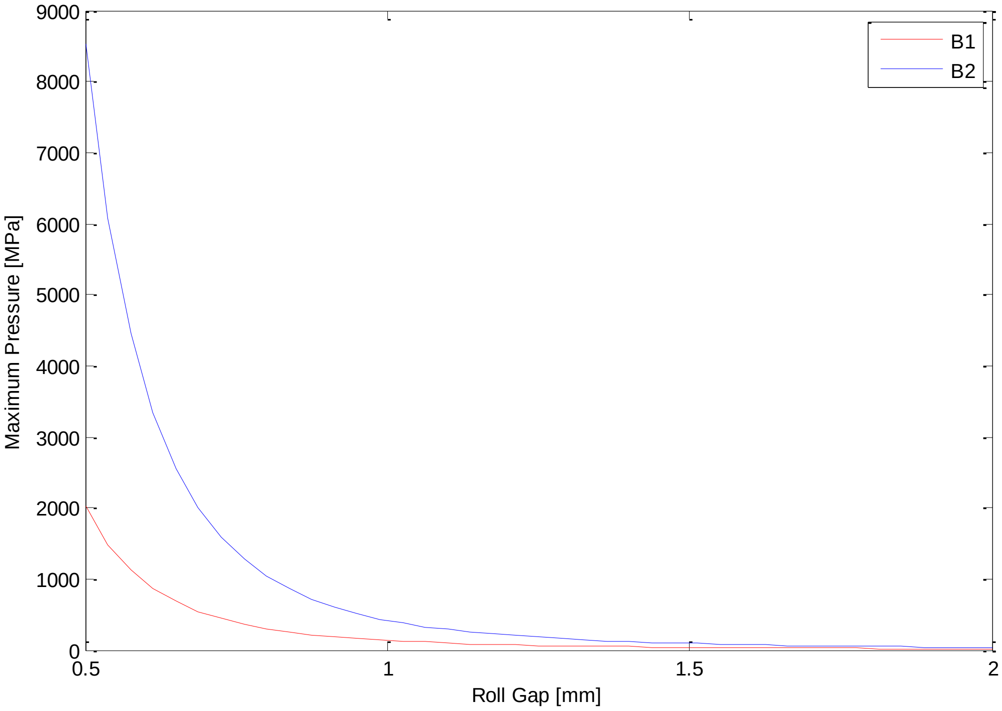

Figure 5.4: Maximum pressure as a function of roll gap size for B1 and B2 powder blends

Large roll gaps resulted in insufficient powder entering the nip region causing poor compaction. As the size of the gap was reduced, an exponential increase in maximum pressure was observed for each blend. Both B1 and B2 blends exhibited an increase in maximum pressure with decreasednroll gap. This is typical and is expected given the increase in uniaxial strain in this region[43]. A study by Gerdemann and Jablonski (2010)[72] observed uniaxial compaction behaviour on eight different titanium powders, including three variably sized sponge fines and two variably sized HDH powders. A density vs compaction curve for three of the sponge fines was plotted[72]. The theoretical full density of titanium (4.54g/ml) was expected to be reached at a pressure of approximately 1550 MPa. This was achieved by extrapolating pressures from the density vs pressure curve. This plot covered a range of pressures applied to different powder types. Since compaction beyond the theoretical density of titanium is not possible, near full density should be reached experimentally at around 1550 MPa. This high pressure was unattainable experimentally in Gerdemann and Jablonski's (2010)[72] work.

Consider the extreme case of maximum pressure outputs for the 0.5 mm roll gap yielding 1997 MPa and 8424 MPa for B1 and B2 powder blends during roll compaction (Figure 5.4). From this it is also clear that these extreme maximum pressures achieved in the simulation were unreasonably high and far exceed any pressures expected to compact titanium powders. They also far exceeded the limitations of the powder and equipment which could not withstand these excessive loads during empirical investigations. This is a limitation of the Johanson model as it does not take into account the material yield condition, thus allowing these excessive pressures to be reached in the simulation. In addition, rolls are protected by the ability to relieve pressure by a spring back effect. Without this safety measure, rolls will seize during overloading where pressures are excessive. The Johanson model assumes a fully rigid roll system where this pressure release is not accounted for. The high pressures are not likely to be realised in practice due to the lack of accountability for this spring back effect. High maximum pressure results may have been due to unrealistic feed pressure inputs. Feed pressures were calculated based on a relationship from the research of Simon and Guigon (2000)[7]. In gravity fed systems, the nip pressure is dominated by the feed pressure[42,73]. As such, a change in feed pressure can have a significant effect on the pressure exerted on the powder.

6. Properties and characteristics of green strips

Green strip production was conducted according to Section 3.5. This section discusses limitations of rolling apparatus based on experimental findings of B1 green strips and a comprehensive study comparing properties of B1 and B2 green strips. A varying roll gap was implemented while keeping roll speed, roll face width and feed hopper outlet diameter constant at 14 rpm, 65 mm and 25 mm respectively. When calculating average green density per strip at various roll gaps, six 20 mm × 30 mm samples were extracted from three sections along the strip length (Figure 6.1) and an average was determined from this sample to give the best representative green density of the entire strip.

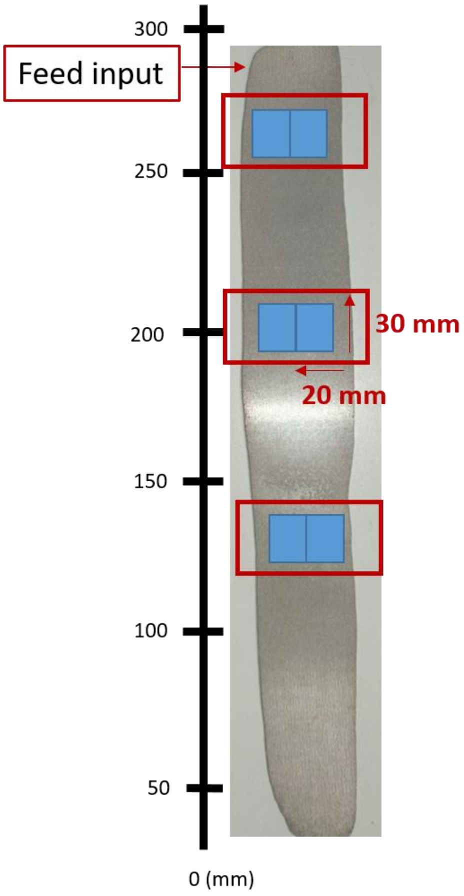

Figure 6.1: An example of the method used when sampling for green densities of strips

6.1 Density profile along strip length due to rolling set up limitations

B1 powders were rolled in duplicate at roll gaps of 1 and 1.5 mm resulting in four strips being investigated. Each strip was sectioned into smaller samples of dimension 20 mm x 30 mm from the centre along the length of the strip and are represented by blue rectangles (Figure 6.2). The densities of these samples were acquired according to ASTM B962 and recorded as a plot of density as a function of distance along strip length in Figure 6.3.

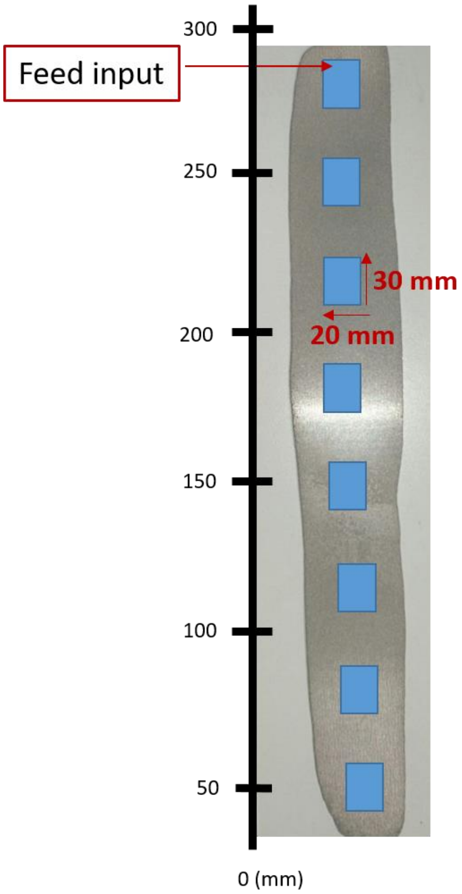

Figure 6.2: Sampling of B1 green strip for density profiling along the length

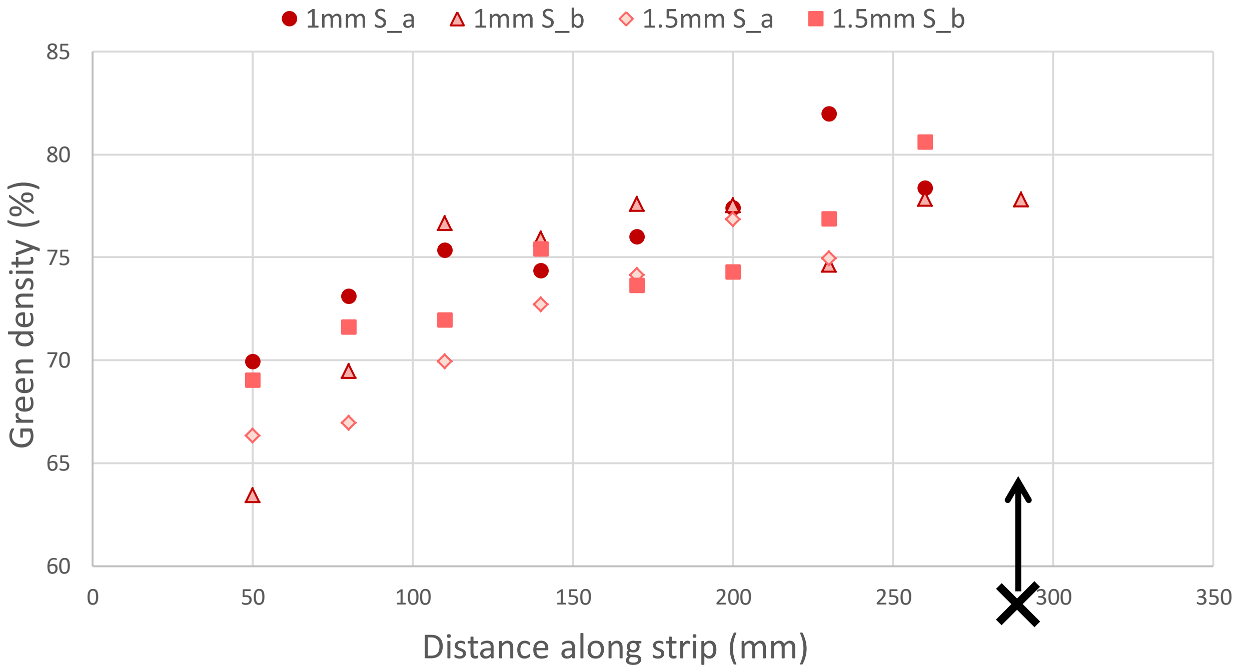

Figure 6.3: Density profile of B1 strips rolled at 1 and 1.5 mm roll gaps (S) ending with the feed input along the strip length; where X indicates feed input

Figure 6.3 shows the procedure undertaken to observe density trends along B1 strip lengths. The graph progresses from the start (origin) by the 20 mm x 30 mm samples that eventually lead to the feed input (the end of the strip that first exits the rolling mill, marked as "X" on Figure 6.3, at approximately 290 mm on the x-axis). A density profile was evident along the length of all four strips investigated. Strips at roll gap, S =1 mm (1mm S_a and 1mm S_b) increased by 17 and 22%, while strips rolled at S=1.5 mm increased by 17% for strips labelled 1.5mm S_a and 1.5mm S_b (see Figure 6.3). The profile observed indicates higher densities at the feed input end of the strips. Initially, as powder was fed into the system there was a pressure exerted by the mass and flow of powder. In gravity fed systems, this feed pressure heavily influences the nip pressure[42,73], which directly affects strip density. Since the feed pressure is a dominating parameter controlling the outcome of strips, it was reasonable to deduce that an increase in pressure (caused by powder flowing into the roll gap) results in higher densities where feed input was at a maximum, while lower densities were observed when the feed powder stock is at a minimum or zero.

A spring-back mechanism in the release region may also have played a contributing role to the density decrease along the length. As the powder passed through the rolls and compaction occurs, the rolls would spring back relieving pressure build-up in the compaction zone. This may have had a minor effect on the segment of the strip that passed through the rolls during/after roll spring-back.

Less density variation seemed to be evident after the 100 mm mark. The portion of the strip that was between 0 and 100mm (as indicated on the x-axis in Figure 6.3) may be disregarded as waste since its density was much lower.

6.2 Density profile across strip width

To characterise the density variations in the strip thoroughly, a density profile across the strip width was taken. Three samples of 10 x 30 mm were taken across the strip width at eight different sites along the strip length of a B1 strip rolled at a roll gap, S of 1mm (Figure 6.4). While there was variation along the strip length as observed in Section 6.1, sampling densities across the strip width were observed to be more uniform. A similar observation was noted in a study by Yu (2012)[42] when studying roll compaction of pharmaceutical excipients at smaller roll gaps. Yu (2012)[42] proposed that this may be attributed to frictional forces caused by interactions between powder particles and powder-roll interactions at small roll gaps, which are in turn directly proportional to the normal force in the nip region. Near the edge of the rolls, high frictional forces pull more powder toward the roll gap causing less density variation across the width of strips.

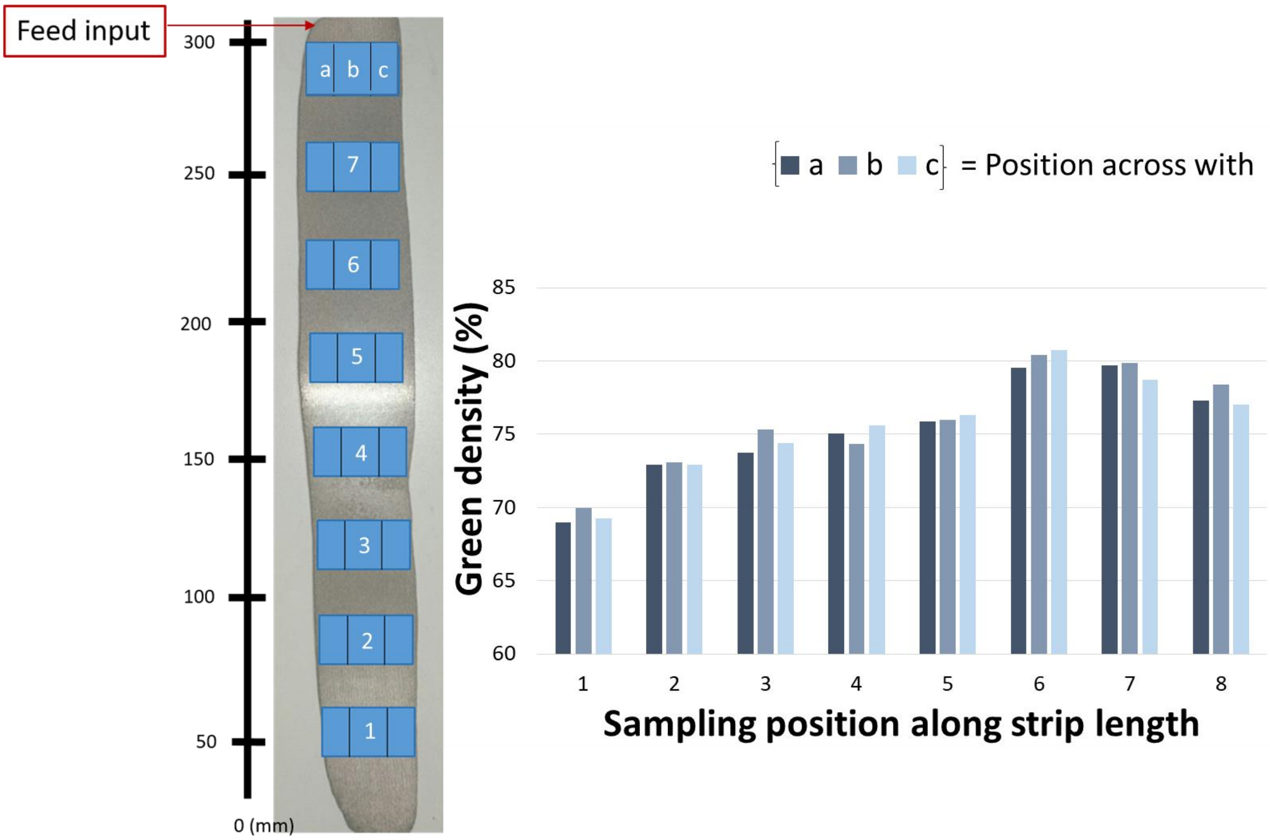

Figure 6.4: Sampling green densities across strip width of a B1 strip at 8 different locations along the strip length

6.3 Effect of roll gap on green strip dimensions and green density

To further investigate and compare the behaviour of B1 and B2 powder blends, strip thicknesses and widths for green strips were examined during rolling. The B1 powder blend was rolled at roll gaps of 0.5, 1 and 1.5 mm while the B2 blend was rolled at roll gaps of 1 and 1.5 mm only. A total of eight B1 and six B2 green strips were documented and investigated in this strip dimension study. Average green density values were determined according to the procedure outlined at the beginning of this section (see Figure 6.1).

Strip thickness and green density

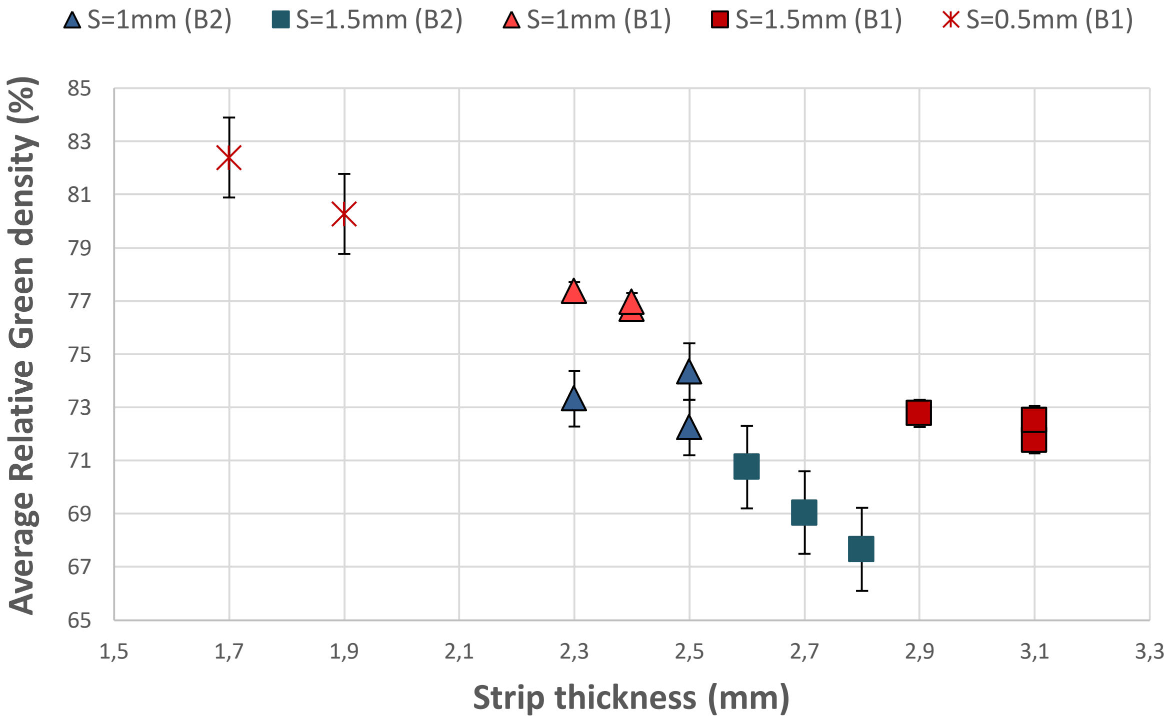

Figure 6.5: Average relative green density vs. strip thickness at varying roll gaps (S) from B1 and B2 powder blends of 14 different strips

A comparison between strip thickness and green density at various roll gaps 0.5, 1 and 1.5 mm is given in Figure 6.5 for B1 and B2 strips. The B2 blend could not be rolled at a 0.5 mm roll gap as rolls seized during the powder feeding stage. This could be explained by the 60Al-40V master alloy addition present in the blend. This master alloy is a harder material compared to the ductile aluminium addition present in the B1 blend. This additional ductility in B1 may explain the allowance for it to be pressed at smaller roll gaps. As roll gap decreased, the respective green densities increased. This was observed for both powder blends.

In all cases strip thicknesses were greater than that of their respective roll gaps. This is a measure of the elastic modulus of metal powders and elastic strain energy stored in the strip as the pressure decreases on exit from the rolls where the material expands in the release zone, thereby resulting in larger thicknesses observed relative to the roll gap at which they were rolled. A contributing factor to the strip expanding as it is released from the rolls may be due to the feed system. Air is trapped between powder particles as it is fed into the system. High pressures within the compaction zone will force particles together while air is still trapped; however on exiting, the material expands further as entrapped air leaves the strip when the pressure decreases.

When considering B1 and B2 powder blends rolled at 1 and 1.5 mm roll gaps, B1 strips exhibited higher green densities. This higher green density may be caused by the presence of ductile elemental aluminium powders in B1. This allowed for greater compaction of B1 powders on rolling resulting in improved densities.

Strip width and green density

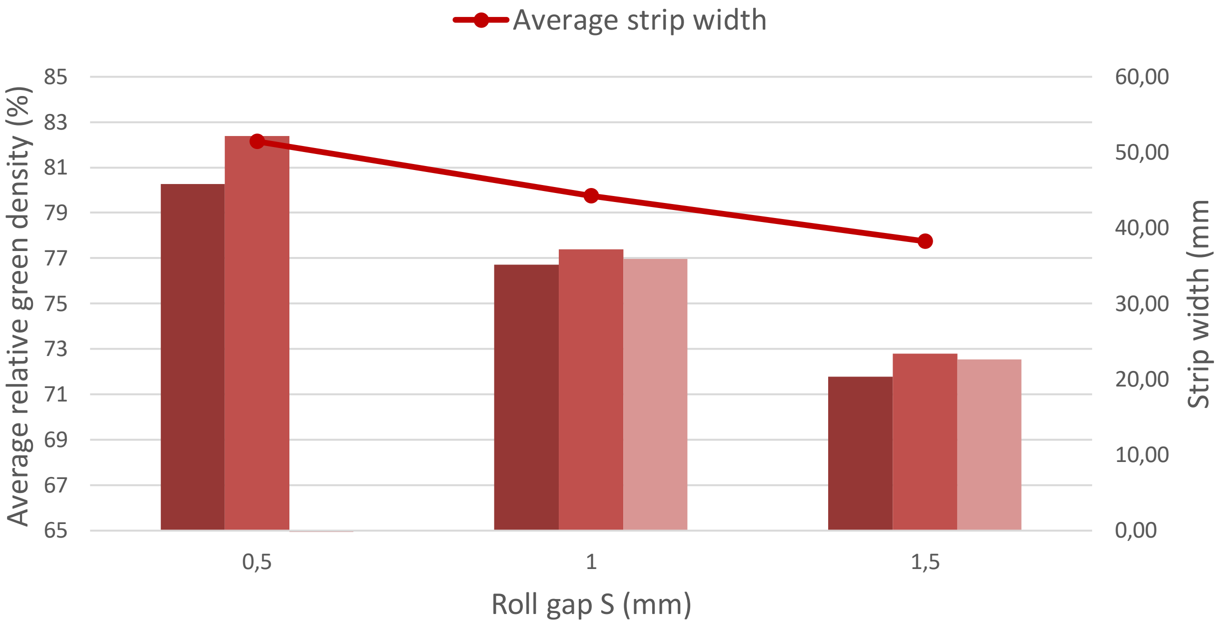

Figure 6.6: Relative green density and strip width of B1 strips at 3 roll gaps (0.5, 1, 1.5 mm)

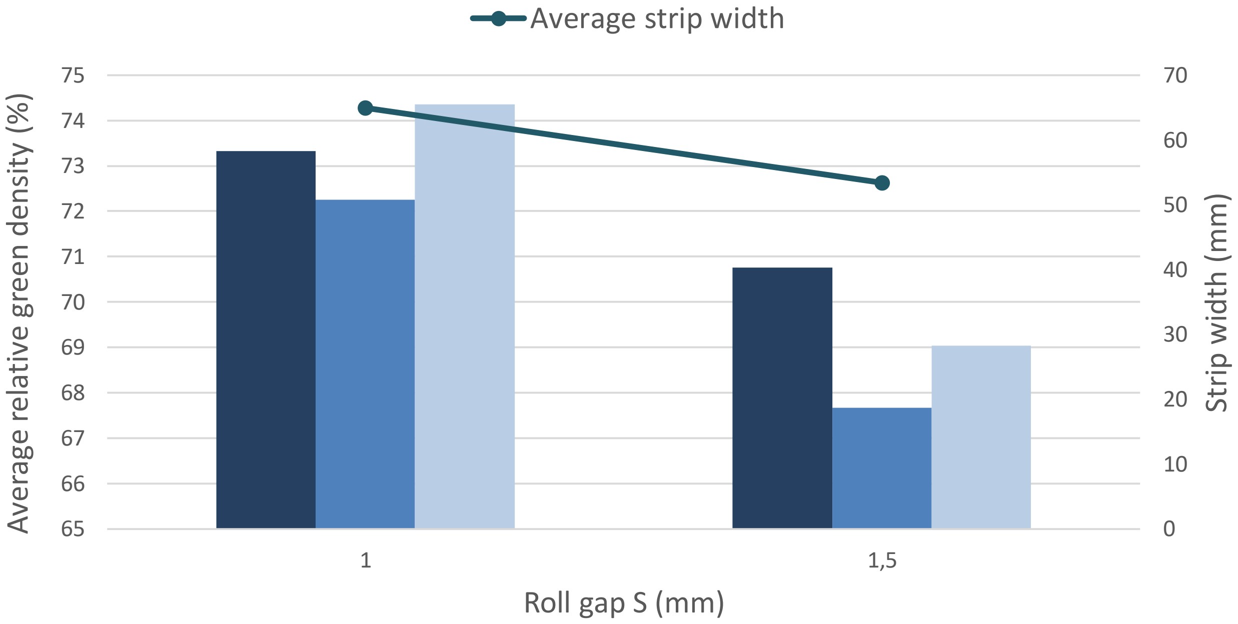

Figure 6.7: Relative green density and strip width of B2 strips at 2 roll gaps (1, 1.5 mm)

The effects of rolling on strip dimensions for B1 and B2 powder blends were further investigated by measuring strip widths (Figures 6.6 and 6.7). Three roll gaps were investigated (0.5, 1 and 1.5 mm). However as stated previously, B2 powders could not be rolled at a roll gap of 0.5 mm due to rolls seizing. Strip widths are represented as bar graphs and respective average strip green densities are displayed on the secondary y-axis. Strip width increased as roll gap decreased across both blends. Reducing the roll gap restricted powder flow through the nip region. This allows the powder to spread and compact resulting in increased in width. Larger roll gaps may allow powder to leak out and slip reducing contact between the roll surface and powder[44].

6.4 Green strength of PM strips

To characterise the mechanical behaviour of green strips, three-point bend tests were conducted on two B1 and two B2 strips rolled at S = 1mm. Section 6.1 revealed strip density variance along its length. These results inferred a sampling technique for green strength samples. This outcome informed the disregard of 100 mm of tail-end of strips which has been shown to be of a lower density. From there, strips were split in half and sectioned into regions A and B. Region A was the end of the strip closest to the feed input (Figure 6.4). Three samples were sectioned from each region of each strip resulting in a total of 24 data sets. An illustration of this method of sampling is given in Figure 6.8. Samples were loaded at a displacement speed of 1mm/min on the three-point bending jig loaded with a 10 kN load cell. Bending strength was calculated using Equation 3-2.

Samples were sectioned according to ASTM standard B312. Only length and width dimension guidelines were controlled according to the standard. This is because strip thicknesses were dependent on the test procedure and could not be altered to fit ASTM guidelines (required thickness = 6.35 mm). Green strength tests are thus purely for comparative purposes between B1 and B2 samples in the current study.

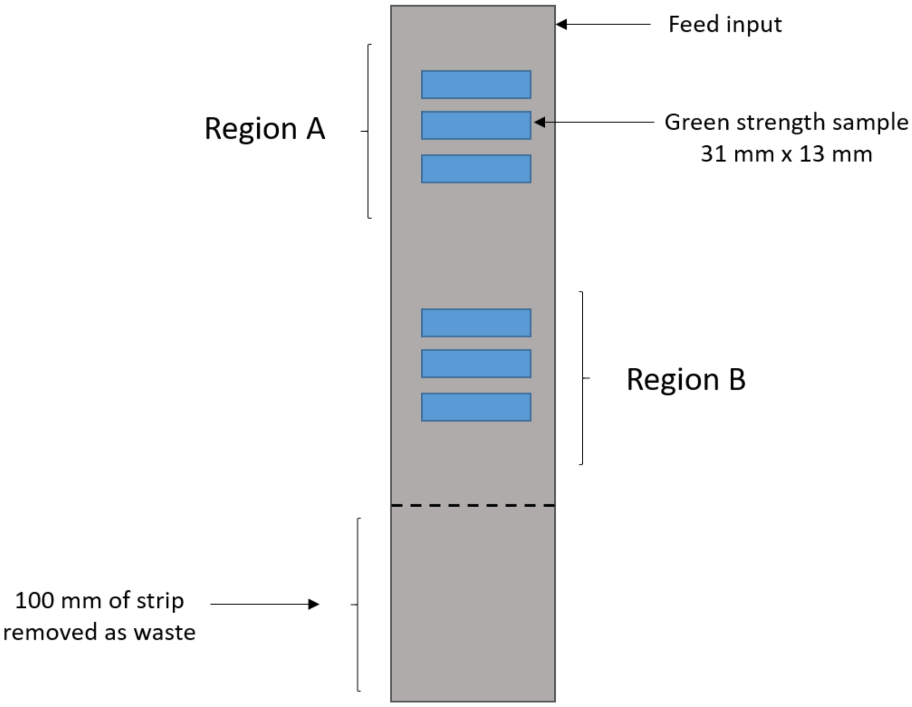

Figure 6.8: Green strength sampling of B1 and B2 strips

The relationship between green density and green strength in Figure 6.9 displays converging trends (black dotted line in Figure 6.9), although there was considerable scatter, the expected trend of increasing green strength with density only occurred above about 75% green density. Higher green densities would imply a greater degree of mechanical bonding with stronger forces acting to keep the powder tightly bound in a self-supporting strip. B2 strips for regions A and B had lower green strengths compared to B1. This is consistent with the behaviour of B2 green strips when handling. B2 strips rolled at a 1.5 mm roll gap fractured at various positions along the roll length (Figure 6.10). B1 strips did not break at all roll gaps investigated. This qualitative observation was in agreement with the green strength results obtained from the three-point bend test. It is also possible that the cold-welding of particles become more effective above 75% green density and hence the green strength increased.

Since the only differences between blends were the alloying additions, this must have been the cause for such a difference in compaction during rolling. B1 contains the elemental powders aluminium and vanadium. Aluminium powders are more ductile than all three powder constituents present in the investigation. A blend with a constituent that is very ductile will have a different mode of compaction. The aluminium particles would be more likely to deform by a greater degree. By increasing the applied pressure, the area of contact between particle interfaces will also increase, allowing for more surface area for the compact to hold its form and also possibly lead to increased cold-welding.

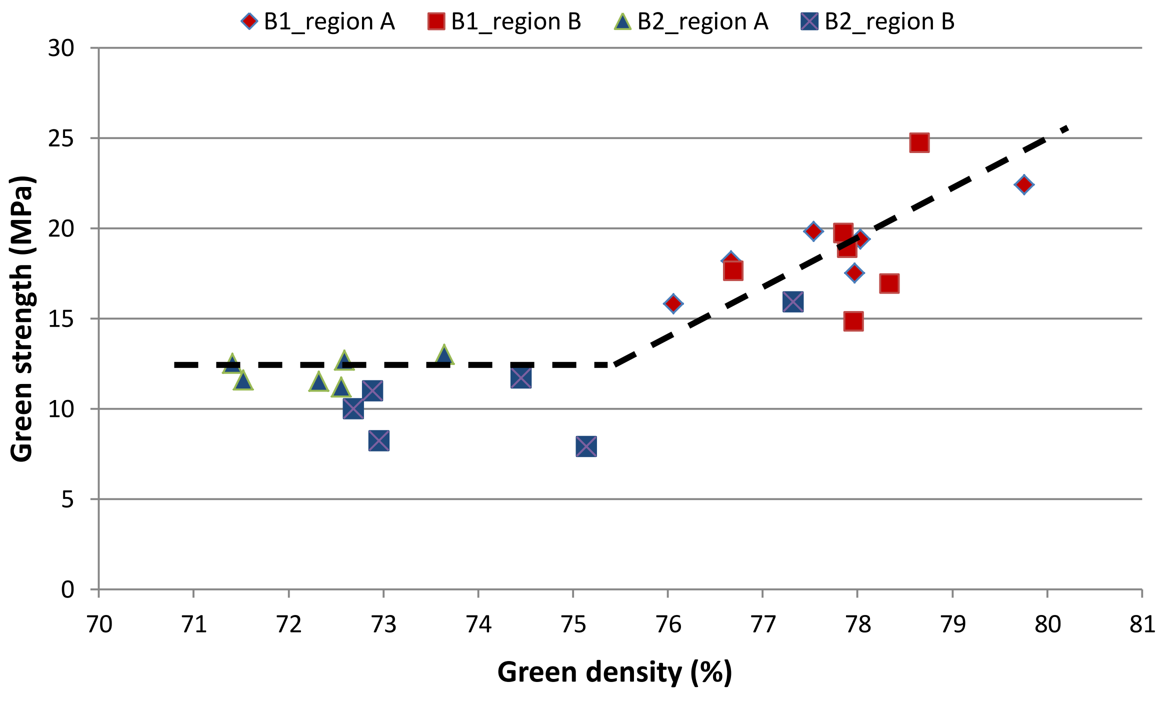

Figure 6.9: Green strength of 2 x B1 and 2 x B2 strips rolled at S= 1mm indicating green strength at regions A and B in B1 and B2 strips described by Figure 6.8

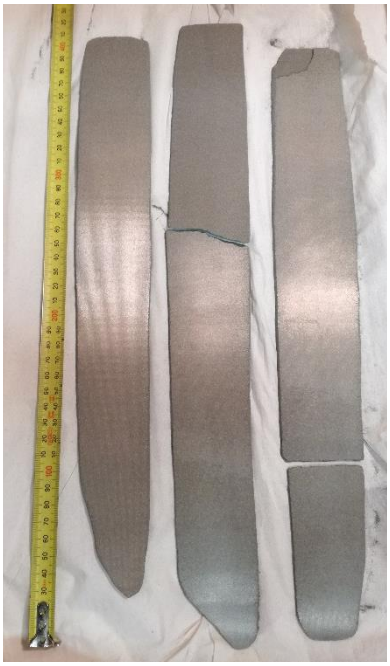

Figure 6.10: B2 strips rolled at a roll gap of 1.5 mm where two of the three fractured during specimen handling

7. Validating the Johanson rolling model for respective powder blends

Roll compaction is an area of study where the information is predominantly held in empirically based studies. Modelling a process allows for prediction methods for tailor-made products, improved process control and to aid in the design of a roll press. The knowledge and theories surrounding roll compaction are however limited to this day. The Johanson model was the first comprehensive roll compaction model for granular solids to predict the performance of granular materials during roll compaction. By comparing experimental results from Chapter 6, to results obtained from Chapter 5, the Johanson model could be effectively validated against B1 and B2 powder blends, to ascertain how well the model is able to predict experimental findings in this study.

Modelling DPR is a concept that requires significant understanding about material properties, roll-press dimensions and operating conditions. To better understand how well existing models predict DPR, empirical findings through experimental work are necessary to validate the theory. A comparison is needed to identify pitfalls and further refine theoretical models to assist in eventually allowing these models to predict the specifications of product process parameters before processing. To investigate whether the Johanson model gives an accurate representation of DPR in this study, it needed to be validated through experimental findings. Variable roll gaps of 0.5, 1 and 1.5 mm were implemented to validate the Johanson model. While the predicted densities for both respective powder blends were determined from these roll gaps, the experimental density for the B2 powder blend rolled at a roll gap at 0.5 mm could not be determined due to seizing of rolls at small roll gaps. Average relative densities were calculated according to the sectioning procedure outlined in the introduction to Chapter 6 (see Figure 6.1). Simulated green densities were calculated by using pressure input values from the Johanson simulation and translating these simulated pressures into green densities through the relationship obtained from the compressibility curve generated from the cold uniaxial compression tests in Section 4.2.

If the Johanson model successfully develops a relationship between material properties, press dimensions and operating conditions, it would be an extremely useful tool in designing DPR methodologies for a range of materials and thus allowing for a reasonable prediction and development of a tailor-made final product.

When considering the feasibility of the maximum pressure values to be achieved during rolling, in both instances, the predicted maximum pressures far exceeded a reasonable pressure for roll gaps below 1 mm for the given material and press dimensions (Section 5.2). The validation for the B1 powder blend (Figure 7.1) showed that predicted green density values were lower than experimental values for roll gaps greater than 0.5 mm. Model validation for B2 powders (Figure 7.2) show predicted green densities to be lower at roll gaps greater than 1 mm. Only two roll gaps were investigated as B2 powders were not able to be rolled at a roll gap of 0.5 mm, due to overloading during compaction resulting in rolls seizing and no strip being formed.

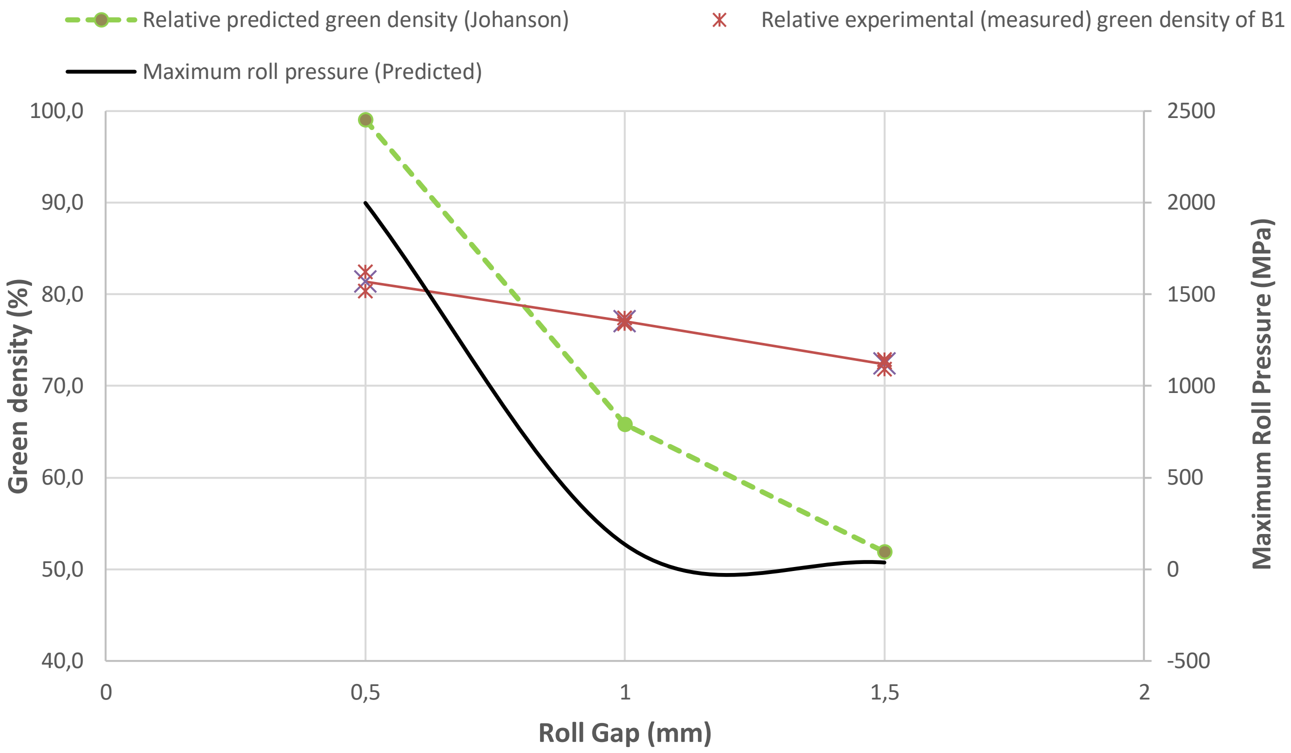

Figure 7.1: Predicted and experimentally determined relative density at respective roll gaps for B1 powder

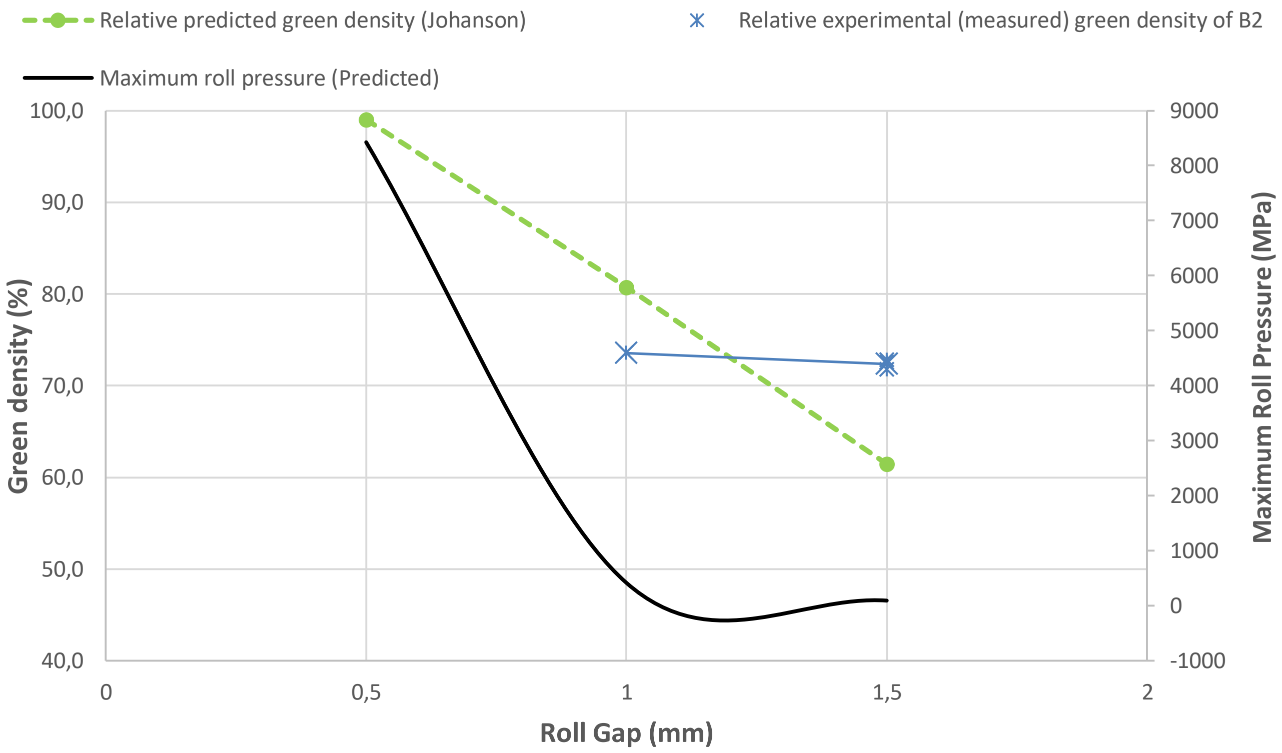

Figure 7.2: Predicted and experimentally determined relative density at respective roll gaps for B2 powder

It is clear that for B2 (Figure 7.2), at roll gaps smaller than 1 mm, the Johanson prediction curve showed a much larger increase in maximum pressure than B1 (Figure 7.1). During rolling, the push-back of the rolls would be so great where the rolls cannot push-back any further, causing the rolls to freeze which will contribute to the inability for B2 powders (comprising of harder MA powder particles) to be rolled at a roll gap smaller than 1 mm. For B1, the maximum pressures predicted by the Johanson model were much lower. If this drop in pressure derived from the Johanson prediction has occurred between rolls, it would be consistent to experimental results as B1 was able to be rolled at smaller roll gaps. The trend for maximum pressure predictions was consistent with experimental findings where B2 was more difficult to roll due to the pressure build-up in the roll gap and there are more limitations on the powders that may be compacted to when comparing to B1.

8. Results and Discussion of Sintered B1 and B2 strips

Sintering was performed on B1 and B2 strips rolled at a roll gap of 1 mm for each blend to: homogenise the strip; achieve the desired Ti-6Al-4V alloy; and observe the contribution of sintering to final strip density. Sintering was conducted at 1200°C[65] (see Section 2.5.3) for 3 hours in a vacuum environment at pressures lower than 10^{-5} mbar. The sintering temperature was reached by heating at 6.6 °C/min. Samples were furnace cooled. It is important to note that density measurements involved impregnating the sample with liquid paraffin. As a result, the sample used for green density measurements could not be used in sintering treatments. To ensure sintering effects were monitored reliably from the green to sintered state, sampling was informed by the outcomes of density variations discussed in Sections 6.1 and 6.2. While there was a gradient along the length of the strip (Section 6.1) there was little difference across the width (Section 6.2). Sectioning two samples (20 mm x 30 mm) adjacent to each other across the width was used to track sintering effects and hence directly compare the green state to the sintered state. Figure 3.14 illustrates the sampling techniques used for the sintering study., where, one sample was used to determine the green density, while the adjacent sample across the width was subjected to sintering conditions and sintered densities recorded for comparison. This method of sampling was done at various sites along the length of B1 and B2 strips.

8.1 Density of as-sintered samples

B1 samples shown in Figure 8.1 generally showed a slight increase in density after sintering with the exception of sample set 6 where a decrease in density was observed. It is evident that sintered densities indicated variable density at different sites within the strip. Therefore the density profile as discussed in Section 6.1 was carried over from green state to sintered state and the uneven distribution in green density had not been mended during sintering.

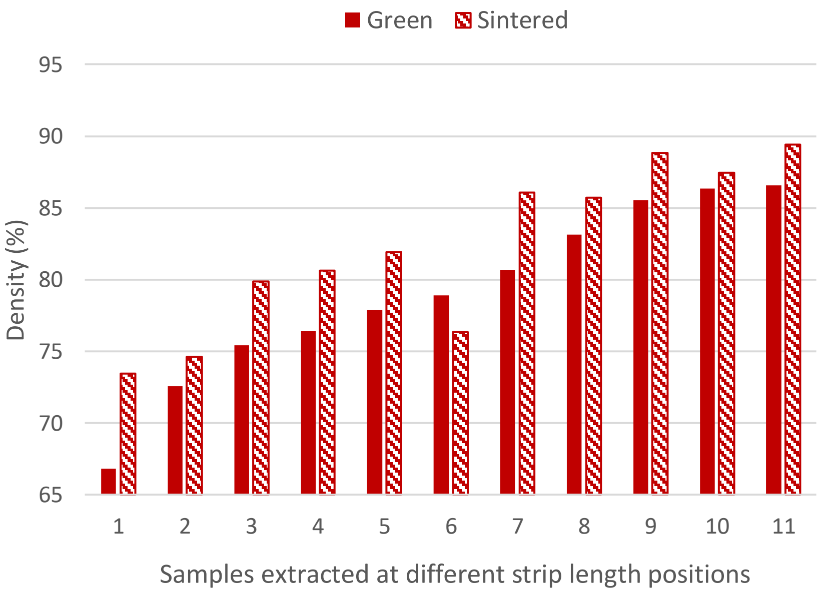

Figure 8.1: Density change of B1 samples at various start green densities on sintering at 1200°C for 3 hours

Low final densities in the case of B1 compacts was apparent across the sample set. Dahms, et al. (1993)[74] found severe swelling of green samples during sintering, inhibiting full densification as a result of several processes, including the formation of Kirkendal[74] pores during solid state diffusion and the violent reaction of titanium with molten aluminium creating macro-pores. Attempts to "heal" these pores were not possible through further annealing due to their large sizes. Dahms, et al. (1993)[74] showed that severe swelling of green samples during the sintering process prevented full and homogeneous densification of the materials. This may be attributed to uneven distribution and size of pores which may also result from large irregular pores formed mechanically on roll compaction due to the irregular nature of elemental powder particles. While the interlocking mechanism of irregular pores may assist in creating a self-supporting strip, there is a draw-back in pore size and shape because of powder particle shape, and resultant cavity formation if melting occurs.

The aluminium powder particles were the second largest in the blend with some of the larger particles being in the region of 142 µm. The largest particles were the titanium particles used with D90 of 181 µm. It is therefore conceivable that the arrangement of these particles during roll compaction could lead to large spaces between adjacent particles.

The as-sintered densities of B2 samples (Figure 8.2) increased from the green state for all samples measured. Master alloy additions improved densities substantially compared to B1 sample counterparts. While it is clear that green densities are also varied within the strip, it was apparent that there was a less varied density profile in B2 samples compared to B1 after sintering. This implied that sintering promoted improvement of the density profile that arises due to rolling limitations for B2 strips.

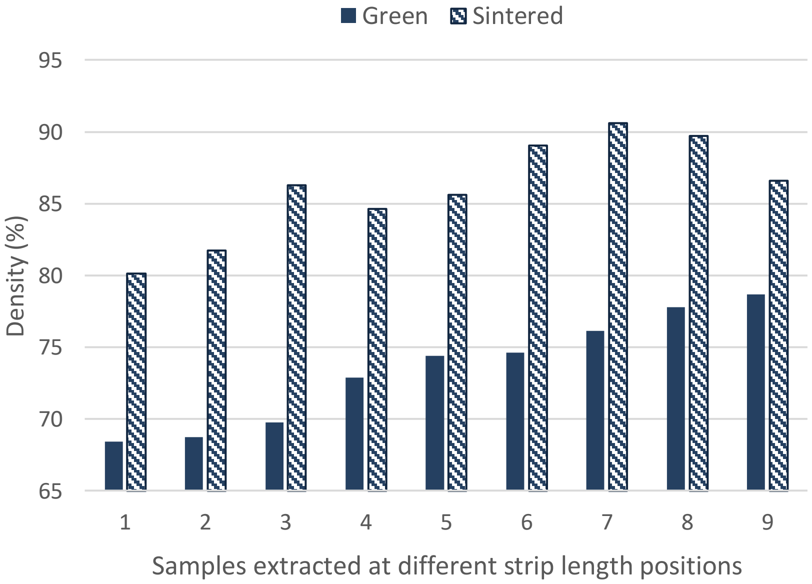

Figure 8.2: Density change of B2 samples at various start green densities on sintering at 1200°C for 3 hours

The average as-sintered densities for B1 and B2 strips were estimated at 78% and 87%. Sintered density averages calculated were not according to the exact methodology outlined at the beginning of Chapter 6 but rather included an average of the sintered densities from samples numbers given in Table 8.1 (the explanation of the chosen sample set are explained in the paragraph below). This revealed that while B2 strips may have started off with lower green densities because of inferior rollability, a sintering step rectified this, by correcting the density variability within the strip after rolling and surpassing the sintered densities achieved for B1 strips, that had the advantage of higher green densities.

A densification parameter (ΔD) was calculated using Equation 2-16[61] and represented in Figure 8.3 to show the effect of sintering on green bodies for each blend. ΔD is defined as the change in density from the green state divided by the maximum possible density change[61]. Since pressure distributions are difficult to control during roll compaction, compared to uniaxial compaction, where a pressure may be set, an attempt to select specific data points was made to better relate the contribution of the sintering effect for each blend. This was decided based on green densities for each sample set and blend. Green densities (Table 8.1) of similar values for each blend were chosen to best demonstrate the comparison and discern the influence of sintering, irrespective of the effects of highly varied green densities. In essence, the green densities for each sample set a – f for B1 and B2 compacts should have been similar. For example, the green densities of B1b = 72.5 % and B2b = 72.9 %. By ensuring these two values were similar in the green state (with regard to density), the relative change in density on sintering was more reliably compared as the initial green densities were at a similar starting point.

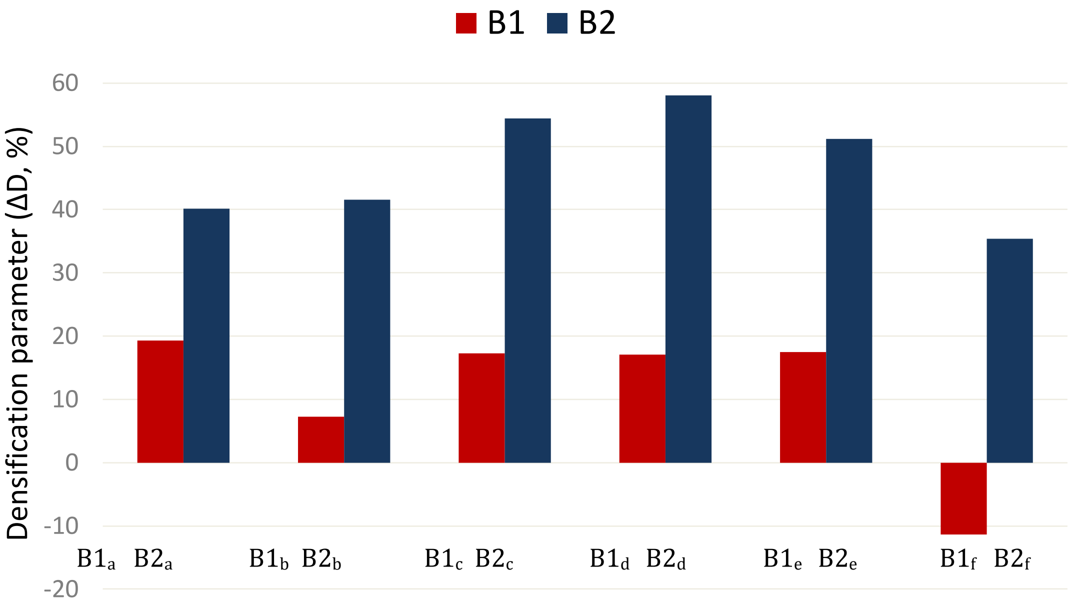

Figure 8.3: Tracking density change of B1 and B2 samples post sinter

$$\Delta D = \frac{\rho_{sintered} - \rho_{green}}{\rho_{theoretical} - \rho_{green}} \times 100$$

Equation 2-16[61]

Table 8.1: Green and sintered densities of selected B1 and B2 samples (values used to calculate densification parameters in Figure 8.3)

Sample no.	**B1$_a$**	**B2$_a$**	**B1$_b$**	**B2$_b$**	**B1$_c$**	**B2$_c$**	**B1$_d$**	**B2$_d$**	**B1$_e$**	**B2$_e$**	**B1$_f$**	**B2$_f$**
Green density (%)	66.8	68.4	72.5	72.9	75.4	74.6	76.4	76.1	77.9	77.8	78.9	78.7
Sintered density (%)	73.4	80.1	74.6	84.6	79.9	89.0	80.6	90.7	81.9	89.8	76.4	86.6

Sinterability in B2 specimens was greater than that of B1 specimens comparing ΔD in Figure 8.3. The low sintered densities were in correspondence with Ivasishin, et al. (2002)[66]. That study[66] compared various powder mixtures including mixtures based on titanium with alloying additions of elemental or master alloy powders. When using the BE approach to produce Ti-6Al-4V compacts with low residual porosity, Ivasishin, et al. (2002)[66] speculated that to achieve a maximum density in the final PM product, it would be necessary to achieve high densities in the green state during initial cold compaction and further increase them by sintering. They[66] later found that this was not always the case and that powder characteristics (elemental powders, MA additions, powder size) played a vital role in final sintered densities, and in some cases, sintered densities were independent of compacting pressures. The study by Ivasishin, et al. (2002)[66] highlights the effect the choice of alloying method has on sintered densities. Master alloys were more favourable, as the high melting points associated with this type of addition prevents the formation of a liquid phase on sintering resulting in higher densities observed compared to elemental alloying additions.

8.2 Chemical homogeneity of as-sintered samples

SEM/EDX was used to determine the level of homogeneity achieved in B1 and B2 sintered specimens. This technique allows for rapid compositional analysis at varying length scales depending on the size of the scanning raster selected. This provided good opportunity to assess the degree of homogenization in sintered BE Ti-6Al-4V powder compacts. In particular, the approach to the EDX analysis is highlighted to illustrate the difference in homogenization progress for the respective powder blends.

An accelerating beam voltage of 20 keV was used. Selecting the correct accelerating voltage is critical to ensure adequate intensities are obtained. Selection depends on the elements present in the specimen. The accelerating voltage should not be less than three times the highest excitation energy of one of the elements present. In this case, the highest excitation energy belongs to vanadium (4.954 keV). A second reason for choosing this voltage was to minimize noise in the system. EDX makes use of exciting X-rays within the sample to generate a spectrum. X-ray intensities are measured by counting pulses generated in the detector by X-ray photons. There is however a limit to the number of pulses that can be processed before the system becomes unresponsive to processing any more photons coming in (dead time). It is therefore necessary to use a certain integrating time to minimize this noise. Throughput reaches a maximum, after which it begins to decrease as the input count rate increases. Energy resolution is also, however, a factor to consider, where the longer the integration time, the more smoothed out the noise is and higher the energy resolution. Therefore a compromise must be made to balance energy resolution and the number of X-rays passing through the system. It is therefore recommended that for maximum throughput rates, a count rate of >100 000 counts s^{-1} is necessary. One way to adjust the system set-up to achieve this is to manipulate the accelerating voltage. For this investigation, 20 keV was found to satisfy the conditions mentioned above.

Defining an appropriate length scale is another critical parameter that needed to be assessed. In the case of continuous solid solution alloys (single phase) the choice of length scale was quite straight-forward in that complete homogenization would ultimately be reflected when spot analyses (stationary beam) produced the same composition everywhere in the metal sample. However, the situation became more complicated when multi-phase alloys were investigated, since the inherent element partitioning between the phases influences the analysis. The challenge was to be able to measure the degree of diffusional mixing of the titanium, aluminium and vanadium powder particles whilst being able to account for the element partitioning that occurred between the α and β-phases that constitute the Ti-6Al-4V alloy. The appropriate length scale for EDX analysis is influenced by initial powder size and the fine lamellar α/β micro-structure that evolved on cooling to room temperature.

Since spot analysis was not suitable given the two-phase nature of Ti-6Al-4V, it was first necessary to determine the minimum scan area that would exclude the effects of α/β element partitioning. To investigate and refine the methodology to use in sintered specimens, a highly refined wrought Ti-6Al-4V sample was analysed under beam conditions ranging from stationary spot to dynamic area scans as large as 1.4x1.4 mm^2. The elemental indexing was limited to the elements titanium, aluminium, and vanadium. The aluminium (Al) and vanadium (V) levels for several locations relating to each of the specific scan areas are indicated in Figure 8.4.

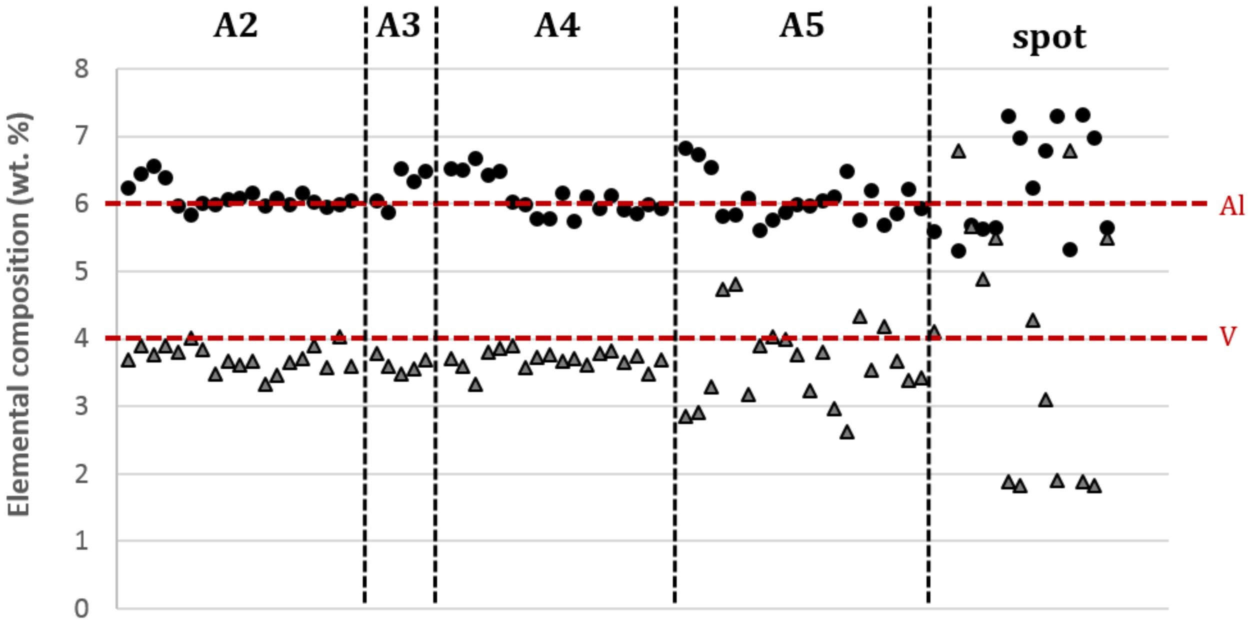

Figure 8.4: EDX analyses of wrought Ti-6Al-4V specimen at various length scales A2- spot. (A2=1.4x1.4mm^2; A3=350x350µm^2; A4=100x100µm^2 and A5=10x10µm^2)

Apart from some minor fluctuations throughout the length scale range, significant aluminium/vanadium partitioning became evident when the scan area was reduced to 10 x 10 μm². This length scale was consistent with the size and distribution of α/β lamellae which evolve during the Widmanstätten decomposition of the high temperature β-phase. Consequently, the minimum scan area for assessing homogenization had to be at least be greater than 100 μm². However, care should be taken that the area was not too large so as to average out possible inhomogeneities on a scale larger than the α/β phase partitioning.

The same EDX scanning methodology was applied to B1 (Figure 8.5) and B2 (Figure 8.6) sintered specimens to observe variability in elemental composition across different length scales, extended to 3 × 3 mm².

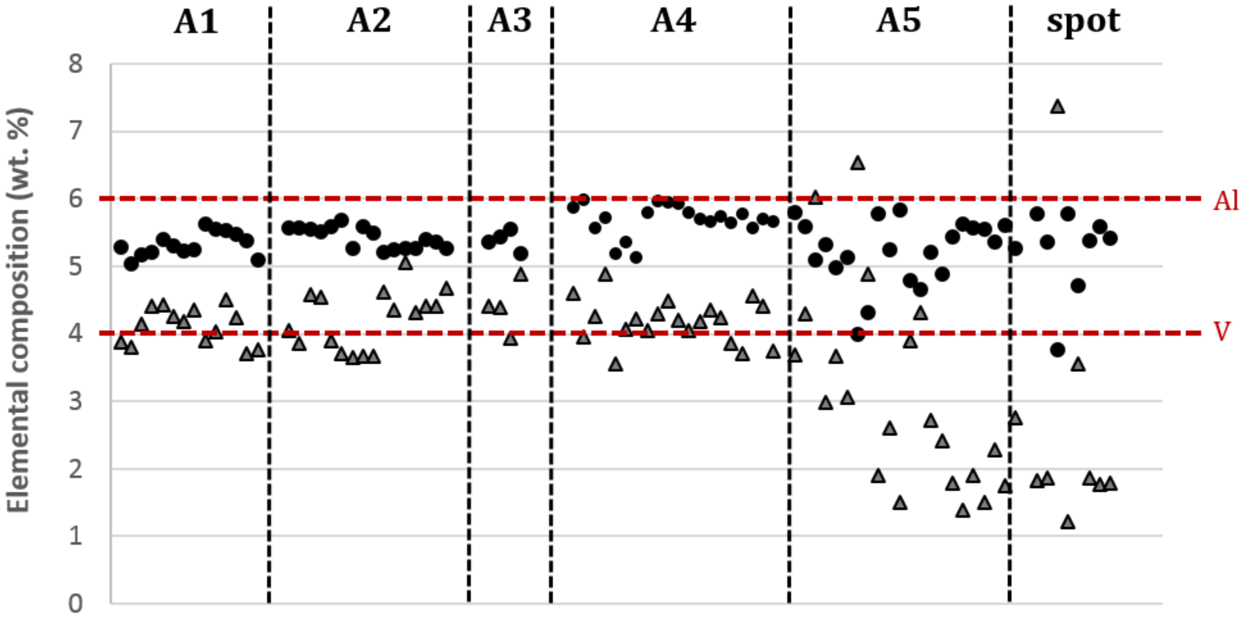

Figure 8.5: EDX analyses of B1 specimens at various length scales A1- spot. (A1 =3 × 3 mm²; A2=1.4x1.4mm²; A3=350x350µm²; A4=100x100µm² and A5=10x10µm²)

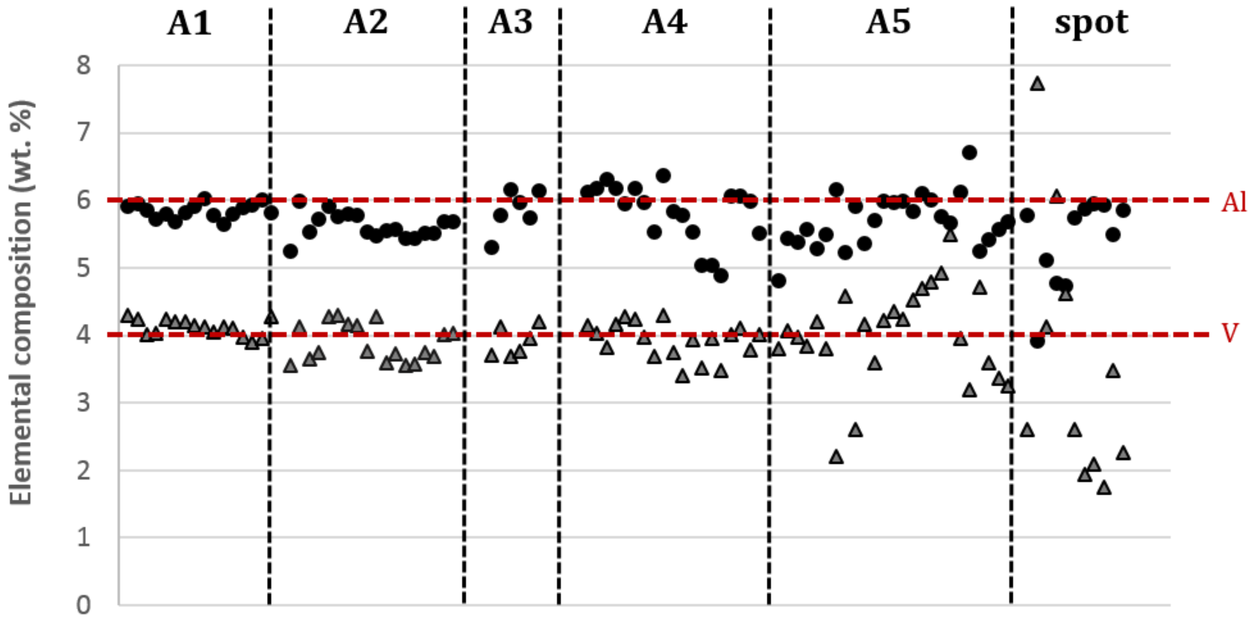

Figure 8.6: EDX analyses of B2 specimens at various length scales A1- spot. (A1 =3 × 3 mm^2; A2=1.4x1.4mm^2; A3=350x350μm^2; A4=100x100μm^2 and A5=10x10μm^2)

Figures 8.5 and 8.6 demonstrate α/β element partitioning at a scan area of 10×10 μm^2 for both B1 and B2 specimens due to the large scatter observed in this region for aluminium and vanadium compositions. An observation of note was the comparison between B1 and B2 at larger scan areas of 3×3 mm^2. Here, a higher degree of variability in aluminium and vanadium levels for B1 was evident at this large scan area.

This methodology shows that when dealing with randomly distributed powder particles of discrete composition, one needs to be mindful of the limiting scan area size above which the EDX analysis would always yield the same composition. Consequently, it was important that homogenization was compared across a range of length scales. For all three cases investigated, α/β element partitioning was evident for the 10 x 10 μm^2 scan area. However, comparing Figures 8.5 and 8.6 indicates significantly more variation in aluminium/vanadium levels for B1 even at scan areas up to 3 x 3 mm^2. The systematic approach to EDX analysis demonstrated the greater difficulty in homogenizing the elemental powder (B1) versus the blended master alloy (B2). It is possible that this behaviour may have been due to local melting of aluminium powder.

8.3 Porosity analysis of sintered specimens

Light microscopy was used to analyse porosity features of specimens sintered at 1200°C under vacuum conditions for three hours. The results of the light microscopy are given in Figure 8.7. To compare between B1 and B2 specimens, porosity analysis was conducted on only two sample sets. The criterion used to select samples was based on initial green densities of sectioned samples explained in Section 8.1, Table 8.1. This was because of the difficulty in acquiring sectioned strip samples of the same green density due to the inherent density profile along the strip length. Since this is a comparative study to track sinterability of each powder blend, it was imperative to keep all other parameters as consistent as possible. Including: sintering time, sintering temperature, and initial green densities. Particularly with respect to green density, it was important to select samples from B1 and B2 sample sets with almost equivalent green densities to accurately monitor the effect of identical sintering conditions for each respective blend. Thus, B1d/B2d and B1e/B2e sample sets were selected to observe the effects of sintering only on the different blends. Table 8.2 displays a subset of Table 8.1 green densities and final sintered densities for these pairs of selected samples used for porosity analysis, corresponding to micrographs in Figure 8.7, where micrograph a = $B1_d$; b = $B2_d$; c = $B1_e$; d = $B2_e$. The densities in Table 8.2 were acquired using the Archimedes method described by ASTM B-962.

Table 8.2: Green and sintered densities measured by Archimedes' method of B1 and B2 sectioned samples sintered at 1200°C for 3 hours

Sample no.	**$B1_d$ (a)**	**$B2_d$ (b)**	**$B1_e$ (c)**	**$B2_e$ (d)**
Green density (%)	76.4	76.1	77.9	77.8
Sintered density (%)	80.6	90.7	81.9	89.8

Across all micrographs presented in Figure 8.7, pore shape is irregular and angular. All powders used in this study were either nodular or angular shaped. It was therefore reasonable that large pore shapes were irregular. The titanium powders were the largest with a D50 of 125.7 µm and D90 of 181.9 µm. Large pores were observed in both blends after sintering. It is therefore conceivable that these large titanium particles may have arranged themselves in certain orientations during rolling and thereby resulted in the formation of these large pores in the green state. As such, these large pores that formed mechanically could not however be healed during sintering and thus left a number of large pores in both B1 and B2 sintered specimens. Since the same base titanium powders were used for each blend, this cannot explain the discrepancies observed between B1 and B2. The second largest powders used were aluminium powders with a D50 of 74.6 µm and D90 of 142.3 µm, which means that 10% of aluminium particles were above this upper D90 limit. Aluminium powders were used in B1 blends. Another feature of aluminium is its low melting point. In the present study, the evolution of aluminium's elemental state during sintering in B1 samples could not be accurately recorded. Given aluminium's melting point is 660°C[12], it is possible that the melting temperature was reached during sintering, giving rise to these large pores being left behind as the aluminium changed from a solid to a liquid state.

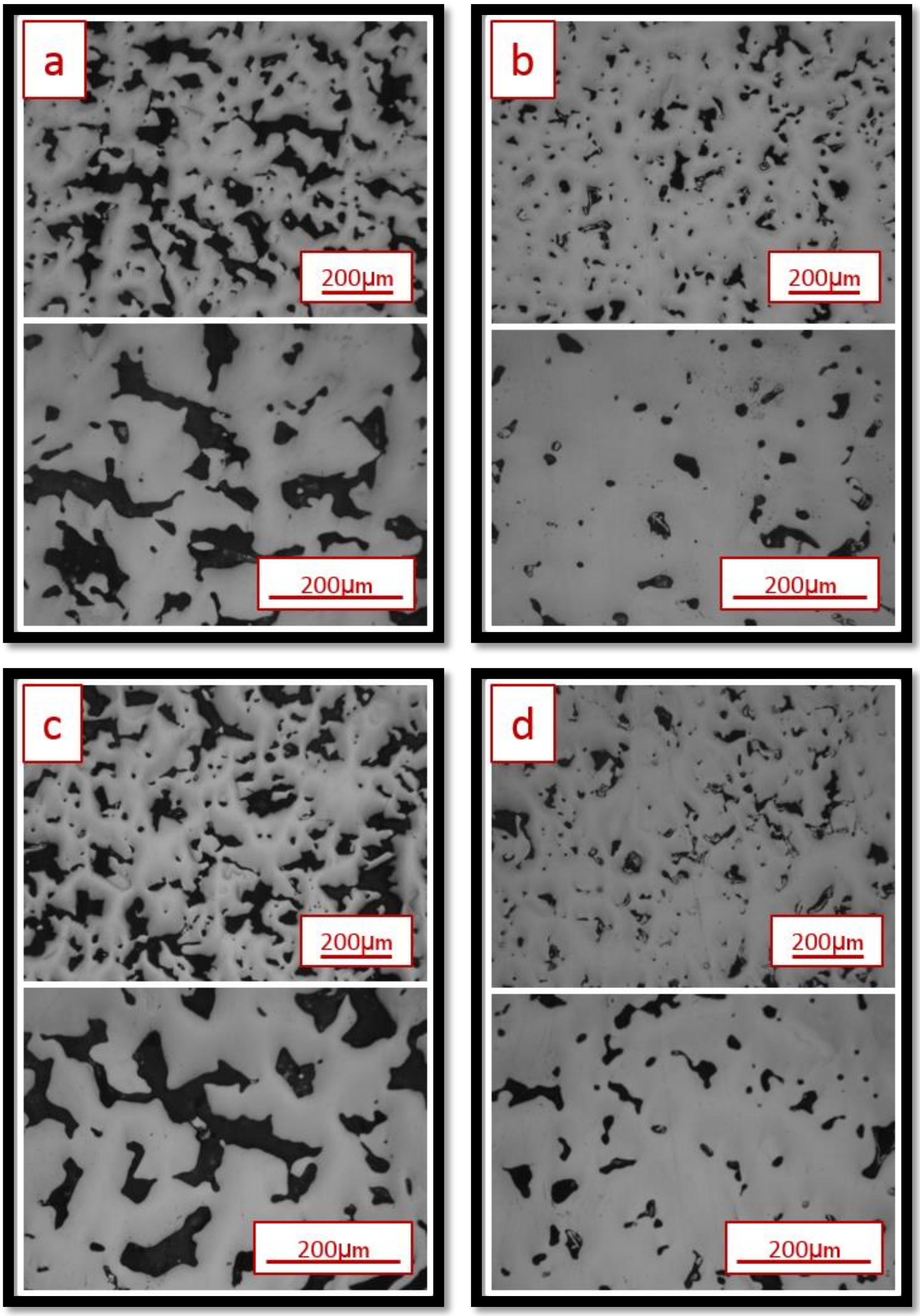

Figure 8.7: : Light micrographs comparing B1 and B2 as-sintered specimens sintered at 1200°C for 3 hours where a-d represent corresponding samples defined in section 8.1 and Table 8.1 [a) B1d, b) B2d, c) B1e and d) B2e]

Given the increased number of large particles present in the B1 blend (titanium and aluminium) combined with aluminium's low melting point (660°C), nearly half that of the sintering temperature used, it is likely that the increased number of large pores was due to these contributing factors.

From Figure 8.7, it is suggested that B2 samples possessed less porosity than B1 samples. To better quantify this, the imaging tool ImageJ was used to quantify the porosity from these light micrographs. Image thresholding was used in ImageJ to measure the porosity of each image. Before the measurement can be taken, the image must first be converted to greyscale to ensure the software may distinguish between pores (black contrast) and solid material (white contrast). Thresholding partitions the image into a foreground and background, allowing for certain areas to be isolated within the image, converting the greyscale image into binary images. In this case, black areas represent pores while white areas are solid material (Figure 8.8a). There are multiple thresholding methods that can be chosen to approximate the proportion of black and white in the image. The Huang method was chosen as the fit most agreed with the original image by inspection. This was done by selecting an overlay of the portions of the image were seen as black (Figure 8.8b).

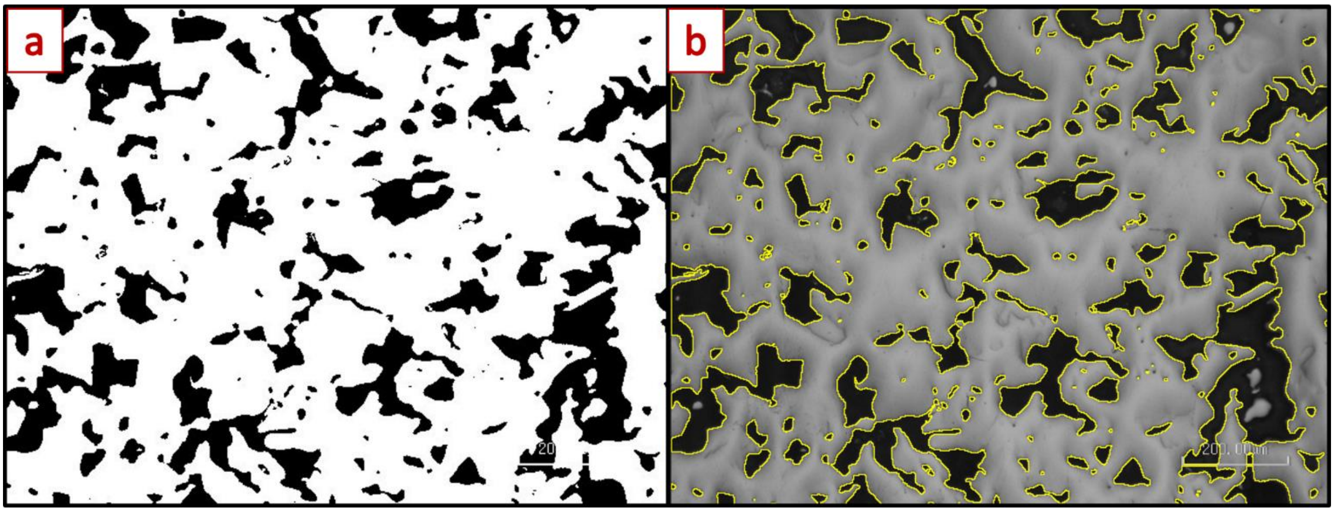

Figure 8.8: B1e sample showing porosity in (a) Huang thresholding black and white image and (b) overlay of original image using Huang thresholding method in ImageJ

All eight images in Figure 8.7 were analysed using this method of thresholding to determine the percentage area of each micrograph made up of pores, which are represented as black shading in Figure 8.8. These values are given in Table 8.3. Overall, it was evident that the porosity in B1 samples was greater than B2 samples. This agreed with the density measurements following ASTM-B962 which makes use of the Archimedes' principle (3.2). There seemed to be less variability in ImageJ processed porosity values of B1 compared to B2. The small sample set and narrow fields of view may account for this variability as only eight images were used.

Table 8.3: Results from ImageJ Huang thresholding for B1d, e and B2d, e samples

Sample ID	**Powder blend**	
	B1	**B2**
d	22.6%	9.7%
	(high magnification) 22.7%	(high magnification) 5.9%
e	24.6%	12.3%
	(high magnification) 25.2%	(high magnification) 9.3%

9. Conclusions

Based on the research conducted and presented in this dissertation, the following conclusions were drawn:

- Powder blends comprising of titanium + elemental aluminium and vanadium (B1), and titanium + MA (B2) to create Ti-6Al-4V strip behaved significantly differently when employing the direct powder rolling methodology to produce near fully dense strip.

- Powder properties derived from internal friction, wall friction and compressibility revealed significant effects on maximum pressures during direct powder rolling. In the case of the wall friction angle, it was found that nip angle calculations were sensitive to wall friction angles, where an increase in wall friction angles resulted in larger nip angles and higher maximum pressures.

- The ability to successfully roll was affected by roll pressure build-up and compactibility. Rolling of the B2 blend led to a higher pressure build-up resulting in its inability to be rolled at smaller roll gaps (0.5 mm). B1 powders exhibited superior rolling properties in making a green strip, and were rolled at a wider range of roll gaps than B2 powders. This was attributed to the presence of ductile aluminium present in the B1 blend.

- Green strength and green density were strongly influenced by the presence of aluminium. Green strength results showed B1 green strips to be higher than B2 indicating a higher quality self-supporting strip for B1 due to the ductile nature of aluminium particles present.

- A density profile of B1 green strips was established. This demonstrated that the green density along the length of the strip was not consistent due to operating conditions and roll press operations. A similar observation was made during sintering of B2 strips and it was concluded that this trend would be observed across blends and was not material dependent.

- The Johanson model was moderately successful as it gave insight into general trends when comparing the same family of powders (B1 and B2 powders). Empirical results of rolling B2 powders showed that this blend was more difficult to roll. This was reflected in the Johanson simulation as much larger pressures were required to compact B2 powders at the same roll gap. It therefore can be used as a tool for minor system adjustments. However, the Johanson model maximum pressure results were clearly unachievable and cannot be used to estimate actual pressures during direct powder rolling.

- Sintering of B1 and B2 compacts at 1200°C for 3 hours resulted in highly porous materials for both blends. Densification parameters demonstrated superior sinterability for B2 strips revealing that inferior rolling ability may be remedied on sintering, leading to sintered densities higher than that of B1 as well as improvement in density variability along strip length. Therefore, while achieving higher green densities during powder rolling may be beneficial for high sintered densities, powder constituents are just as important if not more so, since low green densities for the blend with the MA addition (B2) proved to sinter far better, resulting in a higher final density.

- Porosity observations of B1 and B2 sintered strips were in agreement with Archimedes' density results, where a larger percentage of porosity per area measured was visible in B1 strips. A number of very large pores in excess of 50-100μm may suggest that local melting of larger aluminium particles resulted in the inability for pore healing to occur on sintering, leading to more porosity observed in B1 sintered strips.

- An improvement in homogenisation was observed in the B2 blend when compared to B1. This was attributed to better diffusional mixing. The 60Al-40V MA is an alloy. As such it had the advantage of two of the alloying elements (aluminium and vanadium) having already been homogenised and having a higher melting point. B1's inferior homogenisation properties were attributed to local melting of aluminium powder.

10. Recommendations

As a result of the current research and findings, the author suggests the following:

- Piezoelectric transducers should be installed on the roll press to accurately monitor and acquire pressure data during rolling.

- A sensitivity analysis should be conducted to evaluate effect of different powder constituents (size and composition) on the nip angle.

- Sieving powders should be done prior to any powder compaction study to control powder size and eliminate the possibility of specifically large aluminium powders melting and causing large pores that may not be healed during sintering.

- Experimenting with different ratios of different MA and elemental powders may improve compaction during rolling and/or sinterability as well as be economically beneficial.

- When developing a standard practice to determine homogenisation after sintering of BE powders, it is advised that a near fully dense sintered PM sample made from pre-alloyed Ti-6Al-4V powder (with a comparable particle size range) should be used and not a wrought sample. This is to control an accurately observe the effects of powder particle size on sintering.

- Quantify pore distribution and size more accurately using ImageJ by calibrating software thresholding to measure particle size in a relevant metric (micrometres). This will assist in analysing pore structure and how to mitigate any problems that may be associated with it.

- It is suggested that hot rolling be investigated to achieve the final desired product after sintering. Roll compaction allows for the initiation of a continuous process for strip production using powder metallurgy. This step in necessary for the development of the initial shape and structure. Subsequent sintering allows for improved density and to create a homogenous strip by alloying it through solid-state diffusion. Since the aim is not to produce a porous strip, a final consolidation step is necessary to close final pore structure and improve mechanical properties of the strips.

11. References

1. Johanson, J. R. A Rolling Theory for Granular Solids. *J. Appl. Mech.* **32**, 842 (1965).
2. Donachie, M. J. *Titanium: A technical guide*. (ASM International, 2000).
3. Henriques, V. A. R., de Campos, P. P., Cairo, C. A. A. & Bressiani, J. C. Production of Titanium Alloys for Advanced Aerospace Systems by Powder Metallurgy. *Mater. Res.* **8**, 443–446 (2005).
4. Qian, M. Cold compaction of titanium and its alloys for near-net-shape or perform fabrication. *Int. J. powder Metall.* **46**, 29–44 (2010).
5. Froes, F. H., Mashl, S. J., Moxson, V. S., Hebeisen, J. C. & Duz, V. A. The technologies of titanium powder metallurgy. *JOM* **56**, 46–48 (2004).
6. Zhang, Y. A Study of Direct Powder Rolling Route for Cp-Titanium. (University of Cape Town, 2015).
7. Simon, O. & Guigon, P. Interaction between feeding and compaction during lactose compaction in a laboratory roll press. (Université de Technologie de Compiègne, 2000).
8. Leyens, C. & Peters, M. *Titanium and titanium alloys, fundamentals and applications*. (Wiley-VCH, 2003).
9. Lütjering, G. & Williams, J. C. *Titanium (engineering materials and processes)*. (Springer, 2007).
10. Wanhill, R. & Barter, S. *Fatigue of beta processed and beta heat-treated titanium alloys*. (Springer, 2011).
11. Upadhyay, V. *Manufacturing Processes*. (S. K Kataria & Sons, 2010).
12. Upadhyaya, G. *Powder Metallurgy Technology*. (Cambridge Int Science Publishing, 1997).
13. Thümmler, F. & Oberacker, R. *An Introduction to Powder Metallurgy*. (Oxford Science Publications, 1993).
14. Duz, V., Matviychuk, M., Klevtsov, A. & Moxson, V. Industrial application of titanium hydride powder. *Met. Powder Rep.* **00**, 1–9 (2016).
15. Qian, M. & Froes, F. H. *Titanium Powder Metallurgy: Science, Technology and Applications*. (Butterworth-Heinemann, 2015).

16. Qian, M., Schaffer, G. B. & Bettles, C. J. Sintering of titanium and its alloys. *Sinter. Adv. Mater.* 324–355 (2010).

17. Yan, M., Dargusch, M. S., Ebel, T. & Qian, M. A transmission electron microscopy and three-dimensional atom probe study of the oxygen-induced fine microstructural features in as-sintered Ti-6Al-4V and their impacts on ductility. *Acta Mater.* **68**, 196–206 (2014).

18. Yan. Ming & Tang. H. P. Scavenging of oxygen and chlorine from powder metallurgy (PM) titanium and titanium alloys. *Titan. Powder Metall.* 253–276 (2015).

19. Duz, V. A. & Moxson, V. S. The direct powder rolling process for producing titanium and titanium alloy foils, sheets and plates. *Mater. Sci. Technol. 2005* **4**, (2005).

20. Microtrac. Laser Diffraction Systems. (2019). Available at: https://www.microtrac.com/laser-diffraction-systems-for-particle-size-measurements/. (Accessed: 2nd September 2019)

21. Horiba Scientific. A guidebook to particle size analysis. (2014). Available at: https://www.horiba.com/fileadmin/uploads/Scientific/eMag/PSA/Guidebook/pdf/PSA_Guidebook.pdf. (Accessed: 18th August 2016)

22. Schwedes, J. Measurement of flow properties of bulk solids. *Powder Technol.* **88**, 285–290 (1996).

23. German, R. M. *Powder Metallurgy Science*. (Metal Powder Industries Federation, 1984).

24. Pease, L. F. A quick tour of powder metallurgy. *Adv. Mater. Process.* **163**, 36–38 (2005).

25. Abkowitz, S., Siergiej, J. & Regan, R. Titanium P/M preforms, parts and composites. *Mod. Dev. Powder Met.* **4**, 501–511 (1971).

26. Alman, D. E. & Gerdemann, S. J. Sintering of sponge and hydride-dehydride titanium powders. *P/M Sci. Technol. Briefs* **6**, (2004).

27. Qian, M. & Froes, F. H. *Titanium Powder Metallurgy*. (Butterworth-Heinemann, 2015).

28. Qian, M., Schaffer, G. & Bettles, C. J. Sintering of titanium and its alloys x. *Sinter. Adv. Mater.* 324–355 (2010).

29. Schulze, D. Flow properties of powders and bulk solids (fundamentals). *Powder Technol.* **65**, 321–333 (2010).

30. Jenike, A. & Shield, R. On the plastic flow of Coulomb solids beyond original failure. *J. Appl. Mech.* **81**, 599–602 (1959).

31. Freeman Technology. About the FT4 powder Rheometer: Shear Testing. Available at: http://www.freemantech.co.uk/_powders/powder-testing-shear-cells. (Accessed: 12th March 2018)

32. Simon, O. & Guigon, P. Correlation between powder-packing properties and roll press compact heterogeneity. *Powder Technol.* **130**, 257–264 (2003).

33. Sheskey, P., Pacholke, K., Sackett, G., Maher, L. & Polli, J. Roll compaction granulation of a controlled-release matrix tablet formulation containing HPMC: Effect of process scale-up on robustness of tablets, tablet stability and predicted in vivo performance. *Pharm. Technol.* **24**, 30–52

34. Seville, J. P. K. *Granulation*. (Elsevier, 2006).

35. Rhodes, M. J. *Principles of powder technology*. (Wiley, 1990).

36. Dec, R. T., Zavaliangos, A. & Cunningham, J. C. Comparison of various modeling methods for analysis of powder compaction in roller press. *Powder Technol.* **130**, 265–271 (2003).

37. Balicki, M. & Michrafy, A. Numerical Methods for Predicting roll press powder compaction parameters. (Ecole Des Mines D'Albi- Carmaux, 2003).

38. Leturia, M., Benali, M., Lagarde, S., Ronga, I. & Saleh, K. Characterization of flow properties of cohesive powders: A comparative study of traditional and new testing methods. *Powder Technol.* **253**, 406–423 (2014).

39. Chikosha, S., Shabalala, T. C. & Chikwanda, H. K. Effect of particle morphology and size on roll compaction of Ti-based powders. *Powder Technol.* **264**, 310–319 (2014).

40. Cunningham, J. C., Winstead, D. & Zavaliangos, A. Understanding variation in roller compaction through finite element-based process modeling. *Comput. Chem. Eng.* **34**, 1058–1071 (2010).

41. Gao, H., Ramalingam, S. C., Barber, G. C. & Chen, G. Analysis of asymmetrical cold rolling with varying coefficients of friction. *J. Mater. Process. Technol.* **124**, 178–182 (2002).

42. Yu, S. Roll compaction of pharmaceutical excipients. (University of Birmingham, 2012).

43. Patel, B. A., Adams, M. J., Turnbull, N., Bentham, A. C. & Wu, C. Y. Predicting the pressure distribution during roll compaction from uniaxial compaction measurements. *Chem. Eng. J.* **164**, 410–417 (2010).

44. Yusof, Y. A., Smith, A. C. & Briscoe, B. J. Roll compaction of maize powder. *Chem. Eng. Sci.* **60**, 3919–3931 (2005).

45. Bindhumadhavan, G., Seville, J. P. K., Adams, M. J., Greenwood, R. W. & Fitzpatrick, S. Roll compaction of a pharmaceutical excipient: Experimental validation of rolling theory for granular solids. *Chem. Eng. Sci.* **60**, 3891–3897 (2005).

46. Tikhonov, G. F. *et al.* Production of properties of porous rolled materials. *Sov. Powder Met. Met. Ceram.* **12**, 1011–1014 (1973).

47. Shmelev, L. S. Industrial production of porous strip from stainless steel and titanium powders. *Powder Metall. Met. Ceram.* **10**, 73–74 (1971).

48. Ro, D. H., Toaz, M. W. & Moxson, V. S. The direct powder-rolling process for producing thin metal strip. *JOM* **35**, 34–39 (1983).

49. Cantin, G. M. D. *et al.* Innovative consolidation of titanium and titanium alloy powders by direct rolling. *Powder Metall.* **54**, 188-192z (2011).

50. Peter, W. H. *et al.* Titanium sheet fabricated from powder for industrial applications. *JOM* **64**, 566–571 (2012).

51. Park, N. K., Lee, C. H., Kim, J. H. & Hong, J. K. Characteristics of powder-rolled and sintered sheets made from HDH Ti powders. *Key Eng. Mater.* **520**, 281–288 (2012).

52. Mangabhai, D., Araci, K., Akhtar, M. K., Stone, N. A. & Cantin, D. Processing of titanium powder into consolidated parts and sheet. *Key Eng. Mater.* **551**, 57–66 (2013).

53. Cantin, G. M. D. *et al.* Production of Ti-6Al-4V Strip by Direct Rolling of Blended Elemental Powder. *Mater. Sci. Forum* **654–656**, 807–810 (2010).

54. German, R. M. *Sintering Theory and Practice*. (Wiley-Interscience, 1996).

55. Schade, P. 100 years of doped tungsten wire. *Int. J. Refract. Met. Hard Mater.* **28**, 648–660 (2010).

56. Rahaman, M. N. *Ceramic processing and sintering*. (CRC Press, 2003).

57. Rahaman, M. N. *Sintering of ceramics*. (CRC Press, 2007).

58. German, R. M. *Powder metallurgy and particulate materials processing: the processes, materials, products, properties, and applications*. (Metal Powder Industries Federation, 2005).

59. German, R. M. Sintering Simplified: Surface Area, Density, and Grain Size Relations. *Mater. Sci. Forum* **835**, 50–75 (2016).

60. Watanabe, T. & Horikoshi, Y. The sintering phenomenon of titanium powders – a discussion. *Inter. J. Powder Metall.* **12**, 209–14 (1976).

61. Robertson, I. M. & Schaffer, G. B. Some effects of particle size on the sintering of titanium and a master sintering curve model. *Metall. Mater. Trans. A* **40**, 1968–1979 (2009).

62. Welsch, G., Boyer, R. & Collings, E. W. *Materials Properties Handbook: Titanium Alloys*. (ASM international, 1993).

63. Gülsoy, H. Ö., Gülsoy, N. & Calışıcı, R. Particle morphology influence on mechanical and biocompatibility properties of injection molded Ti alloy powder. *Biomed. Mater. Eng.* **24**, 1861–73 (2014).

64. Abkowitz, S. & Rowell, D. Superior Fatigue Properties for Blended Elemental P/M Ti-6Al-4V. *JOM* 36–39 (1986).

65. Fujita, T., Ogawa, A., Ouchi, C. & Tajima, H. Microstructure and properties of titanium alloy produced in the newly developed blended elemental powder metallurgy process. *Mater. Sci. Eng. A* **213**, 148–153 (1996).

66. Ivasishin, O. M., Savvakin, D. G., Froes, F. H., Mokson, V. S. & Bondareva, K. Synthesis of the Ti-6Al-4V alloy having low residual porosity by powder metallurgy method. *Poroshkovaya Metall.* **7**, 54–64 (2002).

67. Australian microscopy & microanalysis research facility. Accuracy, precision and detection limits. 1–5 (2014).

68. Froes, F. H. Titanium Powder Metallurgy: A Review - Part 1 - British Library. *Adv. Mater. Process.* **170**, 16–23 (2012).

69. Jenike, A. W. *Storage and flow of solids*. (University of Utah, 1964).

70. Sohn, H. Y. & Moreland, C. The effect of particle size distribution on packing density. *Can. J. Chem. Eng.* **46**, 162–167 (1968).

71. Bi, M., Alvarez-Nunez, F. & Alvarez, F. Evaluating and modifying Johanson's rolling model to improve its predictability. *J. Pharm. Sci.* **103**, 2062–2071 (2014).

72. Gerdemann, S. J. & Jablonski, P. D. Compaction of titanium powders. *Metall. Mater. Trans. A Phys. Metall. Mater. Sci.* **42**, 1325–1333 (2011).

73. Simon, O. & Guigon, P. Interaction between Feeding and Compaction During Lactose Compaction in a Laboratory Roll Press. (Université de Technologie deCompiègne, 2000).

74. Dahms, M., Leitner, G., Poessnecker, W., Schultrich, S. & Schmelzer, F. Pore formation during reactive sintering of extruded titanium aluminum powder mixtures. *Zeitschrift für Met.* **84**, 351–357 (1993).

Appendix A – Hall flow results

Table A.1: Hall flow results of B1 and B2 powder blends

Powder type	Time (s) for 50g of powder to flow through flowmeter			Average time (s) for 50g of powder to flow through flowmeter
B1	65	64	65	65
B2	66	65	65	65

Appendix B-Particle size analysis

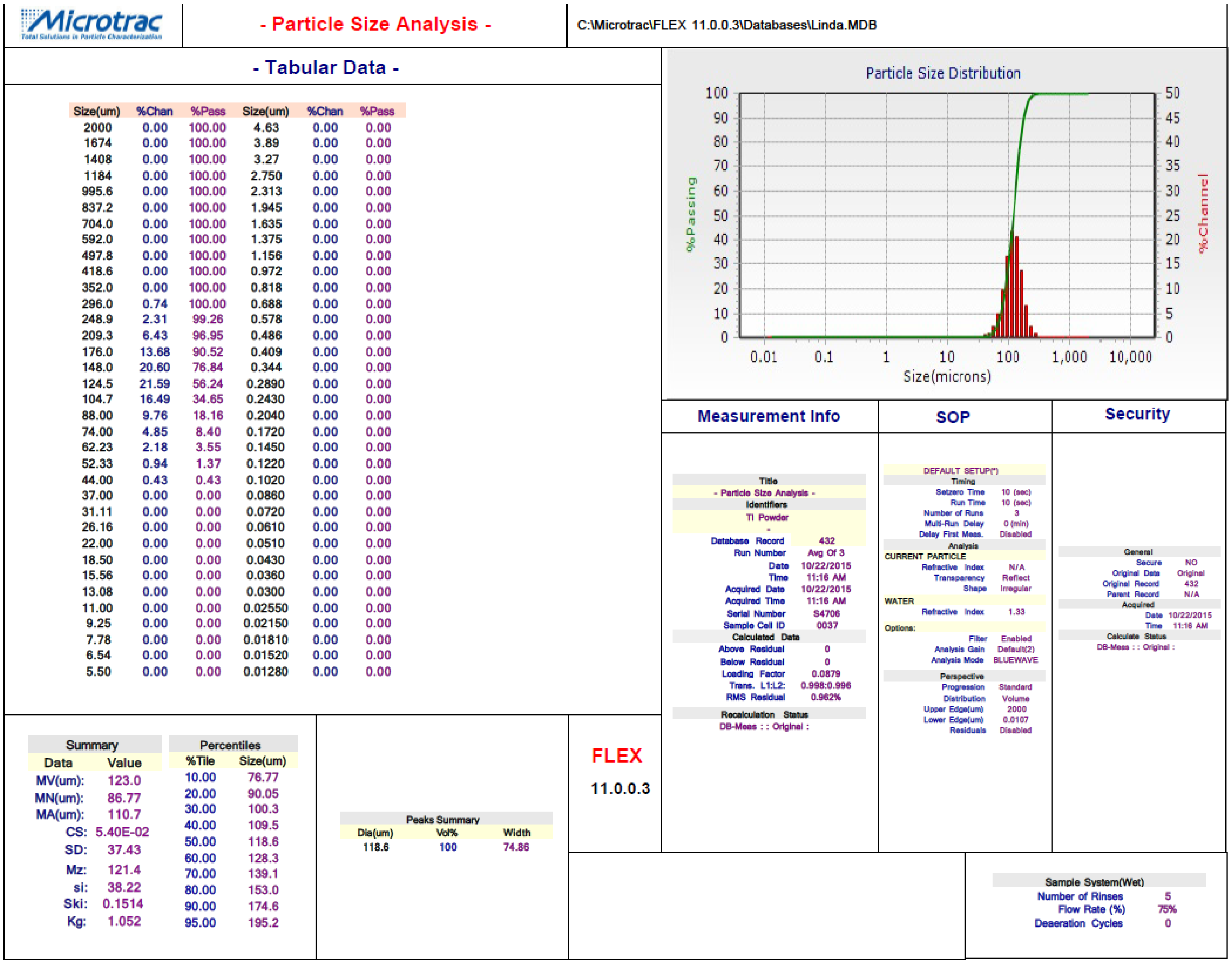

Microtrac Total Solutions in Particle Characterization

- Particle Size Analysis -

C:\Microtrac\FLEX 11.0.0.3\Databases\Linda.MDB

- Tabular Data -

Size(um)	%Chan	%Pass	Size(um)	%Chan	%Pass
2000	0.00	100.00	4.63	0.00	0.00
1674	0.00	100.00	3.89	0.00	0.00
1408	0.00	100.00	3.27	0.00	0.00
1184	0.00	100.00	2.750	0.00	0.00
995.6	0.00	100.00	2.313	0.00	0.00
837.2	0.00	100.00	1.945	0.00	0.00
704.0	0.00	100.00	1.635	0.00	0.00
592.0	0.00	100.00	1.375	0.00	0.00
497.8	0.00	100.00	1.156	0.00	0.00
418.6	0.00	100.00	0.972	0.00	0.00
352.0	0.00	100.00	0.818	0.00	0.00
296.0	0.74	100.00	0.688	0.00	0.00
248.9	2.31	99.26	0.578	0.00	0.00
209.3	6.43	96.95	0.486	0.00	0.00
176.0	13.68	90.52	0.409	0.00	0.00
148.0	20.60	76.84	0.344	0.00	0.00
124.5	21.59	56.24	0.2890	0.00	0.00
104.7	16.49	34.65	0.2430	0.00	0.00
88.00	9.76	18.16	0.2040	0.00	0.00
74.00	4.85	8.40	0.1720	0.00	0.00
62.23	2.18	3.55	0.1450	0.00	0.00
52.33	0.94	1.37	0.1220	0.00	0.00
44.00	0.43	0.43	0.1020	0.00	0.00
37.00	0.00	0.00	0.0860	0.00	0.00
31.11	0.00	0.00	0.0720	0.00	0.00
26.16	0.00	0.00	0.0610	0.00	0.00
22.00	0.00	0.00	0.0510	0.00	0.00
18.50	0.00	0.00	0.0430	0.00	0.00
15.56	0.00	0.00	0.0360	0.00	0.00
13.08	0.00	0.00	0.0300	0.00	0.00
11.00	0.00	0.00	0.02550	0.00	0.00
9.25	0.00	0.00	0.02150	0.00	0.00
7.78	0.00	0.00	0.01810	0.00	0.00
6.54	0.00	0.00	0.01520	0.00	0.00
5.50	0.00	0.00	0.01280	0.00	0.00

Summary

Data	Value
MV(um):	123.0
MN(um):	86.77
MA(um):	110.7
CS:	5.40E-02
SD:	37.43
Mz:	121.4
si:	38.22
Ski:	0.1514
Kg:	1.052

Percentiles

%Tile	Size(um)
10.00	76.77
20.00	90.05
30.00	100.3
40.00	109.5
50.00	118.6
60.00	128.3
70.00	139.1
80.00	153.0
90.00	174.6
95.00	195.2

Peaks Summary

Dia(um)	Vol%	Width
118.6	100	74.86

FLEX
11.0.0.3

Measurement Info

Title
- Particle Size Analysis -
Identifiers
TI Powder
-

Database Record	432
Run Number	Avg Of 3
Date	10/22/2015
Time	11:16 AM
Acquired Date	10/22/2015
Acquired Time	11:16 AM
Serial Number	S4706
Sample Cell ID	0037
Calculated Data	
Above Residual	0
Below Residual	0
Loading Factor	0.0879
Trans. L1:L2:	0.998:0.996
RMS Residual	0.962%

Recalculation Status
DB-Meas : : Original :

SOP

DEFAULT SETUP(*)

Timing	
Setzero Time	10 (sec)
Run Time	10 (sec)
Number of Runs	3
Multi-Run Delay	0 (min)
Delay First Meas.	Disabled
Analysis	
CURRENT PARTICLE	
Refractive Index	N/A
Transparency	Reflect
Shape	Irregular
WATER	
Refractive Index	1.33
Options:	
Filter	Enabled
Analysis Gain	Default(2)
Analysis Mode	BLUEWAVE
Perspective	
Progression	Standard
Distribution	Volume
Upper Edge(um)	2000
Lower Edge(um)	0.0107
Residuals	Disabled

Security

General	
Secure	NO
Original Data	Original
Original Record	432
Parent Record	N/A
Acquired	
Date	10/22/2015
Time	11:16 AM

Calculate Status
DB-Meas : : Original :

Sample System(Wet)

Number of Rinses	5
Flow Rate (%)	75%
Deaeration Cycles	0

Figure B.1: HDH-titanium PSD sample 1

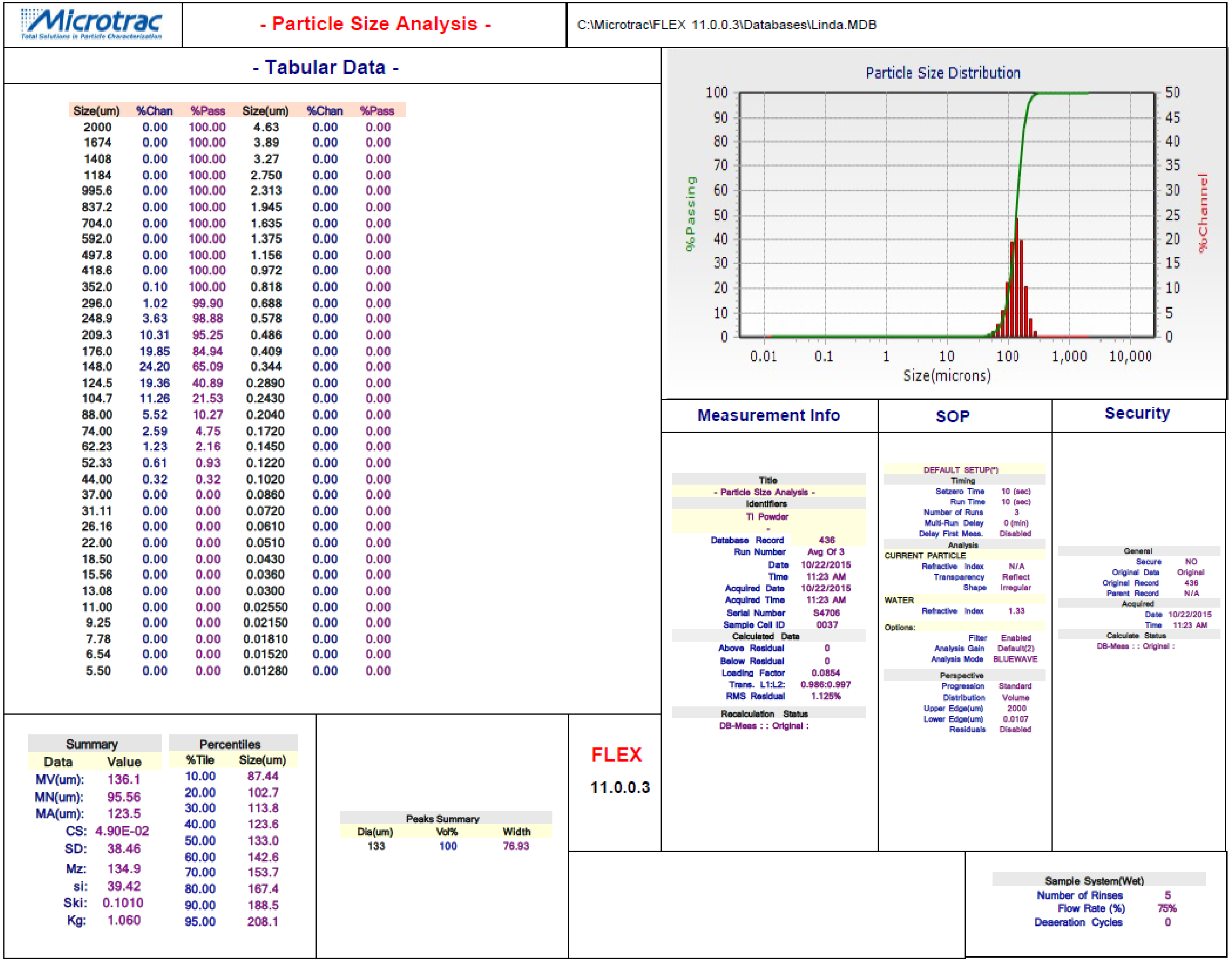

- Particle Size Analysis -

C:\Microtrac\FLEX 11.0.0.3\Databases\Linda.MDB

- Tabular Data -

Size(um)	%Chan	%Pass	Size(um)	%Chan	%Pass
2000	0.00	100.00	4.63	0.00	0.00
1674	0.00	100.00	3.89	0.00	0.00
1408	0.00	100.00	3.27	0.00	0.00
1184	0.00	100.00	2.750	0.00	0.00
995.6	0.00	100.00	2.313	0.00	0.00
837.2	0.00	100.00	1.945	0.00	0.00
704.0	0.00	100.00	1.635	0.00	0.00
592.0	0.00	100.00	1.375	0.00	0.00
497.8	0.00	100.00	1.156	0.00	0.00
418.6	0.00	100.00	0.972	0.00	0.00
352.0	0.10	100.00	0.818	0.00	0.00
296.0	1.02	99.90	0.688	0.00	0.00
248.9	3.63	98.88	0.578	0.00	0.00
209.3	10.31	95.25	0.486	0.00	0.00
176.0	19.85	84.94	0.409	0.00	0.00
148.0	24.20	65.09	0.344	0.00	0.00
124.5	19.36	40.89	0.2890	0.00	0.00
104.7	11.26	21.53	0.2430	0.00	0.00
88.00	5.52	10.27	0.2040	0.00	0.00
74.00	2.59	4.75	0.1720	0.00	0.00
62.23	1.23	2.16	0.1450	0.00	0.00
52.33	0.61	0.93	0.1220	0.00	0.00
44.00	0.32	0.32	0.1020	0.00	0.00
37.00	0.00	0.00	0.0860	0.00	0.00
31.11	0.00	0.00	0.0720	0.00	0.00
26.16	0.00	0.00	0.0610	0.00	0.00
22.00	0.00	0.00	0.0510	0.00	0.00
18.50	0.00	0.00	0.0430	0.00	0.00
15.56	0.00	0.00	0.0360	0.00	0.00
13.08	0.00	0.00	0.0300	0.00	0.00
11.00	0.00	0.00	0.02550	0.00	0.00
9.25	0.00	0.00	0.02150	0.00	0.00
7.78	0.00	0.00	0.01810	0.00	0.00
6.54	0.00	0.00	0.01520	0.00	0.00
5.50	0.00	0.00	0.01280	0.00	0.00

Measurement Info

Title	
- Particle Size Analysis -	
Identifiers	
Ti Powder	
-	
Database Record	436
Run Number	Avg Of 3
Date	10/22/2015
Time	11:23 AM
Acquired Date	10/22/2015
Acquired Time	11:23 AM
Serial Number	S4706
Sample Cell ID	0037
Calculated Data	
Above Residual	0
Below Residual	0
Loading Factor	0.0854
Trans. L1:L2:	0.986:0.997
RMS Residual	1.125%
Recalculation Status	
DB-Meas : : Original :	

SOP

DEFAULT SETUP(*)	
Timing	
Setzero Time	10 (sec)
Run Time	10 (sec)
Number of Runs	3
Multi-Run Delay	0 (min)
Delay First Meas.	Disabled
Analysis	
CURRENT PARTICLE	
Refractive Index	N/A
Transparency	Reflect
Shape	Irregular
WATER	
Refractive Index	1.33
Options:	
Filter	Enabled
Analysis Gain	Default(2)
Analysis Mode	BLUEWAVE
Perspective	
Progression	Standard
Distribution	Volume
Upper Edge(um)	2000
Lower Edge(um)	0.0107
Residuals	Disabled

Security

General	
Secure	NO
Original Data	Original
Original Record	436
Parent Record	N/A
Acquired	
Date	10/22/2015
Time	11:23 AM
Calculate Status	
DB-Meas : : Original :	

Summary		Percentiles	
Data	Value	%Tile	Size(um)
MV(um):	136.1	10.00	87.44
MN(um):	95.56	20.00	102.7
MA(um):	123.5	30.00	113.8
CS:	4.90E-02	40.00	123.6
SD:	38.46	50.00	133.0
Mz:	134.9	60.00	142.6
si:	39.42	70.00	153.7
Ski:	0.1010	80.00	167.4
Kg:	1.060	90.00	188.5
		95.00	208.1

Peaks Summary		
Dia(um)	Vol%	Width
133	100	76.93

Sample System(Wet)	
Number of Rinses	5
Flow Rate (%)	75%
Deaeration Cycles	0

Figure B.2: HDH-titanium PSD sample 2

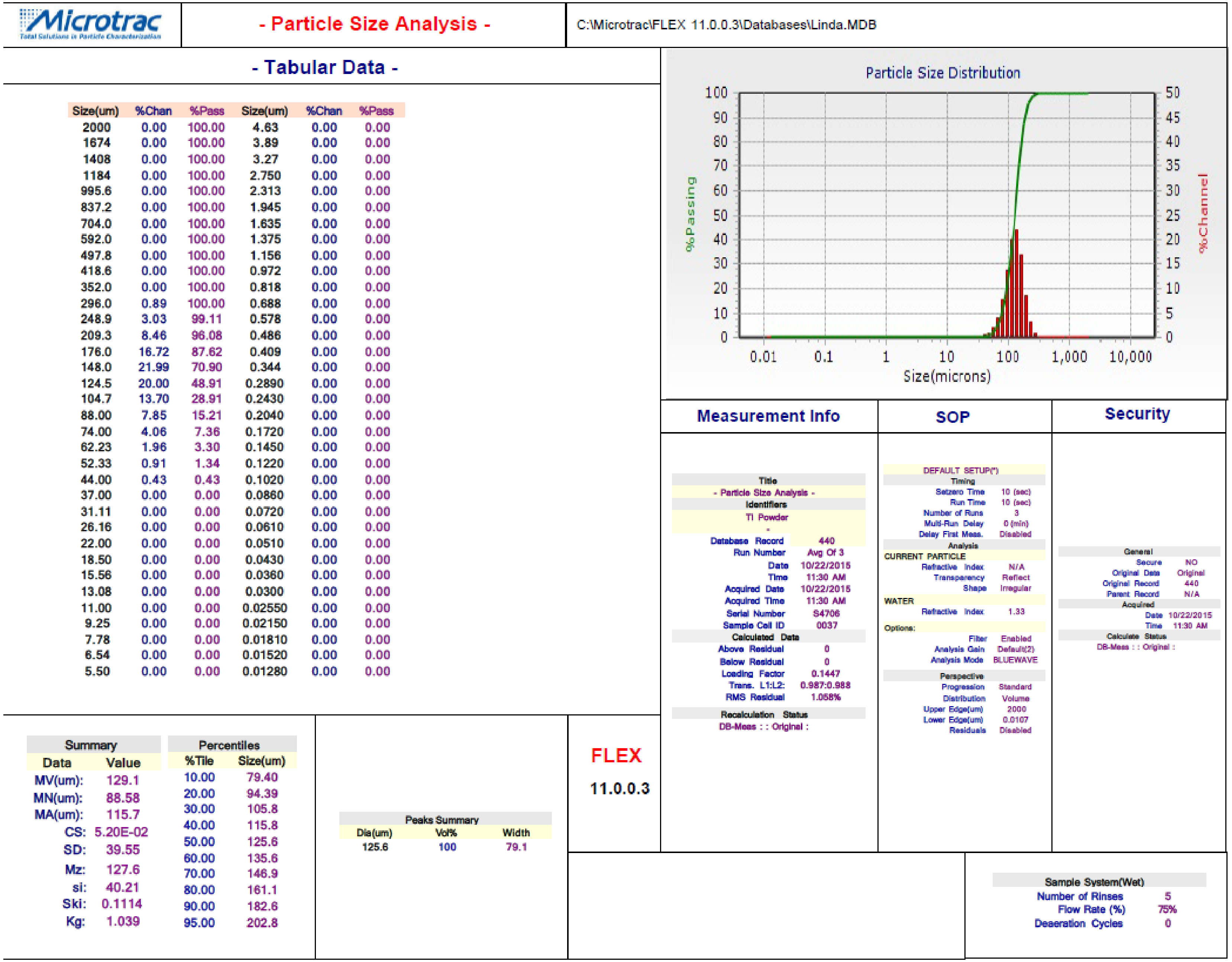

Microtrac Total Solutions in Particle Characterization

- Particle Size Analysis -

C:\Microtrac\FLEX 11.0.0.3\Databases\Linda.MDB

- Tabular Data -

Size(um)	%Chan	%Pass	Size(um)	%Chan	%Pass
2000	0.00	100.00	4.63	0.00	0.00
1674	0.00	100.00	3.89	0.00	0.00
1408	0.00	100.00	3.27	0.00	0.00
1184	0.00	100.00	2.750	0.00	0.00
995.6	0.00	100.00	2.313	0.00	0.00
837.2	0.00	100.00	1.945	0.00	0.00
704.0	0.00	100.00	1.635	0.00	0.00
592.0	0.00	100.00	1.375	0.00	0.00
497.8	0.00	100.00	1.156	0.00	0.00
418.6	0.00	100.00	0.972	0.00	0.00
352.0	0.00	100.00	0.818	0.00	0.00
296.0	0.89	100.00	0.688	0.00	0.00
248.9	3.03	99.11	0.578	0.00	0.00
209.3	8.46	96.08	0.486	0.00	0.00
176.0	16.72	87.62	0.409	0.00	0.00
148.0	21.99	70.90	0.344	0.00	0.00
124.5	20.00	48.91	0.2890	0.00	0.00
104.7	13.70	28.91	0.2430	0.00	0.00
88.00	7.85	15.21	0.2040	0.00	0.00
74.00	4.06	7.36	0.1720	0.00	0.00
62.23	1.96	3.30	0.1450	0.00	0.00
52.33	0.91	1.34	0.1220	0.00	0.00
44.00	0.43	0.43	0.1020	0.00	0.00
37.00	0.00	0.00	0.0860	0.00	0.00
31.11	0.00	0.00	0.0720	0.00	0.00
26.16	0.00	0.00	0.0610	0.00	0.00
22.00	0.00	0.00	0.0510	0.00	0.00
18.50	0.00	0.00	0.0430	0.00	0.00
15.56	0.00	0.00	0.0360	0.00	0.00
13.08	0.00	0.00	0.0300	0.00	0.00
11.00	0.00	0.00	0.02550	0.00	0.00
9.25	0.00	0.00	0.02150	0.00	0.00
7.78	0.00	0.00	0.01810	0.00	0.00
6.54	0.00	0.00	0.01520	0.00	0.00
5.50	0.00	0.00	0.01280	0.00	0.00

Measurement Info

Title	
- Particle Size Analysis -	
Identifiers	
TI Powder	
-	
Database Record	440
Run Number	Avg Of 3
Date	10/22/2015
Time	11:30 AM
Acquired Date	10/22/2015
Acquired Time	11:30 AM
Serial Number	S4706
Sample Cell ID	0037
Calculated Data	
Above Residual	0
Below Residual	0
Loading Factor	0.1447
Trans. L1:L2:	0.987:0.988
RMS Residual	1.058%
Recalculation Status	
DB-Meas : : Original :	

SOP

DEFAULT SETUP(*)	
Timing	
Setzero Time	10 (sec)
Run Time	10 (sec)
Number of Runs	3
Multi-Run Delay	0 (min)
Delay First Meas.	Disabled
Analysis	
CURRENT PARTICLE	
Refractive Index	N/A
Transparency	Reflect
Shape	Irregular
WATER	
Refractive Index	1.33
Options:	
Filter	Enabled
Analysis Gain	Default(2)
Analysis Mode	BLUEWAVE
Perspective	
Progression	Standard
Distribution	Volume
Upper Edge(um)	2000
Lower Edge(um)	0.0107
Residuals	Disabled

Security

General	
Secure	NO
Original Data	Original
Original Record	440
Parent Record	N/A
Acquired	
Date	10/22/2015
Time	11:30 AM
Calculate Status	
DB-Meas : : Original :	

Summary	
Data	Value
MV(um):	129.1
MN(um):	88.58
MA(um):	115.7
CS:	5.20E-02
SD:	39.55
Mz:	127.6
si:	40.21
Ski:	0.1114
Kg:	1.039

Percentiles	
%Tile	Size(um)
10.00	79.40
20.00	94.39
30.00	105.8
40.00	115.8
50.00	125.6
60.00	135.6
70.00	146.9
80.00	161.1
90.00	182.6
95.00	202.8

Peaks Summary		
Dia(um)	Vol%	Width
125.6	100	79.1

FLEX
11.0.0.3

Sample System(Wet)	
Number of Rinses	5
Flow Rate (%)	75%
Deaeration Cycles	0

Figure B.3: HDH-titanium PSD sample 3

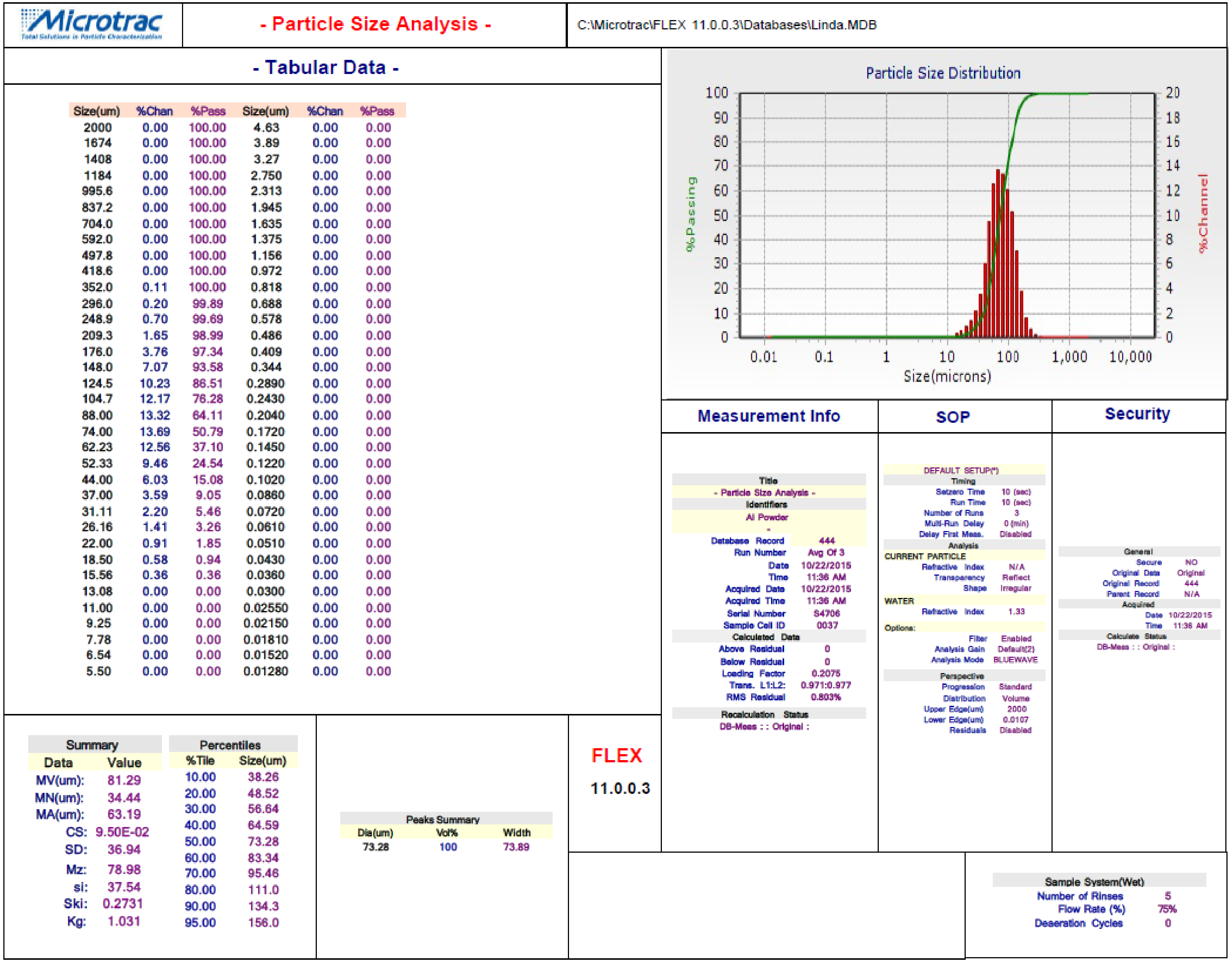

Microtrac
Total Solutions in Particle Characterization

- Particle Size Analysis -

C:\Microtrac\FLEX 11.0.0.3\Databases\Linda.MDB

- Tabular Data -

Size(um)	%Chan	%Pass	Size(um)	%Chan	%Pass
2000	0.00	100.00	4.63	0.00	0.00
1674	0.00	100.00	3.89	0.00	0.00
1408	0.00	100.00	3.27	0.00	0.00
1184	0.00	100.00	2.750	0.00	0.00
995.6	0.00	100.00	2.313	0.00	0.00
837.2	0.00	100.00	1.945	0.00	0.00
704.0	0.00	100.00	1.635	0.00	0.00
592.0	0.00	100.00	1.375	0.00	0.00
497.8	0.00	100.00	1.156	0.00	0.00
418.6	0.00	100.00	0.972	0.00	0.00
352.0	0.11	100.00	0.818	0.00	0.00
296.0	0.20	99.89	0.688	0.00	0.00
248.9	0.70	99.69	0.578	0.00	0.00
209.3	1.65	98.99	0.486	0.00	0.00
176.0	3.76	97.34	0.409	0.00	0.00
148.0	7.07	93.58	0.344	0.00	0.00
124.5	10.23	86.51	0.2890	0.00	0.00
104.7	12.17	76.28	0.2430	0.00	0.00
88.00	13.32	64.11	0.2040	0.00	0.00
74.00	13.69	50.79	0.1720	0.00	0.00
62.23	12.56	37.10	0.1450	0.00	0.00
52.33	9.46	24.54	0.1220	0.00	0.00
44.00	6.03	15.08	0.1020	0.00	0.00
37.00	3.59	9.05	0.0860	0.00	0.00
31.11	2.20	5.46	0.0720	0.00	0.00
26.16	1.41	3.26	0.0610	0.00	0.00
22.00	0.91	1.85	0.0510	0.00	0.00
18.50	0.58	0.94	0.0430	0.00	0.00
15.56	0.36	0.36	0.0360	0.00	0.00
13.08	0.00	0.00	0.0300	0.00	0.00
11.00	0.00	0.00	0.02550	0.00	0.00
9.25	0.00	0.00	0.02150	0.00	0.00
7.78	0.00	0.00	0.01810	0.00	0.00
6.54	0.00	0.00	0.01520	0.00	0.00
5.50	0.00	0.00	0.01280	0.00	0.00

Summary

Data	Value
MV(um):	81.29
MN(um):	34.44
MA(um):	63.19
CS:	9.50E-02
SD:	36.94
Mz:	78.98
si:	37.54
Ski:	0.2731
Kg:	1.031

Percentiles

%Tile	Size(um)
10.00	38.26
20.00	48.52
30.00	56.64
40.00	64.59
50.00	73.28
60.00	83.34
70.00	95.46
80.00	111.0
90.00	134.3
95.00	156.0

Peaks Summary

Dia(um)	Vol%	Width
73.28	100	73.89

FLEX
11.0.0.3

Measurement Info

Title
- Particle Size Analysis -
Identifiers
Al Powder
-

Database Record	444
Run Number	Avg Of 3
Date	10/22/2015
Time	11:36 AM
Acquired Date	10/22/2015
Acquired Time	11:36 AM
Serial Number	S4706
Sample Cell ID	0037
Calculated Data	
Above Residual	0
Below Residual	0
Loading Factor	0.2075
Trans. L1:L2:	0.971:0.977
RMS Residual	0.803%

Recalculation Status
DB-Meas : : Original :

SOP

DEFAULT SETUP(*)
Timing

Setzero Time	10 (sec)
Run Time	10 (sec)
Number of Runs	3
Multi-Run Delay	0 (min)
Delay First Meas.	Disabled
Analysis	
CURRENT PARTICLE	
Refractive Index	N/A
Transparency	Reflect
Shape	Irregular
WATER	
Refractive Index	1.33
Options:	
Filter	Enabled
Analysis Gain	Default(2)
Analysis Mode	BLUEWAVE
Perspective	
Progression	Standard
Distribution	Volume
Upper Edge(um)	2000
Lower Edge(um)	0.0107
Residuals	Disabled

Security

General

Secure	NO
Original Data	Original
Original Record	444
Parent Record	N/A
Acquired	
Date	10/22/2015
Time	11:36 AM

Calculate Status
DB-Meas : : Original :

Sample System(Wet)

Number of Rinses	5
Flow Rate (%)	75%
Deaeration Cycles	0

Figure B.4: Aluminium powder PSD sample 1

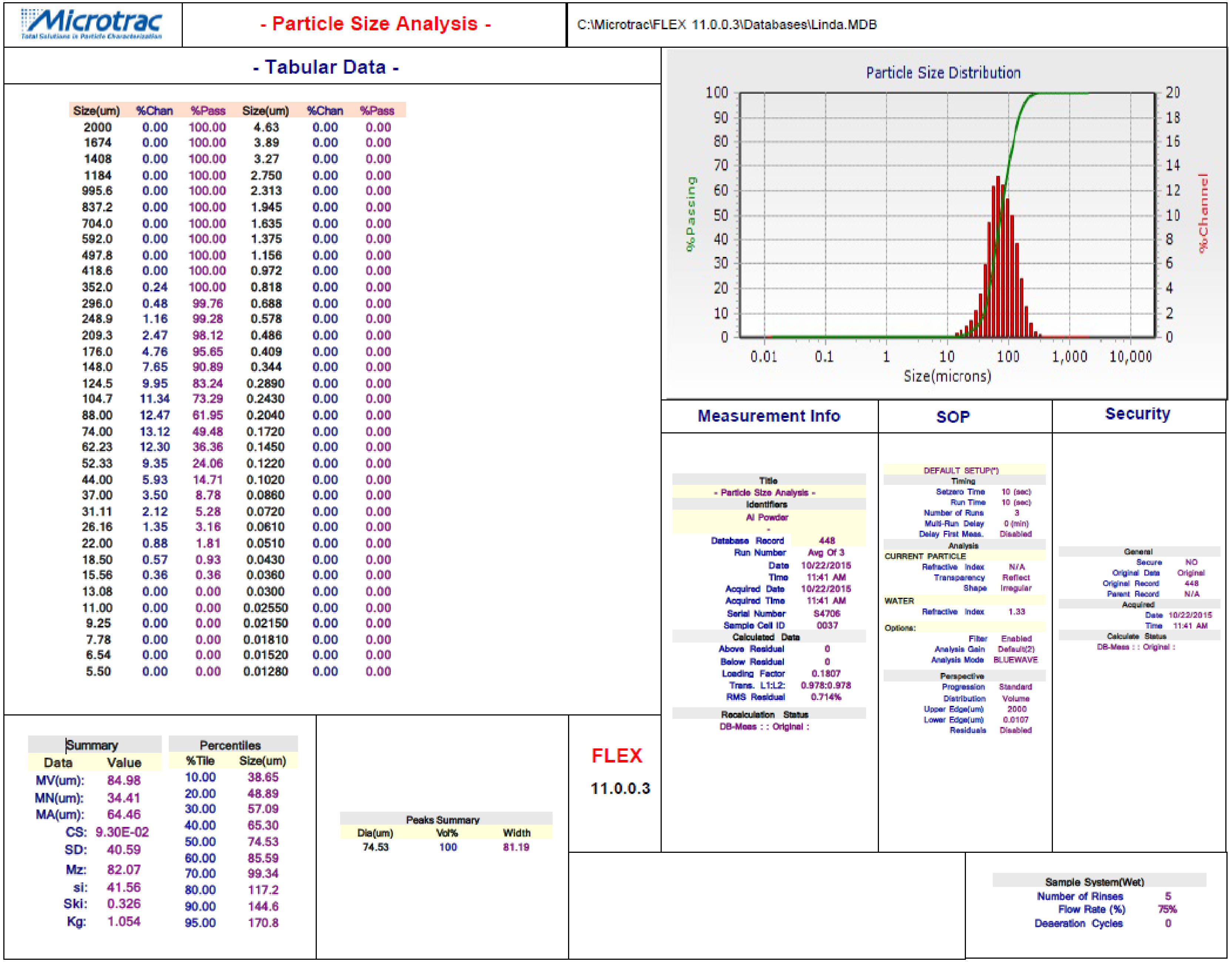

- Particle Size Analysis -

C:\Microtrac\FLEX 11.0.0.3\Databases\Linda.MDB

- Tabular Data -

Size(um)	%Chan	%Pass	Size(um)	%Chan	%Pass
2000	0.00	100.00	4.63	0.00	0.00
1674	0.00	100.00	3.89	0.00	0.00
1408	0.00	100.00	3.27	0.00	0.00
1184	0.00	100.00	2.750	0.00	0.00
995.6	0.00	100.00	2.313	0.00	0.00
837.2	0.00	100.00	1.945	0.00	0.00
704.0	0.00	100.00	1.635	0.00	0.00
592.0	0.00	100.00	1.375	0.00	0.00
497.8	0.00	100.00	1.156	0.00	0.00
418.6	0.00	100.00	0.972	0.00	0.00
352.0	0.24	100.00	0.818	0.00	0.00
296.0	0.48	99.76	0.688	0.00	0.00
248.9	1.16	99.28	0.578	0.00	0.00
209.3	2.47	98.12	0.486	0.00	0.00
176.0	4.76	95.65	0.409	0.00	0.00
148.0	7.65	90.89	0.344	0.00	0.00
124.5	9.95	83.24	0.2890	0.00	0.00
104.7	11.34	73.29	0.2430	0.00	0.00
88.00	12.47	61.95	0.2040	0.00	0.00
74.00	13.12	49.48	0.1720	0.00	0.00
62.23	12.30	36.36	0.1450	0.00	0.00
52.33	9.35	24.06	0.1220	0.00	0.00
44.00	5.93	14.71	0.1020	0.00	0.00
37.00	3.50	8.78	0.0860	0.00	0.00
31.11	2.12	5.28	0.0720	0.00	0.00
26.16	1.35	3.16	0.0610	0.00	0.00
22.00	0.88	1.81	0.0510	0.00	0.00
18.50	0.57	0.93	0.0430	0.00	0.00
15.56	0.36	0.36	0.0360	0.00	0.00
13.08	0.00	0.00	0.0300	0.00	0.00
11.00	0.00	0.00	0.02550	0.00	0.00
9.25	0.00	0.00	0.02150	0.00	0.00
7.78	0.00	0.00	0.01810	0.00	0.00
6.54	0.00	0.00	0.01520	0.00	0.00
5.50	0.00	0.00	0.01280	0.00	0.00

Measurement Info

Title	
- Particle Size Analysis -	
Identifiers	
Al Powder	
-	
Database Record	448
Run Number	Avg Of 3
Date	10/22/2015
Time	11:41 AM
Acquired Date	10/22/2015
Acquired Time	11:41 AM
Serial Number	S4706
Sample Cell ID	0037
Calculated Data	
Above Residual	0
Below Residual	0
Loading Factor	0.1807
Trans. L1:L2:	0.978:0.978
RMS Residual	0.714%
Recalculation Status	
DB-Meas : : Original :	

SOP

DEFAULT SETUP(*)	
Timing	
Setzero Time	10 (sec)
Run Time	10 (sec)
Number of Runs	3
Multi-Run Delay	0 (min)
Delay First Meas.	Disabled
Analysis	
CURRENT PARTICLE	
Refractive Index	N/A
Transparency	Reflect
Shape	Irregular
WATER	
Refractive Index	1.33
Options:	
Filter	Enabled
Analysis Gain	Default(2)
Analysis Mode	BLUEWAVE
Perspective	
Progression	Standard
Distribution	Volume
Upper Edge(um)	2000
Lower Edge(um)	0.0107
Residuals	Disabled

Security

General	
Secure	NO
Original Data	Original
Original Record	448
Parent Record	N/A
Acquired	
Date	10/22/2015
Time	11:41 AM
Calculate Status	
DB-Meas : : Original :	

Summary

Data	Value
MV(um):	84.98
MN(um):	34.41
MA(um):	64.46
CS:	9.30E-02
SD:	40.59
Mz:	82.07
si:	41.56
Ski:	0.326
Kg:	1.054

Percentiles

%Tile	Size(um)
10.00	38.65
20.00	48.89
30.00	57.09
40.00	65.30
50.00	74.53
60.00	85.59
70.00	99.34
80.00	117.2
90.00	144.6
95.00	170.8

Peaks Summary

Dia(um)	Vol%	Width
74.53	100	81.19

FLEX
11.0.0.3

Sample System(Wet)

Number of Rinses	5
Flow Rate (%)	75%
Deaeration Cycles	0

Figure B.5 :Aluminium powder PSD sample 2

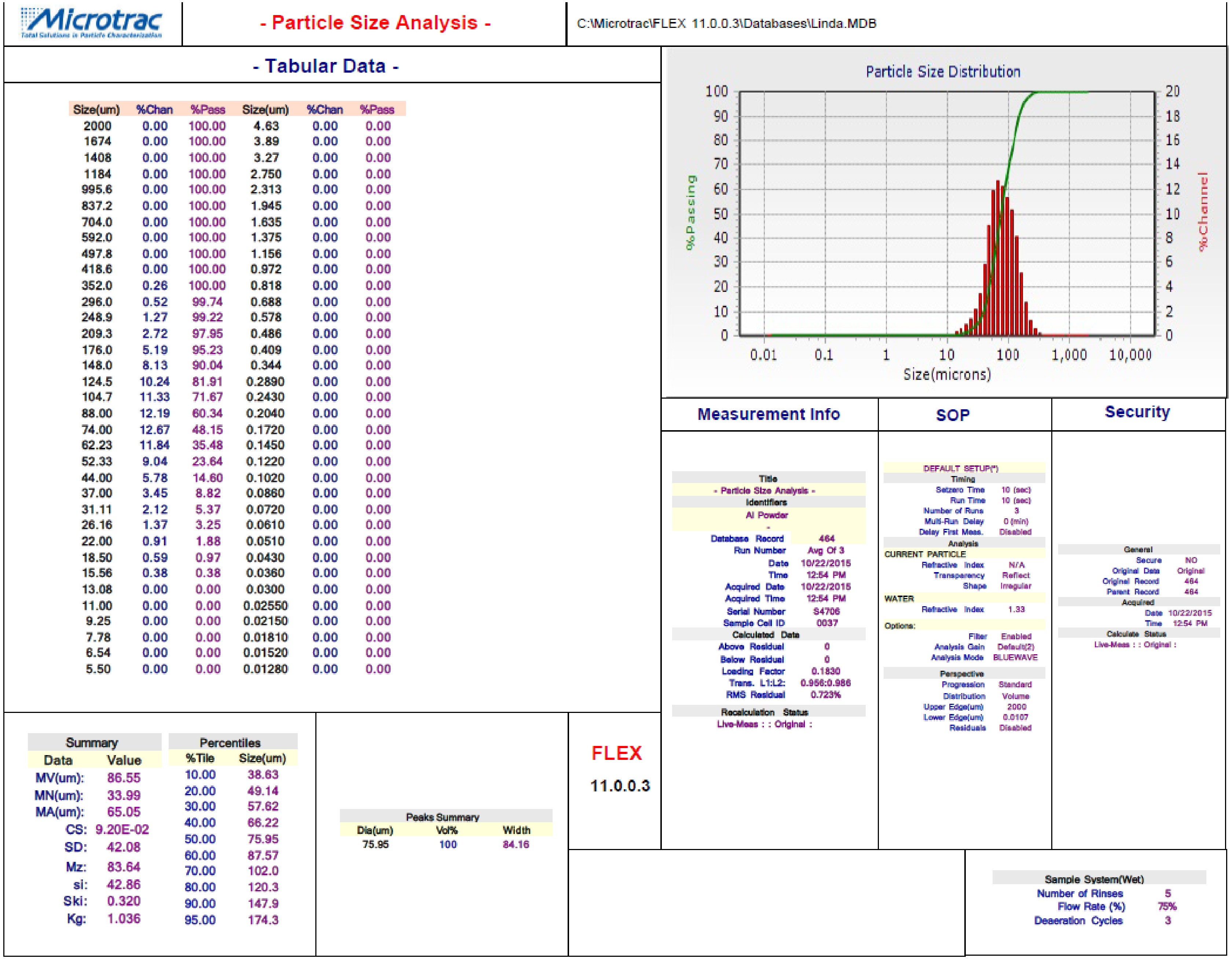

Microtrac

- Particle Size Analysis -

C:\Microtrac\FLEX 11.0.0.3\Databases\Linda.MDB

- Tabular Data -

Size(um)	%Chan	%Pass	Size(um)	%Chan	%Pass
2000	0.00	100.00	4.63	0.00	0.00
1674	0.00	100.00	3.89	0.00	0.00
1408	0.00	100.00	3.27	0.00	0.00
1184	0.00	100.00	2.750	0.00	0.00
995.6	0.00	100.00	2.313	0.00	0.00
837.2	0.00	100.00	1.945	0.00	0.00
704.0	0.00	100.00	1.635	0.00	0.00
592.0	0.00	100.00	1.375	0.00	0.00
497.8	0.00	100.00	1.156	0.00	0.00
418.6	0.00	100.00	0.972	0.00	0.00
352.0	0.26	100.00	0.818	0.00	0.00
296.0	0.52	99.74	0.688	0.00	0.00
248.9	1.27	99.22	0.578	0.00	0.00
209.3	2.72	97.95	0.486	0.00	0.00
176.0	5.19	95.23	0.409	0.00	0.00
148.0	8.13	90.04	0.344	0.00	0.00
124.5	10.24	81.91	0.2890	0.00	0.00
104.7	11.33	71.67	0.2430	0.00	0.00
88.00	12.19	60.34	0.2040	0.00	0.00
74.00	12.67	48.15	0.1720	0.00	0.00
62.23	11.84	35.48	0.1450	0.00	0.00
52.33	9.04	23.64	0.1220	0.00	0.00
44.00	5.78	14.60	0.1020	0.00	0.00
37.00	3.45	8.82	0.0860	0.00	0.00
31.11	2.12	5.37	0.0720	0.00	0.00
26.16	1.37	3.25	0.0610	0.00	0.00
22.00	0.91	1.88	0.0510	0.00	0.00
18.50	0.59	0.97	0.0430	0.00	0.00
15.56	0.38	0.38	0.0360	0.00	0.00
13.08	0.00	0.00	0.0300	0.00	0.00
11.00	0.00	0.00	0.02550	0.00	0.00
9.25	0.00	0.00	0.02150	0.00	0.00
7.78	0.00	0.00	0.01810	0.00	0.00
6.54	0.00	0.00	0.01520	0.00	0.00
5.50	0.00	0.00	0.01280	0.00	0.00

Summary

Data	Value
MV(um):	86.55
MN(um):	33.99
MA(um):	65.05
CS:	9.20E-02
SD:	42.08
Mz:	83.64
si:	42.86
Ski:	0.320
Kg:	1.036

Percentiles

%Tile	Size(um)
10.00	38.63
20.00	49.14
30.00	57.62
40.00	66.22
50.00	75.95
60.00	87.57
70.00	102.0
80.00	120.3
90.00	147.9
95.00	174.3

Peaks Summary

Dia(um)	Vol%	Width
75.95	100	84.16

FLEX

11.0.0.3

Measurement Info

Title	
- Particle Size Analysis -	
Identifiers	
Al Powder	
-	
Database Record	464
Run Number	Avg Of 3
Date	10/22/2015
Time	12:54 PM
Acquired Date	10/22/2015
Acquired Time	12:54 PM
Serial Number	S4706
Sample Cell ID	0037
Calculated Data	
Above Residual	0
Below Residual	0
Loading Factor	0.1830
Trans. L1:L2:	0.956:0.986
RMS Residual	0.723%
Recalculation Status	
Live-Meas : : Original :	

SOP

DEFAULT SETUP(*)	
Timing	
Setzero Time	10 (sec)
Run Time	10 (sec)
Number of Runs	3
Multi-Run Delay	0 (min)
Delay First Meas.	Disabled
Analysis	
CURRENT PARTICLE	
Refractive Index	N/A
Transparency	Reflect
Shape	Irregular
WATER	
Refractive Index	1.33
Options:	
Filter	Enabled
Analysis Gain	Default(2)
Analysis Mode	BLUEWAVE
Perspective	
Progression	Standard
Distribution	Volume
Upper Edge(um)	2000
Lower Edge(um)	0.0107
Residuals	Disabled

Security

General	
Secure	NO
Original Data	Original
Original Record	464
Parent Record	464
Acquired	
Date	10/22/2015
Time	12:54 PM
Calculate Status	
Live-Meas : : Original :	

Sample System(Wet)	
Number of Rinses	5
Flow Rate (%)	75%
Deaeration Cycles	3

Figure B.6: Aluminium powder PSD sample 3

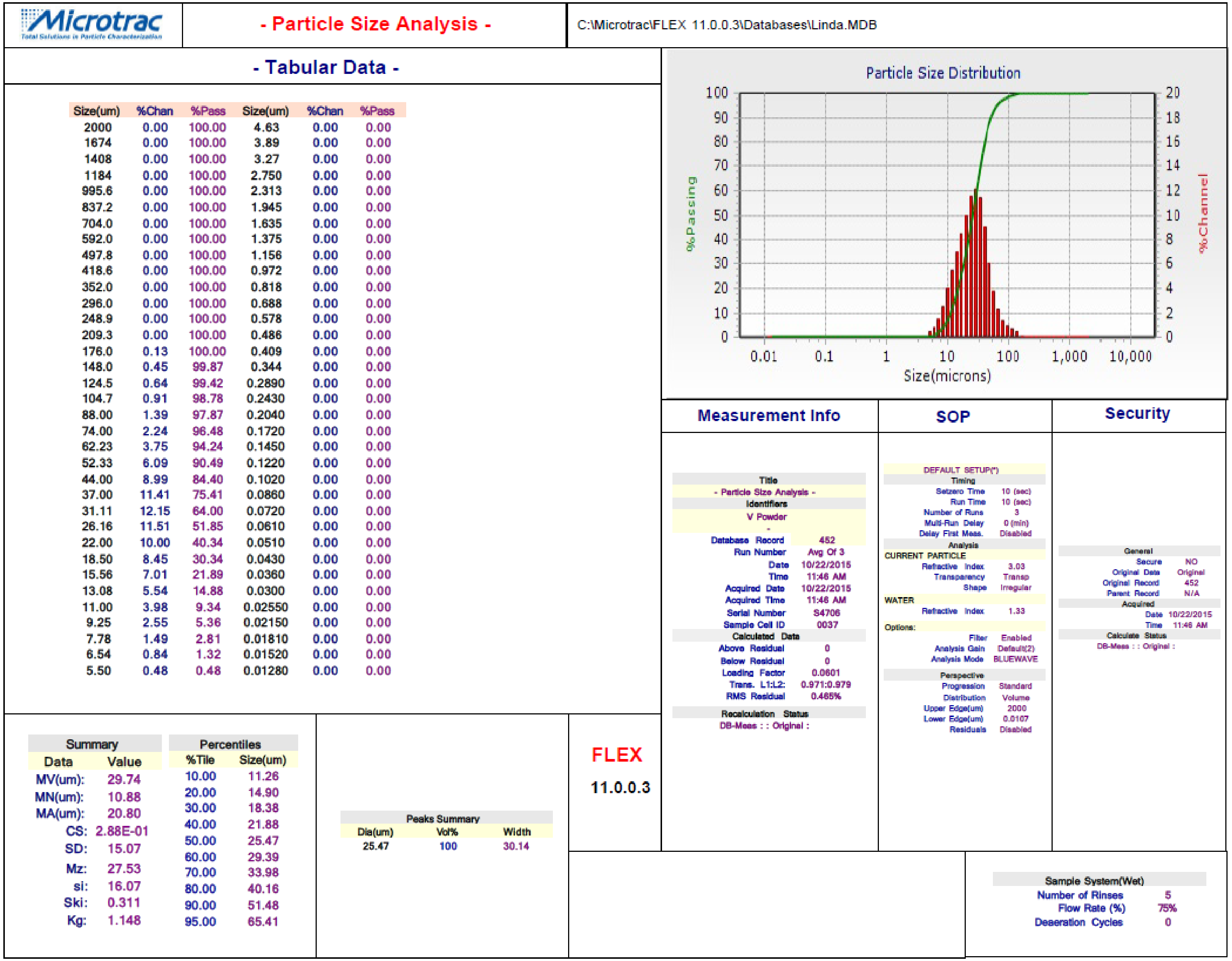

- Particle Size Analysis -

C:\Microtrac\FLEX 11.0.0.3\Databases\Linda.MDB

- Tabular Data -

Size(um)	%Chan	%Pass	Size(um)	%Chan	%Pass
2000	0.00	100.00	4.63	0.00	0.00
1674	0.00	100.00	3.89	0.00	0.00
1408	0.00	100.00	3.27	0.00	0.00
1184	0.00	100.00	2.750	0.00	0.00
995.6	0.00	100.00	2.313	0.00	0.00
837.2	0.00	100.00	1.945	0.00	0.00
704.0	0.00	100.00	1.635	0.00	0.00
592.0	0.00	100.00	1.375	0.00	0.00
497.8	0.00	100.00	1.156	0.00	0.00
418.6	0.00	100.00	0.972	0.00	0.00
352.0	0.00	100.00	0.818	0.00	0.00
296.0	0.00	100.00	0.688	0.00	0.00
248.9	0.00	100.00	0.578	0.00	0.00
209.3	0.00	100.00	0.486	0.00	0.00
176.0	0.13	100.00	0.409	0.00	0.00
148.0	0.45	99.87	0.344	0.00	0.00
124.5	0.64	99.42	0.2890	0.00	0.00
104.7	0.91	98.78	0.2430	0.00	0.00
88.00	1.39	97.87	0.2040	0.00	0.00
74.00	2.24	96.48	0.1720	0.00	0.00
62.23	3.75	94.24	0.1450	0.00	0.00
52.33	6.09	90.49	0.1220	0.00	0.00
44.00	8.99	84.40	0.1020	0.00	0.00
37.00	11.41	75.41	0.0860	0.00	0.00
31.11	12.15	64.00	0.0720	0.00	0.00
26.16	11.51	51.85	0.0610	0.00	0.00
22.00	10.00	40.34	0.0510	0.00	0.00
18.50	8.45	30.34	0.0430	0.00	0.00
15.56	7.01	21.89	0.0360	0.00	0.00
13.08	5.54	14.88	0.0300	0.00	0.00
11.00	3.98	9.34	0.02550	0.00	0.00
9.25	2.55	5.36	0.02150	0.00	0.00
7.78	1.49	2.81	0.01810	0.00	0.00
6.54	0.84	1.32	0.01520	0.00	0.00
5.50	0.48	0.48	0.01280	0.00	0.00

Summary	
Data	Value
MV(um):	29.74
MN(um):	10.88
MA(um):	20.80
CS:	2.88E-01
SD:	15.07
Mz:	27.53
si:	16.07
Ski:	0.311
Kg:	1.148

Percentiles	
%Tile	Size(um)
10.00	11.26
20.00	14.90
30.00	18.38
40.00	21.88
50.00	25.47
60.00	29.39
70.00	33.98
80.00	40.16
90.00	51.48
95.00	65.41

Peaks Summary		
Dia(um)	Vol%	Width
25.47	100	30.14

Measurement Info

Title	
- Particle Size Analysis -	
Identifiers	
V Powder	
-	
Database Record	452
Run Number	Avg Of 3
Date	10/22/2015
Time	11:46 AM
Acquired Date	10/22/2015
Acquired Time	11:46 AM
Serial Number	S4706
Sample Cell ID	0037
Calculated Data	
Above Residual	0
Below Residual	0
Loading Factor	0.0601
Trans. L1:L2:	0.971:0.979
RMS Residual	0.465%
Recalculation Status	
DB-Meas : : Original :	

SOP

DEFAULT SETUP(*)	
Timing	
Setzero Time	10 (sec)
Run Time	10 (sec)
Number of Runs	3
Multi-Run Delay	0 (min)
Delay First Meas.	Disabled
Analysis	
CURRENT PARTICLE	
Refractive Index	3.03
Transparency	Transp
Shape	Irregular
WATER	
Refractive Index	1.33
Options:	
Filter	Enabled
Analysis Gain	Default(2)
Analysis Mode	BLUEWAVE
Perspective	
Progression	Standard
Distribution	Volume
Upper Edge(um)	2000
Lower Edge(um)	0.0107
Residuals	Disabled

Security

General	
Secure	NO
Original Data	Original
Original Record	452
Parent Record	N/A
Acquired	
Date	10/22/2015
Time	11:46 AM
Calculate Status	
DB-Meas : : Original :	

Sample System(Wet)	
Number of Rinses	5
Flow Rate (%)	75%
Deaeration Cycles	0

Figure B.7: Vanadium powder PSD sample 1

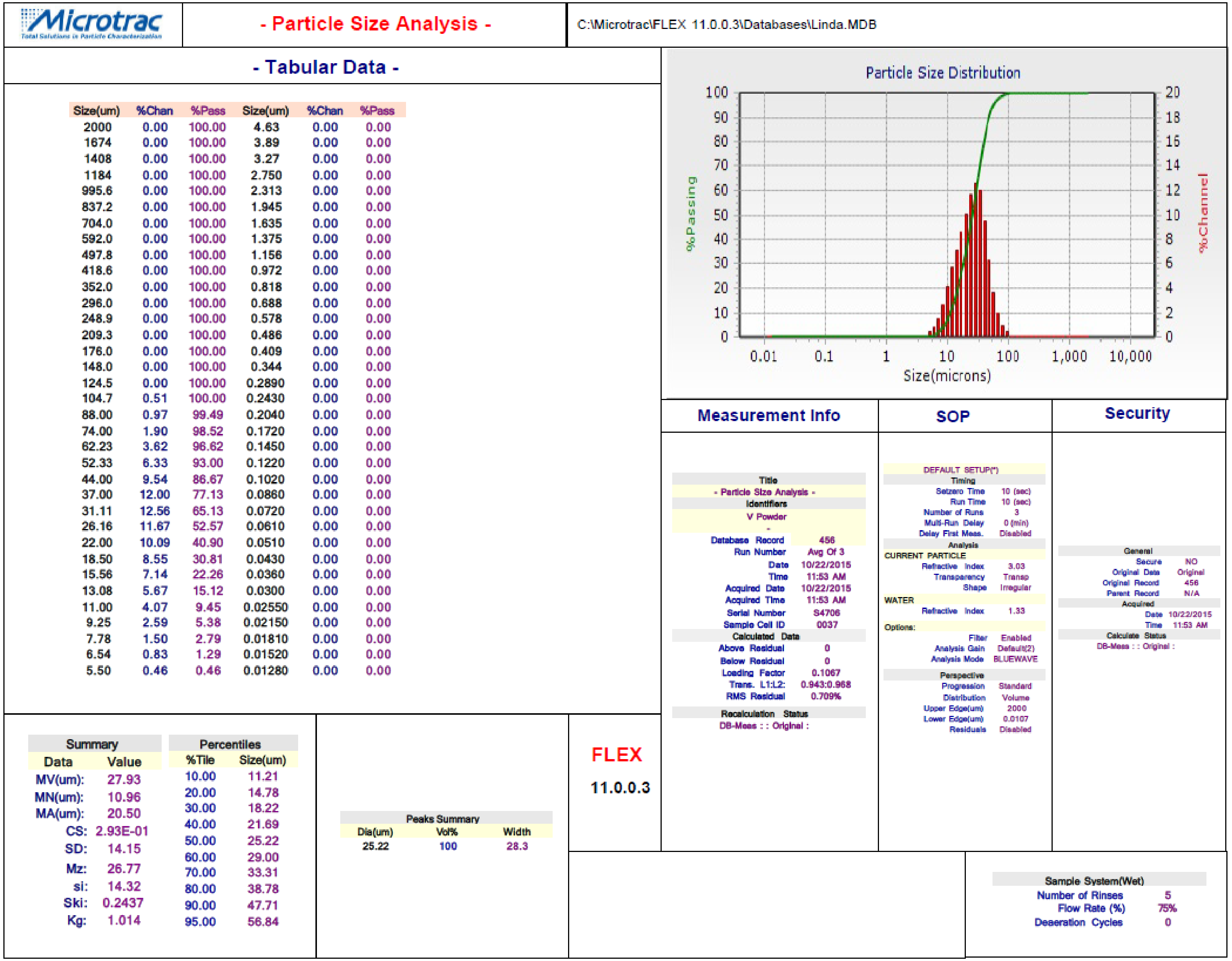

- Particle Size Analysis -

C:\Microtrac\FLEX 11.0.0.3\Databases\Linda.MDB

- Tabular Data -

Size(um)	%Chan	%Pass	Size(um)	%Chan	%Pass
2000	0.00	100.00	4.63	0.00	0.00
1674	0.00	100.00	3.89	0.00	0.00
1408	0.00	100.00	3.27	0.00	0.00
1184	0.00	100.00	2.750	0.00	0.00
995.6	0.00	100.00	2.313	0.00	0.00
837.2	0.00	100.00	1.945	0.00	0.00
704.0	0.00	100.00	1.635	0.00	0.00
592.0	0.00	100.00	1.375	0.00	0.00
497.8	0.00	100.00	1.156	0.00	0.00
418.6	0.00	100.00	0.972	0.00	0.00
352.0	0.00	100.00	0.818	0.00	0.00
296.0	0.00	100.00	0.688	0.00	0.00
248.9	0.00	100.00	0.578	0.00	0.00
209.3	0.00	100.00	0.486	0.00	0.00
176.0	0.00	100.00	0.409	0.00	0.00
148.0	0.00	100.00	0.344	0.00	0.00
124.5	0.00	100.00	0.2890	0.00	0.00
104.7	0.51	100.00	0.2430	0.00	0.00
88.00	0.97	99.49	0.2040	0.00	0.00
74.00	1.90	98.52	0.1720	0.00	0.00
62.23	3.62	96.62	0.1450	0.00	0.00
52.33	6.33	93.00	0.1220	0.00	0.00
44.00	9.54	86.67	0.1020	0.00	0.00
37.00	12.00	77.13	0.0860	0.00	0.00
31.11	12.56	65.13	0.0720	0.00	0.00
26.16	11.67	52.57	0.0610	0.00	0.00
22.00	10.09	40.90	0.0510	0.00	0.00
18.50	8.55	30.81	0.0430	0.00	0.00
15.56	7.14	22.26	0.0360	0.00	0.00
13.08	5.67	15.12	0.0300	0.00	0.00
11.00	4.07	9.45	0.02550	0.00	0.00
9.25	2.59	5.38	0.02150	0.00	0.00
7.78	1.50	2.79	0.01810	0.00	0.00
6.54	0.83	1.29	0.01520	0.00	0.00
5.50	0.46	0.46	0.01280	0.00	0.00

Measurement Info

Title	
- Particle Size Analysis -	
Identifiers	
V Powder	
-	
Database Record	456
Run Number	Avg Of 3
Date	10/22/2015
Time	11:53 AM
Acquired Date	10/22/2015
Acquired Time	11:53 AM
Serial Number	S4706
Sample Cell ID	0037
Calculated Data	
Above Residual	0
Below Residual	0
Loading Factor	0.1067
Trans. L1:L2:	0.943:0.968
RMS Residual	0.709%
Recalculation Status	
DB-Meas : : Original :	

SOP

DEFAULT SETUP(*)	
Timing	
Setzero Time	10 (sec)
Run Time	10 (sec)
Number of Runs	3
Multi-Run Delay	0 (min)
Delay First Meas.	Disabled
Analysis	
CURRENT PARTICLE	
Refractive Index	3.03
Transparency	Transp
Shape	Irregular
WATER	
Refractive Index	1.33
Options:	
Filter	Enabled
Analysis Gain	Default(2)
Analysis Mode	BLUEWAVE
Perspective	
Progression	Standard
Distribution	Volume
Upper Edge(um)	2000
Lower Edge(um)	0.0107
Residuals	Disabled

Security

General	
Secure	NO
Original Data	Original
Original Record	456
Parent Record	N/A
Acquired	
Date	10/22/2015
Time	11:53 AM
Calculate Status	
DB-Meas : : Original :	

Summary		Percentiles	
Data	Value	%Tile	Size(um)
MV(um):	27.93	10.00	11.21
MN(um):	10.96	20.00	14.78
MA(um):	20.50	30.00	18.22
CS:	2.93E-01	40.00	21.69
SD:	14.15	50.00	25.22
Mz:	26.77	60.00	29.00
si:	14.32	70.00	33.31
Ski:	0.2437	80.00	38.78
Kg:	1.014	90.00	47.71
		95.00	56.84

Peaks Summary

Dia(um)	Vol%	Width
25.22	100	28.3

FLEX

11.0.0.3

Sample System(Wet)	
Number of Rinses	5
Flow Rate (%)	75%
Deaeration Cycles	0

Figure B.8: Vanadium powder PSD sample 2

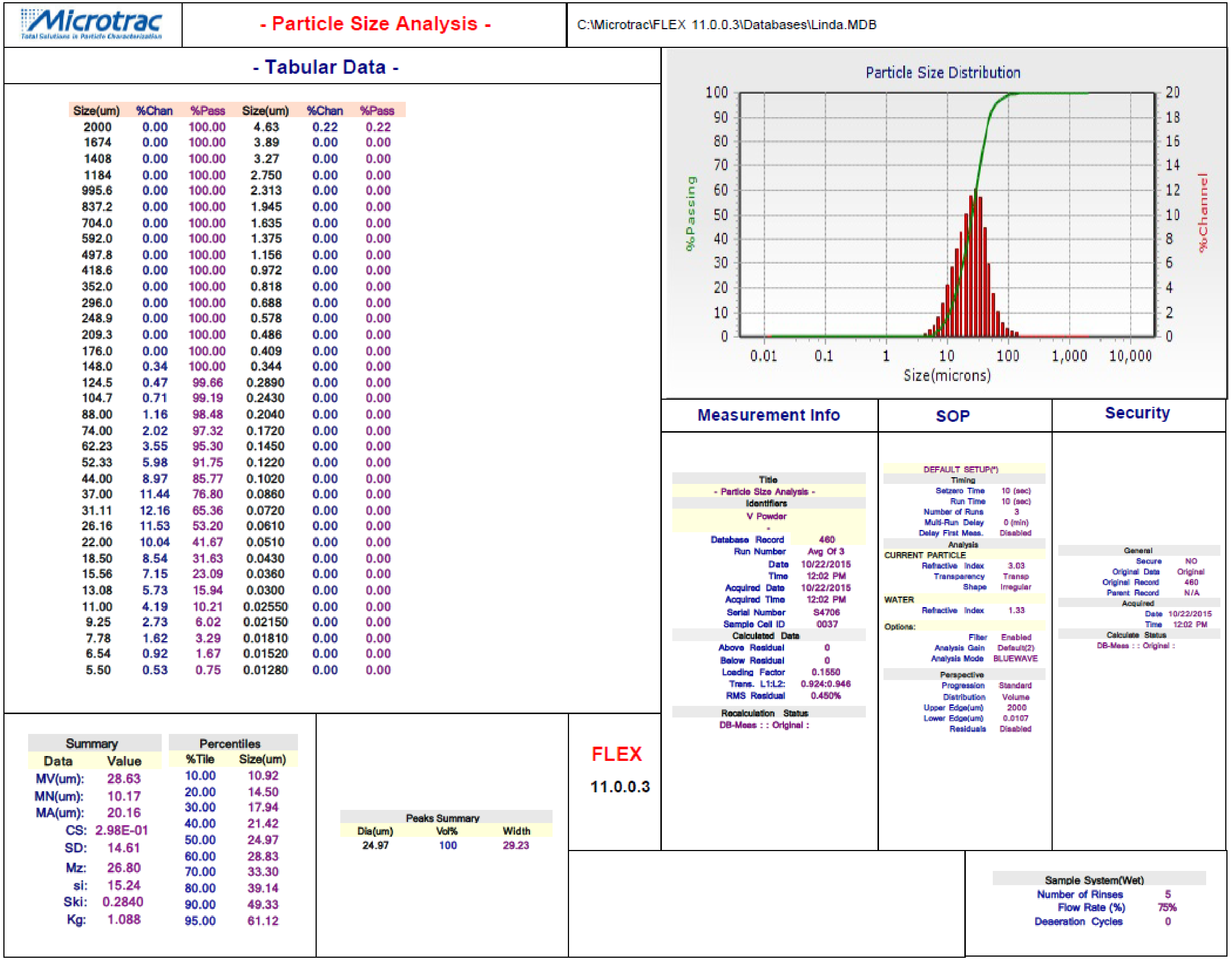

Microtrac Total Solutions in Particle Characterization

- Particle Size Analysis -

C:\Microtrac\FLEX 11.0.0.3\Databases\Linda.MDB

- Tabular Data -

Size(um)	%Chan	%Pass	Size(um)	%Chan	%Pass
2000	0.00	100.00	4.63	0.22	0.22
1674	0.00	100.00	3.89	0.00	0.00
1408	0.00	100.00	3.27	0.00	0.00
1184	0.00	100.00	2.750	0.00	0.00
995.6	0.00	100.00	2.313	0.00	0.00
837.2	0.00	100.00	1.945	0.00	0.00
704.0	0.00	100.00	1.635	0.00	0.00
592.0	0.00	100.00	1.375	0.00	0.00
497.8	0.00	100.00	1.156	0.00	0.00
418.6	0.00	100.00	0.972	0.00	0.00
352.0	0.00	100.00	0.818	0.00	0.00
296.0	0.00	100.00	0.688	0.00	0.00
248.9	0.00	100.00	0.578	0.00	0.00
209.3	0.00	100.00	0.486	0.00	0.00
176.0	0.00	100.00	0.409	0.00	0.00
148.0	0.34	100.00	0.344	0.00	0.00
124.5	0.47	99.66	0.2890	0.00	0.00
104.7	0.71	99.19	0.2430	0.00	0.00
88.00	1.16	98.48	0.2040	0.00	0.00
74.00	2.02	97.32	0.1720	0.00	0.00
62.23	3.55	95.30	0.1450	0.00	0.00
52.33	5.98	91.75	0.1220	0.00	0.00
44.00	8.97	85.77	0.1020	0.00	0.00
37.00	11.44	76.80	0.0860	0.00	0.00
31.11	12.16	65.36	0.0720	0.00	0.00
26.16	11.53	53.20	0.0610	0.00	0.00
22.00	10.04	41.67	0.0510	0.00	0.00
18.50	8.54	31.63	0.0430	0.00	0.00
15.56	7.15	23.09	0.0360	0.00	0.00
13.08	5.73	15.94	0.0300	0.00	0.00
11.00	4.19	10.21	0.02550	0.00	0.00
9.25	2.73	6.02	0.02150	0.00	0.00
7.78	1.62	3.29	0.01810	0.00	0.00
6.54	0.92	1.67	0.01520	0.00	0.00
5.50	0.53	0.75	0.01280	0.00	0.00

Summary	
Data	Value
MV(um):	28.63
MN(um):	10.17
MA(um):	20.16
CS:	2.98E-01
SD:	14.61
Mz:	26.80
si:	15.24
Ski:	0.2840
Kg:	1.088

Percentiles	
%Tile	Size(um)
10.00	10.92
20.00	14.50
30.00	17.94
40.00	21.42
50.00	24.97
60.00	28.83
70.00	33.30
80.00	39.14
90.00	49.33
95.00	61.12

Peaks Summary		
Dia(um)	Vol%	Width
24.97	100	29.23

FLEX

11.0.0.3

Measurement Info

Title	
- Particle Size Analysis -	
Identifiers	
V Powder	
-	
Database Record	460
Run Number	Avg Of 3
Date	10/22/2015
Time	12:02 PM
Acquired Date	10/22/2015
Acquired Time	12:02 PM
Serial Number	S4706
Sample Cell ID	0037
Calculated Data	
Above Residual	0
Below Residual	0
Loading Factor	0.1550
Trans. L1:L2:	0.924:0.946
RMS Residual	0.450%
Recalculation Status	
DB-Meas : : Original :	

SOP

DEFAULT SETUP(*)	
Timing	
Setzero Time	10 (sec)
Run Time	10 (sec)
Number of Runs	3
Multi-Run Delay	0 (min)
Delay First Meas.	Disabled
Analysis	
CURRENT PARTICLE	
Refractive Index	3.03
Transparency	Transp
Shape	Irregular
WATER	
Refractive Index	1.33
Options:	
Filter	Enabled
Analysis Gain	Default(2)
Analysis Mode	BLUEWAVE
Perspective	
Progression	Standard
Distribution	Volume
Upper Edge(um)	2000
Lower Edge(um)	0.0107
Residuals	Disabled

Security

General	
Secure	NO
Original Data	Original
Original Record	460
Parent Record	N/A
Acquired	
Date	10/22/2015
Time	12:02 PM
Calculate Status	
DB-Meas : : Original :	

Sample System(Wet)	
Number of Rinses	5
Flow Rate (%)	75%
Deaeration Cycles	0

Figure B.9: Vanadium powder PSD sample 3

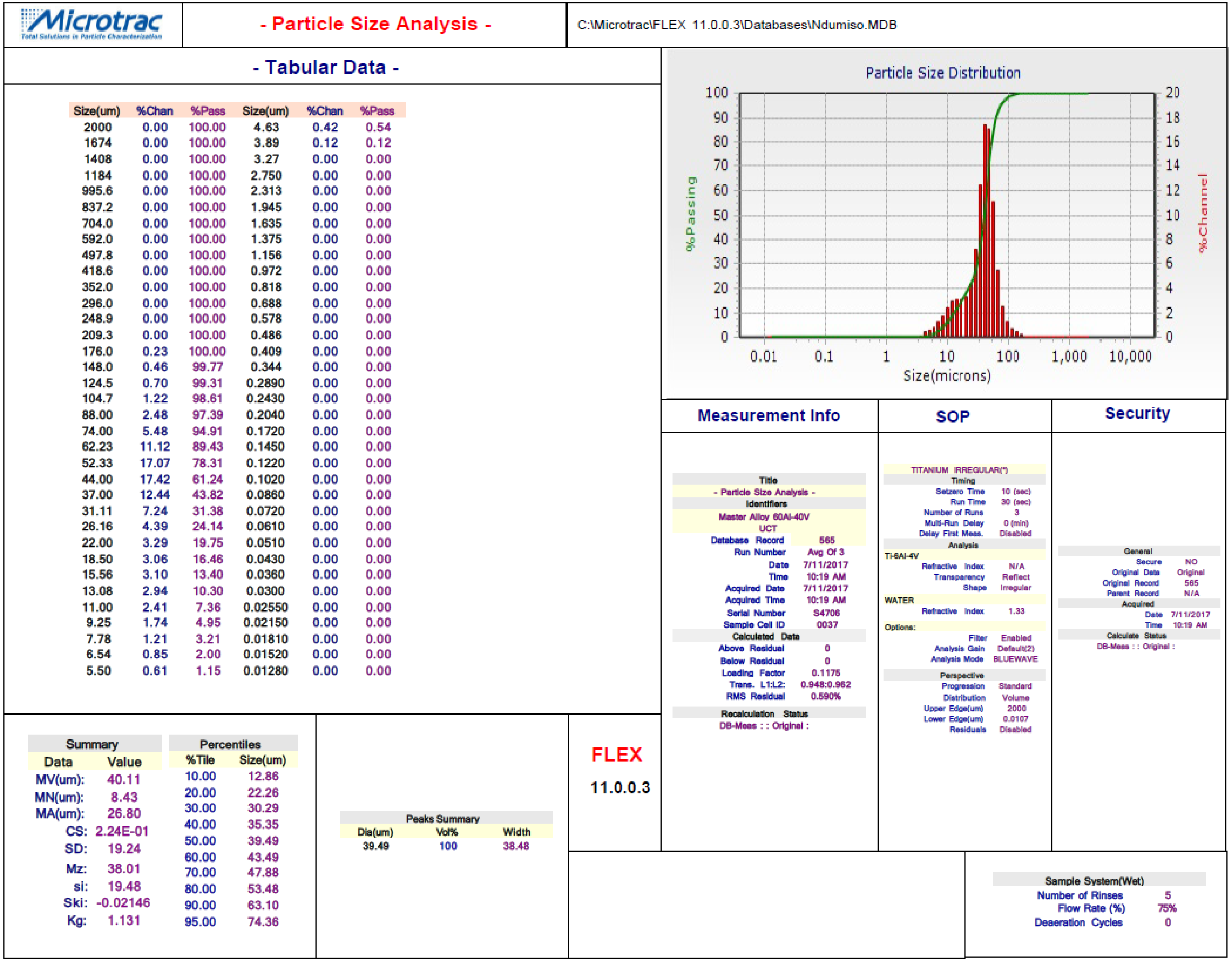

Microtrac

Total Solutions in Particle Characterization

- Particle Size Analysis -

C:\Microtrac\FLEX 11.0.0.3\Databases\Ndumiso.MDB

- Tabular Data -

Size(um)	%Chan	%Pass	Size(um)	%Chan	%Pass
2000	0.00	100.00	4.63	0.42	0.54
1674	0.00	100.00	3.89	0.12	0.12
1408	0.00	100.00	3.27	0.00	0.00
1184	0.00	100.00	2.750	0.00	0.00
995.6	0.00	100.00	2.313	0.00	0.00
837.2	0.00	100.00	1.945	0.00	0.00
704.0	0.00	100.00	1.635	0.00	0.00
592.0	0.00	100.00	1.375	0.00	0.00
497.8	0.00	100.00	1.156	0.00	0.00
418.6	0.00	100.00	0.972	0.00	0.00
352.0	0.00	100.00	0.818	0.00	0.00
296.0	0.00	100.00	0.688	0.00	0.00
248.9	0.00	100.00	0.578	0.00	0.00
209.3	0.00	100.00	0.486	0.00	0.00
176.0	0.23	100.00	0.409	0.00	0.00
148.0	0.46	99.77	0.344	0.00	0.00
124.5	0.70	99.31	0.2890	0.00	0.00
104.7	1.22	98.61	0.2430	0.00	0.00
88.00	2.48	97.39	0.2040	0.00	0.00
74.00	5.48	94.91	0.1720	0.00	0.00
62.23	11.12	89.43	0.1450	0.00	0.00
52.33	17.07	78.31	0.1220	0.00	0.00
44.00	17.42	61.24	0.1020	0.00	0.00
37.00	12.44	43.82	0.0860	0.00	0.00
31.11	7.24	31.38	0.0720	0.00	0.00
26.16	4.39	24.14	0.0610	0.00	0.00
22.00	3.29	19.75	0.0510	0.00	0.00
18.50	3.06	16.46	0.0430	0.00	0.00
15.56	3.10	13.40	0.0360	0.00	0.00
13.08	2.94	10.30	0.0300	0.00	0.00
11.00	2.41	7.36	0.02550	0.00	0.00
9.25	1.74	4.95	0.02150	0.00	0.00
7.78	1.21	3.21	0.01810	0.00	0.00
6.54	0.85	2.00	0.01520	0.00	0.00
5.50	0.61	1.15	0.01280	0.00	0.00

Particle Size Distribution

Summary	
Data	Value
MV(um):	40.11
MN(um):	8.43
MA(um):	26.80
CS:	2.24E-01
SD:	19.24
Mz:	38.01
si:	19.48
Ski:	-0.02146
Kg:	1.131

Percentiles	
%Tile	Size(um)
10.00	12.86
20.00	22.26
30.00	30.29
40.00	35.35
50.00	39.49
60.00	43.49
70.00	47.88
80.00	53.48
90.00	63.10
95.00	74.36

Peaks Summary		
Dia(um)	Vol%	Width
39.49	100	38.48

FLEX

11.0.0.3

Measurement Info

Title	
- Particle Size Analysis -	
Identifiers	
Master Alloy 60Al-40V	
UCT	
Database Record	565
Run Number	Avg Of 3
Date	7/11/2017
Time	10:19 AM
Acquired Date	7/11/2017
Acquired Time	10:19 AM
Serial Number	S4706
Sample Cell ID	0037
Calculated Data	
Above Residual	0
Below Residual	0
Loading Factor	0.1175
Trans. L1:L2:	0.948:0.962
RMS Residual	0.590%
Recalculation Status	
DB-Meas : : Original :	

SOP

TITANIUM IRREGULAR(*)	
Timing	
Setzero Time	10 (sec)
Run Time	30 (sec)
Number of Runs	3
Multi-Run Delay	0 (min)
Delay First Meas.	Disabled
Analysis	
Ti-6Al-4V	
Refractive Index	N/A
Transparency	Reflect
Shape	Irregular
WATER	
Refractive Index	1.33
Options:	
Filter	Enabled
Analysis Gain	Default(2)
Analysis Mode	BLUEWAVE
Perspective	
Progression	Standard
Distribution	Volume
Upper Edge(um)	2000
Lower Edge(um)	0.0107
Residuals	Disabled

Security

General	
Secure	NO
Original Data	Original
Original Record	565
Parent Record	N/A
Acquired	
Date	7/11/2017
Time	10:19 AM
Calculate Status	
DB-Meas : : Original :	

Sample System(Wet)	
Number of Rinses	5
Flow Rate (%)	75%
Deaeration Cycles	0

Figure B.10: 60Al-40V MA powder PSD sample 1

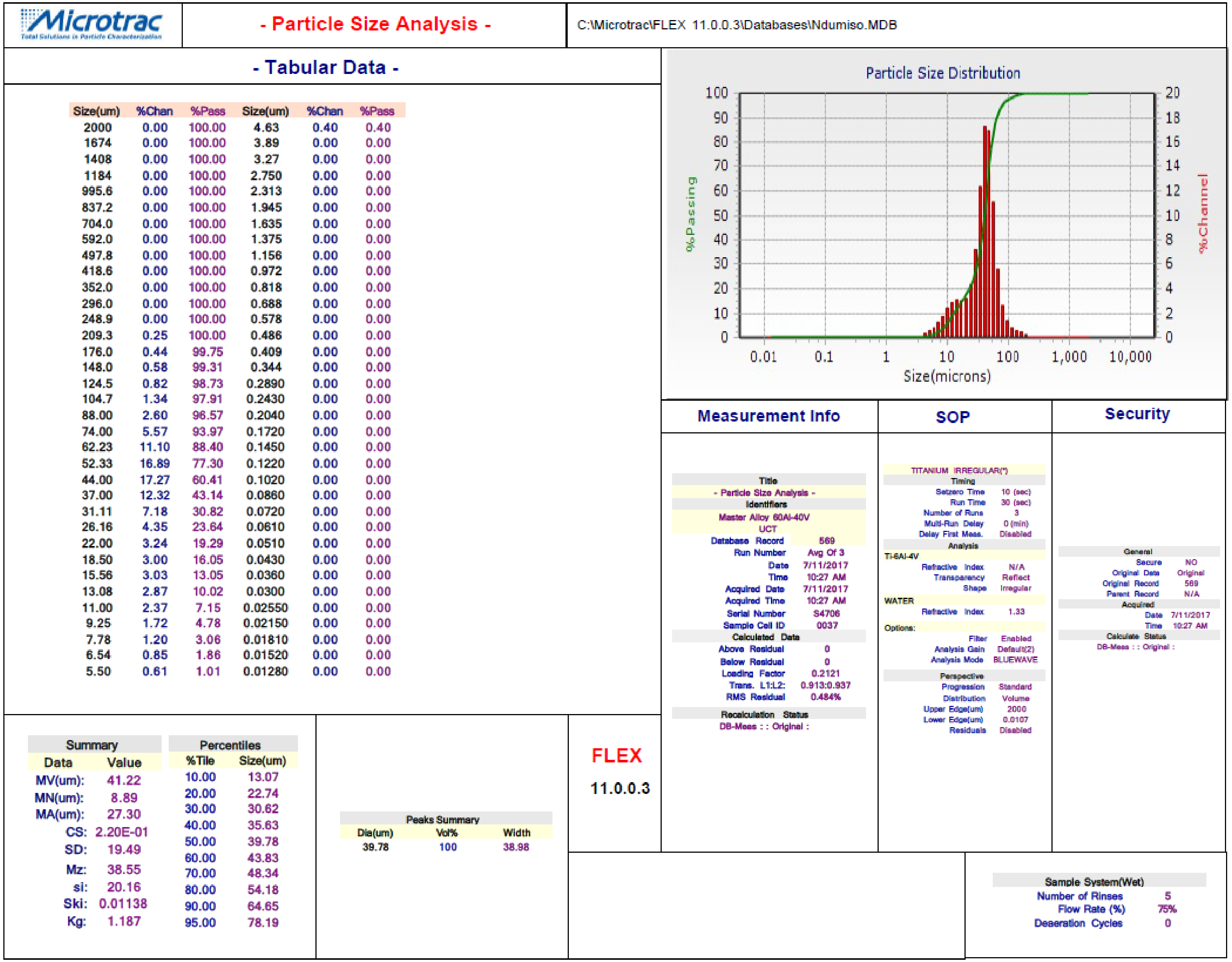

- Particle Size Analysis -

C:\Microtrac\FLEX 11.0.0.3\Databases\Ndumiso.MDB

- Tabular Data -

Size(um)	%Chan	%Pass	Size(um)	%Chan	%Pass
2000	0.00	100.00	4.63	0.40	0.40
1674	0.00	100.00	3.89	0.00	0.00
1408	0.00	100.00	3.27	0.00	0.00
1184	0.00	100.00	2.750	0.00	0.00
995.6	0.00	100.00	2.313	0.00	0.00
837.2	0.00	100.00	1.945	0.00	0.00
704.0	0.00	100.00	1.635	0.00	0.00
592.0	0.00	100.00	1.375	0.00	0.00
497.8	0.00	100.00	1.156	0.00	0.00
418.6	0.00	100.00	0.972	0.00	0.00
352.0	0.00	100.00	0.818	0.00	0.00
296.0	0.00	100.00	0.688	0.00	0.00
248.9	0.00	100.00	0.578	0.00	0.00
209.3	0.25	100.00	0.486	0.00	0.00
176.0	0.44	99.75	0.409	0.00	0.00
148.0	0.58	99.31	0.344	0.00	0.00
124.5	0.82	98.73	0.2890	0.00	0.00
104.7	1.34	97.91	0.2430	0.00	0.00
88.00	2.60	96.57	0.2040	0.00	0.00
74.00	5.57	93.97	0.1720	0.00	0.00
62.23	11.10	88.40	0.1450	0.00	0.00
52.33	16.89	77.30	0.1220	0.00	0.00
44.00	17.27	60.41	0.1020	0.00	0.00
37.00	12.32	43.14	0.0860	0.00	0.00
31.11	7.18	30.82	0.0720	0.00	0.00
26.16	4.35	23.64	0.0610	0.00	0.00
22.00	3.24	19.29	0.0510	0.00	0.00
18.50	3.00	16.05	0.0430	0.00	0.00
15.56	3.03	13.05	0.0360	0.00	0.00
13.08	2.87	10.02	0.0300	0.00	0.00
11.00	2.37	7.15	0.02550	0.00	0.00
9.25	1.72	4.78	0.02150	0.00	0.00
7.78	1.20	3.06	0.01810	0.00	0.00
6.54	0.85	1.86	0.01520	0.00	0.00
5.50	0.61	1.01	0.01280	0.00	0.00

Measurement Info

Title	
- Particle Size Analysis -	
Identifiers	
Master Alloy 60Al-40V	
UCT	
Database Record	569
Run Number	Avg Of 3
Date	7/11/2017
Time	10:27 AM
Acquired Date	7/11/2017
Acquired Time	10:27 AM
Serial Number	S4706
Sample Cell ID	0037
Calculated Data	
Above Residual	0
Below Residual	0
Loading Factor	0.2121
Trans. L1:L2:	0.913:0.937
RMS Residual	0.484%
Recalculation Status	
DB-Meas : : Original :	

SOP

TITANIUM IRREGULAR(*)	
Timing	
Setzero Time	10 (sec)
Run Time	30 (sec)
Number of Runs	3
Multi-Run Delay	0 (min)
Delay First Meas.	Disabled
Analysis	
Ti-6Al-4V	
Refractive Index	N/A
Transparency	Reflect
Shape	Irregular
WATER	
Refractive Index	1.33
Options:	
Filter	Enabled
Analysis Gain	Default(2)
Analysis Mode	BLUEWAVE
Perspective	
Progression	Standard
Distribution	Volume
Upper Edge(um)	2000
Lower Edge(um)	0.0107
Residuals	Disabled

Security

General	
Secure	NO
Original Data	Original
Original Record	569
Parent Record	N/A
Acquired	
Date	7/11/2017
Time	10:27 AM
Calculate Status	
DB-Meas : : Original :	

Summary	
Data	Value
MV(um):	41.22
MN(um):	8.89
MA(um):	27.30
CS:	2.20E-01
SD:	19.49
Mz:	38.55
si:	20.16
Ski:	0.01138
Kg:	1.187

Percentiles	
%Tile	Size(um)
10.00	13.07
20.00	22.74
30.00	30.62
40.00	35.63
50.00	39.78
60.00	43.83
70.00	48.34
80.00	54.18
90.00	64.65
95.00	78.19

Peaks Summary		
Dia(um)	Vol%	Width
39.78	100	38.98

FLEX
11.0.0.3

Sample System(Wet)	
Number of Rinses	5
Flow Rate (%)	75%
Deaeration Cycles	0

Figure B.11: 60Al-40V MA powder PSD sample 2

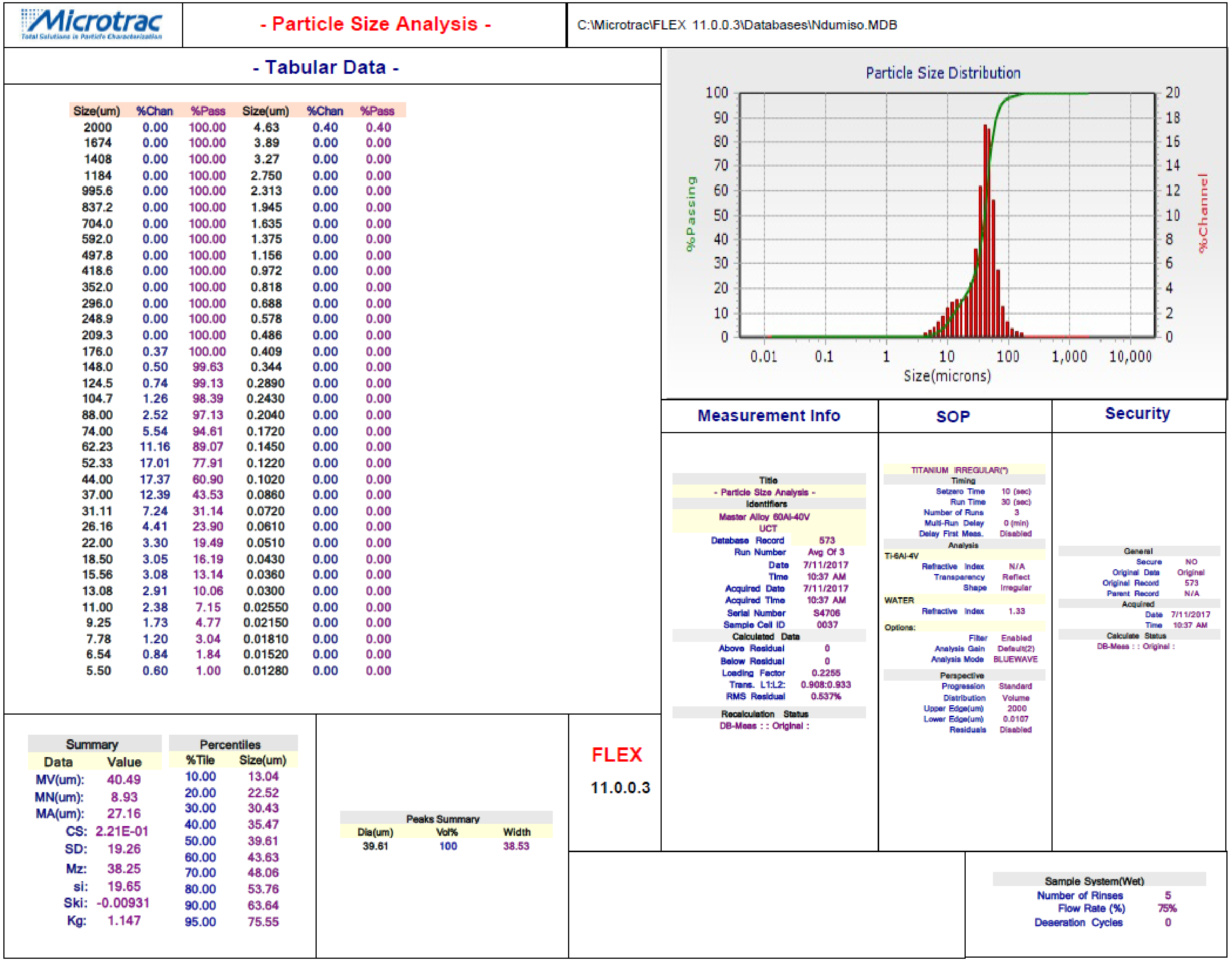

Microtrac
Total Solutions in Particle Characterization

- Particle Size Analysis -

C:\Microtrac\FLEX 11.0.0.3\Databases\Ndumiso.MDB

- Tabular Data -

Size(um)	%Chan	%Pass	Size(um)	%Chan	%Pass
2000	0.00	100.00	4.63	0.40	0.40
1674	0.00	100.00	3.89	0.00	0.00
1408	0.00	100.00	3.27	0.00	0.00
1184	0.00	100.00	2.750	0.00	0.00
995.6	0.00	100.00	2.313	0.00	0.00
837.2	0.00	100.00	1.945	0.00	0.00
704.0	0.00	100.00	1.635	0.00	0.00
592.0	0.00	100.00	1.375	0.00	0.00
497.8	0.00	100.00	1.156	0.00	0.00
418.6	0.00	100.00	0.972	0.00	0.00
352.0	0.00	100.00	0.818	0.00	0.00
296.0	0.00	100.00	0.688	0.00	0.00
248.9	0.00	100.00	0.578	0.00	0.00
209.3	0.00	100.00	0.486	0.00	0.00
176.0	0.37	100.00	0.409	0.00	0.00
148.0	0.50	99.63	0.344	0.00	0.00
124.5	0.74	99.13	0.2890	0.00	0.00
104.7	1.26	98.39	0.2430	0.00	0.00
88.00	2.52	97.13	0.2040	0.00	0.00
74.00	5.54	94.61	0.1720	0.00	0.00
62.23	11.16	89.07	0.1450	0.00	0.00
52.33	17.01	77.91	0.1220	0.00	0.00
44.00	17.37	60.90	0.1020	0.00	0.00
37.00	12.39	43.53	0.0860	0.00	0.00
31.11	7.24	31.14	0.0720	0.00	0.00
26.16	4.41	23.90	0.0610	0.00	0.00
22.00	3.30	19.49	0.0510	0.00	0.00
18.50	3.05	16.19	0.0430	0.00	0.00
15.56	3.08	13.14	0.0360	0.00	0.00
13.08	2.91	10.06	0.0300	0.00	0.00
11.00	2.38	7.15	0.02550	0.00	0.00
9.25	1.73	4.77	0.02150	0.00	0.00
7.78	1.20	3.04	0.01810	0.00	0.00
6.54	0.84	1.84	0.01520	0.00	0.00
5.50	0.60	1.00	0.01280	0.00	0.00

Summary

Data	Value
MV(um):	40.49
MN(um):	8.93
MA(um):	27.16
CS:	2.21E-01
SD:	19.26
Mz:	38.25
si:	19.65
Ski:	-0.00931
Kg:	1.147

Percentiles

%Tile	Size(um)
10.00	13.04
20.00	22.52
30.00	30.43
40.00	35.47
50.00	39.61
60.00	43.63
70.00	48.06
80.00	53.76
90.00	63.64
95.00	75.55

Peaks Summary

Dia(um)	Vol%	Width
39.61	100	38.53

FLEX
11.0.0.3

Measurement Info

Title	
- Particle Size Analysis -	
Identifiers	
Master Alloy 60Al-40V	
UCT	
Database Record	573
Run Number	Avg Of 3
Date	7/11/2017
Time	10:37 AM
Acquired Date	7/11/2017
Acquired Time	10:37 AM
Serial Number	S4706
Sample Cell ID	0037
Calculated Data	
Above Residual	0
Below Residual	0
Loading Factor	0.2255
Trans. L1:L2:	0.908:0.933
RMS Residual	0.537%
Recalculation Status	
DB-Meas : : Original :	

SOP

TITANIUM IRREGULAR(*)	
Timing	
Setzero Time	10 (sec)
Run Time	30 (sec)
Number of Runs	3
Multi-Run Delay	0 (min)
Delay First Meas.	Disabled
Analysis	
Ti-6Al-4V	
Refractive Index	N/A
Transparency	Reflect
Shape	Irregular
WATER	
Refractive Index	1.33
Options:	
Filter	Enabled
Analysis Gain	Default(2)
Analysis Mode	BLUEWAVE
Perspective	
Progression	Standard
Distribution	Volume
Upper Edge(um)	2000
Lower Edge(um)	0.0107
Residuals	Disabled

Security

General	
Secure	NO
Original Data	Original
Original Record	573
Parent Record	N/A
Acquired	
Date	7/11/2017
Time	10:37 AM
Calculate Status	
DB-Meas : : Original :	

Sample System(Wet)	
Number of Rinses	5
Flow Rate (%)	75%
Deaeration Cycles	0

Figure B.12: 60Al-40V MA powder PSD sample 3

Appendix C- Powder feed pressure data

Relevant roll press and powder information to evaluate feed pressure	Powder type		
	Lactose *	**B1**	**B2**
Bulk density, γ (g/cm^3)	0.55	1.94	2.02
Roll face width, RW (mm)	50	65	65
Roll diameter, D (mm)	130	265	265
Roll gap, S (mm)	1	1	1
Feed pressure, P_0 (MPa)	0.06	0.21	0.22

* Lactose data was acquired from Simon and Guigon (2000)[7]

Gravity feed pressure is predominantly dependent on the powder material bulk density[32]. Therefore feed pressure for B1 and B2 powder blends may be approximated using the following relationship where $\gamma \approx P_0$ and data acquired by Simon and Guigon (2000)[7] for lactose powders.

Appendix D- Load-extension plots for green strength

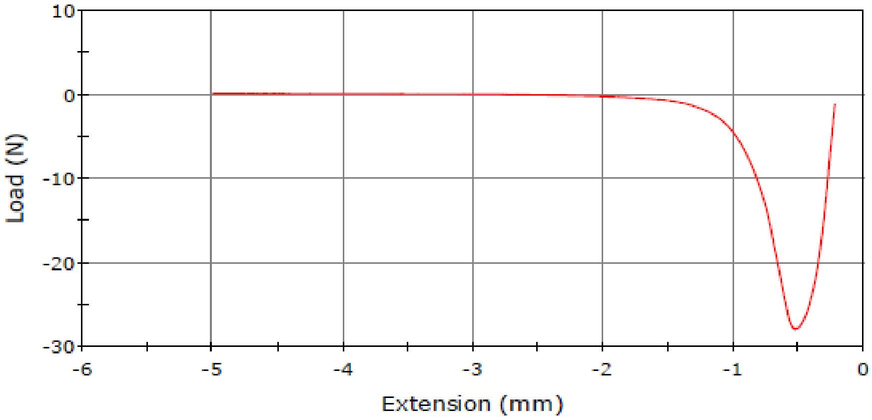

Figure D.1: Load-extension plot of three-point bend test for green strength of sample 1B1ai

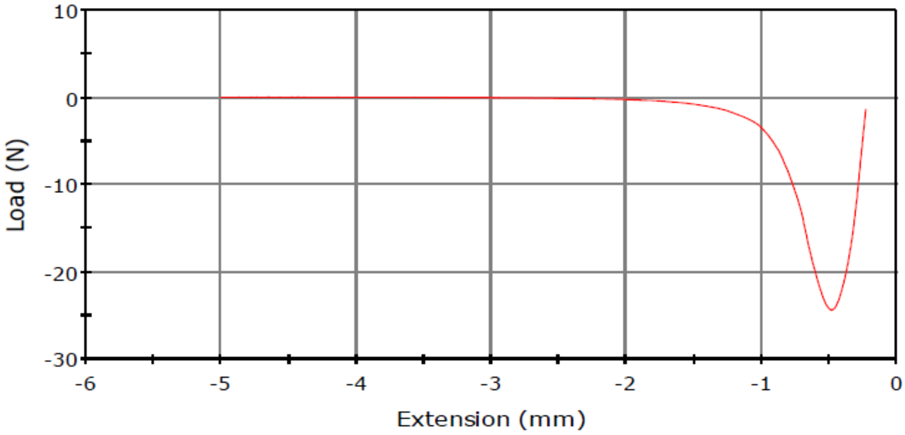

Figure D.2: Load-extension plot of three-point bend test for green strength of sample 1B1aii

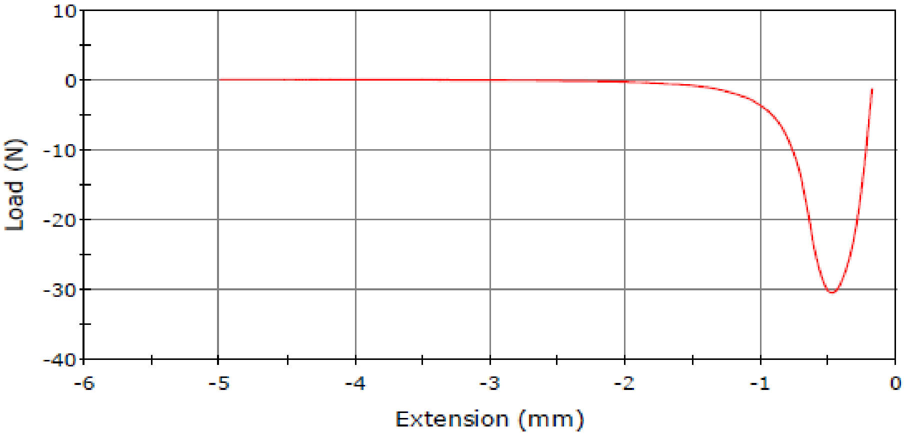

Figure D.3: Load-extension plot of three-point bend test for green strength of sample 1B1aiii

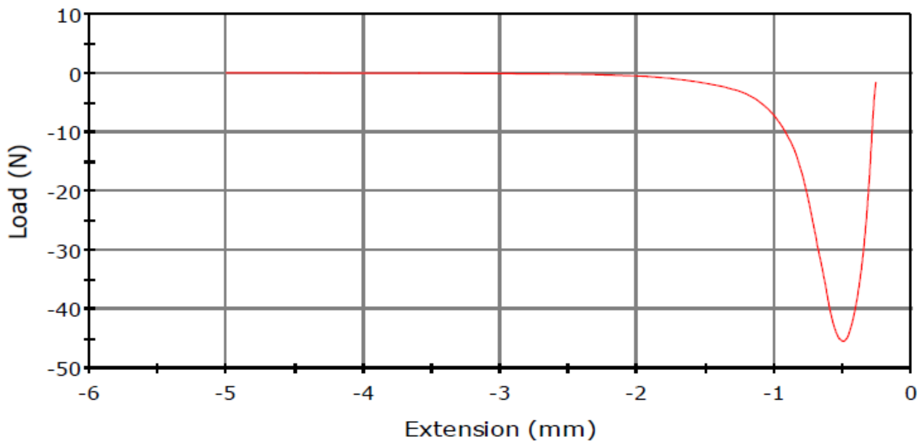

Figure D.4: Load-extension plot of three-point bend test for green strength of sample 1B1bi

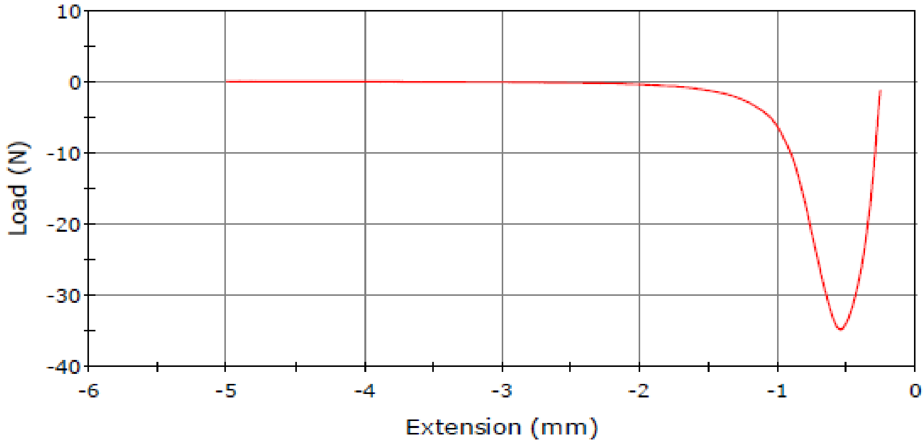

Figure D.5: Load-extension plot of three-point bend test for green strength of sample 1B1bii

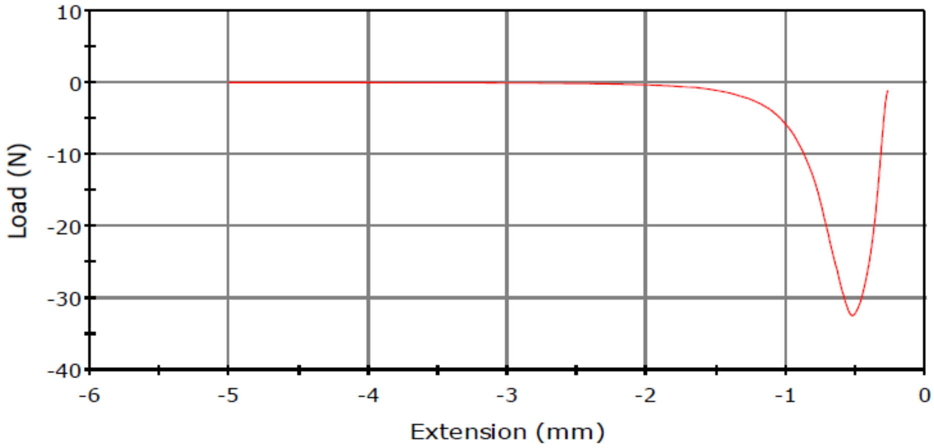

Figure D.6: Load-extension plot of three-point bend test for green strength of sample 1B1biii

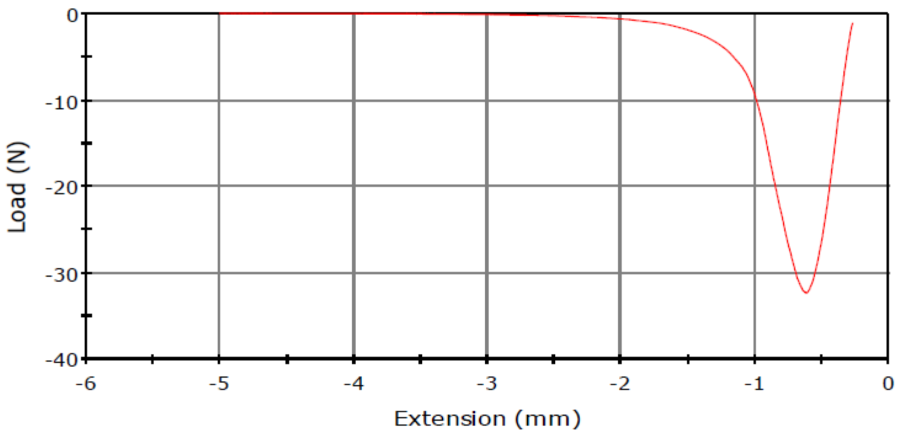

Figure D.7: Load-extension plot of three-point bend test for green strength of sample 2B1ai

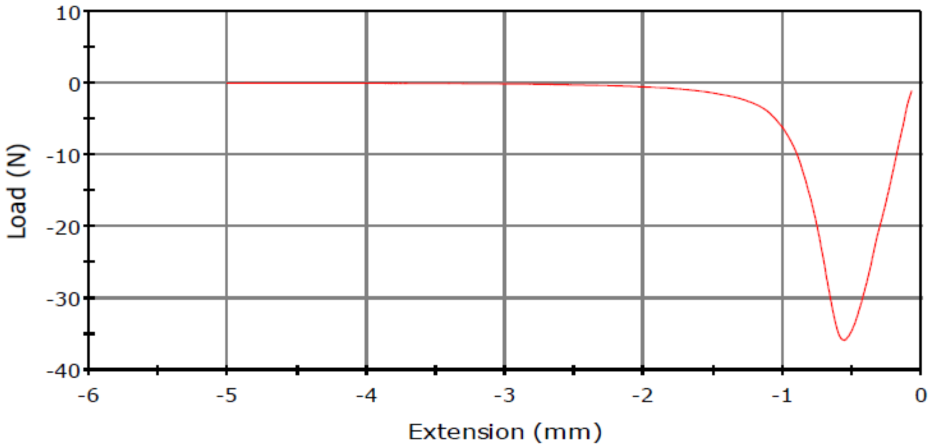

Figure D.8: Load-extension plot of three-point bend test for green strength of sample 2B1aii

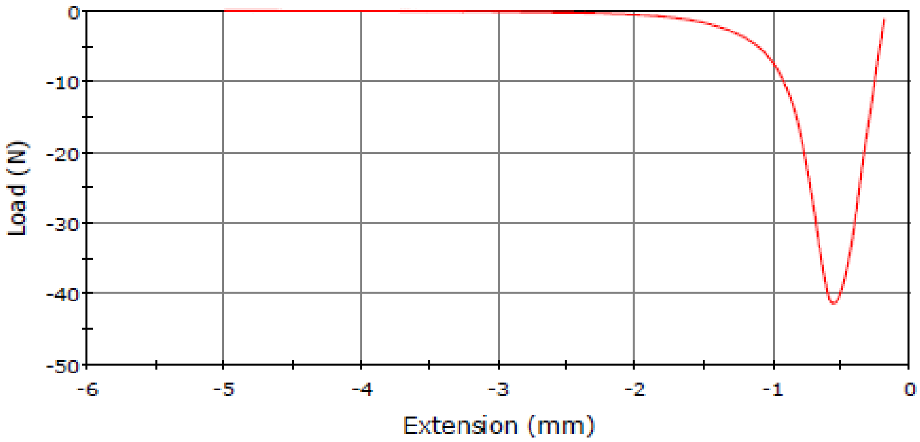

Figure D.9: Load-extension plot of three-point bend test for green strength of sample 2B1aiii

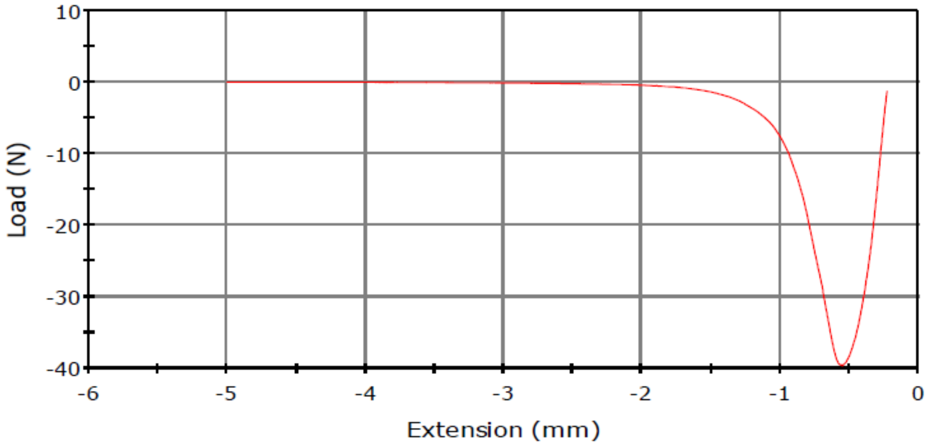

Figure D.10: Load-extension plot of three-point bend test for green strength of sample 2B1bi

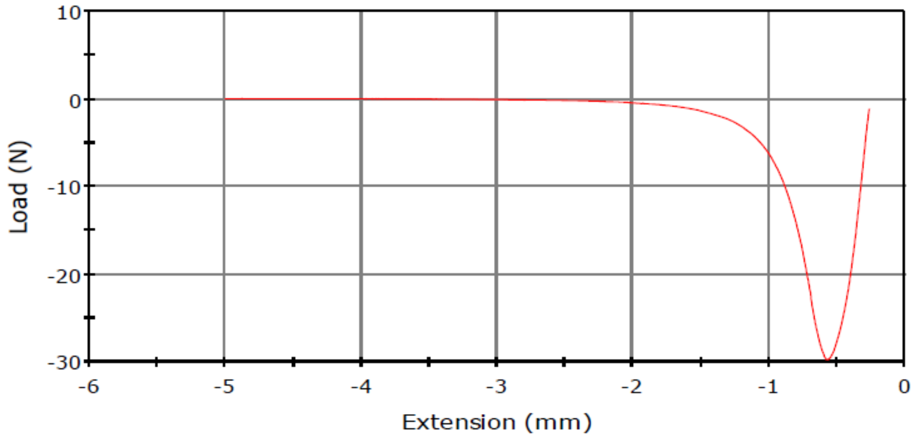

Figure D.11: Load-extension plot of three-point bend test for green strength of sample 2B1bii

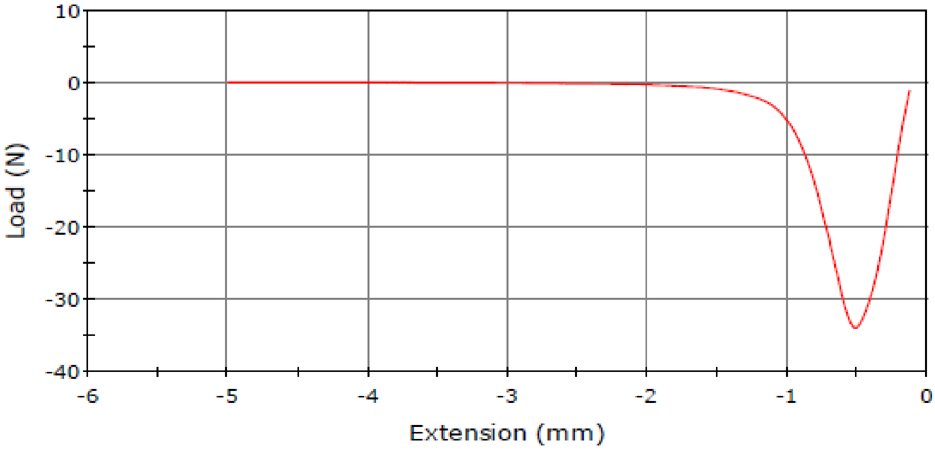

Figure D.12: Load-extension plot of three-point bend test for green strength of sample 2B1biii

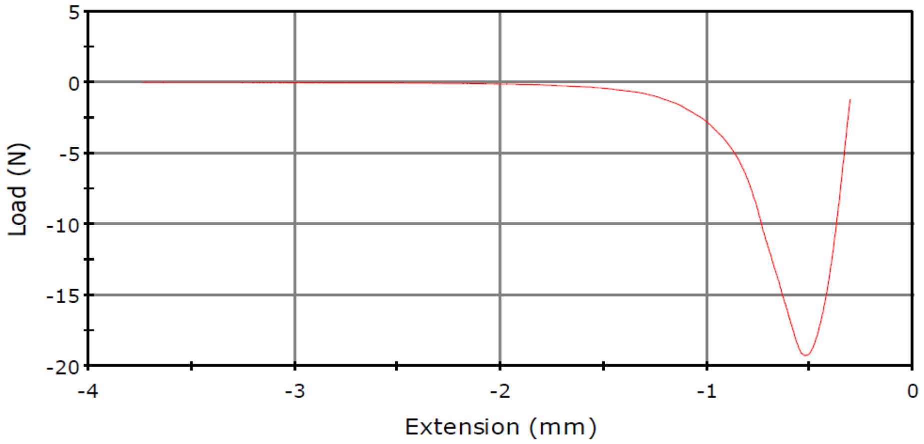

Figure D.13: Load-extension plot of three-point bend test for green strength of sample 1B2ai

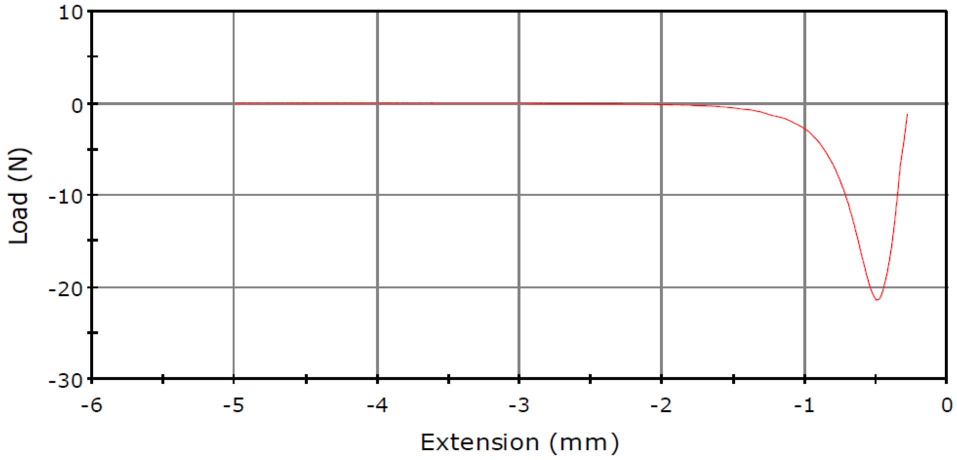

Figure D.14: Load-extension plot of three-point bend test for green strength of sample 1B2aii

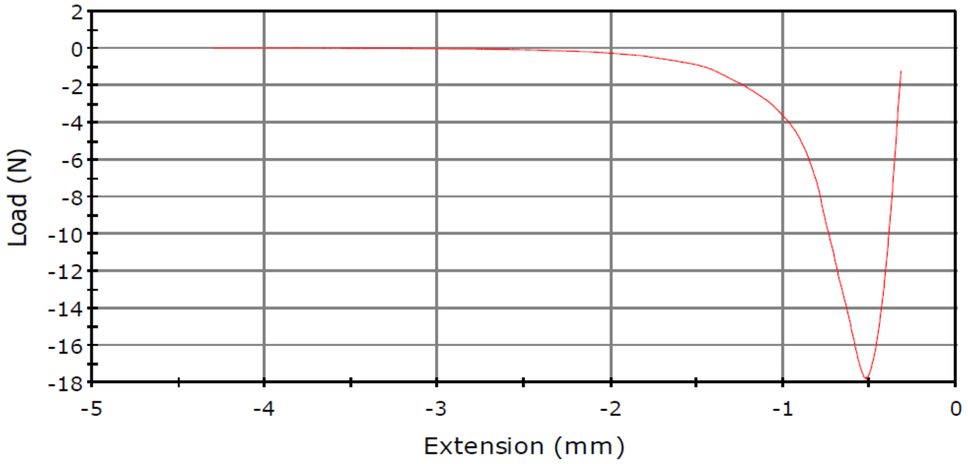

Figure D.15: Load-extension plot of three-point bend test for green strength of sample 1B2aiii

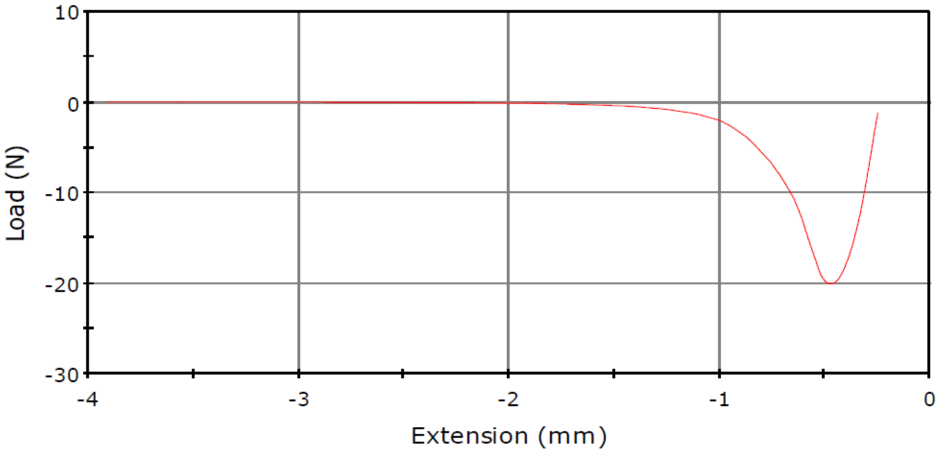

Figure D.16: Load-extension plot of three-point bend test for green strength of sample 1B2bi

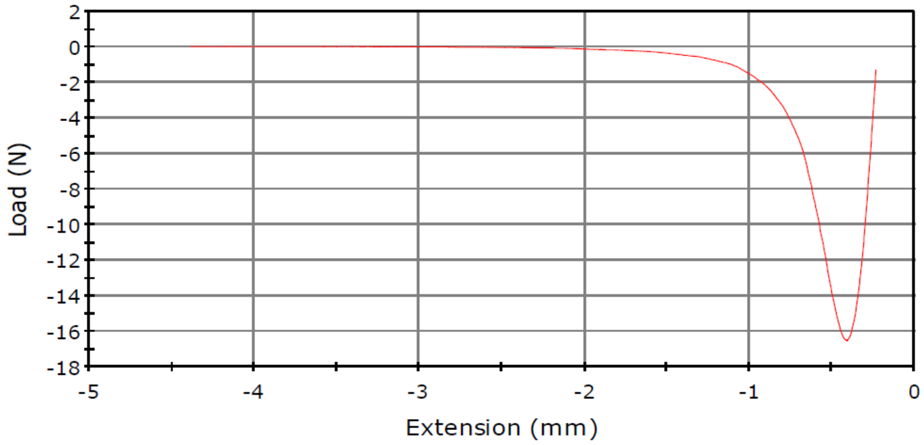

Figure D.17: Load-extension plot of three-point bend test for green strength of sample 1B2bii

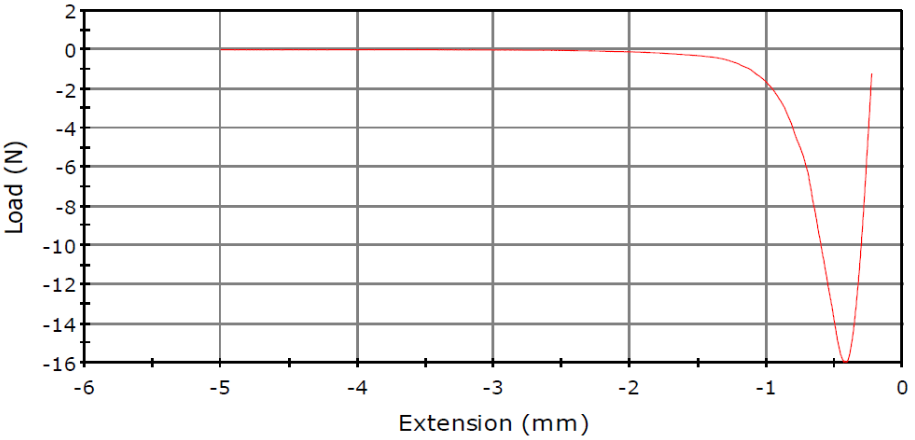

Figure D.18: Load-extension plot of three-point bend test for green strength of sample 1B2biii

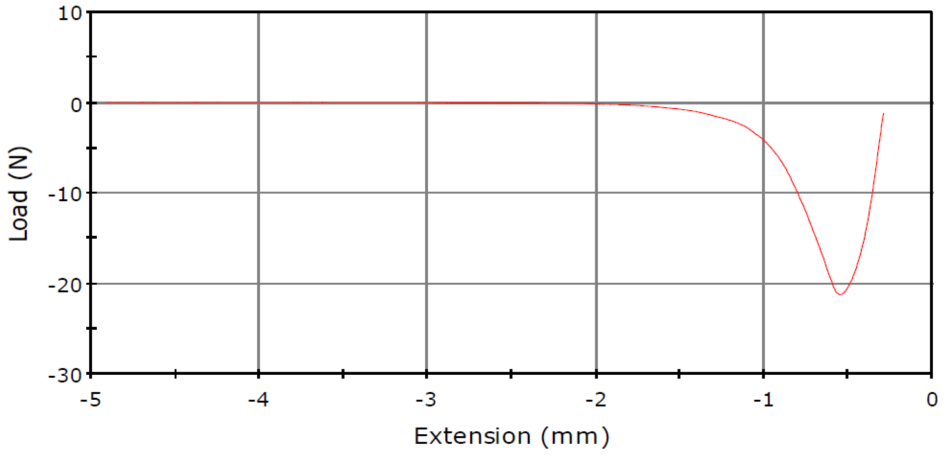

Figure D.19: Load-extension plot of three-point bend test for green strength of sample 2B2ai

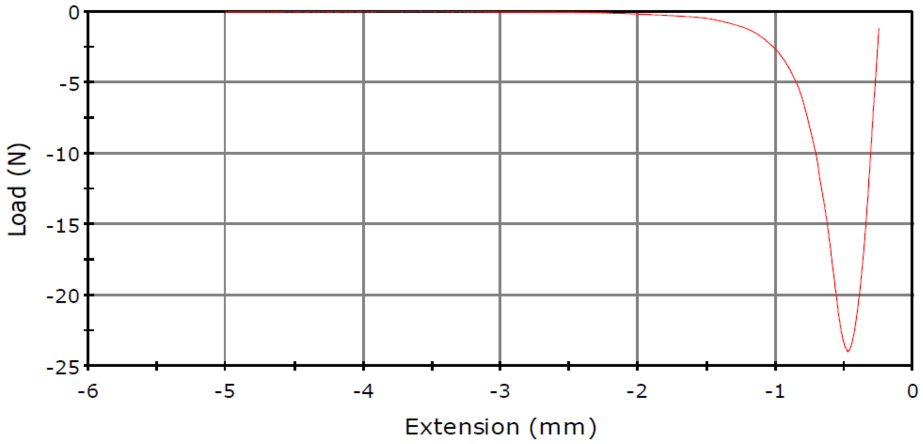

Figure D.20: Load-extension plot of three-point bend test for green strength of sample 2B2aii

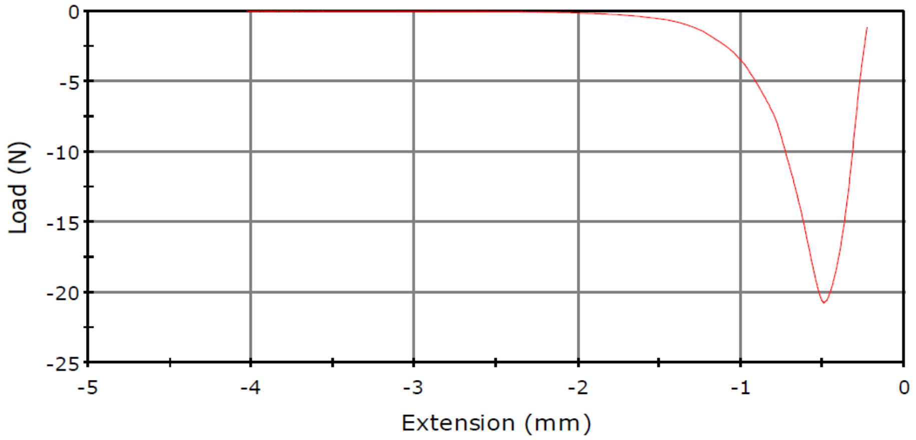

Figure D.21: Load-extension plot of three-point bend test for green strength of sample 2B2aiii

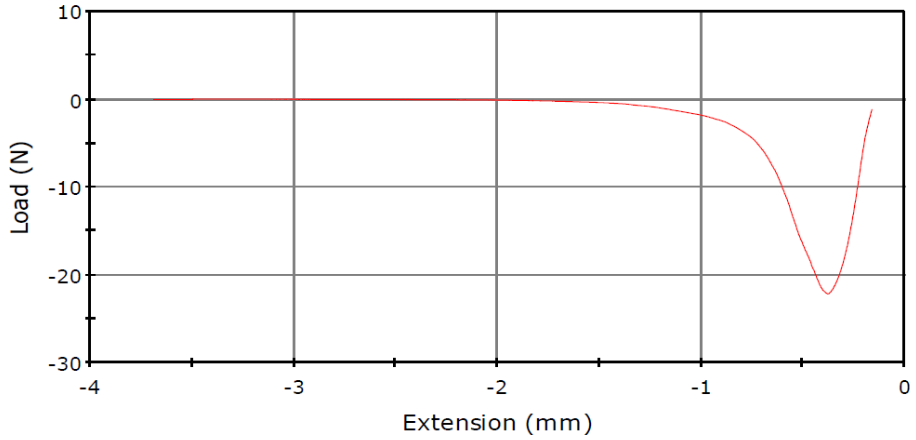

Figure D.22: Load-extension plot of three-point bend test for green strength of sample 2B2bi

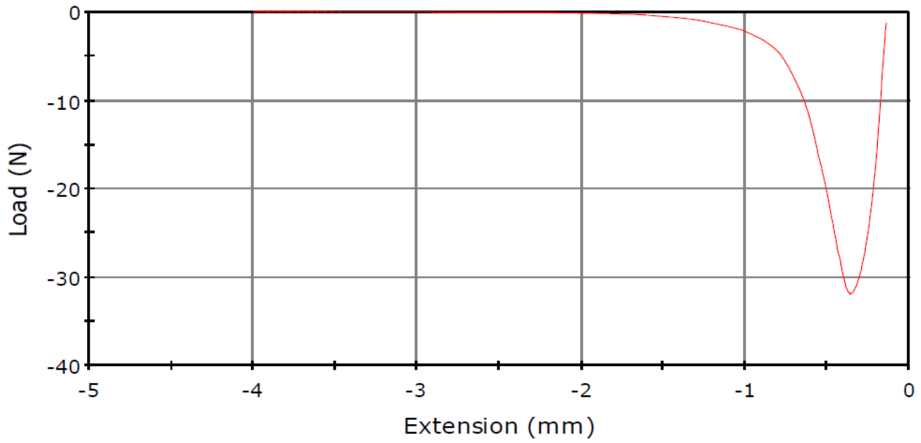

Figure D.23: Load-extension plot of three-point bend test for green strength of sample 2B2bii

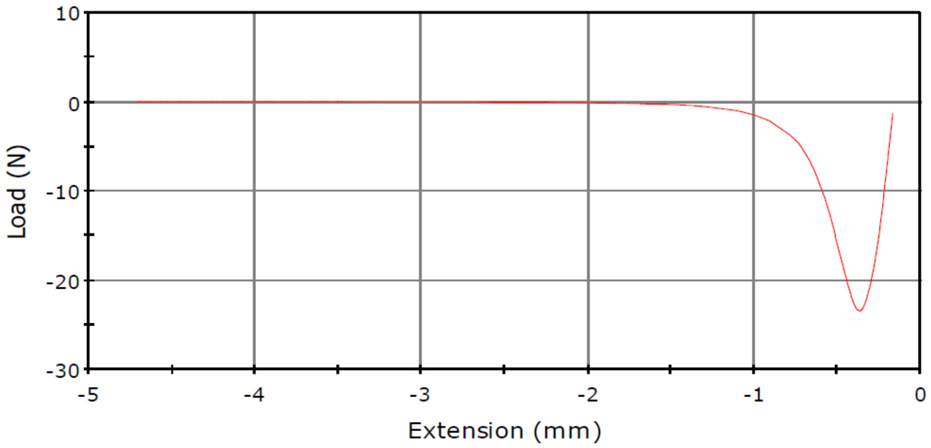

Figure D.24: Load-extension plot of three-point bend test for green strength of sample 2B2biii

Appendix E-Yield loci

Shear cell test results for internal friction angle determination

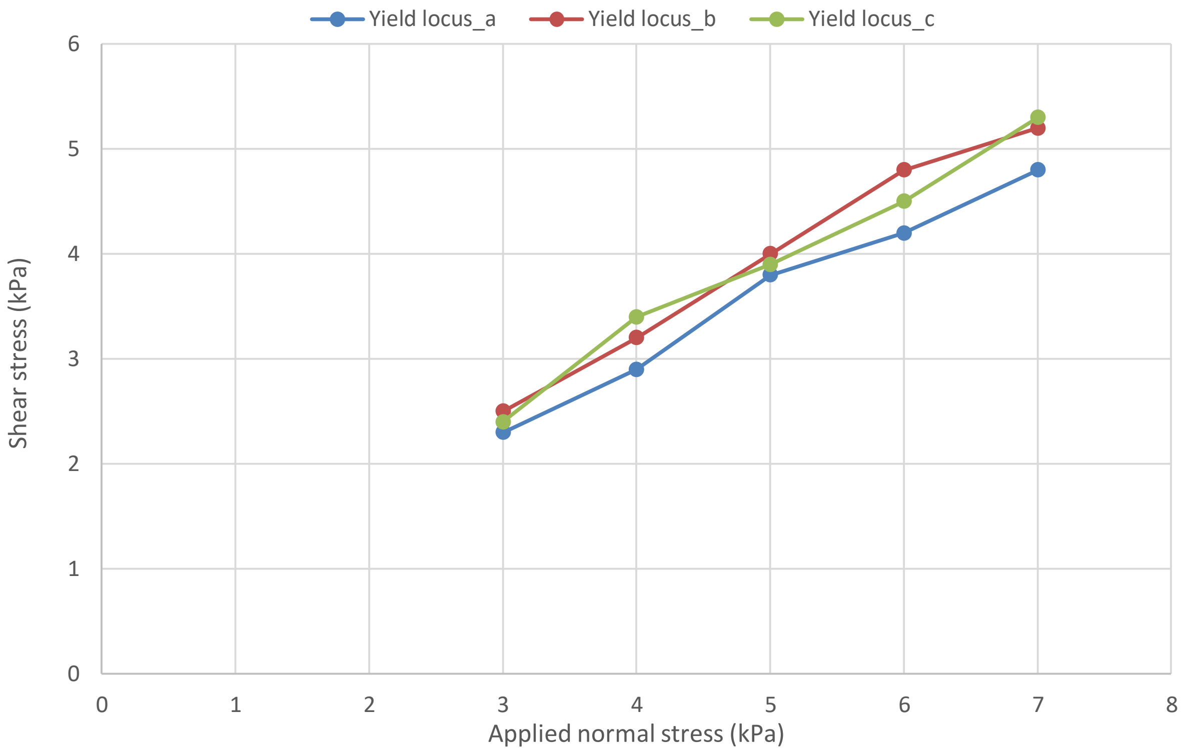

Figure E.1: Yield loci for B1 powder

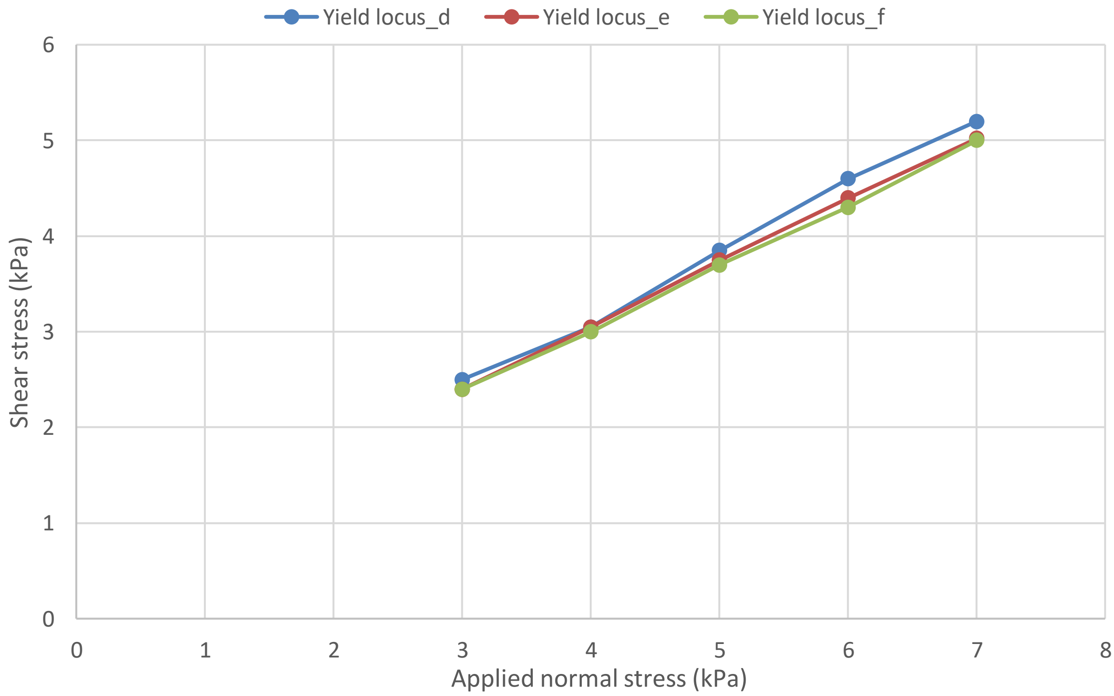

Figure E.2: Yield loci for B2 powder

Table E.1: Shear test results for B1 powder

Series name	UYS (kPa)	MPS (kPa)	MCS (kPa)	ff_c	AIF(E) (°)	AIF$_{average}$ (°)	BD (g/ml)	BD$_{average}$ (g/ml)
Yield locus_a	1.80	14.12	3.85	7.84	34.87	36.61 ± 1.511	1.97	1.94 ± 0.023
Yield locus_b	1.73	14.90	3.60	8.63	37.63		1.92	
Yield locus_c	1.52	15.02	3.68	9.88	37.32		1.93	

Table E.2: Shear test results for B2 powder

Series name	UYS (kPa)	MPS (kPa)	MCS (kPa)	ff_c	AIF(E) (°)	AIF(E)$_{average}$ (°)	BD (g/ml)	BD$_{average}$ (g/ml)
Yield locus_d	1.44	16.36	4.10	11.38	36.80	36.13 ± 0.5892	1.95	1.96 ± 0.0119
Yield locus_e	1.42	15.57	4.06	10.99	35.87		1.97	
Yield locus_f	1.29	16.13	4.24	12.47	35.71		1.97	

Nomenclature as follows:

UYS	Unconfined Yield Strength σ_c
MPS	Major Principal Stress σ_1
MCS	Minor Consolidation Stress σ_2
ff_c	Flow function index
AIF(E)	Effective Internal Friction Angle θ_E
BD	Bulk Density γ

Wall friction test results for B1 and B2 powder blends to determine wall friction angle

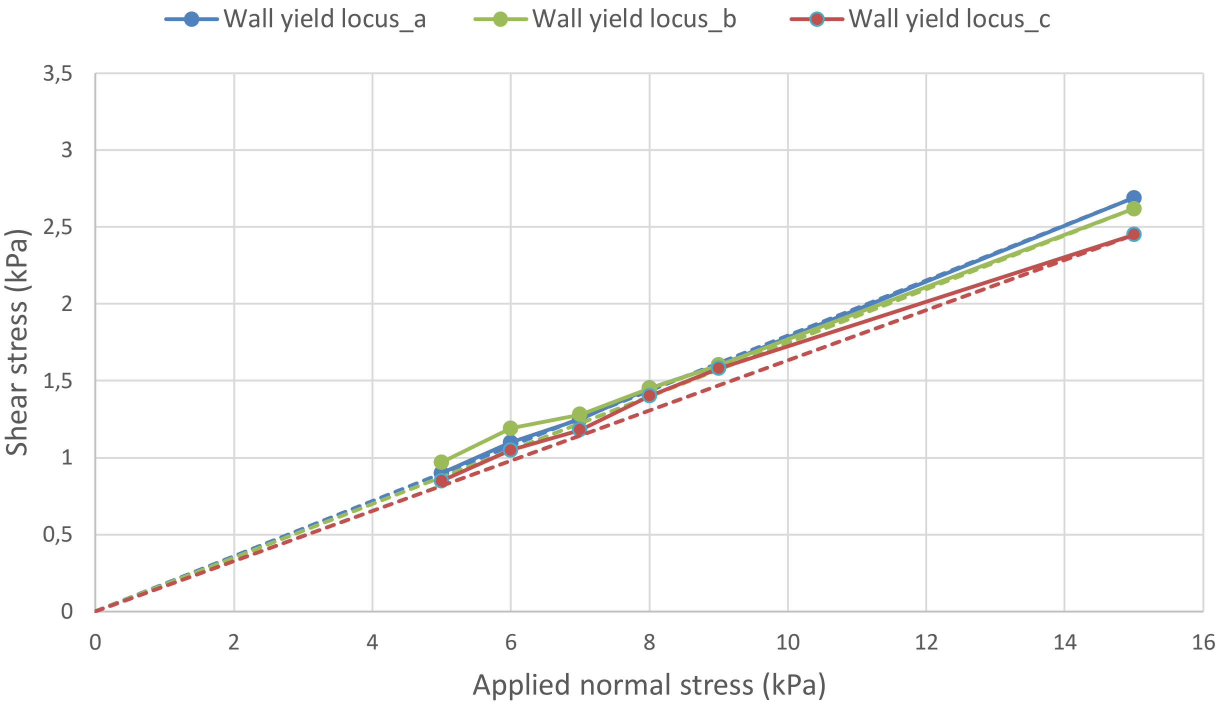

Figure E.3: Wall yield loci for B1 powder

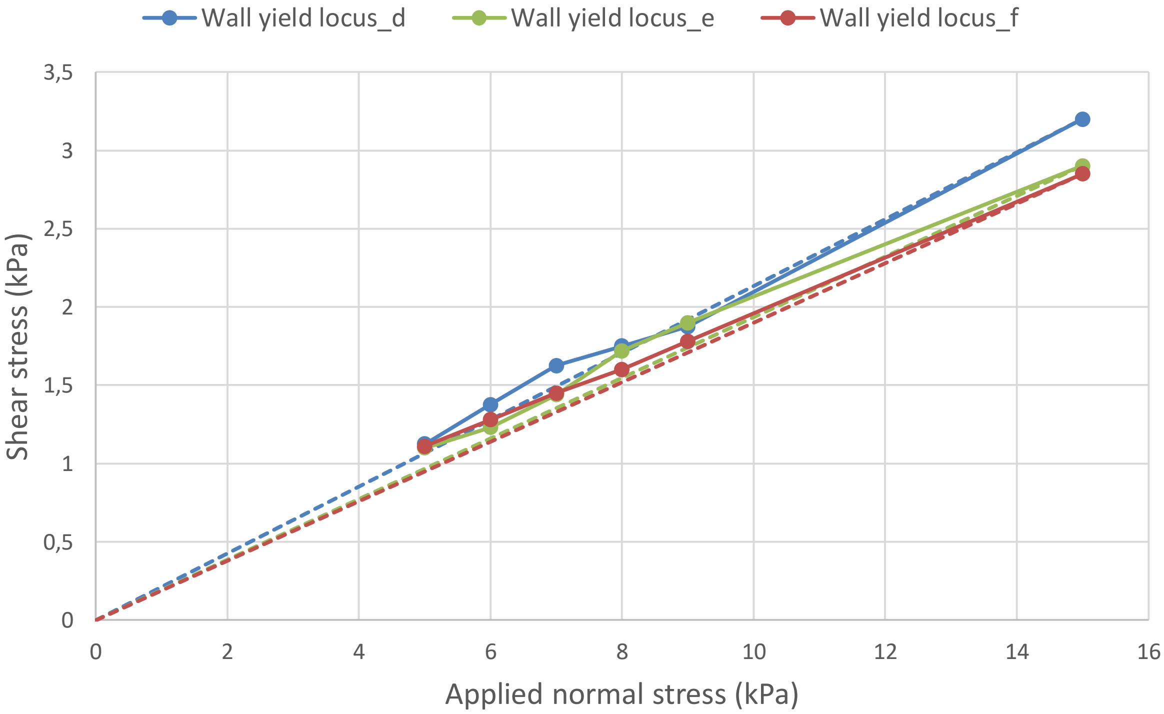

Figure E.4: Wall yield loci for B2 powder

Appendix F

Simulation results for roll gaps 0.5 and 1.5mm

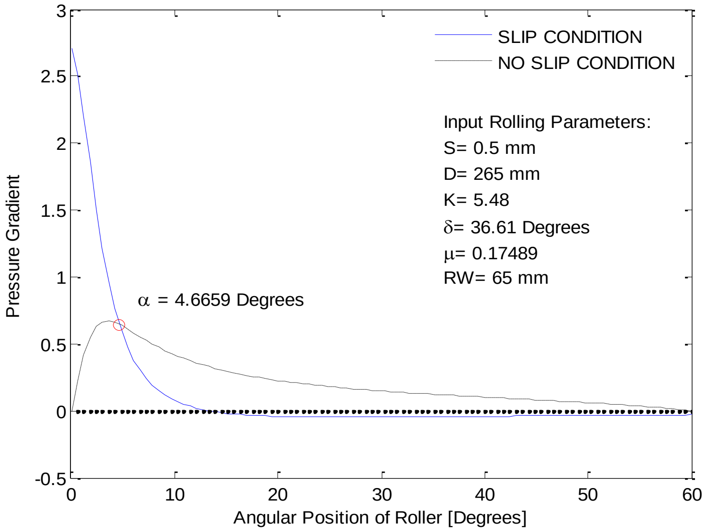

Figure F.1: Evaluation of nip angle for B1 powders at a roll gap of 0.5mm

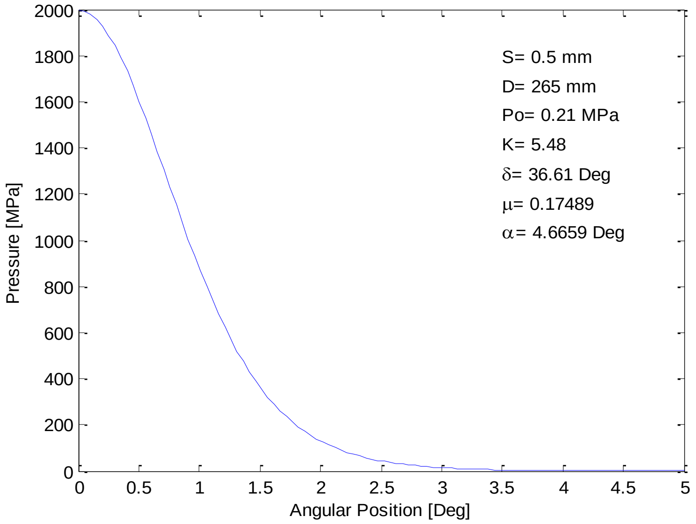

Figure F.2: Pressure distribution in nip region for B1 powders rolled at a 0.5mm roll gap

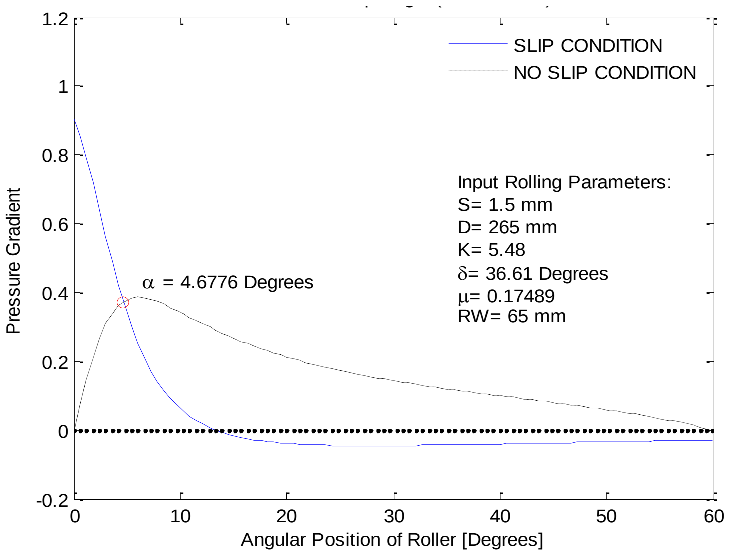

Figure F.3: Evaluation of nip angle for B1 powders at a roll gap of 1.5mm

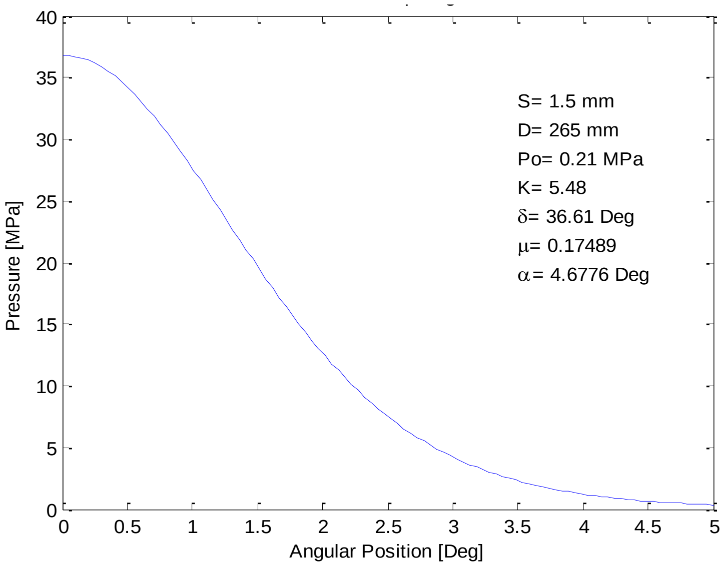

Figure F.4: Pressure distribution in nip region for B1 powders rolled at a 1.5mm roll gap

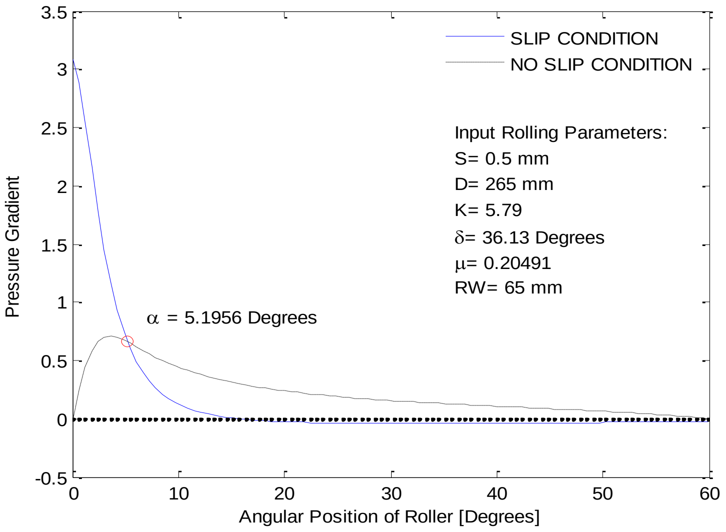

Figure F.5: Evaluation of nip angle for B2 powders at a roll gap of 0.5mm

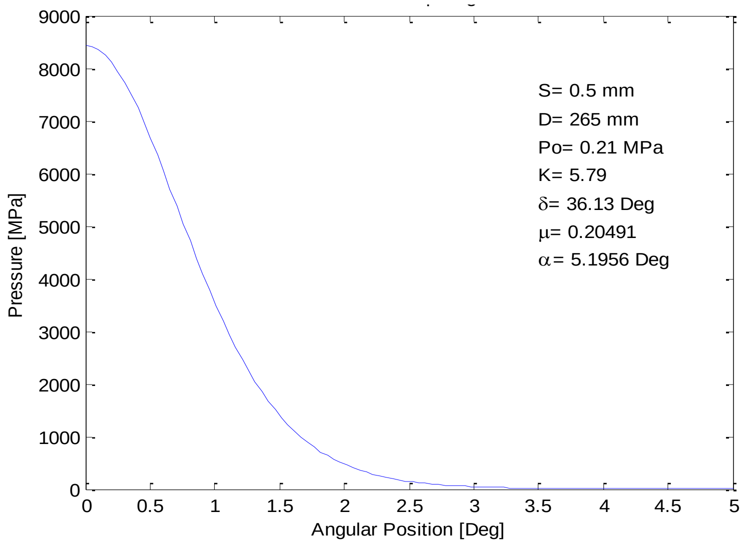

Figure F.6: Pressure distribution in nip region for B2 powders rolled at a 0.5mm roll gap

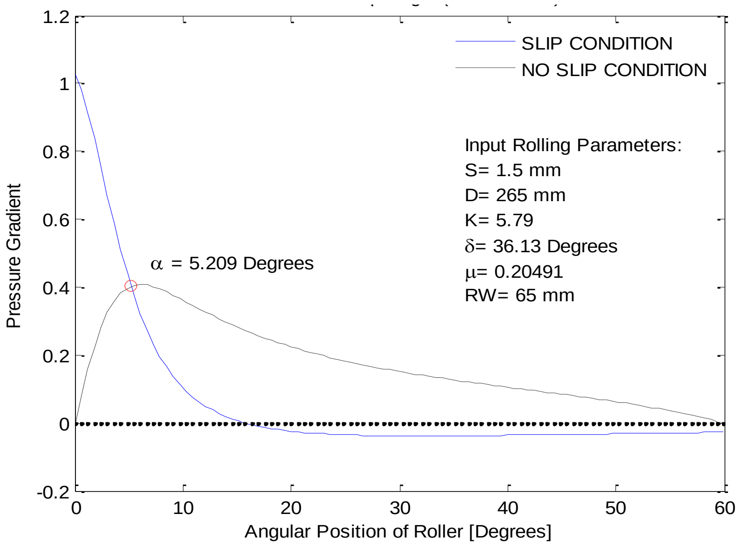

Figure F.7: Evaluation of nip angle for B2 powders at a roll gap of 1.5mm

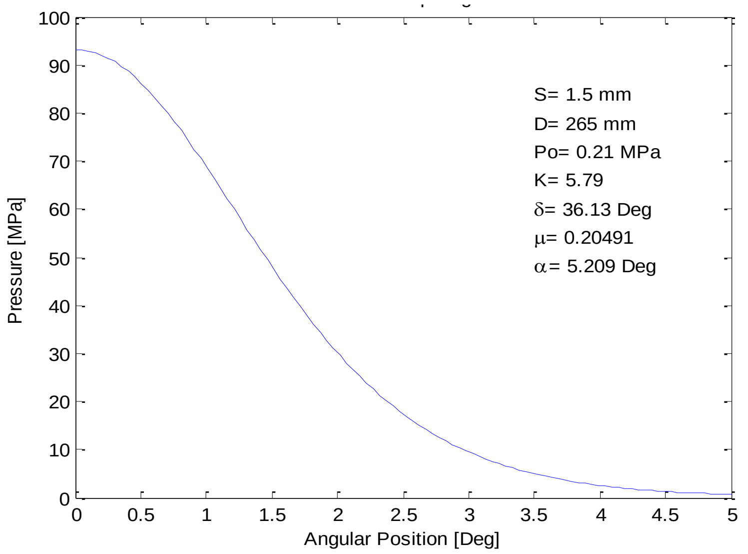

Figure F.8: Pressure distribution in nip region for B2 powders rolled at a 1.5mm roll gap